Dissertation

Mechanical characterization of human cortical bone tissue at the microscale

carried out for the purpose of obtaining the degree of Doctor rerum naturalium (Dr. rer. nat.), submitted at TU Wien, Faculty of Mechanical and Industrial Engineering, by

Mag. rer. nat. Vedran Nedelkovski

Mat.Nr.: 0509218

under the supervision of

Univ.Prof. Dipl.-Ing. Dr.sc.nat. Philipp J. Thurner

Institute of Lightweight Design and Structural Biomechanics, E317

Vienna, March 2023

Reviewed by

……………………..
Prof. Dr.sc.nat. Philipp Schneider
Faculty of Engineering and Physical Sciences
University of Southampton, United Kingdom

……………………..
Prof. DI Dr. techn. Christian Hellmich
Institute for Mechanics of Materials
and Structures, TU Wien, Austria

I confirm, that going to press of this thesis needs the confirmation of the examination committee.

Affidavit

I declare in lieu of oath, that I wrote this thesis and performed the associated research myself, using only literature cited in this volume. If text passages from sources are used literally, they are marked as such.

I confirm that this work is original and has not been submitted elsewhere for any examination, nor is it currently under consideration for a thesis elsewhere.

I acknowledge that the submitted work will be checked electronically-technically using suitable and state-of-the-art means (plagiarism detection software). On the one hand, this ensures that the submitted work was prepared according to the high-quality standards within the applicable rules to ensure good scientific practice "Code of Conduct" at the TU Wien. On the other hand, a comparison with other student theses avoids violations of my personal copyright.

_____   _____
City and Date   *Signature*

Acknowledgements

During my time as a doctoral student, it was my realization that accomplishing a contemporary doctorate is a collective achievement. According to the saying "it takes a village...", I am grateful for the community of young and senior colleagues that supported me in the creation of this thesis. First of all, I would like to thank my supervisor, Prof. Philipp Thurner, for the professional guidance and exciting scientific discussions. But even more I am grateful for your openness, caring and encouraging approach, that enabled me to grow beyond my limits and become confident and resilient in the exploration and research of new fields. Next, I would like to thank my office colleague Orestis Andriotis. Thank you for teaching me AFM and many tips and tricks, our daily talks and endless ideas, as well as your moral support through the hardships of a PhD student. Philipp and Orestis, I have particularly fond memories of the beginning years, when we started building the experimental biomechanics group, you definitely made my doctoral experience a better one. I would also like to thank my two reviewers, Prof. Christian Hellmich and Prof. Philipp Schneider, who agreed to review my thesis.

Further, I would like to thank my collaboration colleagues and fellow doctoral students: Rainer Hahn for sharing the knowledge and fun during the picoindenter experiments, Karin Wieland and Christoph Gasser for their endless motivation and efforts for the Raman measurements, but also for our coffees and discussions of the results, Martin Frank for your tireless and generous help with the micropillars data analysis. Many thanks and much appreciation also go to Prof. Heinz Pettermann for

ACKNOWLEDGMENTS

the review and help with the FE models, Robert Exler for the construction of our experimental setups, Olaf Lahayne and Eva Binder for the support with the testing of the bone micropillars.

I would also like to thank my students, Dorothee Marx and Stefanos Chatzitsopanis for sharing knowledge and learning together in our lab sessions. A central part of my experience as a doctoral student was the time at the Institute of Lightweight Design and Structural Biomechanics (ILSB) with its friendly and professional colleagues, for which I am thankful. In particular, I am grateful to have had these inspiring young scientists within the group of experimental biomechanics, Caitlyn Collins, Andreas Rohatschek, Matthis Nalbach and Martin Handelshauser.

I am forever thankful for my family, without them, my life and studies in Vienna would not have been possible. A huge thanks to all my friends and flatmates back then, Leni, Vale, Rudi for their moral and emotional support during the tough times. Last but not least, a sincere thank you to Lukáš for supporting, helping and just being there.

"Intelligence is the ability to adapt to change."

Stephen Hawking

Contents

CONTENTS

ABSTRACT

X

Abstract

Bone is a complex biological material, that can be considered as a lightweight nanocomposite consisting of an organic phase – collagen fibrils (mostly type I), non-collagenous proteins – and an inorganic phase – carbon-substituted hydroxyapatite (a calcium-phosphate mineral) – as well as water. It has been designed by nature, partially optimized for minimum total weight, to reconcile opposing mechanical properties such as stiffness and strength with toughness. This remarkable versatility is achieved by organization of its constituents into a complex hierarchical structure, from the nano- up to the macroscale, which ultimately enables bone to fulfill its mechanical protective and supporting function. In a hierarchically structured material, such as bone, the material properties of individual components at a lower hierarchical level determine the material properties of structures at the next, higher hierarchical level. Consequently, to fully understand bone mechanics, identification and quantification of the mechanical properties of all structures on every hierarchical level and the way these interact with each other is necessary. Though experimentally not entirely feasible, mechanical investigations of smaller structural levels can be performed to better our understanding of bone material and tissue.

Mechanical testing of whole bones and smaller bone samples has been performed in many studies since the beginning of bone research, about a century ago. On the other hand, atomic force microscopy (AFM) has enabled studying individual bone components at the nanoscale in recent decades. However, mechanical characterization of bone tissue at the microscale, where contributions of larger tissue porosities can be

ABSTRACT

avoided, has been comparatively scarce, except for nanoindentation, due to experimental challenges. In cortical bone, the prominent structures at the lower microscale are bone lamellae, which are the main focus of the present thesis. These are ordered layers of mineralized collagen fibrils, $2 - 10$ μm in thickness, typically arranged in concentrical manner around vascular (Haversian) canals to create the structures of the next hierarchical level, the osteons. Recent developments in experimental techniques for micromechanical characterization have made it feasible to prepare and test miniature, microscopically sized bone specimen (microbeams, micropillars) comprised of single or several bone lamellae. Compared to engineering materials, hard biological tissues, and specifically bone, pose challenges in the context of micromechanical testing, some of which, as detailed below, were addressed in the studies of this thesis.

To investigate the reliability of newly developed methods for micromechanical testing, the accuracy and sources of uncertainties regarding sample preparation and testing were considered in a first study, since these issues have not been discussed in previous studies. Finite element (FE) simulations of microbeam structures and experimental validation with bending of silicon microbeams were performed. It was found that the accuracy of the expected value from bending of Si microbeams was within 24 %, but errors from geometrical uncertainties can be as high as 50 %. Furthermore, boundary constraints of the tested micro-samples may lead to structural, in addition to material deformation mechanisms.

A remaining challenge in micromechanical testing of bone is full sample hydration. Therefore, the effect of hydration state of cortical bone tissue on micromechanical behaviour was investigated. For this an AFM based microbeam bending testing protocol was developed, enabling measurements of fully submerged and wet samples. Human cortical bone microbeams comprised of a single lamella were bent nondestructively both in air, and submerged in aqueous solution. Bending moduli were found to reduce up to 5 times upon rehydration and moreover, mechanical response changed from almost purely linear elastic to viscoelastic. The age range of healthy donors was $65 - 94$ years and a trend of lower dissipated energy with increasing age

was observed, but only in the rehydrated state. These findings are suggestive of the importance of water for the mechanical properties of bone even at the length scale of individual lamellae.

Last but not least, changes of bone material at the lamellar level due to osteoporosis were investigated. A protocol for micropillar compression was employed to test micropillars machined from single lamellae from the cortical portion of the femoral neck, as a specific fracture site of osteoporotic donors, which compared samples to age-matched donors. Bone samples from 8 osteoporotic and 7 control donors were compressed in a cyclic partial unloading manner. Micropillars showed viscoelastic, strain hardening behavior with unloading moduli reaching up to 50 GPa. No significant differences in most mechanical parameters were observed, except for lower unloading modulus and higher strain at max. stress for the osteoporotic female donor subgroup. However, results are not fully conclusive, due to limitations of low donor number and testing in not fully submerged, i.e. rehydrated state.

From the performed studies it becomes evident, that bone material, even at the microscale, where contributions of larger tissue porosities can be avoided, displays a different mechanical behavior compared to engineering materials, which brings specific challenges and limitations for mechanical characterization. So far, bone has mostly been considered as a linear elastic solid, which can be assumed only for very small deformations and a dehydrated state. However, in physiological, hydrated state bone transitions into a mechanically different material exhibiting lower moduli and viscoelastic behavior. Furthermore, bone is a living tissue that changes with ageing and pathology, whereby such changes can be implicated on every hierarchical level. Additional deformation mechanisms dependent on hydration state and composition, that are altered in the course of ageing and pathology could be overlayed with elastic deformation of bone material and should be considered in future studies. These insights should contribute towards a better understanding and design of mechanical testing of bone material, which would ultimately support the development of better diagnostic and treatment tools in the case of bone pathologies.

KURZFASSUNG

Kurzfassung

Knochen ist ein komplexes biologisches Material, das als Leichtbau-Nanokomposit-Werkstoff betrachtet werden kann. Es besteht aus einer organischen – Kollagenfibrillen (vor allem Typ I), nicht-kollagene Proteine – einer anorganischen Phase – kohlenstoff-substituiertes Hydroxylapatit (Calciumphosphat) – und Wasser. Evolutionsbiologisch haben sich knöcherne Strukturen einerseits wie Leichtbaukomponenten, also gewichtsoptimiert entwickelt. Andererseits, vereint Knochen als Material gegensätzliche mechanische Eigenschaften wie Steifigkeit und Festigkeit mit Zähigkeit. Diese außerordentliche Fähigkeit wird im Knochengewebe durch die Anordnung der nanoskaligen Bestandteile in eine komplexe hierarchische Struktur, von der Nano- bis zur makroskopischen Längenskala erreicht. Letztendlich, geben die Bestandteile und ihre Anordnung Knochen seine mechanische Schutz- und Stützfunktion. In einem hierarchisch aufgebauten Material, wie Knochen, bestimmen die mechanischen Eigenschaften der einzelnen Bestandteile einer niedrigeren hierarchischen Ebene die mechanischen Eigenschaften der Strukturelemente auf der nächsthöheren hierarchischen Ebene. Um Knochenmechanik zu verstehen, ist es infolgedessen notwendig, die mechanischen Eigenschaften aller Strukturen aller hierarchischen Ebenen und deren Interaktion zu identifizieren und quantifizieren. Obwohl dies experimentell nicht realisierbar ist, können mechanische Untersuchungen kleiner Strukturen durchgeführt werden, um ein besseres Verständnis der Mechanik des Knochenmaterials zu erzielen.

Mechanische Prüfungen von ganzen Knochen und kleineren (mm-großen) Knochenproben wurden bereits in vielen Studien seit Anfang der Knochenforschung, vor etwa

KURZFASSUNG

einem Jahrhundert durchgeführt. Komplementär, ermöglichte die Entwicklung und Anwendung der Rasterkraftmikroskopie Untersuchungen der einzelnen Knochenkomponenten in den letzten Dekaden. Im Vergleich, ist die mechanische Charakterisierung von Knochen auf der Mikroskala, abgesehen von Nanoindentationsexperimenten, aufgrund experimenteller Schwierigkeiten nur spärlich durchgeführt worden. Jedoch ist diese Längenskala sehr interessant. Beispielsweise können hier Beiträge größerer Gewebeporositäten ausgeschlossen werden. Die bedeutendsten Strukturen auf der Mikroebene sind die Knochenlamellen, die auch Fokus dieser Arbeit darstellen. Diese bestehen aus geordneten Schichten von mineralisierten Kollagenfibrillen, mit einer Dicke von $2-10$ μm, die meistens um vaskuläre (Haverssche) Kanäle konzentrisch angeordnet sind, und somit die Strukturen der nächsten hierarchischen Ebene, der Osteonen, formen. Neueste Entwicklungen experimenteller Techniken für mikromechanische Charakterisierung ermöglichen es miniaturisierte, mikroskopische Knochenproben (Mikrobalken, Mikrosäulen), bestehend aus einzelnen oder mehreren Knochenlamellen zu präparieren und zu testen. Im Vergleich zu technischen Werkstoffen, bringen harte biologische Materialien, insbesondere Knochen, im Kontext der Materialprüfung, eigene Herausforderungen mit sich. Diesen Herausforderungen sind die Studien dieser Arbeit gewidmet.

Um die Verlässlichkeit neuer entwickelten Methoden für die mikromechanische Prüfung von Knochengewebe zu untersuchen, wurden in einer ersten Studie Genauigkeit und Messunsicherheitsquellen bei der Probenvorbereitung und Prüfung untersucht, da diese in bestehenden Studien noch nicht behandelt worden sind. Hier wurden Finite Elemente (FE) Simulationen von Mikrobalken und experimentelle Validierung mittels Biegeversuchen an Mikrobalken aus Silizium durchgeführt. Es stellte sich heraus, dass die Genauigkeit des Erwartungswertes aus Biegeversuchen an Si Mikrobalken innerhalb 24 % gegeben ist, allerdings können Fehler aufgrund geometrischer Unsicherheiten so groß wie 50 % werden. Außerdem, können die Randbedingungen der getesteten Mikroproben zu strukturellen, zusätzlich zu materiellen Deformationsmechanismen führen.

XVI

Eine andauernde Herausforderung bei der mikromechanischen Prüfung von Knochen ist die vollständige Hydrierung der Proben. Daher wurde in einer zweiten Studie der Effekt des Hydrierungszustandes auf das mikromechanische Verhalten des kortikalen Knochengewebes untersucht. Dafür wurde ein Rasterkraftmikroskop-basiertes Versuchsprotokoll entwickelt, das Biegungs-Messungen an vollständig hydrierten Mikrobalken ermöglicht. Mikrobalken aus humanem kortikalen Knochen, bestehend aus einer einzelnen Knochenlamelle wurden somit nicht-destruktiv, sowohl in Luft als auch hydriert in wässriger Lösung unter Biegung getestet. Die gemessenen Biegemoduli der rehydrierten Proben waren um bis zu 5 fach niedriger als im trockenen Zustand. Zudem, änderte sich das mechanische Verhalten von fast rein linear elastisch auf viskoelastisch. Die Altersspanne der gesunden Spender war 65 – 94 Jahre und ein Trend niedrigerer dissipierter Energie mit steigendem Alter konnte festgestellt werden. Dies allerdings nur im rehydrierten Zustand. Diese Resultate sind indikativ für die Bedeutung von Wasser für die mechanischen Eigenschaften von Knochen, sogar auf der Längenskala einzelner Knochenlamellen.

Zuletzt, wurden in einer dritten Studie die potenziellen Veränderungen der mechanischen Eigenschaften von Knochenmaterial auf der lamellaren Ebene aufgrund von Osteoporose untersucht. Ein Protokoll für einen Druckversuch an Mikrosäulen wurde herangezogen um Proben bestehend aus einzelnen Knochenlamellen aus der Kortikalis des Oberschenkelhalses unter Druckbelastung zu testen. Der Oberschenkelhals ist eine relevante Bruchstelle bei osteoporotischen Patienten. Hier wurden Proben von osteoporotischen und gesunden Spender_innen verglichen. Knochenproben von 8 osteoporotischen und 7 gesunden Spender_innen wurden mittels zyklischen partiellen Entlastung unter Druckbelastung getestet. Das Verhalten der Mikrosäulen war viskoelastisch und zeigte Verfestigung, wobei Entlastungsmoduli bis zu 50 GPa erreichten. Es wurden keine signifikanten Unterschiede in den meisten mechanischen Parametern festgestellt, außer einen niedrigeren Entlastungsmodul und höhere Verzerrung bei maximaler Spannung bei der osteoporotischen weiblichen Untergruppe. Diese deutet auf eine mögliche pathologische Veränderung hin. Allerdings, müssen die Resultate,

KURZFASSUNG

aufgrund limitierter Anzahl von Spender_innen, Probenanzahl und Trockenheit mit Vorsicht behandelt werden.

Aus den durchgeführten Studien ergab sich die Einsicht, dass Knochenmaterial, auch auf der Mikroebene, wo Effekte größerer Porositäten vermieden werden können, ein anderes mechanisches Verhalten im Vergleich zu klassischen technischen Werkstoffen aufweist. Dies bringt eigene Herausforderungen und Limitierungen bei der mechanischen Charakterisierung mit sich. Bis heute, ist Knochen meistens als linear elastischer Festkörper betrachtet worden, was streng genommen nur für sehr kleine Deformationen und einen dehydrierten Zustand angenommen werden kann. Im physiologischen, hydrierten Zustand, wird Knochenmaterial zum einen weniger steif (niedrigere Moduli) und zum anderen viskoelastisch. Außerdem, ist Knochen ein lebendes Gewebe, das sich im Laufe von Alterung und Pathologien ändern kann, wobei Änderungen auf jeder hierarchischen Ebene stattfinden können. Zusätzliche Deformationsmechanismen, die vom Hydrierungszustand und Zusammensetzung abhängen und sich ebenfalls im Laufe von Alterung und Pathologien ändern, könnten der elastischen Deformation von Knochenmaterial überlagert sein und sollten in künftigen Studien miteinbezogen werden. Solche Erkenntnisse können zu einem besseren Verständnis und Design von besseren mechanischen Prüfprotokollen von Knochenmaterial beitragen. Letztendlich würde dies die Entwicklung besserer diagnostischer und therapeutischer Maßnahmen bei Knochenpathologien unterstützen.

XVIII

List of Figures

LIST OF FIGURES

List of Tables

Chapter 1

Introduction

Bone tissue is a biological nano-composite material comprised of an organic phase: collagen type I fibrils, non-collagenous proteins (NCPs) and an inorganic phase: hydroxyapatite (a calcium phosphate mineral) and water. It is designed by nature on the lightweight principle, i.e. achieving high stiffness while retaining low weight. Moreover, in the context of composite structures, it is able to combine generally opposing mechanical properties, such as strength and toughness, due to a complex hierarchical structure from the nano- to the macroscale [154, 200]. In such a hierarchical architecture, the apparent mechanical properties, e.g. stiffness, strength, toughness etc. of a structure at a larger scale are determined by the mechanical properties of the underlying structural elements at the lower length-scales. So, to better understand and be able to predict bone's mechanical behavior, knowledge of the mechanics of all structures and the way they interact with each other at every length-scale is necessary. This in turn implies that mechanical testing of bone material at every length-scale should be performed. Mechanical testing of bone has, on the one hand, been conducted on the macroscale for at least half of a century [26, 34, 170, 203] and on the other hand only in the last two decades on the micro- and nanoscale, due to experimental advancements in atomic force microscopy (AFM) techniques [5, 41, 62, 63, 92, 180, 181, 194]. In addition, at the level of bone struc-

tures at the microscale, e.g. bone lamellae, comparatively much less studies have been performed, due to experimental challenges in preparing as well as mechanical testing of microscopic or microscale samples. Utilizing focused ion beam (FIB) for milling at the microscale, beam- and pillar-shaped microstructures comprised of single bone lamellae have been tested under bending [82, 84] and compression [85, 109, 167, 169], either with an atomic force microscope (AFM) or a nanoindenter. It is noteworthy, that all of these studies have been conducted in a dehydrated or only partially rehydrated state (except for [169]), and/or on bone material from animal origin (murine, ovine and bovine), whereas studies of this type conducted on human bone material have, to the best of the author's knowledge, not been reported.

From mechanical point of view, bone tissue is inhomogeneous – mechanical properties of bone tissue are different at different anatomical locations as well as different positions within the same bone [129] and anisotropic – mechanical properties are different in different anatomical directions, e.g. axial vs. transverse. In addition, bone tissue is porous due to the vascularization present in the form of Haversian canals and the lacuno-canalicular network of the embedded osteocytes at the microscale [29]. At the macroscopic scale, the mechanics of whole bones are predominantly governed by porosity, where e.g. changes in porosity account for more than 75 % variability of the strength of cortical bone [29, 120]. However, in a mechanical context, porosity as a structural parameter for mechanical characterization is related to the amount, i.e. quantity of bone material present and does not include information about the mechanical quality of the bone material itself. To exclude (or largely reduce) the influence of porosity, one approach is to test bone material at lower length-scales, e.g. micro- and nanoscale, where larger porosities can be avoided by choosing an appropriate region of interest (ROI).

Furthermore, bone is not a static material and is subjected to metabolic activity and undergoes a constant process of remodeling, during which mechanical properties of the tissue can be adapted or altered. The major two factors affecting bone mechanical behavior are age and pathology, the effects of which are often superimposed. The ability

to test mechanical properties of the bone substance itself, i.e. the bone extracellular matrix (ECM) may provide invaluable information and insight into mechanisms that lead to changes of bone mechanics. A prominent example underpinning the necessity of detecting changes in the mechanical performance of bone tissue is the pathology of osteoporosis. The current gold-standard for diagnosis is assessment of the bone mineral density (BMD), which however, can only account for 60 % of the variation in bone fragility, generally resulting in a broad under-diagnosis of osteoporosis, as it is unable to capture further compositional and structural alterations beyond amount of bone tissue present [138]. Early detection of altered mechanical performance would contribute to timely onset of therapeutic measures and ultimately reducing the risk of fractures. Direct mechanical characterization implies performing mechanical testing, which requires samples of certain size and geometry prepared from the material of interest (typical specimen size lies in the mm to several cm range), as well as choice of applied loading case, e.g. compression, tension, bending, etc. In the case of bone, ideally, such samples should be extracted from a tissue portion of a relevant site, e.g. fracture site, due to bone's inhomogeneity and additionally, unknown correlation between mechanical properties of different tissue positions within the same bone or between different bones within the same organism. One of the most prevalent fractures due to osteoporosis are hip fractures occurring predominantly at the femoral neck [86]. Zooming in at the local microscale, all of the regions of the femoral neck do not get loaded in the same manner, so the bone tissue does not experience the same type (compression or tension) and magnitude of mechanical loading. Moreover, the macroscopic size and thus the amount of potentially available material for testing of the femoral neck is very limited (in the mm range).

Therefore, considering the above discussed aspects, the necessity of investigations of the bone material itself at the microscale and the advantages such measurements would provide, becomes apparent, where the influence of larger porosities can be largely circumvented and even the smallest macroscopic volume of tissue could provide more than sufficient material for mechanical testing. Currently, the time and

efforts for mechanical testing of extracted bone material from patients would be too high for a direct clinical implementation. Nevertheless, the insights gained regarding the mechanisms leading to alteration of the mechanical properties of bone tissue, would provide valuable information and contribute towards further development of diagnosing and treating bone fragility in the context of ageing and osteoporosis. The bone tissue structures encountered at the lower microscopic length scale, i.e. one to several microns, are the bone lamellae, their interfaces (interlamellar interfaces), cement lines of osteons and interstitial bone located among osteons [154, 200]. For the above-stated arguments of lack of sufficient data on the mechanical properties of bone structures at the microscale, largely reducing the effect of porosity in mechanical tests and unravelling changes of mechanical properties due to ageing and pathology, the main focus of this thesis lies on bone lamellae, which represent packed layers of 2 - 10 μm thickness and are constituted of the basic building block of bone material – the mineralized collagen fibril. These lamellar layers are further stacked with different orientations and are concentrically ordered to form the circular structures of the next, higher hierarchical level – the osteons, whose diameters are in the $100 - 400$ μm range (see Chapter 2.1.2.). Bone lamellae are created and subject to metabolic changes in the process of bone remodeling, which may alter their composition and consequently their mechanical properties. To date, there have only been few studies conducted at the level of single bone lamellae and major aspects regarding their mechanics remain to be investigated, such as the effects of dehydration and rehydration, donor age and pathology. Furthermore, collecting data from bone material of human origin should impel findings of fundamental research towards clinical relevance.

1.1 Hypothesis

All of the above discussed aspects indicate that there are many influences that may affect bone's mechanical performance at different hierarchical levels, out of which the structures at the lower microscale have been investigated least, so far. Mechanical

testing of bone lamellae offers the possibility of eliminating the influence of larger porosities and directly probing the mechanical properties of the bone material, i.e. bone's ECM itself. Should there indeed be changes in mechanical parameters of bone material translated through the metabolic turnover of the tissue in the course of ageing and pathology, then they should be investigated at this level. Hence, the present work is motivated by the following hypotheses:

(i) It is possible to develop a mechanical test protocol to investigate cortical bone at the level of individual lamellae in a hydrated environment.

(ii) There are changes in the mechanical properties of bone tissue beyond porosity, at the level of individual bone lamellae due to ageing.

(iii) There are changes in the mechanical properties of bone tissue beyond porosity, at the level of individual bone lamellae due to pathology/osteoporosis.

Ultimately, data obtained from mechanical testing of bone structures at the microscale is expected to provide valuable input for computational modeling for better prediction of tissue behavior and scaled-up whole bone performance in normal and critical scenarios, e.g. fracture. Moreover, insights and understanding of bone's mechanical behavior and mechanisms could contribute to the development of new, more accurate and patient specific diagnostic tools as well as inspire novel therapeutic methods.

1.2 Scope of work and structure of thesis

The present work focuses on the mechanical characterization of bone's extra-cellular matrix (ECM), i.e. bone material itself, attempting to eliminate or largely reduce the effects of porosities in the tissue by testing at the microscale. For this purpose, from the two main types of bone tissue, cortical and trabecular, experimental investigations were solely focused on cortical bone for practical, experimental reasons of sample extraction, as it is of denser, more compact nature, and is significantly lower in

porosity (5 – 15 %) than trabecular, cancellous (40 – 95 %) bone [29, 34, 120], although at the microscale these two types of tissue might be more similar.

Most of the mechanical assessment of bone tissue at the micrometer length-scale has been conducted via nanoindentation [102, 181], a technique widely used due to its convenience and straightforward application. However, extraction of mechanical parameters obtained by nanoindentation, mainly the indentation modulus, are based on theoretical assumptions about the material and are derived from a complex multiaxial stress state, which, when induced in an inhomogeneous and anisotropic material like bone often remains ambiguous for interpretation and thus restricted in its investigative potential of underlying deformation mechanisms.

Comparatively to nanoindentation, only a very limited number of experiments have been performed on isolated microscopic bone specimens in recent decades. Most of these were utilizing the focused ion beam (FIB) technique, to perform bending [24, 82, 84] or uniaxial compression tests [85, 109, 168, 169] at the microscale. The main advantage of such approaches is in the more well-defined, more homogeneous stress state induced within a specimen, from which mechanical parameters can be directly and easily determined and interpreted from measured curves. However, reported values of these studies for e.g. "elastic" moduli lie in a broader range (1 – 30 GPa) and bone material of different animal origin (murine, ovine, bovine) was used, which makes a systematic comparison difficult. Moreover, despite their promise calibration and precision of these novel methods for micromechanical testing of bone has essentially not been reported or discussed.

The present thesis is structured in following manner: Since the main object of investigation in this work is bone material, the following Chapter 2 is dedicated to background information regarding bone composition and its complex hierarchical structure, the mechanical performance achieved through such a structure and the factors assumed to have the largest impact on altering the mechanical behavior of the tissue, i.e. age and pathology. Subsequently, the experimental techniques for sam-

ple preparation and testing of bone material enabling investigations at the microscale used throughout the studies in this work are presented in Chapter 3.

To address aspects of reliability and contribute towards further development of micromechanical characterization methods for biological tissues, the first study in this thesis (Chapter 4) was conducted to investigate the precision of such studies and sources of errors in the calculation of mechanical parameters. For this purpose, a microscopic three-point bending test was performed with a material of known mechanical constants – silicon as a validation study and further, experimental uncertainties due to imperfections or deviations of nominal geometry were investigated via finite element modeling (FEM) of used structures and load cases in micromechanical experiment, e.g. beams loaded in bending and pillars loaded in compression.

Next, an experimental study was designed to enable the micromechanical measurement of cortical bone microbeams in a bending configuration in fully rehydrated conditions (Chapter 5). A method utilizing atomic force microscopy (AFM) in a cantilever-based bending configuration combined with a custom-made water bath for fully submerged application was developed for a three-point bending measurement performed at the microscale. For this study, microbeams from human cortical bone from the femur were prepared and tested both in dehydrated and rehydrated condition. Moreover, the age range of the donors spanned (65 – 94) years to investigate into age related changes of bone tissue at the level of single lamellae.

The third study conducted in this thesis (Chapter 6) used an adapted version of a previously established protocol for isolation of cortical bone micropillars and their transfer onto a rigid substrate for testing under uniaxial compression. Bone material of two donor groups, osteoporotic and control group (cadaveric donors of no diagnosed bone pathology) extracted from a relevant fracture site - the femoral neck, were used to investigate putative changes of bone material due to the pathology of osteoporosis.

Finally, the outcomes of the conducted experimental approaches are summarized and discussed in Chapter 7. Particularly interesting is the direct demonstration of the role

of water and rehydration of bone material regarding its mechanical behavior and the possibly related effect of ageing on hydration ability of the tissue. Even more intriguing are the unexpected results regarding the effect of osteoporosis on the mechanics of the tissue at the microscale. Although new insights could be gained through such micromechanical experiments, the time costs and experimental complexity of such approaches become evident. These challenges are discussed in the context of direct translation into clinical practice.

Chapter 2

Background

2.1 Bone composition and structure

2.1.1 The basic building block of bone and bone composition: mineralized collagen fibrils, water, non-collagenous proteins (NCPs)

Mineralized collagen fibrils

In bone literature the mineralized collagen fibril is regarded and referred to as the main building block of bone material [28, 181, 200]. It is comprised of collagen (mostly type I) and carbonated hydroxyapatite (a calcium phosphate mineral). Collagen protein molecules are a larger family of chemically similar, but distinct proteins with different structures, of which the fibril-forming collagen type I is most abundant in bone. The molecular structure of the collagen type I protein is a triple helix, named tropocollagen, which consists of three polypeptide chains: two identical, denoted as α1 and one different, α2 chain, fig. 2.1top [44]. Tropocollagen of this type is generally not found in its singular form, as it associates and undergoes self-assembly with other tropocollagen molecules to create a larger fibrillar structure, the collagen fibril (see
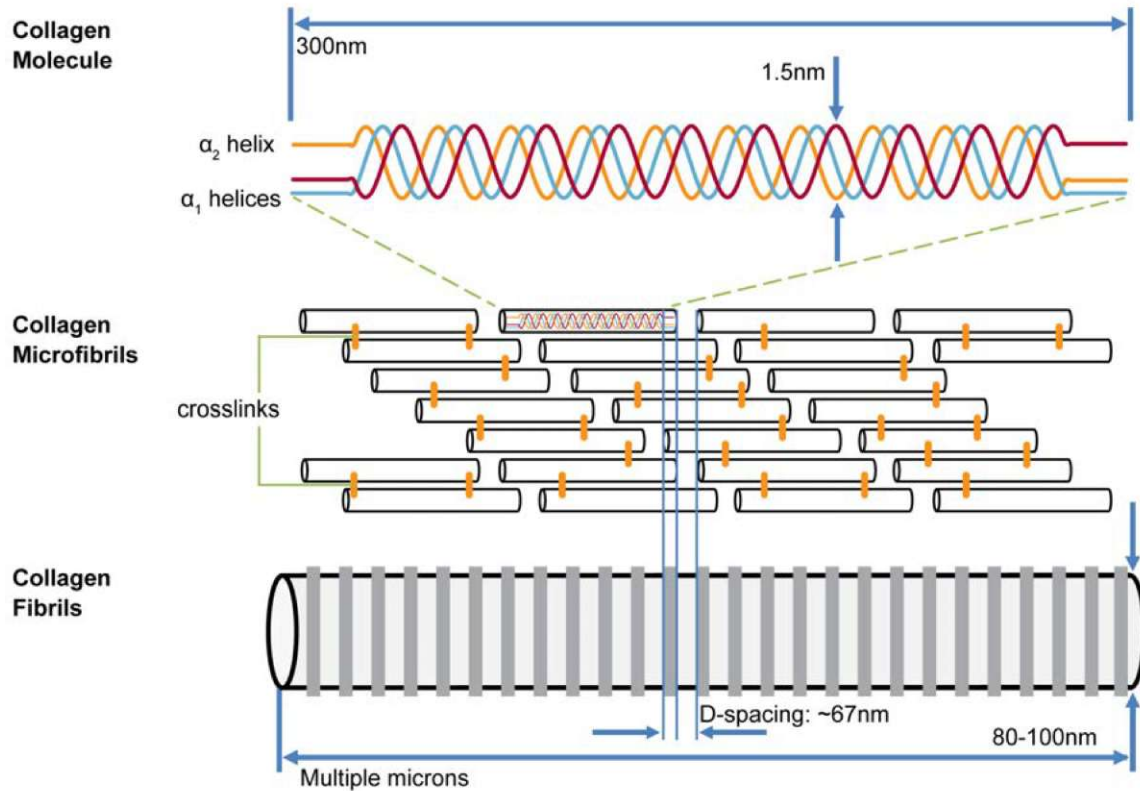
Figure 2.1: Structure and assembly of collagen type I molecules. (Top) The triple helix tropocollagen molecule consists of two α1 and one α2 chains. (Middle) The tropocollagens undergo self-assembly in a staggered fashion. The assemblage is stabilized via crosslinks between individual tropocollagen helices. (Bottom) The end product of the process is a collagen fibril displaying a typical D-banding pattern, stemming from the characteristical overlap of the collagen molecules. Image from [22].

figure 2.1). The ordering of the tropocollagen triple helices during the packing process is by no means random and results in a periodic (quasi liquid-crystalline) structure, that can be observed via techniques with sub-micron resolution, such as scanning electron microscopy (SEM) [55, 103, 105, 114] or atomic force microscopy (AFM) [17, 152].

Several models have been proposed for the origin of this characteristic periodicity, known as the D-banding of collagen, from which the staggered model of Hodge and Petruska has been predominantly referenced in the last decades, fig. 2.1 and fig. 2.2
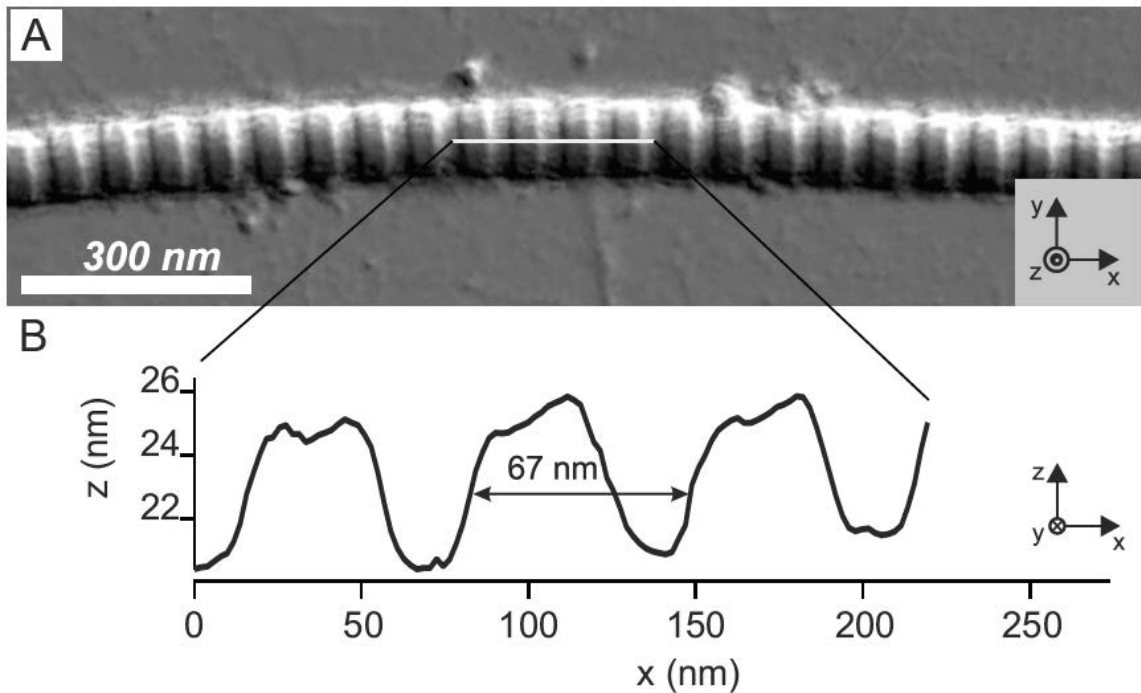
Figure 2.2: The collagen molecule. (A) Atomic force microscopy (AFM) image of a collagen fibril displaying the typical D-banding pattern. (B) Longitudinal height profile, as obtained from the AFM image. Image reprinted from [4].

[142]. According to this model, the triple helix molecules align end to end with a small gap of 35 nm in the longitudinal direction, but in the lateral direction they associate in a staggered fashion with an offset of 67 nm. It is this offset that, when many tropocollagens stack in 3D directions, gives rise of the apparent D-banding of the collagen type I fibrils, which are found with dimensions 10 – 500 nm in diameter and can reach lengths in the μm and up to mm range.

During fibril formation, the assembly of the above-described macromolecular construction of collagen is stabilized by crosslinks between neighboring strands. There are two types of crosslinks, enzymatic and non-enzymatic [44]. The enzymatic crosslinks are facilitated by enzymes in which, initially a divalent bond, called the immature crosslink, is created at specific positions between two adjacent helices. With time, specific variants of these divalent bonds can be further modified to create a

trivalent bond via interaction with a neighboring enzymatically modified amino acid, binding to a third helix and is referred to as the mature crosslink. The formation of both immature and mature enzymatic crosslinks is considered to have a stabilizing and mechanical strengthening function for the fibrillar structure [160]. The non-enzymatic crosslinks occur by direct chemical reaction of glucose and other sugars with collagen and are named advanced glycation endproducts (AGEs). These crosslinks, contrary to the enzymatic ones, are formed at relatively random, but amino acid specific, e.g. lysine or arginine, positions along the collagen helices and tend to accumulate with increasing tissue age. Whereas some portion of AGEs also contribute towards stabilization of the fibril structure, an overaccumulation of such crosslinks becomes constringent and stiffening to the fibrillar structure, rendering the tissue stiffer and more brittle [21]. There is accumulating data, that crosslinks have an effect on the mineralization process in hard tissues and play a role in alterations of mechanical behavior of the tissue with age and pathology and have gained more attention in recent investigations [160].

The specific arrangement of the collagen protein phase is regarded to both facilitate mineralization by providing a scaffold for mineral aggregation and control this process by spatial obstruction [200]. The gaps between consecutive tropocollagen molecules provide regions where mineralization starts. As the mineral aggregation continues, the gaps are filled, so the process is then obstructed to some extent by the densely packed collagen molecules. However, mineralization continues and extends in the overlap region, pushing collagen molecules apart and increasing their relative distance. This mineral portion is referred to as the intrafibrillar mineral (see figure 2.3(b)), which has also been confirmed in experimental studies [9, 199]. The mineralization is not confined within the fibrils and an even larger portion of the mineral is found between fibrils, referred to as the interfibrillar mineral (see figure 2.3(a)). The relative distribution of inter- to intrafibrillar mineral was estimated to be 77 % and 23 %, respectively [162]. The exact position, relative distribution and the way mineral
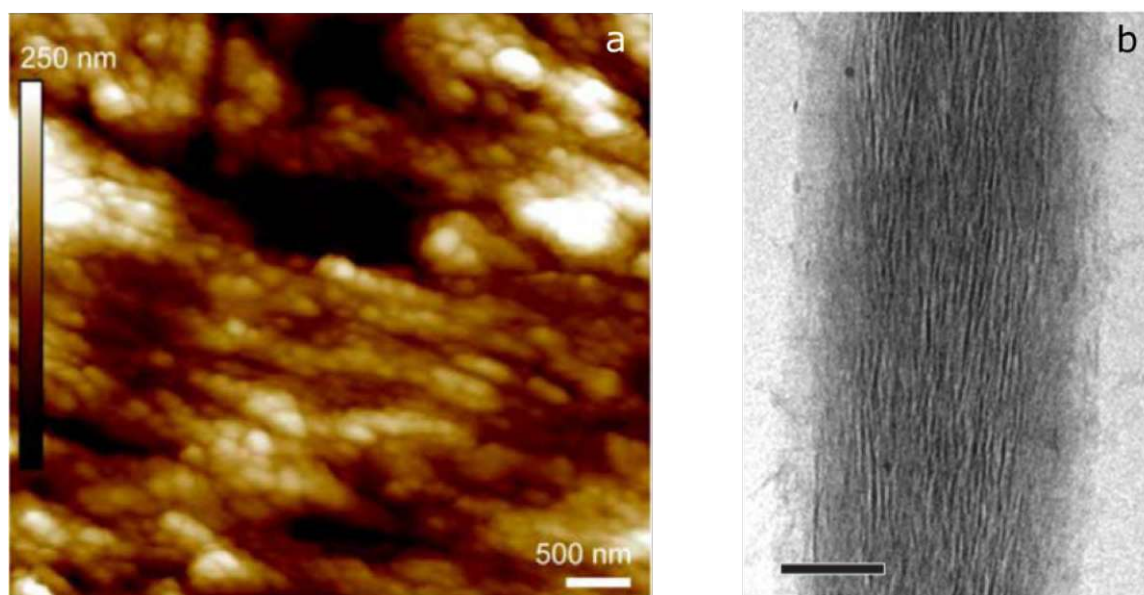
Figure 2.3: Inter- and intrafibrillar mineral. (a) AFM height image (color legend bar on the left side) from a fresh fracture surface of bovine cortical bone. Image displays collagen fibrillar structures covered by particulates of interfibrillar mineral (image adapted from [183]). (b) Cryo-electron tomography of a single mineralized collagen fibril (scale bar is 100 nm) displaying a longitudinal striation resulting from mineral crystals within the collagen fibril, i.e. intrafibrillar mineral (image adapted from [132]).

interfaces with collagen is still not fully understood and remains an ongoing discussion [166, 181].

What is generally agreed upon by authors, based on multiple experimental data is that the mineral is in a plate-like form with the c-axis of the crystals oriented parallel to the longitudinal direction of the fibrils, suggesting their role as a template for deposition and organization of the mineralization process. Moreover, the complex coordination of mineralization cannot be attributed to collagen alone, but non-collagenous proteins (NCPs) are increasingly recognized to play a crucial role in regulation of interfibrillar mineral deposition, see also NCPs subsection.

Water

As a biological material, embedded in a physiological environment, bone tissue exists in a hydrated state. Even though it is the third main component of bone, repre-

sented by approx. 20 % by volume, its implications on bone mechanics has gained least attention, even less than NCPs [56]. The apparent effects of dehydration on bone mechanics, e.g. increased stiffness and strength, are generally known from experiments, however, the underlying mechanisms and role of water leading to such alterations are still unknown [136]. In the context of bone mechanics, water's contribution is considered to be both direct, in the form of hydrostatic pressures and gradients of the unbound water present in pores of the tissue, which is free to move during bone deformation, and implied, by interfacing the organic and mineral phases of the tissue. Indeed, water molecules are present at every hierarchical level of bone tissue, fig. 2.4 [56]: (A.) Pore water is the free unbound water residing in the macro- and microscopic pores of the tissue, able to move i.e. flow according to pressure gradients during deformation of bone and is inversely proportional to bone tissue porosity, (B.) Loosely bound water at the single micron- to nanoscale hydrating and coating the mineralized collagen fibrils creating an interface and facilitating interfibrillar sliding, (C.) Tightly bound water at the molecular scale of collagen providing hydrogen bonding between the protein chains and stabilizing the packing structure of tropocollagen, and (D.) Structural water integrated in the crystalline lattice structure of the mineral, which is only removed with high energies achieved at high temperatures > 540 ℃.

Non-collagenous proteins (NCPs)

The organic phase of bone material consists of 90 % collagen protein. The remaining 10 % are constituted by a group of smaller proteins and proteoglycans collectively termed non-collagenous proteins (NCPs). Whereas collagen provides a scaffold for mineralization, the NCPs are considered to have the regulatory function of this process [73, 115, 125, 189]. Their role on the mechanical performance of bone, in a descending length scale order, has been classified as indirect – by affecting the morphological outcome of bone organs and constitution of material properties of bone tissue and direct – by participating directly in toughening mechanisms, such as providing dilatational bands and molecular self-healing during bone deformation and
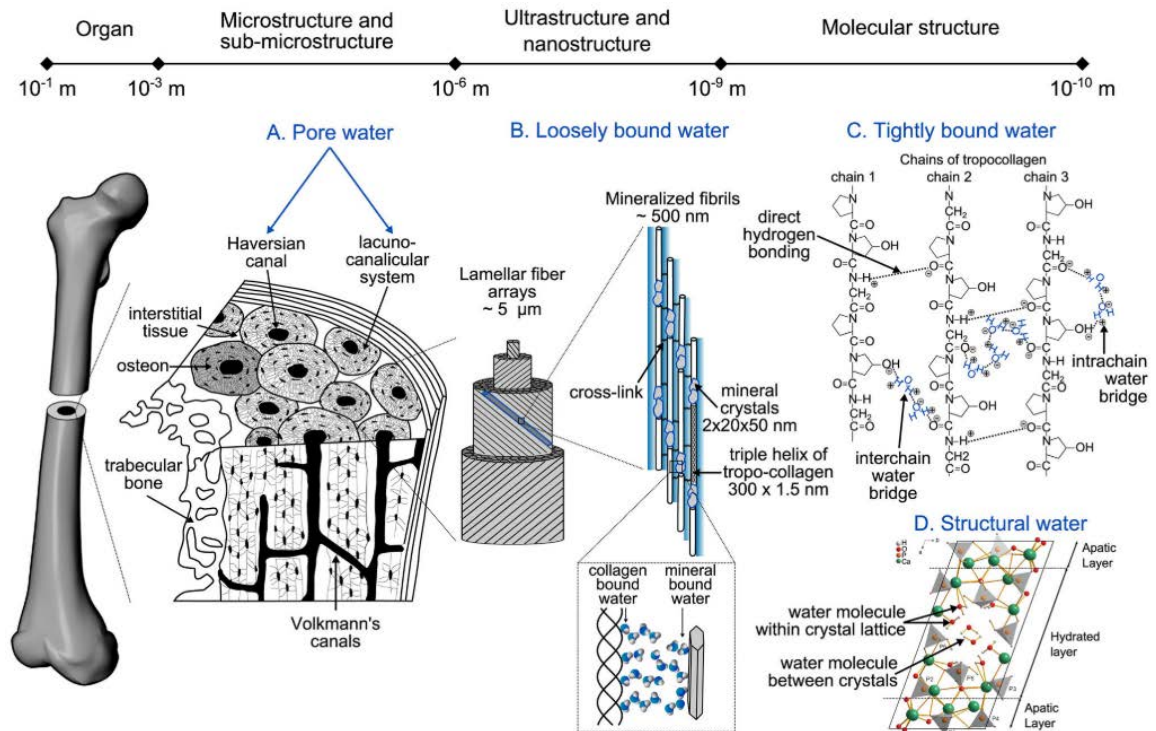
Figure 2.4: Presence of water at every length scale of bone tissue, from organ down to molecular hierarchical level. See text for detailed description (adapted from [56]).

fracture (see figure 2.5) [40, 64, 121, 181]. It can be argued that NCPs facilitate the interaction between the collagen and the extrafibrillar mineral phase. On the one hand, they conduct the mineralization process by determining mineral content, but also its quality, i.e. crystal shape and size during mineral crystal formation. On the other hand, they are also involved in determination of fibril geometry and size, as well as the number of crosslinks between mineralized collagen fibrils. The role of NCPs is mainly provided by their presence (or absence) and their number. So, their indirect impact on mechanics, by affecting the mineral and collagen phases, has been detected as decrease in mechanical parameters like stiffness, elastic modulus and fracture toughness, when their number is decreased in bone tissue [121]. Furthermore, NCPs provide an interface between the mineral and collagen phase (see figure 2.5(a, b)) and can play a direct role in bone mechanics (see figure 2.5(c)). The direct mechanical implications have only gained attention of researchers recently and
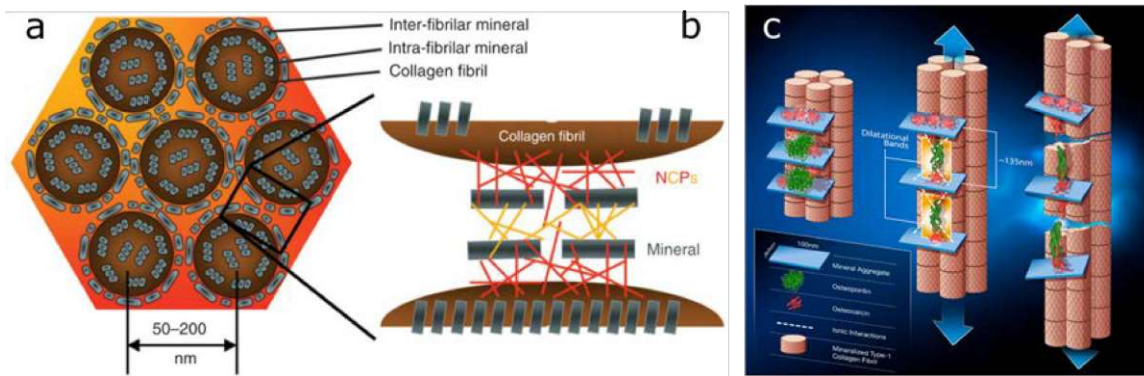
Figure 2.5: Schematic representation of the direct mechanical role of NCPs on bone tissue mechanics. (a) A nanoscale model of the cross section of mineralized collagen fibrils depicting inter- and intrafibrillar mineral. (b) NCPs providing interfaces in the interfibrillar space. (c) Complexes of NCPs between mineral platelets (left) providing dilatational bands upon mechanical loading (yellow sheets, middle) prior to rupture and shearing of collagen fibrils (right). (a), (b) adapted from [181], (c) adapted from [144].

has been least studied so far. Most of the findings have been obtained by studying fracture behavior and fracture surfaces of bone samples. Their increased presence in collagen-poor areas like cement lines and interlamellar areas (see section 2.1.2) has been associated with fracture toughness ability, by providing dilatational bands during bone deformation (see figure 2.5(c)), diffuse damage creation for energy dissipation of cracks and molecular self-healing properties [92, 121, 185].

Studies of NCPs in the past have mainly been focused on elucidating the biological relevance of these proteins within the bone matrix. Indeed, their roles are revealed in complex signaling pathways ranging from cell recruiting and intercellular communication of osteoclasts and osteoblasts for bone resorption and bone formation, respectively, as well as protein-protein interactions during the bone remodeling process (see section 2.1.3) [104]. Some of the most prominent NCPs include: transforming growth factor - $\beta 1$ (TGF-$\beta 1$) (according to [104]), decorin (DCN), osteonectin (ON), osteopontin (OPN), bone sialoprotein 2 (BSP-2) and osteocalcin (OCN) to name but a few and their structures vary from randomly uncoiled to structurally organized.

Some of the processes they enable and regulate are: increase number of osteoblasts (TGF-β1), providing of cell adhesion to the bone matrix (OPN, BSP-2, OCN), bone formation (BSP-2, ON, OCN), aid correct fibril assembly (DCN) and determine fibril diameter (ON), regulation of calcification (DCN), binding Ca^{2+} ions (ON, OCN) and binding of HA (OPN, OCN) [104].

Whereas older studies provided valuable insights into NCPs roles and acting mechanisms, current studies are more focused on identifying markers for certain bone pathologies, e.g. osteoporosis, when the balance of bone metabolism is shifted. One of the pioneering studies investigated the amount of NCPs in osteoporotic bone compared to healthy controls and found that NCPs levels in osteoporotic bone are much less, likely resulting in impaired mechanical performance of bone [58]. Recent studies reveal a more complex onset and causal relationships of disbalances in NCPs, e.g. in the case of osteoporosis, increased levels of OPN and increased resorption activated by increased BSP-2 levels, but decreased amounts of ON, Vitamin K and OCN resulting in reduced number of osteoblasts and osteoclasts ultimately decreasing bone formation. The latter, OCN, is currently regarded as a marker for osteoporosis [104]. Furthermore, not only the amount of NCPs, but their phosphorylation e.g. of OPN, mediated through post-translational modification, has been recently discovered to play a major role in rendering mechanical performance to bone tissue [8]. Bailey et al. report that phosphorylation increased cohesion among OPN proteins and adhesion of OPN to the hydroxyapatite mineral, thus increasing interfacial bond formation and ultimately favoring fracture toughness of the tissue.

2.1.2 Hierarchical structure

The individual components described above represent the constituents of bone material at the nanoscale. These building blocks are further combined and arranged in a very intricate and specific manner to form larger structures at the next higher length scale level, which are in turn organized into the larger structures of the next hierar-

chical level. Bone has distinct structures at different length scales and up to seven hierarchical levels have been identified, ranging from the nano- to the macroscale of whole bones [200]. It is this, highly-ordered and hierarchical structuring of molecular components that ultimately provides bone with its unique and versatile mechanical properties.

The molecular components of mineral (hydroxyapatite), collagen and NCPs are considered as the first level at the nano- and sub-nano scale. Their arrangement into a mineralized collagen fibril (MCF) is already considered as the next, second level of organization (see figure 2.6). MCFs do not exist isolated in tissues as they are further bundled into larger fibers, created during the mineralization and self-assembly process. Some authors identify the mineralized collagen fibers as the basic construction unit of all bone-like tissues across the animal kingdom [200]. On the next levels, the fibers are stacked together along their longitudinal axis into larger bundles, which can be arranged in different patterns, out of which the most prominent and abundant in adult bones are the bone lamellae (see figure 2.6). Bone lamellae are tightly packed layers of MCFs along their longitudinal axes, predominantly oriented in the same direction. They are sheet-like structures with a thickness ranging $2 - 10$ μm and, in mature cortical bone, are mostly concentrically ordered around cylindrical canals to form the structure of the next hierarchical level, the osteons [154]. Another type of lamellar bone is the interstitial bone, found between osteons and is comprised of partially remodeled osteons or more parallel ordered interstitial lamellae. The latter are remnants from the initially deposited primary lamellar bone during bone formation and can still be found in mature adults [2, 155].

As mentioned above, at the microscale, the most abundant structures found in mature cortical bone are the osteons. Osteons are cylindrical structures, found with diameters ranging $(100 - 500)$ μm, made out of concentric layers of lamellae wrapping around a central Haversian canal, that contains blood vessels and nerves [45]. Osteons are the product of metabolic activity in bone tissue called remodeling, which will be discussed in detail in the following subsection. The orientation of MCFs from one
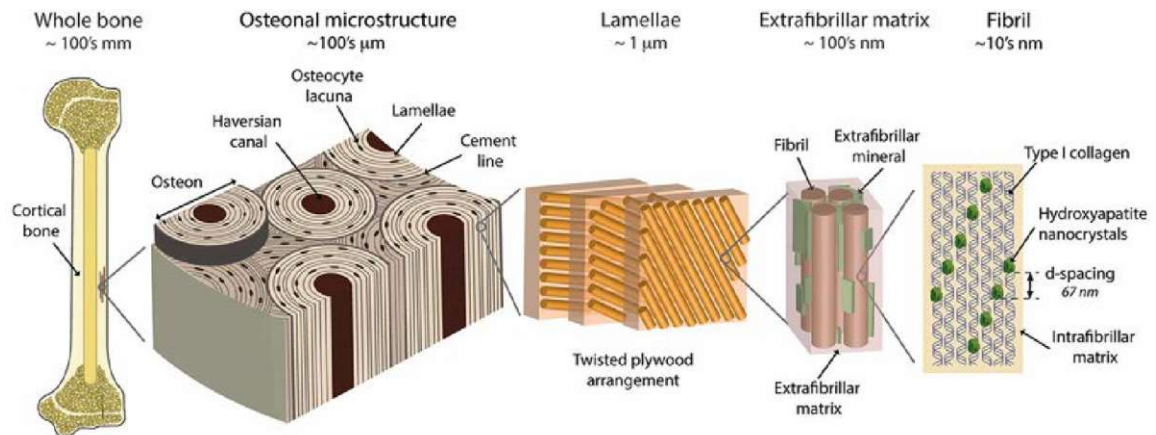
Figure 2.6: Hierarchical structure of bone (Image from [213]).

lamella to the next within an osteon is a matter of ongoing research, the details of which are still not completely known, i.e. the exact angular degree of change from lamella to lamella and the periodicity of the arrangement. However, the model of twisted plywood is currently mostly used across the literature [198, 200, 214].

Furthermore, the transition regions between successive lamellae were also puzzling features [214]. Initially described as transverse lamellae [148], or lamellar boundaries [199], they are now regarded as distinct structural elements, named either thin lamellae or inter-lamellar areas (ILAS), due to their compositional difference to the lamellae [35, 92, 130]. These interfacial or transitional regions are slightly lower in collagen, and slightly enriched in NCPs compared to the lamellae [35, 214]. The outermost layer of an osteon is called a cement line and is a thicker region than ILAS, having also a different composition than lamellae [33, 173]. The cement line connects the osteon with the surrounding bulk tissue between other osteons, found as a non-osteonal lamellar form, i.e. the interstitial lamellae or tissue. Due to their distinctly different composition than the tightly packed lamellae, the function of these interfaces (ILAS and cement lines) is regarded to play a role in fracture toughness mechanisms by deflecting cracks alongside them [92, 156].

The osteons also contain a notable amount of porosity, starting with the longitudinally oriented, central Haversian canals (see figure 2.6), which are further interconnected

with smaller transverse canals, called Volkmann's channels. Through these canals vascularization is established, where circulation of blood and nutrients can reach the embedded bone cells, the osteocytes. These reside in further small porosities, the lacunae, sized several tenths of micrometers. Moreover, the osteocytes remain interconnected between each other and to the Haversian canals via even smaller channels of nanoscopic diameters, the canaliculi, thus establishing the lacuno-canalicular network of osteocytes [97].

At the hierarchical level of the larger microscale, the distinction between the two major types of bone tissue occurs. Whereas mature cortical bone tissue is osteonal, i.e. made out of many osteons, the other type does not contain osteons and is of lesser density and higher porosity. For this reason it is termed cancellous or trabecular bone and is made out of mm-sized plates and rods - the trabeculae, which in turn are made of lamellar bone packets, instead of osteons [154]. Finally, the last, macroscopic hierarchical level is given by the organs of whole bones (see figure 2.6), which contain the two mentioned bone tissue types. Trabecular bone is found at the epiphysial ends of long bones (or within the body of whole bones) and cortical bone builds the middle shaft section (diaphysis) of long bones and provides the thin outer cortical shell of all bones, that has to sustain higher mechanical loads [32, 57].

2.1.3 Lamellae - bone biology and remodeling

The entire hierarchical architecture of bone is a product of cellular activity, in which the main four types of bone cells are included: bone lining cells, osteoblasts, osteoclasts and osteocytes [116]. These cells are not only responsible for the creation of bone mass during growth, but also for its maintenance and adaptation during a lifetime. So, despite the apparent impression of bone as a stiff and inert part of the body, it is subjected, like any other organ, to a constant metabolic activity, called remodeling.

When initiated, the remodeling process starts with recruitment of osteoclasts that perform bone resorption. Osteoclasts are giant cells with a typical lengths of up to 100 µm and contain multiple, up to 50, nuclei [116]. They are found at bone surfaces that need to be resorbed and create a sealed contact area with the bone tissue (ruffled border). In this area, they dissolve the bone mineral (hydroxyapatite) by secreting hydrochloric acid, thus lowering the pH, and additionally enzymes for degradation of the collagen matrix. Through this activity, small pits – the Howship's lacunae, in the bone tissue are created and bone material gets resorbed.

The osteoblasts are then recruited to the bone surface, where new material should be deposited. Their role is primarily the deposition of the collagen matrix into the extracellular space, where mineralization subsequently takes place and also the secretion of non-collagenous proteins (NCPs, see also section 2.1.1). Osteoblasts are much smaller cells than osteoclasts, 15 – 30 µm in length, and contain only one nucleus. They originate from pluripotent mesenchymal stem cells present at bone surfaces and in the bone marrow, which have the potential to proliferate and differentiate into osteoblasts upon bone remodeling initiation signals. Some of the osteoblasts stop dividing and flatten on the bone surface to become bone lining cells.

Bone lining cells are flat, containing only a few organelles, and stretch over the outer bone surface. Underneath them is a layer of unmineralized connective tissue, called the osteoid, which provides a barrier between the final mineralized layer of the bone tissue and the bone lining cells. Upon exposure to parathyroid hormone, these cells contract and secrete enzymes to remove osteoid and reveal resorption sites, where osteoclasts can attach to start the bone resorption process [116]. This role of bone lining cells is only recently recognized, which attributes them also as a part of the bone remodeling process.

Other osteoblasts stop dividing and remain to get embedded in the surrounding bone material and further differentiate into osteocytes, cells that reside in small pits within the bone tissue, the lacunae (see section 2.6). Osteocytes are the most abundant cells in bone, comprising more than 90 % of all cells in a mature skeleton.

Although fully entrapped within the bone matrix, they are far from being isolated. Rounded in shape, they possess numerous cytoplasmic processes reaching in all directions through the smallest, sub-microscopic canals in the bone tissue, the canaliculi, through which they connect with other osteocytes. This establishes a rich, lacuno-canalicular network for communication and exchange of nutrients, and, in the context of bone remodeling, sensing and reacting to mechanical stimuli. It is the current understanding of the bone remodeling process, that the osteoclasts and osteoblasts are the executors of bone resorption and formation, respectively, and the osteocytes provide the sensing, i.e. ability of detection of mechanical stimuli, and regulation of the remodeling process.

Equipped with such regulatory mechanisms, healthy bone tissue can: adapt to external mechanical stimuli by changing shape and increasing/decreasing net bone mass, called modeling or adaptation; perform constant maintenance and renewal of old and (micro)damaged tissue without change of net bone mass, called remodeling; as well as perform the remarkable, site specific and targeted process of bone healing of fractures [18]. Although the effects of bone's exceptional adaptability have been known for over a century, the exact mechanisms behind the mechanical sensing, whether it is direct sensing of mechanical stresses or strains or indirect via fluid flow sensing within the canalicular network detected by the cells, are still matter of ongoing research. These functions of bone tissue activity have been summarized in the abstract concept of the mechanostat by Frost, in which decreased and increased mechanical loading shifts the balance of osteoclastic and osteoblastic activity resulting in decrease and increase in bone mass at specific sites, respectively [48]. In this way, induced deformations in the tissue are maintained within a normal range, in which bone mass is preserved.

Bone lamellae, as ordered layers in an osteon, are a product of the coordinated activity of osteoclasts and osteoblasts within the "basic multicellular unit" (BMU) of bone remodeling, fig. 2.7. In cortical bone, the BMU has a three-dimensional cylindrical shape and moves preferentially in the longitudinal direction of long bones. The process is coordinated with respect to time and position. First, osteoclasts erode a
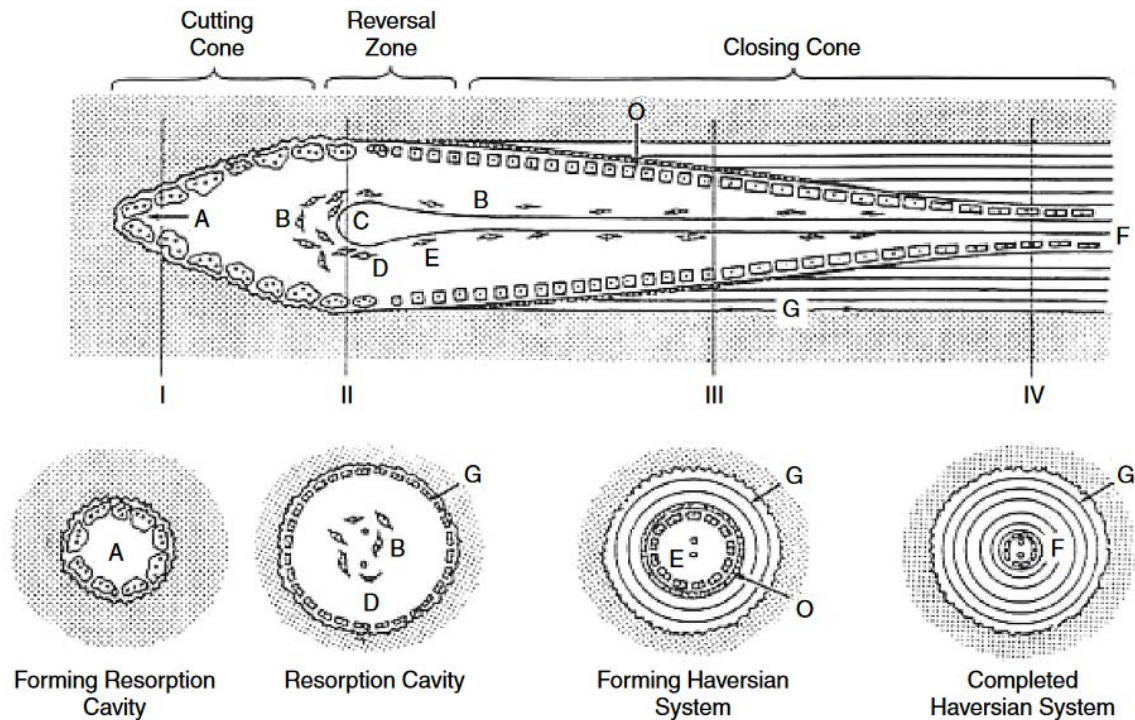
Figure 2.7: Schematic representation of the bone remodeling process in cortical bone in which osteonal lamellae are created. Upper part, a longitudinal cut through the process of the basic multicellular unit (BMU). Lower part, cross sections representing different stages of the remodeling process. Image adapted from [77].

conical tip, after which the osteoblasts deposit the lamellar layers in a circular fashion, which are separated from the interstitial (old) tissue by the cement line and end in the middle with a Haversian canal lined with bone lining cells. The end product of the BMU activity is the well-structured "secondary osteon". The transverse cut of such an osteon shows the distinctive concentrical pattern of lamellae, whereas the longitudinal cut displays its parallel layered structure.

2.2 Bone mechanics

The processes of bone formation and remodeling presented in the previous section result in a complex hierarchical architecture, from molecular up to the dimensions

of whole bones (see figure 2.6). It is this hierarchical organization in combination with the specific properties of the built-in substances (the soft organic phase and the hard mineral phase) that ultimately provide bone with its mechanical competence. Constructed this way, bone is able to sustain a multitude of mechanical loading cases, such as compression and tension, bending, shearing and torsion, as well as resisting onset and propagation of fracture, while at the same time also retaining a low mass. So how can the mechanics of such a versatile material be investigated and elucidated? In a hierarchical structure, the mechanical response of a higher hierarchical level is determined by the mechanics of its structures at the lower organizational level and the way these interact with each other. Since the present thesis is of experimental character, an attractive approach is performing mechanical experiments on structural elements from hierarchical structure levels at different length scales, plus mechanical testing of their interfaces. The other complementary approach would be multiscale computational modeling, by inputting material properties of constituents at low(est) hierarchical levels and calculating mechanical output at larger hierarchical levels and comparing this with experimental data [66, 67, 75, 107, 117, 186, 195]. However, this approach is beyond the scope of this thesis.

Furthermore, apart from numerous hierarchical structures and interfaces, being a biological tissue interwoven with cells and vascular canalization, bone tissue contains a substantial amount of porosities down to the nano-scale, which poses additional challenges for mechanical characterization.

Whole bone testing

Historically, mechanical characterization, i.e. investigation of the load bearing capacity of bones has been developed with a top down approach, starting from the macroscale of whole bones and small macroscopic samples, going to lower length scales of trabecular or cortical bone. Experimental mechanical tests typically utilize mechanical testing devices, in which specimens (either a whole bone, e.g. femur, tibia, humerus, single vertebra; a smaller part of larger bones, e.g. proximal femur, distal radius, coxal bone; or small samples machined from bone material) can be
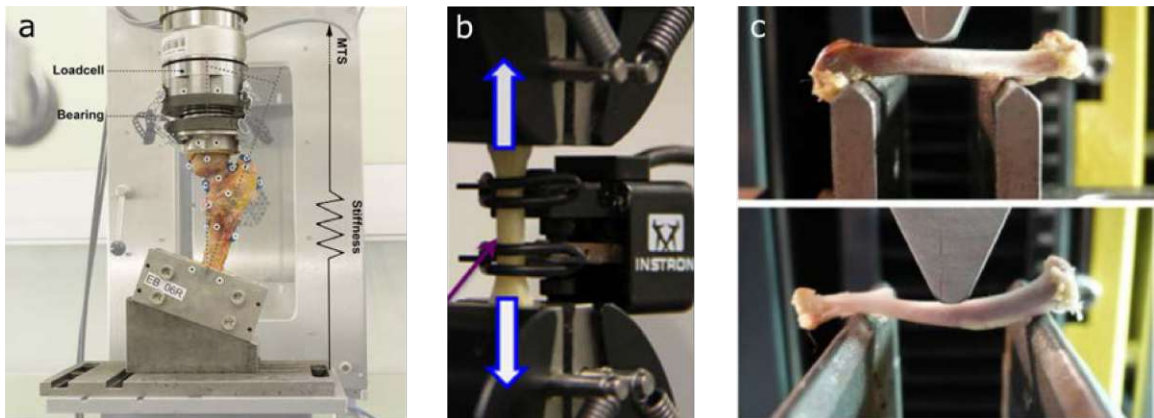
Figure 2.8: Macroscopic testing of bone. (a) Proximal femur tested under compression (adapted from [11]). (b) Tensile testing of a small macroscopic bone sample machined from cortical bone (adapted from [133]). (c) Three-point bending of a whole rat femur (top) and tibia (bottom) (adapted from [145]).

mounted and tested in different loading modes such as compression, tension, bending or torsion, including also physiological loading modes (see figure 2.8). The goal of mechanical testing is the recording of a load vs. displacement curve, from which mechanical parameters can be derived, such as: stiffness, elastic (Young's) modulus, yield point, strength, physiological load limit etc., which will be presented and discussed in detail in the following chapter (see chapter 3).

Utilizing well-established instrumentation and methods, initially developed for mechanical testing of engineering materials, testing of whole bones has been extensively performed [26, 34, 170, 203]. Bones of mainly human, but also of animal origin (murine, ovine, bovine) have been tested. From the set of mechanical parameters and measurement regimes, e.g. the order of magnitude for the elastic (Young's) modulus of cortical bone has been determined to be in the range 15 – 25 GPa [170], but also post-yield quantities, as a measure of fracturing behavior, such as yield and ultimate stresses and strains have been obtained [203].

Indeed, the primary motivation for testing of whole bones has been the fracture behavior, once the load sustaining capacity of the organ has been surpassed, due to

a critical loading, e.g. a fall, or compromised strength due to pathology. However, whole bones, as parts of biological origin, show a large variability with respect to size, shape and geometry as well as large inter-species, inter-sex, inter-organism and intra-organism variability. Whole bones are also comprised of two distinct types of bone tissue, cortical and trabecular bone (see section 2.1.2), displaying different mechanical properties and level of porosity, which when combined result in a unique apparent mechanical behavior. All of these aspects have a substantial influence on the mechanical response and make a systematic comparison of mechanical data difficult. Moreover, bones in the body are embedded in a physiological, hydrated environment, which poses an additional experimental challenge compared to engineering materials, necessitating the usage of water baths or sample hydration management during testing for obtaining physiologically and clinically relevant data.

Small macroscopic samples

To exclude the influence of structural, geometrical variability of whole bones, testing of small macroscopic, mm- to cm-sized bone samples at the so called "material level" has been performed. Using precision saws and milling machines, it is possible to machine a sample, usually from the cortical portion of long bones, of well-defined shape and dimensions, allowing for more comparable mechanical characterization. At this level, the further complexity of mechanical testing of the material bone become apparent. Unlike engineering materials, where a large number of samples can be prepared of comparable composition and preparation protocol, bone material is not readily available and the sample number is more limited within a single study. Moreover, the bone material is largely inhomogeneous, displaying inter-organ (mechanical properties of e.g. the tibia are different from the humerus) and intra-organ variability (mechanical properties are different from the middle or end portions of a single bone). Bone is also anisotropic, i.e. samples prepared in different anatomical directions display different mechanical properties, e.g. in long bones, the longitudinal direction is stiffer than the transverse direction (see figure 2.9).
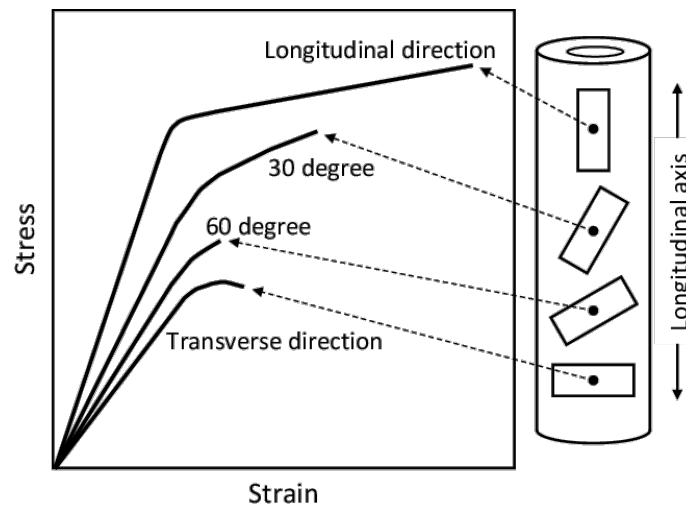
Figure 2.9: Bone anisotropy. Measured stiffness is reducing, when bone samples are produced from the longitudinal direction towards the transverse direction. (Image from [131]).

If it is possible to minimize the latter variabilities by a good study design, then still only apparent mechanical behavior would be recorded in a mechanical test, due to the complex underlying hierarchical structure. The microstructure of cortical bone is provided by osteons of different numbers, sizes and orientations of their lamellar layers, as well as interstitial lamellae, all displaying different mechanical properties. These microstructures interact with interfaces of different composition, e.g. interlamellar areas and cement lines (see section 2.1.2), also contributing to the mechanical response. Furthermore, the porosities present by the Haversian systems and the lacuno-canalicular network only adds to the complexity of mechanical characterization of the bone material. Hence, small macroscopic samples can still contain significant amounts of defects (e.g. Haversian canals, lacunae etc.) and are heterogeneous. One approach to reduce both defects and heterogeneity is size reduction.

2.2.1 Bone mechanics at the microscale

As mentioned above, the complex structure of bone and its mechanical response has motivated researchers to push experimental efforts to smaller length scales, at the ma-
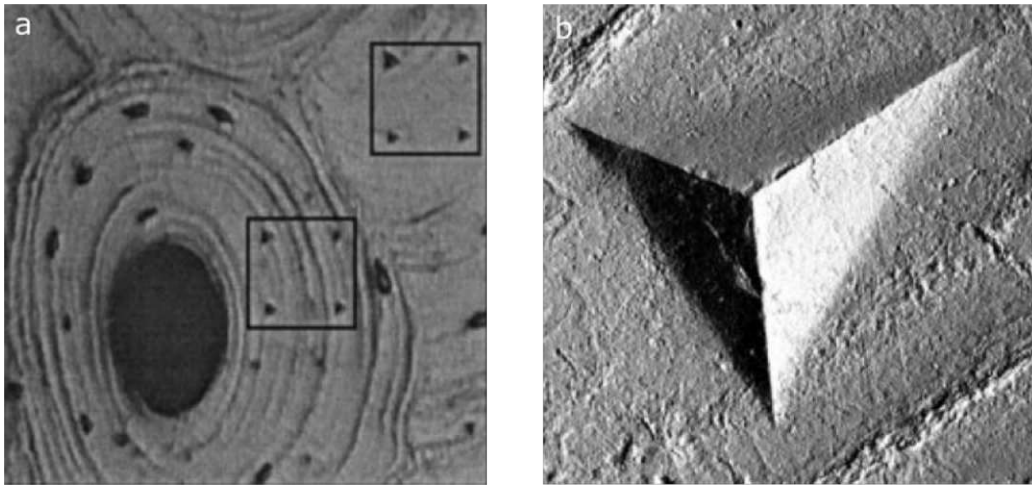
Figure 2.10: Nanoindentation performed on bone. (a) 2 x 2 indents performed on osteonal and interstitial lamellae (lower left and upper right square, respectively) (adapted from [216]). (b) Atomic force microscopy (AFM) image in contact mode of a single indent (adapted from [74]).

terial level of the tissue, in order to eliminate effects due to variability in geometrical size and shape and due to larger porosities like Haversian canals and lacunae. At the microscale, nanoindentation has proved to be an attractive technique, performed either in conventional nanoindentation instruments or atomic force microscopes (AFM) utilized in numerous studies, summarized in extensive reviews by [102, 181]. With indentation depths of several hundred nm to few μm, this technique probes bone material at the length scale of bone lamellae (see figure 2.10). Valuable insights have been gained through nanoindentation, e.g. the higher values range of elastic moduli of cortical bone lamellae of approx. 20 – 30 GPa, outlining the importance not only of the individual components, but also their interfaces and the substantial effect of hydration state of the tissue, where dehydrated bone consistently yields a higher elastic modulus, than the wet or rehydrated counterpart group. Although attractive for its established and straightforward application, nanoindentation is limited by the high stress and strain gradients induced in the material as well as damage uncertainties about the surrounding bulk material, leading to difficulties in interpretation of data [3, 109, 161].

To overcome this drawback, focused ion beam (FIB) utilized to isolate individual micron sized volumes (e.g. single bone lamella) of defined geometry has gained attention in the biomechanics community, since the last decade. One of the first studies performed on mineralized tissue dates back to 2009, in which microbeams of triangular cross section were FIB milled from single lamella of human tooth enamel and bent with a conventional nanoindenter [24]. Further studies followed on small microbeams, 5 μm in length and approx. rectangular cross section, FIB-machined from murine cortical bone lamellae and bent or compressed via an AFM cantilever (see figure 2.11(right)). The examined effects on single lamella mechanics included dehydration by high vacuum exposure during FIB preparation [82], fibril orientation within lamellae [84] and to some extent bone pathology of osteoporosis [83]. Post-yield properties and fracture mechanisms at the sub-micron length scale were also studied via micropillar compression performed on concentrically FIB-milled micropillars from cortical ovine bone lamellae and compared to microindentation and macroscopic compression results (see figure 2.11(left)) [168]. These investigations were later also achieved in wet, fully submerged conditions, further confirming the substantial effect of water on bone matrix, even at the lamellar length scale [169].

In all these studies, the structures prepared by FIB milling remained attached to the bulk material, which also deforms during loading, thus affecting the mechanical measured response. To overcome this effect and additionally, achieve a constant cross section, non-tapered micropillars were FIB milled and transferred to a more rigid substrate via a micromanipulator and subsequently tested under compression in a conventional nanoindenter [109]. These micropillars, of rectangular cross section were machined from single cortical bone lamellae of bovine origin and were compressed monotonically, to obtain more well-defined values of elastic moduli, which were (29.09 ± 2.39) GPa. Due to the sample preparation technique (FIB milling within the chamber of an SEM under vacuum) and the testing method and equipment (within SEM in situ mechanical testing, nanoindentation), all of the relevant studies mentioned above were conducted in dry conditions, except for one study,
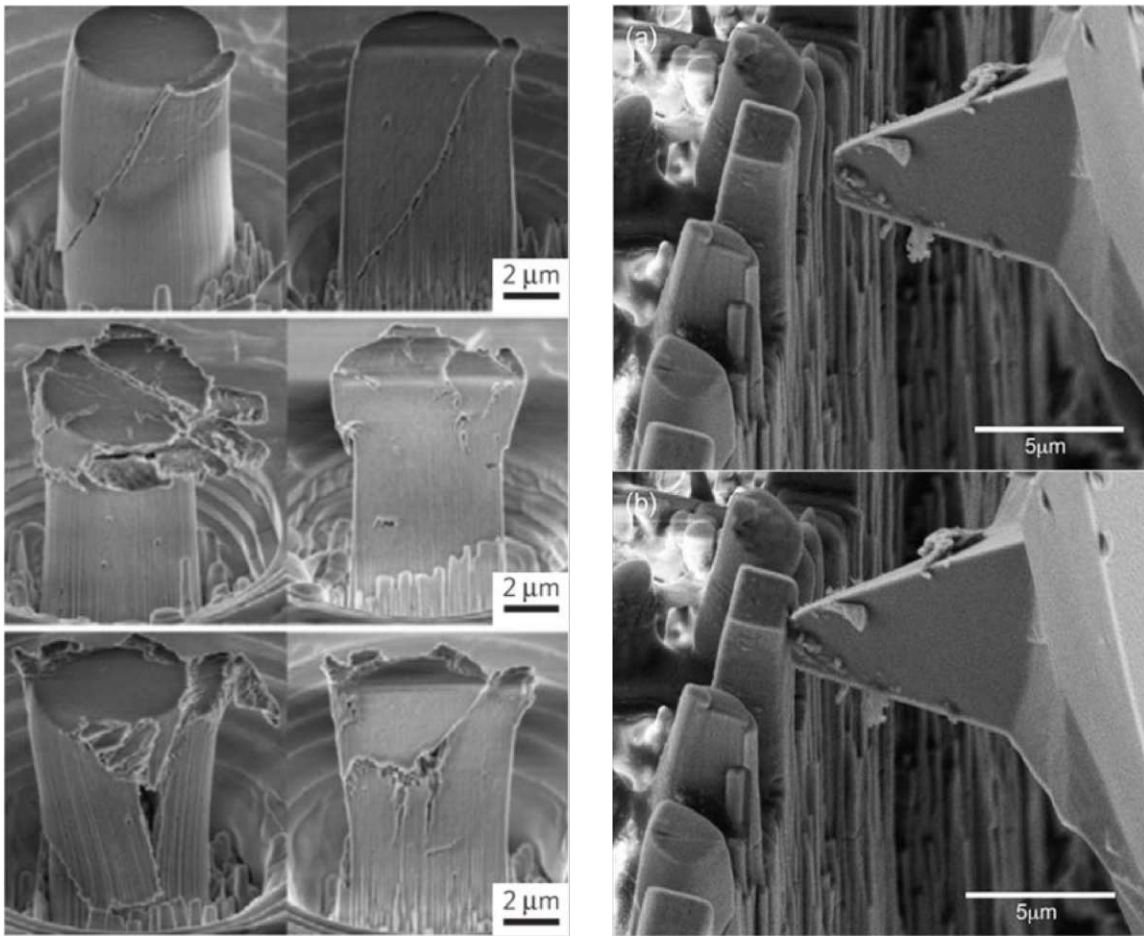
Figure 2.11: Micromechanical testing of bone. (Left) Three failure modes of micropillars FIB-machined from ovine osteonal lamellae after compression testing (adapted from [168]). (Right) Microbeam bending of murine cortical bone lamellae with an in-situ AFM with a flattened tip (adapted from [82]).

which tested fully submerged bone micropillars [169]. Consequently, performing (micro)mechanical testing at the length scale of single bone lamellae in fully hydrated conditions, is a challenging task with little published experimental data so far. For this reason, testing in a fully submerged, hydrated state was also developed and performed in a study of this thesis (chapter 5).

30

2.3 Bone ageing and pathology

Achieving mechanical measurements of bone tissue at all hierarchical levels, does not imply that these properties remain constant over time. Bone is a living tissue undergoing constant remodeling and, in that process, substantially changes its macroscopic mechanical properties during the course of a lifetime, unfortunately mostly in the deteriorative direction after reaching adulthood. For this reason, one major motivation behind bone research is the understanding of why and how bones break, and, particularly in the clinical context, if such a failure can be predicted or estimated in the form of a diagnostic parameter indicating fracture risk of an individual patient. The natural, non-pathologic evolution of bone tissue, in the sense of its amount, is that it reaches a peak approx. at the age of 30 years, whereas men reach a higher level than women, and starts reducing after that. Particularly in women, there is a significant drop in bone mass after onset of menopause around the age of 50 (see figure 2.12), due to decreased levels of estrogen.

The main technique for assessing amount of bone in patients, i.e. bone mass, has been the measurement of bone mineral density (BMD), typically by performing a dual energy x-ray absorptiometry (DXA or DEXA) scan [70, 111]. What has led to the wide utilization of this technique, especially in clinical setting, is the classical view of the correlation of (lowered) BMD with bone fragility or fracture risk. This has made BMD the gold standard for diagnosis of the most prominent bone pathology – osteoporosis [16, 111].

Osteoporosis is described as a systemic skeletal disorder characterized by low bone mass and micro-architectural deterioration of bone tissue (see figure 2.13) leading to bone fragility and consequent increase in fracture risk. Already from this definition, the large overlap of the symptomatology of lowered bone mass, on the one side, due to normal ageing and, on the other, due to the pathology of osteoporosis, becomes apparent. The measurement of BMD has been crucial in clinical practice for the evaluation and diagnosis of osteoporosis. Since the introduction of DXA scanning
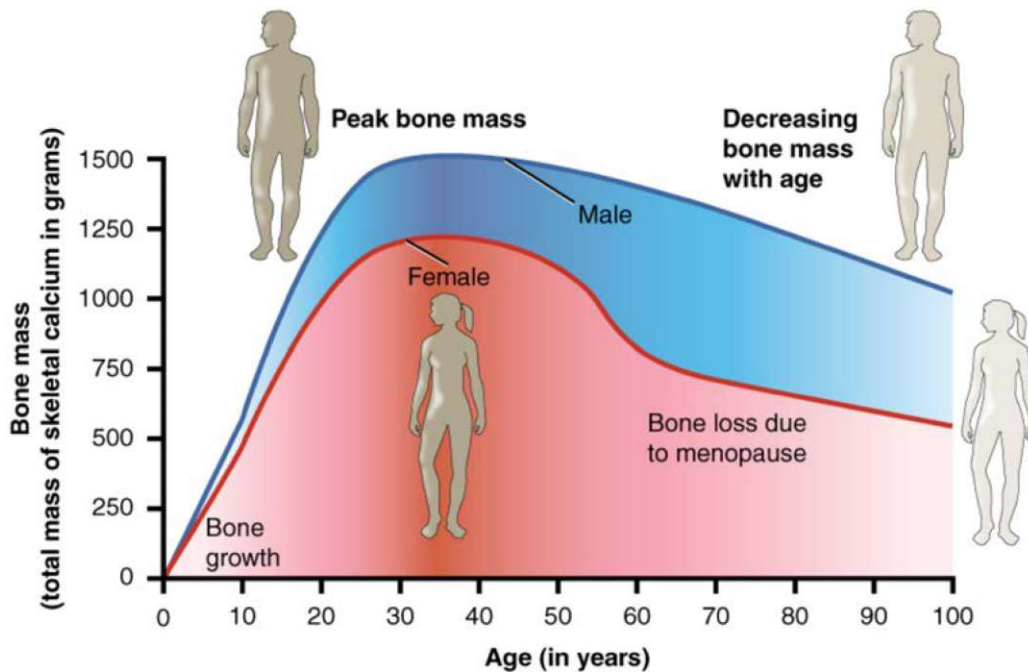
Figure 2.12: Reduction of bone mass due to ageing. Bone mass is higher in men than in women, reaching its maximum at an approx. age of 30 and starting to decrease after the age of 50. Loss of bone mass is particularly prominent in women, due to menopause (adapted from [13]).

as a tool for reliable measurement of BMD into clinical evaluation 35 years ago, the technique has become the gold standard for diagnosis of osteoporosis and monitoring of effectiveness of treatments [16, 70]. The clinical evaluation of DXA scans is the comparison of the patient's measured BMD with the mean BMD of a gender and ethnicity matched, young and healthy population, or gender, ethnicity and age matched healthy population, by calculation of the T- or Z-score, respectively [16]. The World Health Organization (WHO) definition of osteoporosis, based on the T-score value (obtained from a BMD measurement via DXA), is given by a threshold value of -2.5, meaning, if a patient's (in particular post-menopausal white women) T-score is lower than -2.5, then osteoporosis is diagnosed. However, although this definition is good indicator for a fracture risk in a population [90], it suffers from rather low sensitivity of approx. 60 % for an individual, resulting in many positive cases remaining undetected [165, 204].

This is perhaps not surprising, as the number of factors having an impact on the mechanical function of bone tissue are manifold, including genetics, disease treatment history, nutrition, lifestyle, consumption of tobacco and alcohol etc. The most prominent of these factors, having the most substantial effect on bone mechanics discussed here are ageing and the pathology of osteoporosis, which compromise mechanical performance by ultimately reducing overall bone mass, although these factors alone are not sufficient for a comprehensive fracture risk prediction. The continuing problem regarding diagnosis of osteoporosis is the early identification and assessment of fracture risk factors. More than a decade ago, relevant clinical factors for osteoporosis such as age, gender, body mass index (BMI), cortisol treatment and similar were collected in a questionnaire and analyzed by an algorithm in combination with a BMD value to calculate a 10-year fracture risk factor via the fracture risk assessment tool – FRAX [91]. Although providing an additional helpful improvement in the subject matter, a recent broader study found it performs better in detecting patients that will not surfer fracture, with a sensitivity of only 46 % [81]. However, the sensitivity for detecting patients that do have an increased risk of fracture due to osteoporosis was not significantly improved compared to BMD alone [188]. Hence, the quest remains, for additional tools and potential markers with the ultimate ability of detection with higher sensitivity, but also early on detection prior to the effect of substantial reduction of bone material, e.g. changes in mechanical properties of bone tissue and structures at lower length scale.

Mechanical performance and whole bone strength depend, not only on the amount of bone tissue, but also on the geometry and the mechanical properties of bone material itself. With its complex, hierarchical structure bone may experience changes from the optimal composition and structure at every length scale. Such changes can include e.g. alterations in the collagen-mineral interactions, which would result in changes of lamellar composition and their interfaces. Furthermore, alterations in number and shape of osteons in cortical bone as well as the most prevalent concept of thinning and loss of trabeculae in cancellous bone can occur, leading to thinning
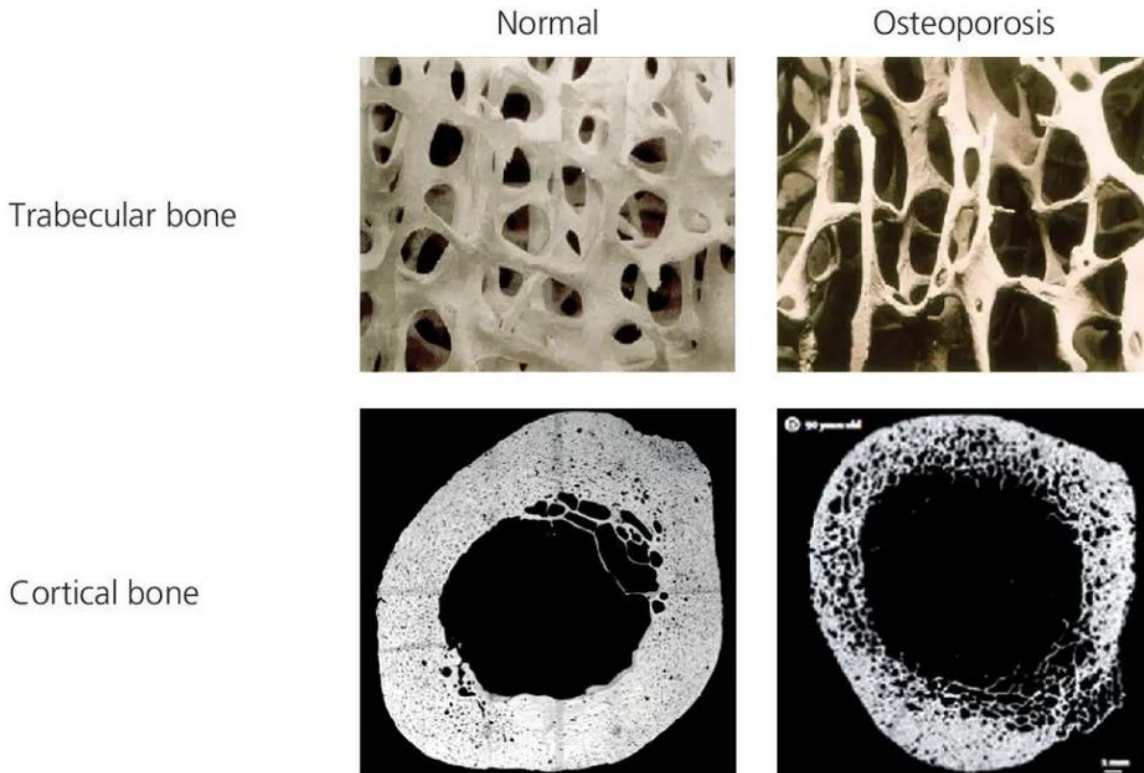
Figure 2.13: Effect of osteoporosis on the two types of bone tissue, trabecular bone (top) and cortical bone (bottom). Reduction of the amount of bone material takes place, inversely leading to increased porosity. Such structural changes ultimately result in reduced load bearing capacity of the tissue and thus to increased fragility of the bone organ and increased risk of fracture (adapted from [209]).

and geometrical changes of whole bones, ultimately resulting in impaired mechanical performance. So, apart from bone quantity (in the sense of total bone mass present), investigations into mechanical properties of bone's constituents, i.e. bone quality should also be performed. In this context, the questions arising are, whether the mechanical material properties of bone tissue are a function of age and pathology, and if so, which properties are affected? Due to overlapping set of symptoms (bone loss as most prevalent), studies found in literature predominantly investigate on entangled effects of both ageing and pathology. Here, an attempt is made, to give an overview and summarize current findings, where insights of ageing and pathology on bone tissue could be considered independently to some degree. Since this thesis deals with

experimental mechanical characterization of bone tissue at the lamellar level, the effects of age and pathology at this hierarchical level will be particularly discussed in the following.

Ageing

Regarding ageing, early studies performed on collagen from skin, tendon and cartilage tissue found changes in the amount of crosslinks between collagen molecules, with immature crosslinks decreasing and mature crosslinks increasing with tissue age [7]. These findings implied that mechanical properties at the tissue level are associated with crosslinks of collagen. A more recent study looking into mechanisms of fracture toughness of human cortical bone observed compositional changes of the collagen and disorder of the typical D-banding structure and measured lower indentation modulus of older collagen fibrils [124]. This deterioration of the collagen was related to the increase of non-enzymatic crosslinks (AGEs) with age. On the other hand, regarding the mineral phase, based on vibrational spectroscopic techniques, i.e. Fourier Transform Infrared Microscopy (FTIR) and Raman Spectroscopy, it is generally considered that mineralization and crystallinity of mineral crystals increase with age [2, 140]. In this context, the rationale of the relative change in stabilizing enzymatic crosslinks, the increase in AGEs and mineralization lead to a more brittle bone material with ageing. Furthermore, the NCPs, playing multiple roles in mineralization, mineral-collagen interface and toughening mechanisms, may reduce with age and osteoporosis [58], but more importantly, their phosphorylation levels (post-translational modifications) were found to reduce with age [175]. The role of water on bone mechanics was also investigated and it was found that removal of water increases modulus and strength, but decreases viscoelasticity and toughness of the tissue. Interestingly, bound water was indeed found to decrease with age [56, 136]. All of these findings would be expected to have implications on the mechanics of the next structural level, i.e. the bone lamella. In recent studies, reduced heterogeneity in nano-elasticity between osteonal lamellae and inter-lamellar interfaces was found to occur in older bone and was correlated with increased fracture toughness [92, 93].

Osteoporosis

A further factor that adds to the complexity of identification and detection of changes in bone tissue, which result in an impaired mechanical competence, is the prevalent pathology of osteoporosis. The main challenges here are due to the superposition of mechanisms and effects on bone mechanics with those of ageing, discussed above.

One of the approaches, which is one main motivation behind this thesis, is performing direct mechanical testing on bone structures at small length scales, here the bone lamella. At this length scale, the influences of decreased bone mass (BMD) and increased porosity, in the context of osteoporosis, can be largely eliminated and a more direct mechanical characterization of the tissue material can be performed. The mechanical behavior of bone lamellae should then be determined by their constituents, the mineralized collagen fibrils (MCF) and potential alterations should be measurable. Particularly the interaction between MCFs mediated via NCPs and the crosslinks within the collagen structure have been found to change in osteoporotic tissue. Although NCPs are reduced and altered in the course of ageing, the amount measured in osteoporotic tissue is even less [8, 58, 175]. As NCPs mediate collagen formation and provide interfaces of inter-fibrillar sliding, this should have an influence on the mechanical response of the bone matrix. Furthermore, collagen crosslinks have been found to be affected in osteoporotic tissue [160]. The enzymatic crosslinks, both immature and mature are substantially reduced in OP tissue. These crosslinks provide stability of the collagen matrix, which in turn affects also mineralization. On the other hand, the amount of non-enzymatic crosslinks, AGEs, is found in increased amounts in OP tissue. Whereas a certain amount of AGEs stabilizes the collagens, a too large amount of them reduces intermolecular deformation and stiffens the collagen structure. It can be argued, that these two alterations in crosslinks amounts renders the material less tough and more brittle, thus increasing its fracture susceptibility. The implications on mechanical parameters of the lamellar structure, might be a decrease in e.g. elastic modulus, as reported for ovariectomized murine bone tissue (representing a model for osteoporosis) [83]. However, the number of samples

tested in this study are insufficient and the measurement uncertainty too large to draw convincing conclusions. Thus, the putative effect of material changes of bone tissue due to osteoporosis on mechanical parameters (elastic modulus, strength, max. strain etc.) of subosteonal structures, e.g. lamella remain still largely unknown.

Chapter 3

Experimental Techniques

Performing experimental mechanical characterization of biological hard tissue at the lower microscale, i.e. the length scale of a few to a few tens of micrometers, is a contemporary, approx. one-decade-old, approach, requiring advanced experimental techniques from sample preparation and visualization to mechanical testing and structural investigation. In this chapter, the relevant techniques for the work reported in this thesis, will be presented in a general manner. This shall provide the reader with basic understanding and enable to follow specific details on techniques used in the work presented in the Materials and Methods subsections of the respective studies (Chapters 4, 5 and 6). All of the microscopically-sized bone specimens utilized in the studies of this thesis were machined using focused ion beam (FIB) and visualized using scanning electron microscopy (SEM), which are discussed in section 3.1. The obtained specimens were transferred to a different setup, where mechanical testing was performed, either in bending or compression. From mechanical tests, material properties can be obtained, the extraction of which is presented in section 3.2. A novel technique for performing mechanical testing at the microscale by utilizing an atomic force microscope (AFM) is described in section 3.3. Finally, one spectroscopic technique – Raman microspectroscopy was used for characterization of bone, in par-

ticular, this technique was used to detect the orientation of collagen fibrils and is presented in section 3.4.

3.1 Electron and Ion Microscopy

The basic principle of performing electron or ion microscopy is targeting a sample with a beam of charged particles, i.e. small negatively charged electrons or much larger positively charged ions, and detecting signals that are generated due to the interaction of these particles with the sample material. In order for the beam of particles to remain bundled and focused and reach the target, collisions and interactions of the charged particles with other surrounding atoms or molecules, e.g. from air, is reduced by placing the whole setup under high vacuum. The necessity of a vacuum chamber for both electrons and ions is utilized by modern microscopy instruments, termed a "dual beam" microscopy system, in such a way that an electron and an ion beam column are combined into a single instrument sharing the same vacuum chamber. This advancement in instrumentation substantially increases usability and reduces measurement times, which in turn has led to extension of applicability of these techniques to biological samples.

3.1.1 Focused ion beam (FIB)

Performing mechanical testing requires machined samples of defined shape (geometry) and dimensions. Performing microscopic mechanical testing of samples invisible to the eye, requires techniques and instrumentation for manipulation and machining of micron-sized specimens of well-defined geometry and microscopic dimensions, e.g. in the range of $1 - 50\,\mu\mathrm{m}$.

The focused ion beam (FIB) technique emerged in the 1970s, for applications in the semiconductor industry and materials sciences and gained increasing interest for investigations of biological samples in recent years. An important advancement of

the technique in the late 1970s, enabling fine probe sputtering, was the development of the liquid metal ion source (LMIS) providing a very fine and thin source of ions approx. 5 nm in diameter [52]. An LMIS typically consists of a metal reservoir and a tungsten needle (see figure 3.1). For the metal reservoir typically gallium (Ga) is used due to a low, close to room temperature melting temperature of T_m = 29.8 °C, but there are metal sources of other metals available as well, e.g. gold and iridium. During operation the liquid gallium wets the tungsten needle and reaches the needle tip of radius 2 - 5 μm. Here, an extraction electric field is applied, which causes the liquid Ga to form an even finer tip of 2 – 5 nm in diameter and shape into a so-called "Taylor cone". This shape is generated as a result of balance of surface tension and electrical field forces that act on the Ga atoms. At this small diameter of the Taylor cone, the electrical field is so strong (> 108 V/cm), that the Ga atoms get ionized and extracted by the strong field. The large advantage of an LMIS source is that it provides ion beams with large current densities (on the order of 108 A/cm²) with very small energy spread [52]. Once the ions leave the source, they are accelerated in the range of 1 – 50 keV, further collimated, shaped and directed in a column of electrostatic lenses. Different apertures are used to deliver different currents of ions to the sample in the range of 1 pA up to 1.3 μA; larger currents are used for sputtering of larger amounts of sample material and the smaller ones are used for finer precision sputtering or finish polishing of surfaces. The acceleration voltage used for the machining of microscopic bone samples for this thesis was 30 keV and the apertures used were 1 pA – 20 nA.

When the focused beam of ions hits a sample, several ion – solid interactions occur: ion backscattering, electron emission, electromagnetic radiation, atomic sputtering and ion emission, sample damage and sample heating [197]. The ions interact with a certain portion of the sample, called the interaction volume. Within this volume the kinetic energy and momentum of the incident ions is transferred onto the sample atoms. The occurring processes are classified either as inelastic or elastic. For inelastic processes, the ion energy is transferred to the electrons leading to ionizations
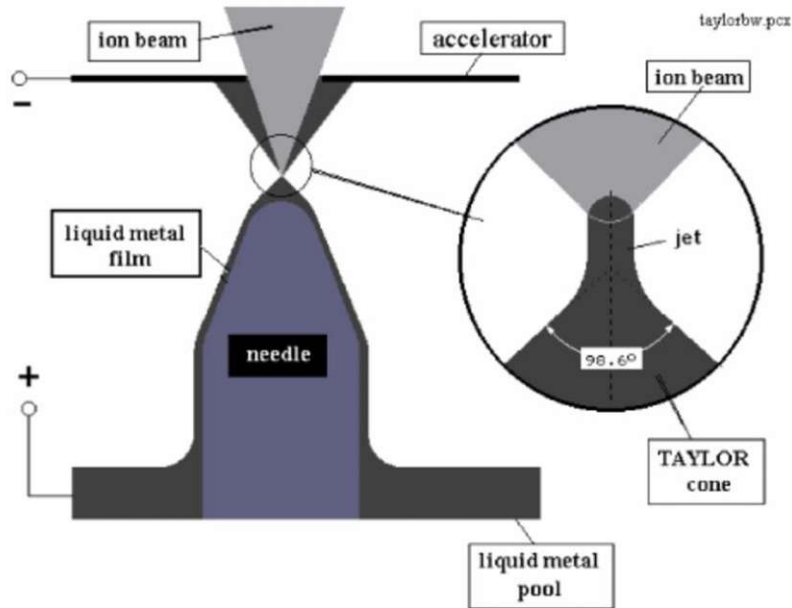
Figure 3.1: Working principle of a liquid metal ion source (LMIS). A nanometer sized fine tip of Ga atoms is formed first by coating the tip of a tungsten needle and further shaped into a Taylor cone (inset) via a strong electric field. At this small radius, exposed to a strong electric field, the Ga atoms are ionized and extracted from the tip, emerging from the source as a Ga^+ ion beam (adapted from [187]).

and emission of electrons (and electromagnetic radiation); these electrons are called secondary electrons, that can be collected via a detector and used for imaging (see also section 3.1.2). For elastic collision processes, the ion energy is transferred to the sample atoms, which, depending on their position are displaced to collide with further atoms, or, they are sputtered from the surface resulting in ion emission.

The total event evolution of these ion – solid interactions is currently understood as a collision cascade (see figure 3.2). The energy of the incoming ion is subsequently transferred to the sample atoms, that now have excessive energy to displace further atoms, which continues until all the energy of the incident ion is exhausted and the ion comes to a halt within the sample and the collision cascade ends. The result of these processes are emitted particles, radiation, damage and heat induced in the sample, as well as an implantation of (Ga^+) ions in the target material. The collision cascade leads to an affected interaction volume, typically characterized via a projected
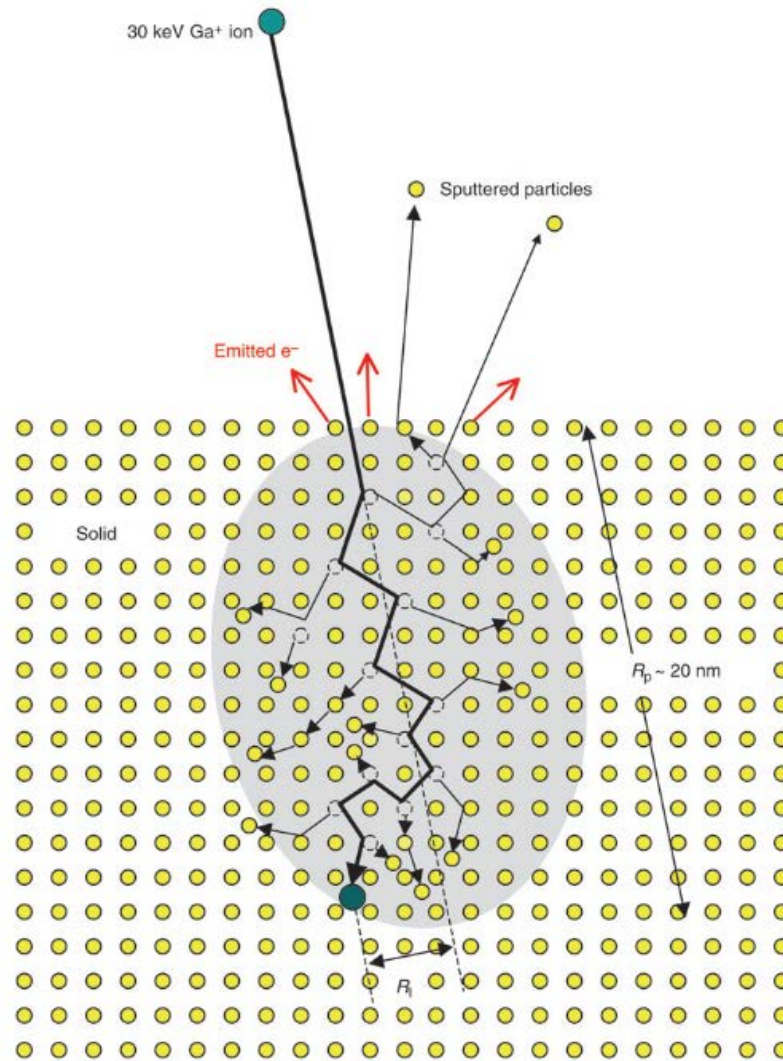
Figure 3.2: Schematic representation of the collision cascade of a Ga^+ ion interacting with the crystal lattice of a solid. The incident ions energy is used for sputtering particles, emission of secondary electrons and sequentially transferred to the atoms of the target sample within the interaction volume characterized by the projection and lateral range, R_p and R_l, respectively. After the ion's energy is used up, the ion remains implanted within the sample (image adapted from [197]).

and lateral range, R_p and R_l, respectively (see figure 3.2). These parameters scale inversely with the density of the material, i.e. need to be obtained specifically for every investigated material. For a typical Ga^+ ion energy of 30 keV, R_p an R_l are in the range of 1 to 20 nm. These numbers are calculated via Monte Carlo simulations and, in the context of this thesis, have also been obtained for bone material. For Ga^+ ions of 30 keV energy, it was found that the damage range is confined within 25 nm beneath the surface and gallium ion implantation within 15 nm beneath the surface [168, 212].

The practically obtainable dimensions that can be achieved via FIB milling are in the range of approx. 100 nm to approx. 100 μm. The bone structure at the microscopic length scale of primary interest for this thesis, i.e. the bone lamella, with thicknesses between 2 – 10 μm is well within the range for FIB milling. Different geometries have been achieved by bone researchers during the last decade, whereas the main goal was to FIB-mill a sample, suitable for mechanical testing comprising of single bone lamella (see figure 3.3). Perhaps the first study utilizing FIB-milled samples of mineralized tissue was published in 2009 by Chan et al., who prepared enamel microbeams of triangular cross section and tested them under bending with the tip of a conventional nanoindenter [24]. Further studies followed with microstructures FIB-machined from the cortical bone of animal origin, e.g. rat, ovine and bovine bone. The microstructures were either microbeams of rectangular cross section to be tested under bending with a nanoindenter or an AFM probe [82, 84], or micropillars of circular [168] or rectangular cross section to be tested under uniaxial compression [83, 109]. One of the recent studies even achieved micropillar compression under hydrated conditions by fully hydrating the bone sample containing the micropillars prior to compression testing with a nanoindenter [169].
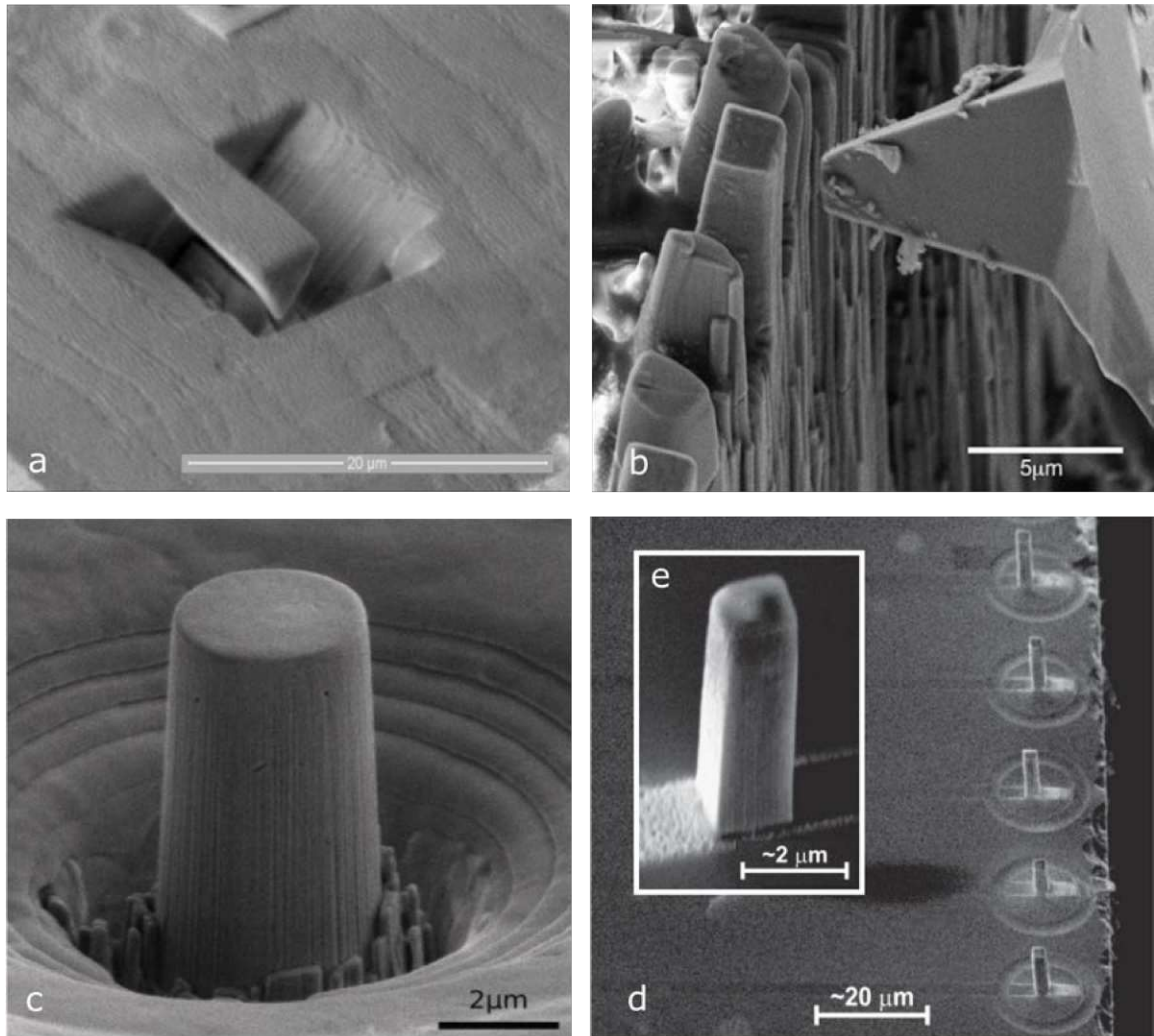
Figure 3.3: SEM images of FIB machined micron sized bone specimens. (a) Microbeam of triangular cross section FIB milled from an enamel prism (adapted from (Chan et al., 2009)). (b) Microbeam of rectangular cross section machined via FIB from rat cortical bone and bent with a flattened in situ AFM probe within the vacuum chamber (adapted from [82]). (c) Micropillar of circular cross section FIB machined from single osteonal lamellae from ovine cortical bone to be tested under uniaxial compression with a flat punch nanoindenter probe (adapted from [168]). (d) Bovine cortical bone micropillars of rectangular shape (inset e) FIB milled and subsequently transferred onto a more rigid silicon wafer substrate via an in situ micromanipulator within the vacuum chamber, also to be tested in compression with a nanoindenter (adapted from [109]).

3.1.2 Scanning electron microscopy (SEM, BEI)

The bombarding of sample material with ions (see section 3.1.1) is inherently damaging, i.e. ion implantation and sputtering of target's material always take place. While these effects can be minimized by using small ion currents and short exposure times, imaging and measuring within a modern dual beam system (combined ion and electron microscopy) is performed by using electrons instead. The electron microscopy technique that utilizes a fine and focused beam of electrons scanning over a sample surface to produce a topography or compositional image is called scanning electron microscopy (SEM).

When electrons in the form of a beam, typically accelerated in the range of 1 – 30 kV, hit a material, numerous interactions with the host atoms occur, leading to signals, such as: secondary electrons (SE), backscattered electrons (BSE), Auger electrons, characteristic X-rays, cathodoluminescence etc. (see figure 3.4). The most commonly used signal for imaging are the secondary electrons (SE). These are low-energy electrons emitted by excited host atoms from the sample material. Since all of the interaction signals occur simultaneously, an energy threshold of 50 eV has been defined by convention, whereas all the electrons with energies up to 50 eV are regarded as secondary electrons and all electrons with higher energies are regarded as backscattered electrons [149]. Due to their low energy, the SE are only able to escape the sample surface within few nm, so they need to be collected to be able to produce an image. This is done by applying a positive bias voltage in front of the detector, to which the SE are attracted and collected. The conventional detector for SE is an Everhart Thornley Detector (ETD), named after its inventors, which uses a scintillator plate and a photomultiplier for signal enhancement. The yield of SE is strongly dependent on the surface tilt angle, resulting in topographical contrast, which is the reason why SE are the signal of choice for topography imaging. Furthermore, the penetration depth of the primary electrons is dependent on the acceleration voltage, with higher voltage electrons resulting in a larger penetration depth. So, by applying different electron beam voltages, information via SE can be
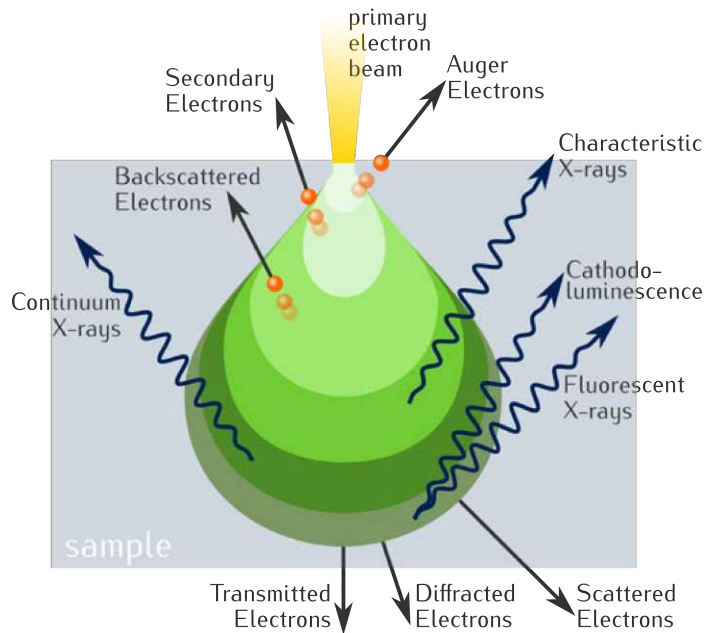
Figure 3.4: Schematic representation of types of signals generated from electron-sample interactions and light bulb shape of the interaction volume (adapted from [143]).

collected either from several nm depth of the sample or only from within the surface layers. This however, comes with a trade off in resolution. The bone material imaged with SE for this thesis was typically imaged with electron acceleration voltages 5 kV – 20 kV.

Backscattered electrons (BSE) have a much larger energy than SE and are backscattered in the half-space where the primary electrons come from. They do not have to be collected with a bias voltage and are generally detected by semiconductor-based detectors arranged around the pin hole of the electron beam. The yield of BSE is dependent on the atomic number Z, leading to a so-called Z-contrast, whereas lager yield is produced by larger atomic numbers [149]. Consequently, the BSE signal is often used to gain compositional information of the sample. In the context of biological samples, this can e.g. be used for imaging colloidal gold particles used in immunohistochemical labelling against the background of biological material [185], or in the context of bone, for imaging of areas with different mineral composition
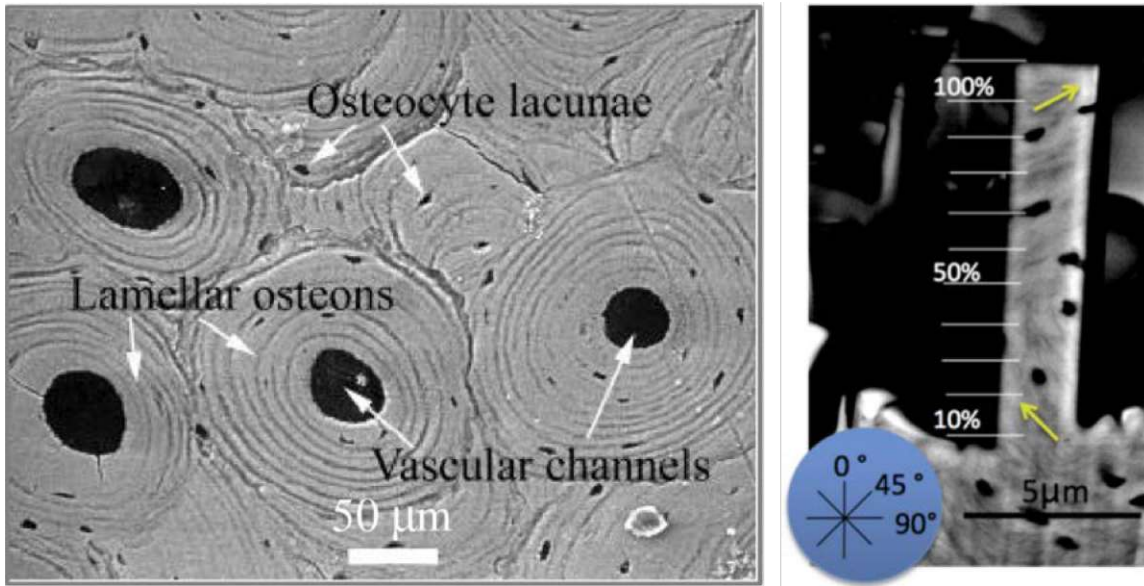
Figure 3.5: SEM images of bone. (Left) ESEM image of the osteonal structure of human cortical bone (adapted from [176]), (right) BSE image of a microbeam comprised of cortical bone lamellae. Due to compositional contrast from the BSE signal, the distribution and orientation of bone lamellae can be discerned. Additionally porosities at this length scale can also be captured (adapted from [84]).

e.g. bone lamellae and lamellar interfaces (see figure 3.5) and even quantification of the bone mineral density distribution via quantitative backscattered electron imaging (qBEI) [157, 158].

Sample preparation

Samples that are to be imaged via SEM need to have a conductive surface and be able to sustain an extreme environment of very low pressure, i.e. high vacuum, in the range of 10^{-5} mbar – 10^{-7} mbar. This is easily provided for metals, which were the initial samples used for SEM imaging, that only need to be contacted to the sample stage with a conductive adhesive. Non-conductive samples accumulate charges on the surface, which leads to large distortions of the image, due to electrostatic repulsion of the targeting electrons. This can be solved by providing a very thin, several nm-thick layer of conductive coating, usually of a metal or an alloy source. Furthermore, biological samples need to be able to mechanically sustain the high extraction forces

of the vacuum. Soft biological samples are usually chemically modified in a protocol called fixation, that induces chemical crosslinking among biological constituents and provides increased mechanical stability of the tissue. After fixation, the sample also needs to be dried to reduce cracking and destruction of the structures during drying, and additionally interfere with the pumping for achieving a high vacuum. For this, samples can be chemically dehydrated by replacing water with alcohol (ethanol) molecules and subsequently left to dry in air or at increased temperature in an oven or via critical point drying. Mineralized biological tissue, such as bone has sufficient mechanical stability compared to unmineralized, soft biological material and does not need to undergo fixation. The bone specimens used for this thesis were neither chemically (fixation or dehydration by ethanol) nor thermally (dehydration at an elevated temperature) treated, since such steps alter the mechanical properties of the tissue [61, 136]. The bone samples for the studies presented in this thesis were dried in air at room temperature and sputter-coated with approx. 10 nm of Au/Pd (60:40) alloy to achieve a conductive coating prior to SEM imaging.

3.2 Mechanical Characterization

Mechanical testing requires samples of well-defined shape and geometry and the methods for preparing microscopically-sized bone specimens utilized in this thesis were presented in the previous chapter. After preparation within the chamber of a dual beam FIB system, the samples were transferred to another setup, where they were either tested under compression or in bending. The general motivation for mechanical characterization is the acquisition of material properties, i.e. quantitative and normalized information on how a certain material responds to mechanical loading. In this context, properties such as the elastic or Young's modulus, yield or transition stress and strength are investigated.

3.2.1 Uniaxial compression

In a uniaxial compression test a specimen is mounted in a mechanical testing device and compressed in a plan-parallel geometry in line with the longest symmetry axis of the specimen (see figure 3.6a). Here, generally a minimum aspect ratio is required such that boundary effects do not influence the load state in the middle of the sample, e.g. the aspect ratio of length to width should typically be in the range 0.8 - 10 (e.g. for metallic materials) to avoid buckling, as recommended by standards for engineering materials (ASTM (e.g. ASTM E09 [6]), ISO, or similar). For mechanical testing of bone such standards are not available, only recommendations for macroscopic bone samples [211]. Loading can be performed in displacement control mode, where a certain displacement (or more precise a displacement rate) of the cross-head within the loading frame is prescribed and the resulting force from the specimen is recorded, or in load control mode, where a compressive force (or more precise a force rate) is prescribed and the resulting deformation displacement of the specimen is recorded. The latter is a more advanced approach and requires a feedback loop translating measured forces into displacements for each sample for appropriate control during testing. The goal of a uniaxial compression test is the recording of a force (load) vs. sample displacement curve obtained as raw data from the testing apparatus (and corrected for superimposed displacements of its parts, such as the load frame compliance, the force sensor deformation etc.). A typical progression of such a curve is presented in figure 3.6b.

The initial portion of the force vs. displacement curve represents the linear region , which is often associated with elastic deformation. The slope of this portion $K = \Delta P / \Delta u$, where P denotes the force and u the displacement of the compressive platen, is the stiffness of the tested sample, giving a measure of how much force is sustained per change in length, i.e. $[K] = [\text{N/m}]$. Loaded beyond this region, the sample enters the non-linear region, where a permanent deformation mechanisms become dominant. If loading is continued, the maximum force that a sample can sustain is reached, after which failure occurs. To exclude the influence of geometry, force vs. displacement
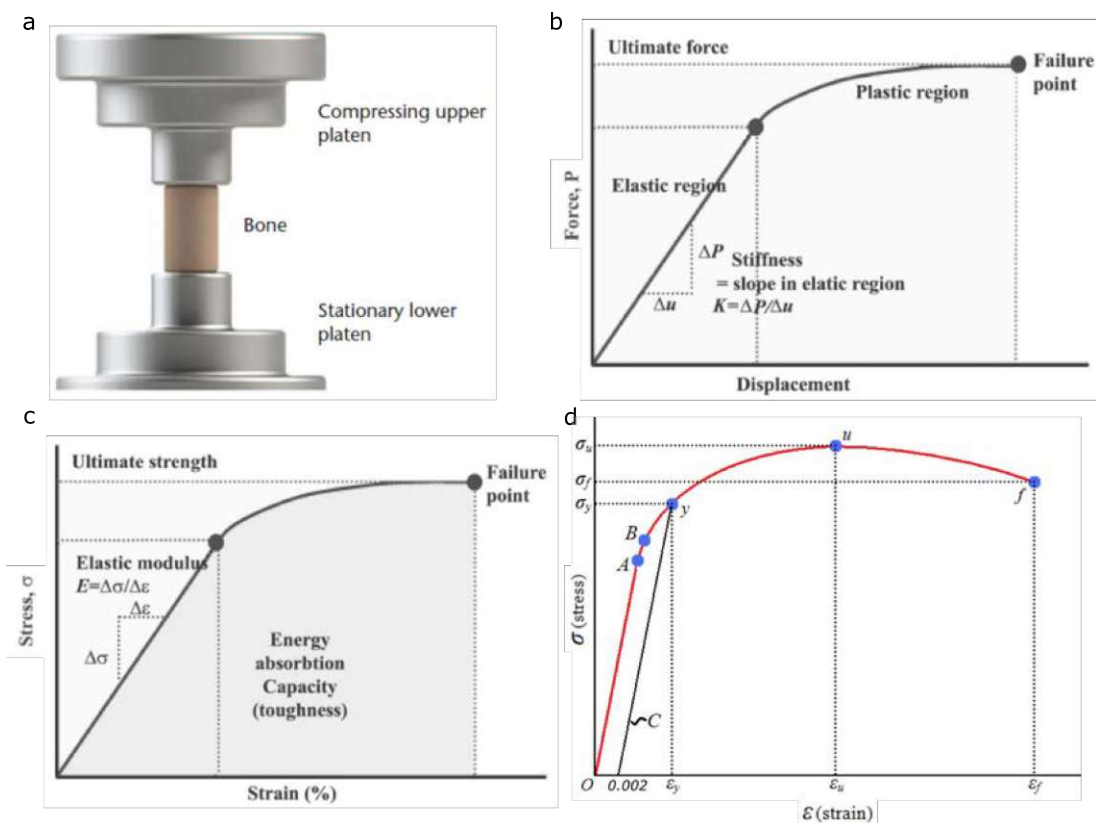
Figure 3.6: Schematic representation of a uniaxial compression test. (a) Schematic visualization of a specimen, e.g. bone, that can be of circular or rectangular cross section, mounted within two platens to undergo uniaxial compression (adapted from [211]). (b) Schematic depiction of a force vs. displacement curve obtained as raw data from a compression test, displaying a region characterized with a linear slope (classically associated with linear elastic behaviour) of stiffness $K = \Delta P/\Delta u$, a nonlinear region with strain hardening and a failure point (adapted from [36]). (c) Schematic depiction of a corresponding stress vs. strain curve obtained from (b) by normalizing with respect to sample geometry, displaying an elastic modulus $E = \Delta\sigma/\Delta\varepsilon$ as the slope of the linear portion of the stress vs. strain curve, ultimate strength, energy absorption (area under the curve) and failure point (adapted from [36]). (d) Schematic depiction of characteristic points on the stress vs. strain curve and the offset method for determination of the yield point. Segment C represents the slope of the portion OA, typically obtained via fitting of the linear portion OA, and offsetting by $0.2\,\%$ the strain. The intersect of segment C with the stress vs. strain curve marks the yield point $y(\sigma_y, \varepsilon_y)$. Point A represents the proportionality limit, point B the elastic limit as classically defined for metals, point $u(\sigma_u, \varepsilon_u)$ the ultimate stress (strength) and $f(\sigma_f, \varepsilon_f)$ the failure point (adapted from [177]).

curves are generally transformed into stress vs. strain curves, by normalizing the data with respect to the sample's initial, dimensions, i.e.:

$$\sigma = \frac{P}{A} \tag{3.1}$$

, where σ is the engineering stress, P the force measured, which is then divided by the sample's cross sectional area A, and

$$\varepsilon = \frac{u}{L} \tag{3.2}$$

, where ε is the engineering strain, u the imposed displacement and L the initial length of the sample, thus representing the percent of relative change in length of the sample. The slope of the stress vs. strain curve represents the elastic (or Young's) modulus (see figure 3.6c), defined as:

$$E = \frac{\Delta\sigma}{\Delta\varepsilon} \tag{3.3}$$

Since E is now independent of the sample's geometry, it is considered to be a true and constant material parameter, giving measure of the material's elasticity. The elastic region extends up to a point where the deformation transitions from elastic and reversible to plastic and irreversible. This point on the stress vs. strain curve is denoted as the yield point, represented by a σ_y yield stress and ε_y yield strain value. Depending on the physical nature of the investigated material, the transitional region can be complex and look very different for different types of materials, so very often a yield point is difficult to be determined. For this reason, for many engineering materials the offset method is adopted (see figure 3.6d). Typically, an offset of 0.2 % strain is chosen, whereby the slope of the linear portion of the stress vs. strain curve is offset by 0.002, i.e. 0.2 % strain along the ordinate and the point of intersection with the stress vs. strain curve determines the yield point.

Stress vs. strain curves can display a large variety of progression for different materials. Beyond elastic modulus E and yield values σ_y, ε_y further parameters and points on the curve can be determined, e.g. strength, given by the maximum stress value, also called ultimate stress σ_{max}, the corresponding strain at max. stress $\varepsilon_{\sigma max}$, a failure point or maximum deformation etc.

The stress and strain measures as defined by equations (3.1) and (3.2) are more specifically termed engineering stress and engineering strain. For their determination, the initial, i.e. undeformed dimensions of the sample are used for the cross sectional area A and length L. However, these values change during deformation leading to deviation of the engineering stresses and strains from their true values. Alternatively, instantaneous values of A and L can be used to calculate true stresses and true strains. Under the assumption of constant volume and uniform deformation, these are connected to engineering stress and engineering strain as:

$$\sigma_t = \sigma(1 + \varepsilon) \tag{3.4}$$

and

$$\varepsilon_t = ln(1 + \varepsilon) \tag{3.5}$$

, where σ and ε are calculated by equations (3.1) and (3.2). The true strain measure ε_t is sometimes also termed logarithmic stretch lnU.

Generalized Hooke's law

The general elastic behavior of solids, introduced above through an experimental approach (see figure 3.6), is governed by the Hooke's law:

$$F = kx \tag{3.6}$$

, which was initially postulated for a mechanical spring [71], where F is a deformation force acting on a representative spring, x the change in length of the spring and k the characteristic stiffness of the spring. It states that the force is proportional to the length change due to deformation, with the proportionality factor k being the stiffness that is dependent on the spring's properties. This law holds for most solid materials undergoing only small deformations, loaded within the linear elastic region of their force vs. displacement curve and not surpassing the yield point. This formulation of Hooke's law also only considers a one dimensional behavior, where force and displacement occur in the same direction.

However, considering continuous elastic materials, the stresses and strains around a point within the material cannot be described by single vectors, but rather with two second order tensors, the stress tensor $\boldsymbol{\sigma}$ and the strain tensor $\boldsymbol{\varepsilon}$ [112, 191]. The components of these tensors are still linearly connected, which mathematically can be represented by the tensorial equation

$$\boldsymbol{\sigma} = C\boldsymbol{\varepsilon} \tag{3.7}$$

and in analogy to eq. (3.6) is sometimes referred to as the generalized Hooke's law. Here C is a fourth order tensor referred to as the stiffness or elasticity tensor, in analogy to eq. (3.3). In three dimensions $\boldsymbol{\sigma}$ and $\boldsymbol{\varepsilon}$ are (3 x 3) matrices and C a (3 x 3 x 3 x 3) tensor, thus in index notation eq. (3.7) can be written as

$$\sigma_{ij} = C_{ijkl}\varepsilon_{kl} \tag{3.8}$$

, where $\boldsymbol{\sigma}$ and $\boldsymbol{\varepsilon}$ have 9 components and C has 81 components. Due to symmetry of $\boldsymbol{\sigma}$ and $\boldsymbol{\varepsilon}$, the number of their independent components is reduced to 6 and the number of independent components of C to 36, which by means of the Voigt notation can be represented by the matrix equation

$$
\begin{bmatrix} \sigma_1 \\ \sigma_2 \\ \sigma_3 \\ \sigma_4 \\ \sigma_5 \\ \sigma_6 \end{bmatrix} = \begin{bmatrix} C_{11} & C_{12} & C_{13} & C_{14} & C_{15} & C_{16} \\ C_{21} & C_{22} & C_{23} & C_{24} & C_{25} & C_{26} \\ C_{31} & C_{32} & C_{33} & C_{34} & C_{35} & C_{36} \\ C_{41} & C_{42} & C_{43} & C_{44} & C_{45} & C_{46} \\ C_{51} & C_{52} & C_{53} & C_{54} & C_{55} & C_{56} \\ C_{61} & C_{62} & C_{63} & C_{64} & C_{65} & C_{66} \end{bmatrix} \begin{bmatrix} \varepsilon_1 \\ \varepsilon_2 \\ \varepsilon_3 \\ \varepsilon_4 \\ \varepsilon_5 \\ \varepsilon_6 \end{bmatrix}
\tag{3.9}
$$

, whereby $\boldsymbol{\sigma}$ and $\boldsymbol{\varepsilon}$ are represented as 6-components vectors and the elasticity tensor C as a (6 x 6) matrix, with the following index numeration of the stress and strain components: $1 - 11$, $2 - 22$, $3 - 33$ for the normal stress and strain components; $\sigma_4 - \sigma_{23}$, $\sigma_5 - \sigma_{31}$, $\sigma_6 - \sigma_{12}$ for the shear stress components; and $\varepsilon_4 - 2\varepsilon_{23}$, $\varepsilon_5 - 2\varepsilon_{31}$, $\varepsilon_6 - 2\varepsilon_{12}$, with a factor 2, for the shear strain components. Furthermore, from energy considerations it is established that the C matrix from eq. (3.9) is also symmetric, thus the number of independent elastic constants is reduced to maximum 21.

Equation (3.9) holds for general, fully anisotropic materials. In practice, further symmetries of materials are investigated and applied for a mathematical description, to substantially simplify and reduce the number of independent components of C, which are discussed in the following.

Orthotropic materials are materials with different mechanical properties in three orthogonal directions. Due to this type of symmetry and additional invariance conditions to the C matrix, eq. (3.9) for orthotropic symmetry takes the form:

$$
\begin{bmatrix} \sigma_1 \\ \sigma_2 \\ \sigma_3 \\ \sigma_4 \\ \sigma_5 \\ \sigma_6 \end{bmatrix} = \begin{bmatrix} C_{11} & C_{12} & C_{13} & 0 & 0 & 0 \\ C_{21} & C_{22} & C_{23} & 0 & 0 & 0 \\ C_{31} & C_{32} & C_{33} & 0 & 0 & 0 \\ 0 & 0 & 0 & C_{44} & 0 & 0 \\ 0 & 0 & 0 & 0 & C_{55} & 0 \\ 0 & 0 & 0 & 0 & 0 & C_{66} \end{bmatrix} \begin{bmatrix} \varepsilon_1 \\ \varepsilon_2 \\ \varepsilon_3 \\ \varepsilon_4 \\ \varepsilon_5 \\ \varepsilon_6 \end{bmatrix} \tag{3.10}
$$

, where the number of independent components reduces to 9 elastic constants. The stress vs. strain relationships are simplified and it is feasible to write the elastic components of the C matrix in terms of the mechanical material constants elastic (Young's) moduli E_i, the Poisson ratios ν_{ij} and the shear moduli G_{ij}. Often it is more convenient to express the inverse of the elasticity matrix C^{-1}, also called the compliance matrix, and calculate the strains in terms of the stresses:

$$
\boldsymbol{\varepsilon} = C^{-1}\boldsymbol{\sigma} \tag{3.11}
$$

, which in the case of orthotropic symmetry takes the form:

$$
\begin{bmatrix} \varepsilon_1 \\ \varepsilon_2 \\ \varepsilon_3 \\ \varepsilon_4 \\ \varepsilon_5 \\ \varepsilon_6 \end{bmatrix} = \begin{bmatrix} \frac{1}{E_1} & -\frac{\nu_{21}}{E_2} & -\frac{\nu_{31}}{E_3} & 0 & 0 & 0 \\ -\frac{\nu_{12}}{E_1} & \frac{1}{E_2} & -\frac{\nu_{32}}{E_3} & 0 & 0 & 0 \\ -\frac{\nu_{13}}{E_1} & -\frac{\nu_{23}}{E_2} & \frac{1}{E_3} & 0 & 0 & 0 \\ 0 & 0 & 0 & \frac{1}{G_{23}} & 0 & 0 \\ 0 & 0 & 0 & 0 & \frac{1}{G_{31}} & 0 \\ 0 & 0 & 0 & 0 & 0 & \frac{1}{G_{12}} \end{bmatrix} \begin{bmatrix} \sigma_1 \\ \sigma_2 \\ \sigma_3 \\ \sigma_4 \\ \sigma_5 \\ \sigma_6 \end{bmatrix} \tag{3.12}
$$

A further subgroup are transversely isotropic materials, which are symmetric about an axis and have a plane of symmetry that is perpendicular to that axis, that is itself fully isotropic. Applying these symmetries to the C matrix leads to its form:

$$
\begin{bmatrix} \sigma_1 \\ \sigma_2 \\ \sigma_3 \\ \sigma_4 \\ \sigma_5 \\ \sigma_6 \end{bmatrix} = \begin{bmatrix} C_{11} & C_{12} & C_{13} & 0 & 0 & 0 \\ C_{12} & C_{11} & C_{13} & 0 & 0 & 0 \\ C_{13} & C_{13} & C_{33} & 0 & 0 & 0 \\ 0 & 0 & 0 & C_{44} & 0 & 0 \\ 0 & 0 & 0 & 0 & C_{44} & 0 \\ 0 & 0 & 0 & 0 & 0 & \frac{C_{11}-C_{12}}{2} \end{bmatrix} \begin{bmatrix} \varepsilon_1 \\ \varepsilon_2 \\ \varepsilon_3 \\ \varepsilon_4 \\ \varepsilon_5 \\ \varepsilon_6 \end{bmatrix}
\tag{3.13}
$$

with only 5 independent elastic constants. Similar as above, the compliance matrix C^{-1} for transversely isotropic materials can be expressed via the engineering mechanical constants E, ν and G:

$$
\begin{bmatrix} \varepsilon_1 \\ \varepsilon_2 \\ \varepsilon_3 \\ \varepsilon_4 \\ \varepsilon_5 \\ \varepsilon_6 \end{bmatrix} = \begin{bmatrix} \frac{1}{E_1} & -\frac{\nu_{21}}{E_1} & -\frac{\nu_{31}}{E_3} & 0 & 0 & 0 \\ -\frac{\nu_{12}}{E_1} & \frac{1}{E_1} & -\frac{\nu_{31}}{E_3} & 0 & 0 & 0 \\ -\frac{\nu_{13}}{E_1} & -\frac{\nu_{13}}{E_1} & \frac{1}{E_3} & 0 & 0 & 0 \\ 0 & 0 & 0 & \frac{1}{G_{13}} & 0 & 0 \\ 0 & 0 & 0 & 0 & \frac{1}{G_{13}} & 0 \\ 0 & 0 & 0 & 0 & 0 & \frac{2(1+\nu_{12})}{E_1} \end{bmatrix} \begin{bmatrix} \sigma_1 \\ \sigma_2 \\ \sigma_3 \\ \sigma_4 \\ \sigma_5 \\ \sigma_6 \end{bmatrix}
\tag{3.14}
$$

In the special case of isotropic materials, the material properties are the same in all directions. For the equations relating the stresses and strains, i.e. the C matrix, this means they have to be independent of any coordinate system in which they are described. For the compliance matrix, application of these symmetry boundary conditions yields the form

$$
\begin{bmatrix} \varepsilon_1 \\ \varepsilon_2 \\ \varepsilon_3 \\ \varepsilon_4 \\ \varepsilon_5 \\ \varepsilon_6 \end{bmatrix} = \frac{1}{E} \begin{bmatrix} 1 & -\nu & -\nu & 0 & 0 & 0 \\ -\nu & 1 & -\nu & 0 & 0 & 0 \\ -\nu & -\nu & 1 & 0 & 0 & 0 \\ 0 & 0 & 0 & 2+2\nu & 0 & 0 \\ 0 & 0 & 0 & 0 & 2+2\nu & 0 \\ 0 & 0 & 0 & 0 & 0 & 2+2\nu \end{bmatrix} \begin{bmatrix} \sigma_1 \\ \sigma_2 \\ \sigma_3 \\ \sigma_4 \\ \sigma_5 \\ \sigma_6 \end{bmatrix} \tag{3.15}
$$

By means of this equation, if uniaxial loading and strains along one axis, e.g. x_1 are now considered, i.e.

$$
\varepsilon_1 = \frac{1}{E}(\sigma_1 - \nu(\sigma_2 + \sigma_3)) \tag{3.16}
$$

as well as the absence of stresses other than σ_1 are assumed, then

$$
\varepsilon_1 = \frac{1}{E}\sigma_1 \tag{3.17}
$$

is recovered in analogy to equation 3.3.

From equation 3.15 it is evident, that the number of independent constants is reduced to only 2. This means an isotropic material can be fully described by the two mechanical constants, the Young's modulus E and the Poisson's ratio ν (for isotropic materials the shear modulus G can be calculated via E and ν as $G = \frac{E}{2(1+\nu)}$). Thus, Hooke's law for isotropic materials, written in the form of eq. (3.7) and (3.9) is

$$
\begin{bmatrix} \sigma_1 \\ \sigma_2 \\ \sigma_3 \\ \sigma_4 \\ \sigma_5 \\ \sigma_6 \end{bmatrix} = \frac{E}{(1+\nu)(1-2\nu)} \begin{bmatrix} 1-\nu & \nu & \nu & 0 & 0 & 0 \\ \nu & 1-\nu & \nu & 0 & 0 & 0 \\ \nu & \nu & 1-\nu & 0 & 0 & 0 \\ 0 & 0 & 0 & \frac{1-2\nu}{2} & 0 & 0 \\ 0 & 0 & 0 & 0 & \frac{1-2\nu}{2} & 0 \\ 0 & 0 & 0 & 0 & 0 & \frac{1-2\nu}{2} \end{bmatrix} \begin{bmatrix} \varepsilon_1 \\ \varepsilon_2 \\ \varepsilon_3 \\ \varepsilon_4 \\ \varepsilon_5 \\ \varepsilon_6 \end{bmatrix} \qquad (3.18)
$$

Due to its hard nature, bone has mainly been considered as a linear elastic solid. Using the described mathematical framework, bone tissue has been characterized as isotropic, transversely isotropic or orthotropic, depending on the length scale of interest [119]. At the lower macroscale, the effective mechanical response of cancellous bone has been described as isotropic, due to its spongy structure [88] and in more recent studies, transverse isotropy of cancellous bone has been investigated [100]. At the tissue level, anisotropy of cortical bone has also been investigated, motivated from predominant loading directions of long bones, in the context of transversely isotropic [128] and later orthotropic material as well [51]. At the microscale, at the length scale of single osteons down to individual lamellae, the hierarchical structure of bone becomes more evident, suggesting that an isotropic approach might be overly simplistic. Indeed, both numerical and experimental efforts have been made to quantify orthotropic elastic constants including considerations of lamellar orientation at the level of single osteons [151].

Bone tissue is a biological material and with its hierarchical structure over several length scales (see section 2.1.2) it is a more complex material than many engineering materials. Another concept initially determined from mechanical testing of metals is the yield point. The yield point is the (theoretical) point on the stress vs. strain curve (see figure 3.6d), corresponding to a yield strain and yield stress (also named

yield strength) value, determining the end of the elastic region and onset of the plastic region. Within the elastic region, i.e. the linear portion of the stress vs. strain curve, deformation of the material is reversible when loading of the material is removed. If loading is continued beyond the elastic region, then plastic deformation occurs leading to yielding of the material and residual, non-reversible deformation is present when loading is removed. For crystalline materials or metals, this is understood in terms of slippage along atomic planes or movement of dislocations. For bone material, the deformation mechanisms might be more complex and moreover, superimposed during loading within the elastic region. For this reason, an adapted designation of such a point on the stress vs. strain curve has been chosen – transition point (instead of yield point), to indicate a transition in deformation mechanisms from linear to non-linear.

The elastic properties of solids are mainly characterized by the elastic (Young's) modulus E, or components of the elasticity matrix C. The definition of E is given by eq. (3.3) and in analogy eg. (3.7), as a constant and time-independent material parameter. Considering a mechanical spring and Hooke's law, the stress vs. strain response will be the same, independent of how fast the spring is loaded, i.e. the strain rate of loading. Bone is composed of a solid mineral phase and organic, hydrated collagen phase, collagen being a biopolymer, which are known to exhibit viscoelastic behavior. Additionally, non-collagenous proteins (NCPs), which are polymer-like structures as well, are present at the interfaces of these two phases across the hierarchical levels of bone tissue. As will be shown later (chapter 5), different mechanical response was measured from bone samples at different loading rates, which is indicative of viscoelastic behavior. Indeed, there has been experimental evidence in recent years regarding viscoelasticity of bone tissue, especially in wet conditions, e.g. in cortical bone [205], as well as in trabecular bone [43, 150]. A simple, monotonic compression (or tension) test is not sufficient to reveal contributions of different superimposed deformation mechanisms based on a loading curve alone. Elasticity is defined as the ability of the system to restore mechanical deformation, thus better detectable after loading is removed. For a mechanical test, this would imply that unloading should

be also recorded in a force vs. displacement curve in addition to loading and elastic properties, in terms of the slope of the curve (eq. (3.3)) should be extracted from the unloading portion of the curve. Additionally, measurements should be performed at different loading rates for examination of viscoelastic contributions. In this context, further development of a mechanical testing protocol are possible, as presented in the following.

Cyclic partial unloading

The concept of the stress vs. strain curve presented above, that plays a central role in mechanical characterization of materials and determination of mechanical parameters such as elastic modulus E, strength etc., is generally used by applying a monotonically increasing force resulting in monotonic compression of the sample. This type of compression is usually applied to study elastic solids, e.g. engineering materials, but has also been used for macroscopic and microscopic bone samples such as micropillars (see figure 3.7a)[109]. Such tests ultimately result in destruction of the sample and can limit the amount of information and parameters that can be extracted from a single test. Moreover, monotonic tests at a single rate do not allow to identify any rate-dependent behavior, as previously outlined.

Alternatively, loading can also be performed in an incremental fashion in loading and (partial) unloading cycles. For complex materials like bone, non-elastic in addition to purely elastic (reversible) deformations can be superimposed during loading, resulting in a different pathway of the unloading curve compared to the loading curve. The motive for such type of loading regime initially comes from the technique of nanoindentation, where a sample is indented with a sharp tip to induce plastic deformation and create a permanent imprint on the sample surface. The analysis of the resulting force vs. displacement curve has been largely performed utilizing the method of Oliver and Pharr, where the initial part of the unloading portion of the curve is used to calculate an elastic (indentation) modulus [137]. For this calculation often the assumption of material isotropy is made and, in the case of bone, a Poisson's ratio of 0.3 is generally used. The technique probes the material within depths of <
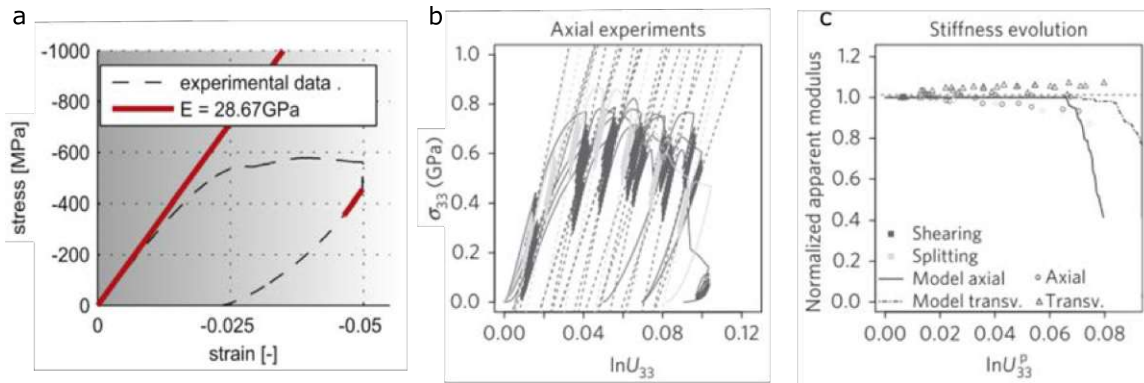
Figure 3.7: Monotonic and cyclic compression of bone micropillars. (a) Monotonic uniaxial compression of a bone micropillar conducted for extraction of the elastic modulus from the unloading portion of the curve (adapted from [109]). (b) Cyclic loading and partial unloading of bone micropillars in the axial direction conducted for study of the unloading moduli and post-yield behavior of bone. (c) The evolution of unloading moduli for bone micropillars displaying relatively constant values up to large strains of 0.08 (b and c adapted from [168]).

1 μm and in the context of the mechanical properties of bone has provided invaluable data and insights of bone tissue at the microscale, summarized in extensive reviews [102, 181](see also section 2.2.1).

A further development of the nanoindentation technique is the utilization of a flattened (flat punch) tip instead of a sharp tip, to compress single specimen rather than indenting the bulk material. In this way a compression test at the single to several microns length scale can be performed, if micron sized bone specimen can be prepared [109, 168]. In such a microcompression test, by application of cyclic partial unloading information can be recorded in the apparent linear and elastic region, but also elucidate behavior in the post-yield regime (see figure 3.7b,c)[168]. Moreover, more information about the mechanical behavior can be collected prior to complete failure of the sample, which was also one motivation for adopting such a protocol for testing of the extensively prepared and valuable microscopic bone samples in this thesis.

3.2.2 Bending

While uniaxial compression (or tension) is a load case that is easy to analyze and represents a clearly defined and (ideally) homogeneous stress state, it is not always straightforward to prepare samples that can be tested uniaxially. Therefore, bending tests may be preferable from a sample preparation perspective, where loading is imposed perpendicular to the longest symmetry axis. Bending tests have been performed on whole bones, particularly extracted from mice models, due to their small size [79, 145]. The convenience of preparing small macroscopic samples in the mm - cm range has also been used for testing at the bone tissue level, both for individual trabeculae [23, 87], as well as cortical bone samples [178]. Employing beam theory to such tests can be used to derive material properties, as in appropriate geometries stresses also arise only or to the largest extent in axial direction. Nevertheless, while experimentally often easy to achieve, a bending test always results in a heterogeneous stress state including both tensile and compressive stresses.

Due to the capabilities of FIB milling (see figure 3.3a,b) for preparation of beam like structures at the microscale (e.g. [24, 82]), also bending of (micro)beams was utilized in this thesis (see chapter 4 and 5). Bending of FIB machined microbeams has been performed either with a nanoindentation instrument [24], or with a flattened tip of an atomic force microscope (AFM)[82, 84]. During mechanical interaction, all solid components taking part in a mechanical test will undergo some deformation, including the parts of the testing instrumentation. However, only the deformation behavior of the tested sample is of interest and the contributions of the testing machine, termed machine compliance, however small should be corrected in the recorded displacement data [30]. To minimize such contributions, testing machines are generally constructed of a stiff and robust loading frame as well as much stiffer components compared to the (estimated) stiffness of the sample, which is the case with nanoindenters. With AFM the situation is different, since bending on the sample is imposed with an AFM probe, which itself undergoes bending and at the same time utilizes the bending of the probe for force sensing. On the one hand the AFM probe needs to be sufficiently

stiff to cause bending of the sample and on the other hand sufficiently compliant to allow for detectable deflection of the probe via the AFM system. Hence, compared to nanoindentation, bending via AFM has limitations regarding the sample stiffness and stiffness matching (of the tested sample and AFM probe) needs to be estimated for optimal force and displacement sensing (see section 3.3.2 and chapter 5)[89]. However, AFM offers other advantages of imaging resolution, positioning and operation remaining largely unaffected when performed in an aqueous environment, whereas nanoindentation, though generally feasible on submerged samples, offers limited positioning capacities.

For calculation of material parameters from bending experiments, e.g. elastic modulus E, the Euler-Bernoulli theory can be used, given that tested beams are of slender shape (length to height ratio > 5). This theory is widely used for engineering materials, and it relies on several assumptions, which need to be considered [12]:

(1) Transverse sections that are plane before bending, remain plane during bending.

(2) Transverse sections will be perpendicular to circular arcs having a common center of curvature.

(3) The radius of curvature of the beam during bending is large compared with the transverse dimensions.

(4) Longitudinal elements of the beam are subjected only to simple tension or compression, i.e. there is no additional loading, such as lateral stresses or torsion.

(5) The material is linearly elastic and has the same Young's modulus in tension and compression.

For slender beam-like structures, i.e. the longitudinal dimension (length) is much larger (i.e. > 5 times) than the transverse dimensions (height and width) and bending resulting in small deflections assumptions 1. - 4. can be met. Assumption 5. can pose a challenge, especially for complex materials like bone. However, since the beam is bent in the linear elastic regime, i.e. not beyond the yield/transition point, the

assumption of a linear elastic response was made for the calculation of a bending modulus.

The Euler-Bernoulli bending theory relates the deflection of the beam ν to the bending moment M, elastic modulus E of the beam material and the second moment of area I (calculated as $I = \iint y^2 dA$) of the beam's cross section A. The governing equation of the deflection curve according to this theory and sufficient validity of the above mentioned assumptions is given by [12]:

$$\frac{d^2\nu}{dx^2} = -\frac{M}{EI} \tag{3.19}$$

where x is the direction of the longitudinal axis of the beam (see figure 3.8a). Here the minus sign stems from a common convention, where the deflection of the beam is oriented downwards and bending moments are positive in counter-clockwise manner. This differential equation can be solved by several methods, e.g. double integration, superposition, moment-area method etc., with application of boundary conditions for the beam's deflection and slope at the supports. The boundary conditions and loading cases used for bending of microbeams in this thesis were the ones for a single-clamped (or cantilevered, denoted here as sc) beam (see figure 3.8b) and a double-clamped (also called fixed, denoted here as dc) beam (see figure 3.8c).

For a bending load P in y direction applied at the end of a single-clamped beam of length L, the deflection of the free end in y direction can be calculated as [12]:

$$\nu_{sc} = \frac{1}{3}\frac{PL^3}{EI} \tag{3.20}$$

For a beam double-clamped at both ends and a load applied in the middle of the beam, i.e. at $L/2$, the deflection is calculated as:

$$\nu_{dc} = \frac{1}{192}\frac{PL^3}{EI} \tag{3.21}$$
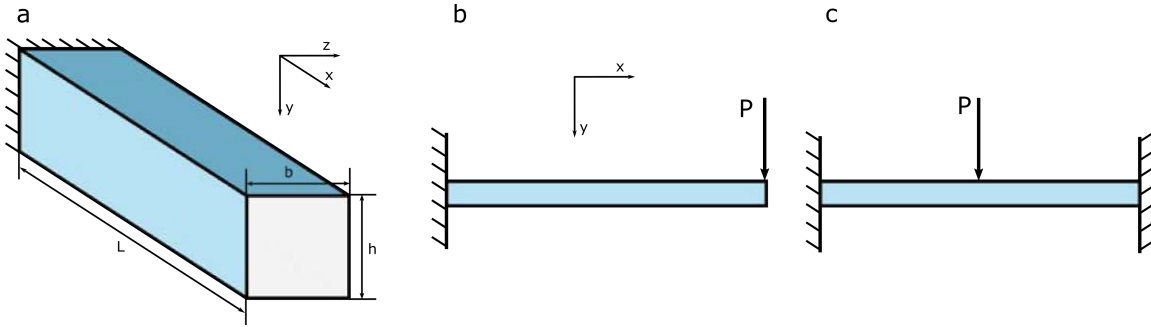
Figure 3.8: Schematic representation of relevant beam dimensions, boundary conditions and load cases for beam bending employed in this thesis. (a) Three dimensional beam dimensions of length L, beam width b and beam height h, where the longitudinal beam axis parallel to L is oriented in the x-direction. (b) loading case of a single-clamped beam (sc) loaded at the free end via load P in y-direction. (c) loading case of a double-clamped beam (dc) loaded in the middle of its span length $L/2$ via load P.

During a bending experiment a force vs. displacement, i.e. force vs. beam deflection curve is recorded by the testing apparatus. The slope of the linear elastic region is the stiffness of the beam $S = P/\nu$ (see also figure 3.6b). So, by obtaining the stiffness value from experiment, equations (3.20) and (3.21) can be rearranged to calculate the bending modulus:

$$E_{sc} = \frac{1}{3}\frac{PL^3}{\nu_{sc}I} = \frac{1}{3}S_{sc}\frac{L^3}{I} \tag{3.22}$$

and

$$E_{dc} = \frac{1}{192}\frac{PL^3}{\nu_{dc}I} = \frac{1}{192}S_{dc}\frac{L^3}{I} \tag{3.23}$$

In case of a linear elastic and isotropic material the bending modulus is then identical to the elastic or Young's modulus of the materials. The (micro)beams utilized in this thesis had a nominal rectangular cross section, their second moment of area can be calculated as [12]:

$$I = \frac{bh^3}{12} \tag{3.24}$$

, where b is the width and h is the height of the beam. Here the assumption of symmetric cross section(s) is made, since asymmetry across the height of cross sections would lead to additional, e.g. torsional deformation that needs to be accounted for.

Equations (3.22) and (3.23) represent a method for calculation of a single E value, from a single bending experiment, performed either at the free end of a single-clamped beam or at the middle point of a double-clamped beam, respectively. Moreover, they also reveal a 3$^{\text{rd}}$ power dependency on the beam's length L. The development of atomic force microscopy (AFM) techniques as means for mechanical characterization at the micro- and nanoscale (see section 3.3) and its application in a bending experiment is suggestive of imposing loading at several positions along a beam instead of a single position. The advantage of such a procedure is that the absolute distance along the beam, i.e. with respect to the clamping point(s) can be varied, as this measurement likely has a larger error compared to the relative distances between load application points. In this context, equation (3.19) can be solved for loads applied at different positions x along the length of a beam and yields following equations for the stiffness dependance on the position of the imposed bending load, $S(x)$ [12]:

$$S_{sc}(x) = \frac{1}{3}\frac{E_{sc}I}{x^3} \tag{3.25}$$

for the single-clamped beam, where x is the distance of the load application point measured from the clamped point, and

$$S_{dc}(x) = 3E_{dc}I\frac{L^3}{x^3(L-x)^3} \tag{3.26}$$

for the double-clamped beam. According to these equations, if a beam structure can be bent at several positions x along its length, a set of stiffness values can be measured. The stiffness values can then be plotted against the beam position and

should follow an arrangement of a 3rd order parabola due to the x^3 dependence. This implies that the stiffness data can be fitted by equations (3.25) or (3.26) respectively, where E is now obtained as a fit parameter. For this method several bending curves, i.e. more mechanical information is used for the calculation of E compared to a single bending curve as per equations (3.22) and (3.23).

3.3 Atomic Force Microscopy (AFM)

The atomic force microscope (AFM) is a subtype of the scanning probe microscope (SPM) family, i.e. it is based on the principle of a probe interacting with the surface of a sample material, scanning the surface in a raster manner to produce an image. The probes typically used in AFM are very sharp, i.e. they have tip radii of several nanometers and so the interactions with the sample involve interatomic attractive and repulsive forces, hence the name of the technique. Other interactions can also be exploited, e.g. electric or magnetic, with the adequate choice of probe and sample properties. Due to the very localized interaction, AFM is known for achieving much higher resolution compared to diffraction limited light microscopy. In fact, AFM resolution can be tuned down to the scale of individual atoms and also individual electron orbitals [53, 54]. Furthermore, since the operation mode is mechanical the abilities of the technique extend beyond imaging, enabling force measurements and (micro)manipulation, which contributed to the popularity of the technique and the development of nanotechnology in recent decades. An additional practical feature of AFM is the ability of operation in both gaseous (air) and liquid (aqueous) media (compared to e.g. necessary vacuum conditions of SEM), both of which were employed in the present thesis.

An AFM instrument generally consists of a scanning unit moving either the AFM sensor (cantilever) or the sample laterally and a unit moving either the AFM sensor (cantilever) or the sample perpendicular to the lateral movement plane. The AFM used for the work presented here consists of a so-called scanning-lever system, mean-

ing that the sample is at rest, whereas all movements are performed on the sensor (cantilever). Below the head, holding and moving the cantilever, a sample stage is placed, whereupon a sample is mounted (see figure 3.9a). The x, y, z movement of the cantilever is provided by piezo elements and an additional motorized sample stage provides larger x and y movement of the sample. As the cantilever scans over the surface, its deflection (and torsion) is generally detected via a laser beam reflected on the back side of the probe and collected in a photodiode detector. The piezo unit driving the cantilever movement and the detector signal are coupled in a feedback control unit constantly adapting the cantilever's scanning height (when in contact mode, see section 3.3.1). So, e.g. when the cantilever encounters a heightened feature on the sample surface (see figure 3.9b), the cantilever deflects due to the interaction of the tip and the sample feature, whereby the deflection signal is registered by the instrument and adjusted to a specified setpoint via the feedback loop (when in contact mode, see section 3.3.1). The scanning is performed in a raster manner, ultimately producing an indirect image of the feature by depicting the deflection signal versus the (x, y) position (see figure 3.9c).

3.3.1 Imaging

Imaging with modern AFM instruments can be performed in three general modes: contact mode, tapping or intermittent contact mode and non-contact mode. The choice depends on the type and fragility of the sample, the amount and distance of the desired contact between the probe and the sample as well as the driving force of the cantilever.

Contact mode

In contact mode the probe tip is "dragged" in such proximity to the sample surface, that it can be assumed that the tip is in contact with the sample. For samples that are mechanically stable, an AFM cantilever that is soft enough to reasonably deflect to the sample's surface features and appropriate scanning velocity, this is generally
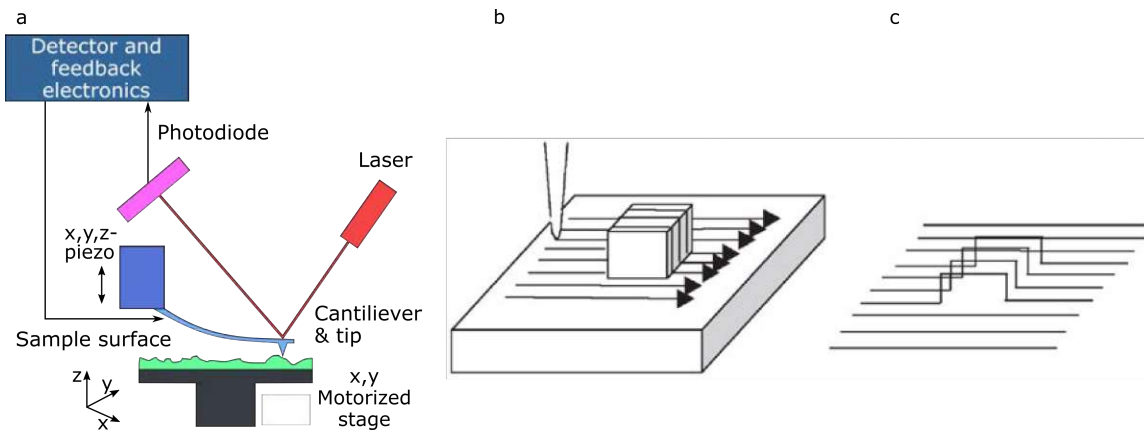
Figure 3.9: Measuring principle of AFM. (a) The tip of an AFM probe scans over the sample surface. As the scan progresses, the deflection of the cantilever is detected via reflected laser light on the back of the cantilever collected in a photodiode detector (adapted from [139]) (b) Schematic representation of the tip pathway as it scans over a 3-dimensional feature on a sample's surface and (c) the cantilever deflection information creating an "indirect" image impression recorded from the cantilever interaction with the sample's topography (image adapted from [202]).

the simplest imaging mode. In this mode, considering figures 3.9b and c, instead of scanning at a constant height and recording the cantilever deflection, whereby the imaging force would increase and decrease, the deflection signal is used as a feedback signal to the control electronics, which adjusts the scanning height in attempt to maintain a constant contact distance (and thus constant tip sample interaction i.e. imaging force) to minimize alterations to the tip or damage to the sample. Since the sample surface experiences a scratch-like effect in this mode, not all damage of the sample surface, due to leveling and surface roughness effects can be avoided, sometimes this also results in a destructive alteration of tip or sample. This is the main drawback of this mode and was historically the reason for the development of other modes (e.g. tapping mode).

Tapping mode

Compared to contact mode, the tapping mode also called intermittent contact mode is a dynamic imaging mode. Instead of using a static signal, the AFM cantilever

is oscillated at a frequency close to its resonance frequency and the amplitude (and frequency) of the cantilever are monitored. The scanning distance to the sample is larger than in contact mode. When the oscillating cantilever encounters a feature on the sample surface, this leads to a change in the oscillation amplitude, which is used as a feedback signal to adjust the tip height. Although the peak forces exerted on the sample can be larger compared to contact mode, the overall amount of contact and thus damage to the sample is largely reduced.

Non-contact mode

In non-contact mode the cantilever is oscillated at an even larger distance from the sample, so that the tip does not come in contact with the surface. For this mode of imaging stiffer cantilevers are used which are oscillated at resonance, or near resonance frequency and a much smaller amplitude. The interaction forces in non-contact mode are usually Van der Waals forces or other longer range interactions that cause a shift in the cantilever frequency, which is used as a feedback signal to adjust the scanning height, that is used to produce an image. This mode is generally used for imaging of very soft, biological samples or thin and liquid films on harder samples.

Different applications and imaging modes require specific types of AFM cantilevers. One primary parameter is the stiffness of the cantilever, since the deflection and exerted force of the cantilever on the sample will depend on it. AFM cantilevers nowadays are available in a large range of stiffnesses, e.g. soft cantilevers of 0.001 N/m – 0.01 N/m typically for contact mode imaging, mid-range stiffness 0.01 N/m – 1 N/m and stiff to very stiff cantilevers of 1 N/m – 400 N/m for oscillating imaging modes of indentation of solid materials. The tips of AFM cantilevers are also available in different shapes and sizes depending on the application (see figure 3.10). They can be fabricated from the same material of the cantilever or from a much harder material, e.g. diamond for a better wear resistance. They can be also flattened and shorted, e.g. via FIB milling to reduce indentation in the sample material, or completely removed and exchanged for a sphere with a much larger radius, e.g. for mechanical
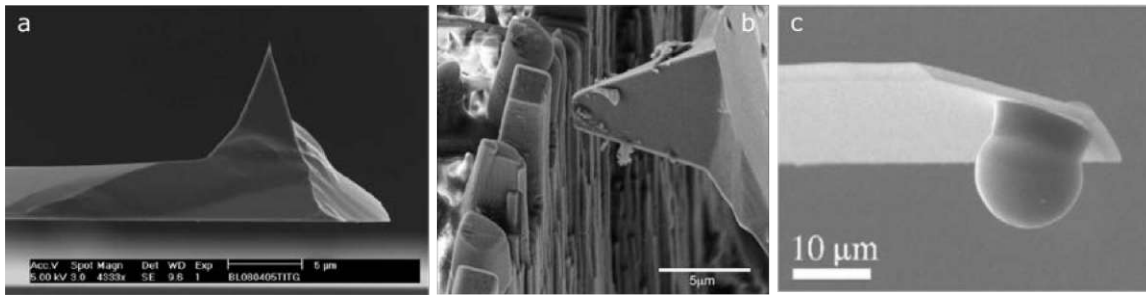
Figure 3.10: Types of AFM tips. (a) Most common type of an AFM tip with a sharp tip of radius of several nm (adapted from [106]) (b) Within SEM in situ AFM cantilever with a flattened tip via FIB milling prepared for bending of microbeams (adapted from [82]) (c) Modified AFM tip with a glued glass microsphere instead of a sharp tip for mechanical testing of soft biological materials (adapted from [89]).

testing of hydrated biological material, such as tissue sections or cells. The latter technique was also employed in a study of the present thesis.

The AFM technique has been extensively used for investigation of bone tissue and has enabled the experimental study of bone structures of several hierarchical levels (see figure 3.11), from the microscale down to the nanoscale, an overview and summary is provided in the comprehensive review of [181]. Investigations include both imaging of structures, but also mechanical testing via cantilever based nanoindentation (see figure 3.11d). Applications range from imaging constituent structures of bone tissue at the nanoscale, e.g. bone mineral (hydroxyapatite) platelets of mineralized collagen fibrils (see figure 3.11a) and the underlying collagen structure of demineralized collagen fibrils, where the typical collagen d-banding pattern is resolved via AFM [96], imaging at the lower microscale of individual to several osteonal lamellae (see figure 3.11c), and imaging of a microcrack propagation at the larger microscale of whole osteons, while at the same time resolving the crack at the level of lamellae and in particular, the cement line (see figure 3.11e).
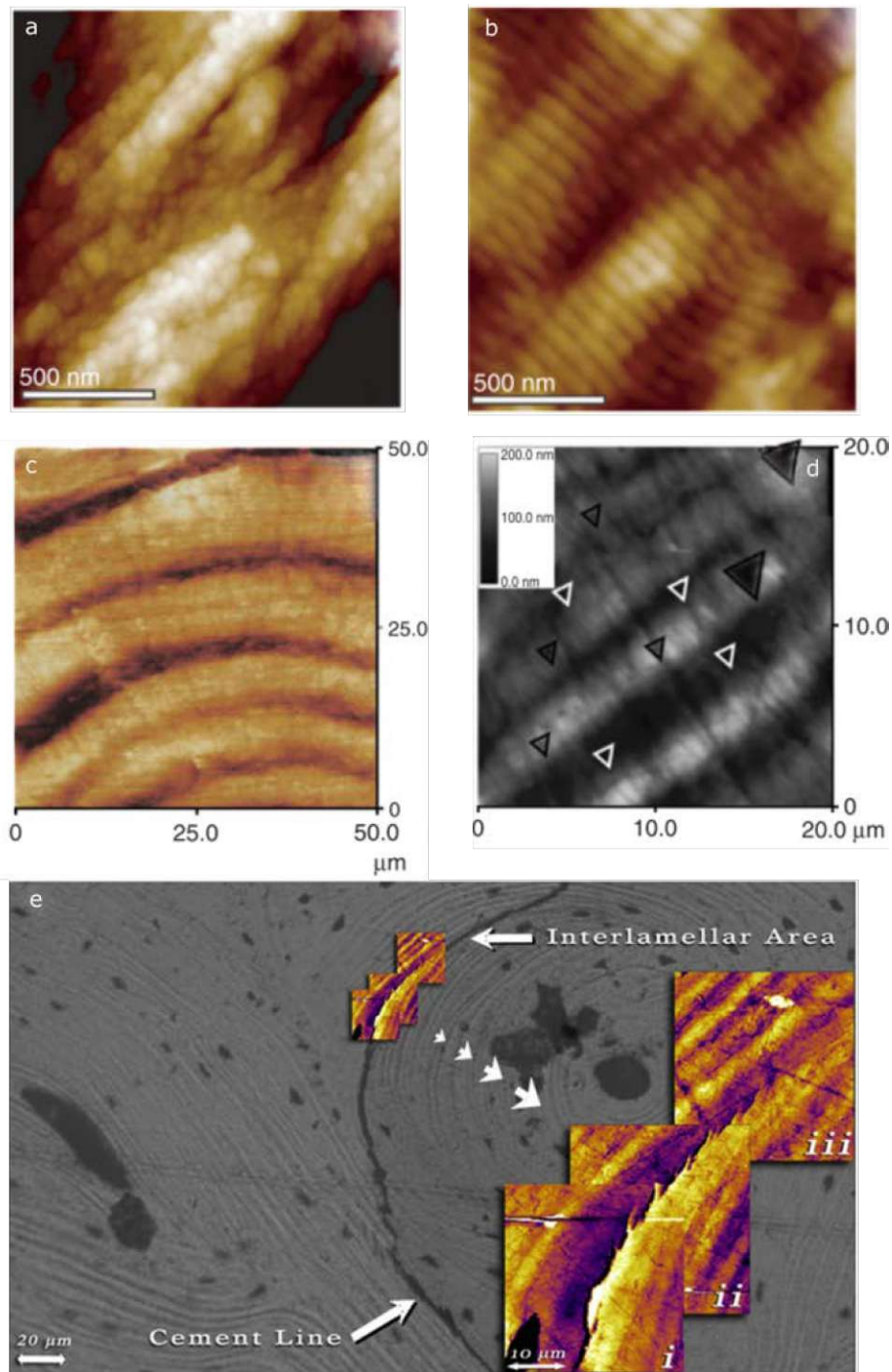
Figure 3.11: Applications of AFM to bone tissue. AFM imaging of freshly fractured bone surface revealing hydroxyapatite crystal platelets before (a) and after (b) demineralization, the latter displaying the typical d-banding of collagen at the nanoscale (adapted from [96]), (c) AFM imaging of an osteon at the microscale displaying concentrically arranged lamellar structures (adapted from [206]), (d) AFM-based nanoindentation applied for mechanical characterization of osteonal lamellae and subsequently imaged via AFM (adapted from [38]) and (e) Tracking of the evolution of a microcrack in osteonal bone, propagating along an osteonal cement line during loading (adapted from [92]).

3.3.2   Cantilever based bending

Since the operating principle of AFM is mechanical, i.e. it involves applying an imaging force to a sample, it can also be used for mechanical testing at lower length scales as well. This operation mode is generally often called force spectroscopy, where instead of rastering over a surface, the cantilever is placed at specified x and y position(s) and then driven towards, into or onto a sample with a specified setpoint force and then retracted away from the sample, via the extension and contraction of the z-piezo. In this operation mode, the cantilever approaches the sample, then interacts with the sample causing the cantilever to deflect, after which it gets retracted away from the sample. During one such cycle the deflection of the cantilever (providing measure on the acting force) is recorded as a function of the cantilever-sample distance recorded by the piezos or LVDTs to provide a force vs. displacement curve (see figure 3.12).

In AFM, the deflection of the AFM cantilever is used as a force sensor. To accurately measure force data, each cantilever should be calibrated prior to measurement, since the manufacturers generally only provide nominal stiffness values. The most common method used for calibration of AFM cantilevers is the method according to Sader, due to its quick, easy and straightforward application and was also applied prior to AFM measurements in the present thesis [159]. It utilizes measurement of the resonant frequency of the AFM cantilever either from thermal noise or driven oscillation in air, depending on the AFM instrument. Generally, from material data, dimensions and measured resonant frequency the actual stiffness k of the cantilever is obtained by [159]:

$$k = M_e \rho_c b h L \omega_{vac}^2 \tag{3.27}$$

, where ω_{vac} is the radial resonant frequency of the cantilever in vacuum, b, h and L are the width, thickness and length of the cantilever, respectively, ρ_c is the density of the cantilever and M_e is the normalized effective mass which has the value M_e

$= 0.2427$ for $L/b > 5$. In practice, however, the resonant frequency is measured in a fluid medium, typically air instead of vacuum, the actual density is unknown and the relatively small thickness of the cantilever is difficult to measure, whereas the plan view dimensions b and L can be easily obtained from e.g. measurement with an optical microscope. Equation (3.27) has been further developed to include only known parameters,

$$k = 0.1906\rho_f b^2 L Q_f \Gamma_i(\omega_f)\omega_f^2 \tag{3.28}$$

where ρ_f is the density of the fluid, b and L the plan view dimensions of the cantilever, Q_f the quality factor in fluid, $\Gamma_i(\omega_f)$ the imaginary component of a hydrodynamic function Γ and ω_f the resonant frequency in the fluid. For more details regarding the individual parameters the reader is referred to [159].

Additionally, to the spring constant k of the cantilever, the sensitivity of the detection of the deflection of the cantilever needs to be determined for a calibrated and accurate force measurement. This is dependent on the mounting of the cantilever, positioning of the laser spot on the back of the cantilever (see figure 3.9a) and the measuring medium (air or aqueous environment) and needs to be performed for every change of these conditions. The measurement of the sensitivity relates the measured voltage on the photo diode from the reflected laser signal to the deflection of the cantilever (as imposed by the z piezo, typically in nm) and is more accurately termed optical lever sensitivity. For this, a force curve is measured on a flat and hard surface, e.g. glass or mica (see figure 3.12). The curve is then displayed in Volts vs. z-displacement of the piezo in nm. The initial portion of the unloading curve is then fitted to obtain the slope in [V/nm]. The inverse of the slope is then the optical lever sensitivity of the cantilever S, given in nm/V. Thus, during measurement, the measured voltage U can be multiplied by S to relate the voltage signal to the cantilever deflection in nm. Finally, using the calibrated spring constant of the cantilever k and applying Hooke's law (eq. 3.6), the resulting force of the cantilever acting on the surface is obtained as

$$F = k \cdot S \cdot U \tag{3.29}$$

Due to imperfections on the measured surface, instead of performing one force curve for the determination of the optical lever sensitivity, 16 curves are performed and averaged in every measurement medium (air and HBSS) for a better statistical certainty.

A further consideration that needs to be made when performing mechanical testing with an AFM is the choice of an appropriate cantilever stiffness. The amount of deflection of the cantilever is dependent on its stiffness and sufficient deflection is necessary for a reliable force measurement. If the AFM cantilever is too soft compared to the tested microbeam, then most of the detected deflection will be from the AFM cantilever and insufficient bending will be imposed on the microbeam. In the opposite case, if the AFM cantilever is much stiffer than the tested microbeam, then the AFM cantilever will deflect too little to provide a reliable force signal. Matching of the stiffnesses of cantilever and tested sample can be understood if both structures are considered as two mechanical springs connected in series [89]. Since the force acting on this system is the same it can be written

$$k_b = k_c D_c / \nu \tag{3.30}$$

, where k_b and k_c are the spring constants of the measured microbeam and the AFM cantilever, respectively and D_c and ν are the corresponding deflections of the cantilever and microbeam, respectively. The maximum measurement sensitivity is achieved when $D_c = \nu$, i.e. the cantilever spring constant matches exactly with the microbeam stiffness. With further considerations regarding the limits of stiffness matching it was found that sufficient sensitivity of the force measurement is achieved with a cantilever spring constant up to about 2 times higher or 4 times lower than the sample stiffness. In the study regarding human bone microbeams bent with and

AFM cantilever of this thesis (chapter 5), the average dimensions of the microbeams were L x b x h = 25.1 μm x 3.3 μm x 1.1 μm, which with an assumed elastic modulus of E = 30 GPa yields a bending stiffness (for a double clamped configuration) of 133.3 N/m. For this reason an AFM cantilever of (nominal) stiffness of 200 N/m (RTESP-525, Bruker, Billerica, Massachusetts, USA) was chosen as sufficiently matched for the microbending experiments.

After a (micro)bending measurement is performed, the obtained force vs. displacement (i.e. in case of bending, deflection) curve, which generally has a form as schematically presented in figure 3.12 can be analyzed. From the slope of the curve mechanical information, e.g. stiffness or modulus can be extracted. Here, the raw measured data still entails the deflection of the AFM cantilever, resulting in a reduced apparent slope of the curve. By using the optical lever sensitivity, the displacement data has to be corrected for the AFM cantilever deflection, to obtain a force vs. sample deflection curve, which can then be further analyzed.

Mechanical testing with an AFM offers several possibilities. If a sharp tip (see figure 3.10a) is used then the sample will be indented and a nanoindentation experiment is performed, from which an indentation modulus can be obtained. If a blunt tip is used, e.g. a flattened AFM probe tip (see figure 3.10b) or a sphere (see figure 3.10c), then penetration of the sample will be minimized and depending on the tested structure, e.g. a compression or bending modulus can be obtained. If bending measurements are repeated on several x,y positions on the sample surface, e.g. a stiffness map of the sample surface can be created.

Mechanical testing with an AFM has mainly been applied as nanoindentation measurements, due to its straightforward application, also in the context of bone mechanics at the micro- and nanoscale [181]. However, in the recent decade, experimental efforts have also been made for direct mechanical testing of bone microstructures, e.g. single bone lamellae, in which small lamellae microbeams have been prepared via FIB and subsequently tested under bending [82, 84] or compression [83] with a blunted AFM tip (see figure 3.10b) to minimize indentation. The calculation of mechani-
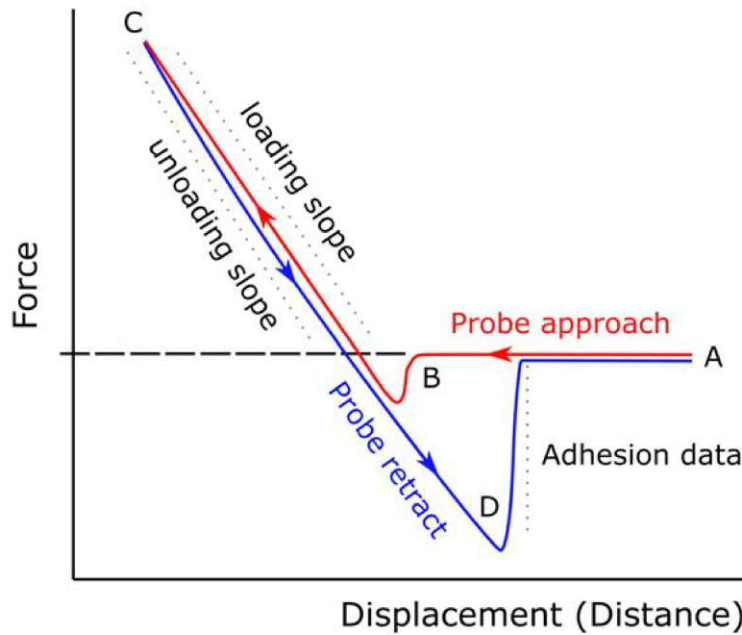
Figure 3.12: Schematic representation of an AFM force vs. displacement curve. The red line represents the approach curve and the blue line represents the retraction curve. From A to B the AFM probe approaches the sample, at point B a characteristic snap on of the probe to the sample surface is typically measured. After the snap on at point B up to point C the acting force of the AFM cantilever on the sample is increased as the distance is decreased, after which the probe is retracted from the sample, C to D. If there are adhesion forces between the sample and the tip this will be recorded in the retraction curve, point D.

cal parameters from bending measurements is dependent on the position x at which the bending force is applied (Eqs. (3.25) and (3.26)). For a bending measurement performed with an AFM at the lower microscale, a certain uncertainty of the exact position of the AFM tip on the sample can be assumed, if the tip-sample contact position cannot be verified in situ, via additional techniques, e.g. light or electron microscopy. However, the position dependency of the measured stiffness combined with the convenience of performing subsequent bending measurement with the AFM at different positions on the beam structure can be utilized to bypass this uncertainty. One approach is performing at least two bending measurements at two beam

positions, described in Appendix A. The other method utilizing bending at several positions was discussed in section 3.2.2.

3.4   Raman Spectroscopy

Raman spectroscopy (named after the Indian physicist C. V. Raman) is a spectroscopy technique, probing the vibrational modes of molecules. It is often used to provide compositional information about a sample of interest. Its measurement principle is based on inelastic scattering of light when it interacts with matter (Raman scattering), leading to a change in wavelength or frequency depending on the vibrational levels available in probed molecules. This is in contrast to elastic scattering, where energy of the incident light (photons) is conserved. In practice a monochromatic laser beam is used as incident light, typically in the visible or near infrared region, but also other regions are possible, e.g. ultraviolet or X-ray, depending on the application. Most of the incident light is scattered elastically (Rayleigh scattering), which is the strongest signal and gets filtered out from the measurement (see figure 3.13a). A much smaller portion is scattered inelastically, resulting in a shift towards lower energies (Stokes), but also shifts to higher energies (Anti-Stokes) (see figure 3.13a,b). The shifts are specific and correspond to the energies of the vibrational modes of the characteristic molecular groups contained in the sample, thus providing information of the presence of chemical species within the interaction volume. In a spectrogram of a biological sample, the shifts appear as bands (rather than sharp peaks) vs. the wavenumber (a unit inverse to the wavelength, directly related to photon energy) and these bands represent a chemical fingerprint of the sample (see figure 3.13c).

In biological materials Raman spectroscopy is mainly used for chemical analysis, since it probes the vibrational modes of characteristic molecular groups, such as PO_4, CO_3, CH, amides, etc. and can be also used to study changes of these groups in different conditions. The energy of vibrational modes of molecules lies in the region of infrared
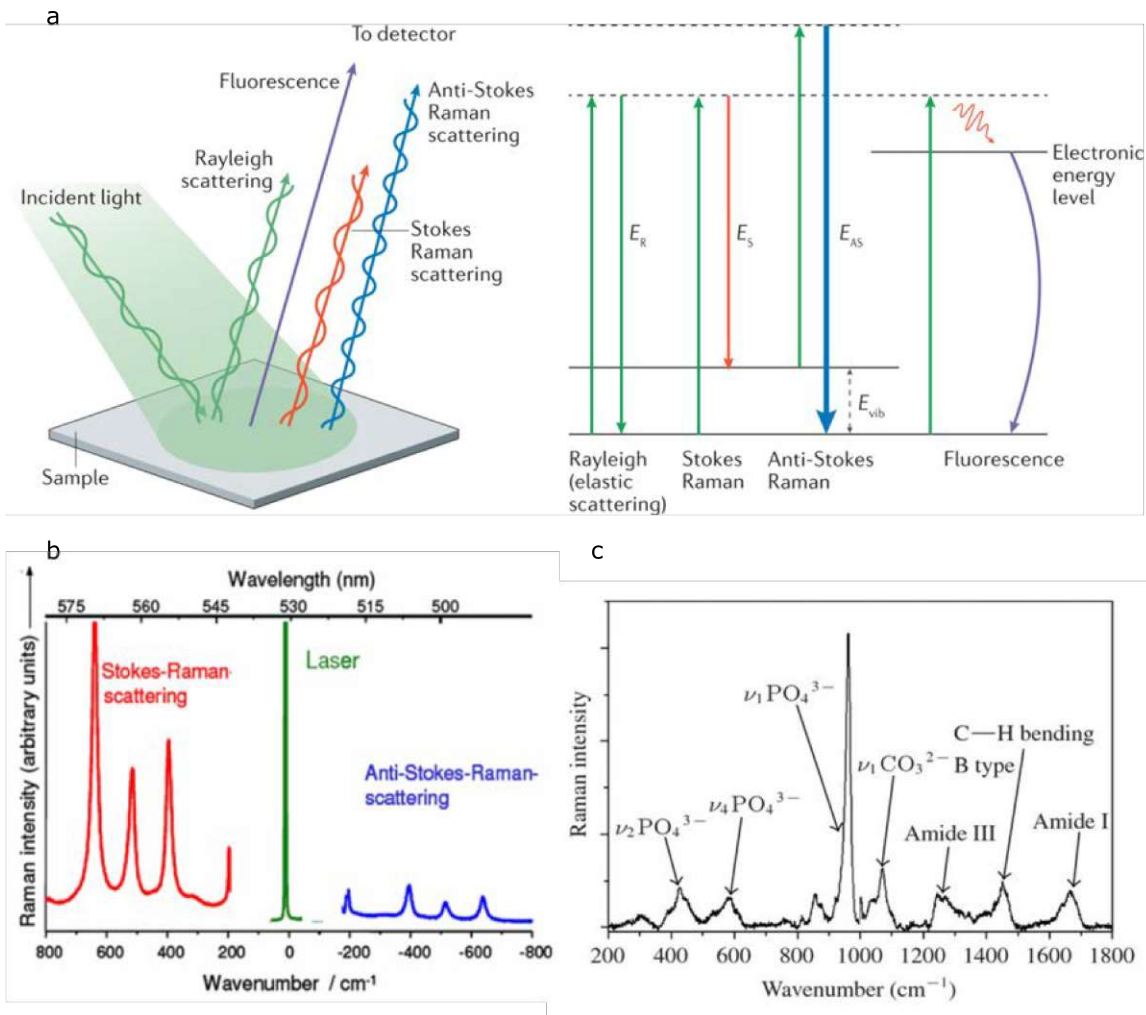
Figure 3.13: Raman scattering and spectra. (a) A monochromatic incident light (here green) gets scattered by sample molecules, either elastically (Rayleigh scattering) and keeps the initial energy (color) or inelastically, whereas the energy of the scattered photon shifts to lower energies (Stokes shift, here red) or higher energies (Anti-Stokes, here blue) (adapted from [122]), (b) Resulting spectra of the detected scattered light, displaying the large laser Rayleigh peak and the Anti-Stokes and Stokes shifts peak, left (longer wavelengths) and right (shorter wavelengths) from the laser peak (adapted from [179], (c) A representative Raman spectrum of bone tissue (wavenumber axis scaled inversely than in (b)) displaying specific and typical peaks (Raman shifts) resolving chemical information of constituents by vibrational modes of molecular groups present in the sample (adapted from [19]).

radiation, so the technique is complementary to infrared spectroscopy (IR). It is however, distinct in the basic physical principle, i.e. scattered light is detected in Raman spectroscopy, whereas absorbed wavelengths of the infrared electromagnetic region are detected in infrared spectroscopy. The fingerprint region of organic molecules lies in the wavenumber region of $500 - 2000$ cm^{-1}, so the technique is largely used to study samples of organic origin (see figure 3.13c).

Raman spectroscopy can be performed with a conventional light microscopy setup equipped with a laser light source and a spectrograph, called Raman microspectroscopy. Depending on the wavelength of the irradiation light and the numerical aperture of the objective a spatial resolution down to approx. 1 μm in lateral and 10 μm in depth direction of the interaction volume can be achieved. It is a noninvasive and light-based technique, so samples can readily be measured and do not need to be fixed or sectioned. Furthermore, water does not pose a major interference during measurement (in contrast to IR spectroscopy), thus measurements can easily be performed with samples submerged in water, with usage of the according optical equipment, which makes the technique attractive for applications to biological materials in aqueous environments. Additionally, the aqueous environment also helps to avoid excessive heating of the sample during imaging.

An additional feature of Raman scattering is the polarization dependency of some vibrational modes of molecules. This dependency can in turn provide information on the predominant orientation of molecular groups as part of larger molecular structures in a sample, e.g. polymers. The effect can be exploited by using a polarizer on the incident light and a second polarizer to analyze the scattered light. When the linearly polarized incident light interacts with a symmetric (isotropic) mode, the scattered light retains the same polarization. On the other hand, if it interacts with an asymmetric (anisotropic, orientation dependent) mode, the polarization of the scattered light will be altered and can be analyzed by the analyzer. From the polarization dependency orientation information of the molecules in the sample can be reconstructed.

Vibrational spectroscopic techniques like Fourier-transform infrared spectroscopy (FTIR) and Raman spectroscopy have extensively been applied to study both the mineral phase and organic phase of bone tissue. Since the orientation of collagen fibrils within adjacent osteonal lamellae have puzzled bone researchers for decades and still remains an ongoing discussion, it has been the main topic under investigation in hard tissues both with FTIR [14, 140] and Raman spectroscopy [49, 164]. Furthermore, from mechanical point of view, the orientation of collagen fibrils should correlate with the mechanical behavior of structures at larger hierarchical levels and investigations of this correlation have also been performed [15, 192]. More recently the capabilities of polarized Raman spectroscopy have been further developed to achieve 3D mapping of collagen fibrils within lamellar bone (see figure 3.14) [164], a protocol that was also applied to and further developed on the bone microbeams of the present thesis as well.
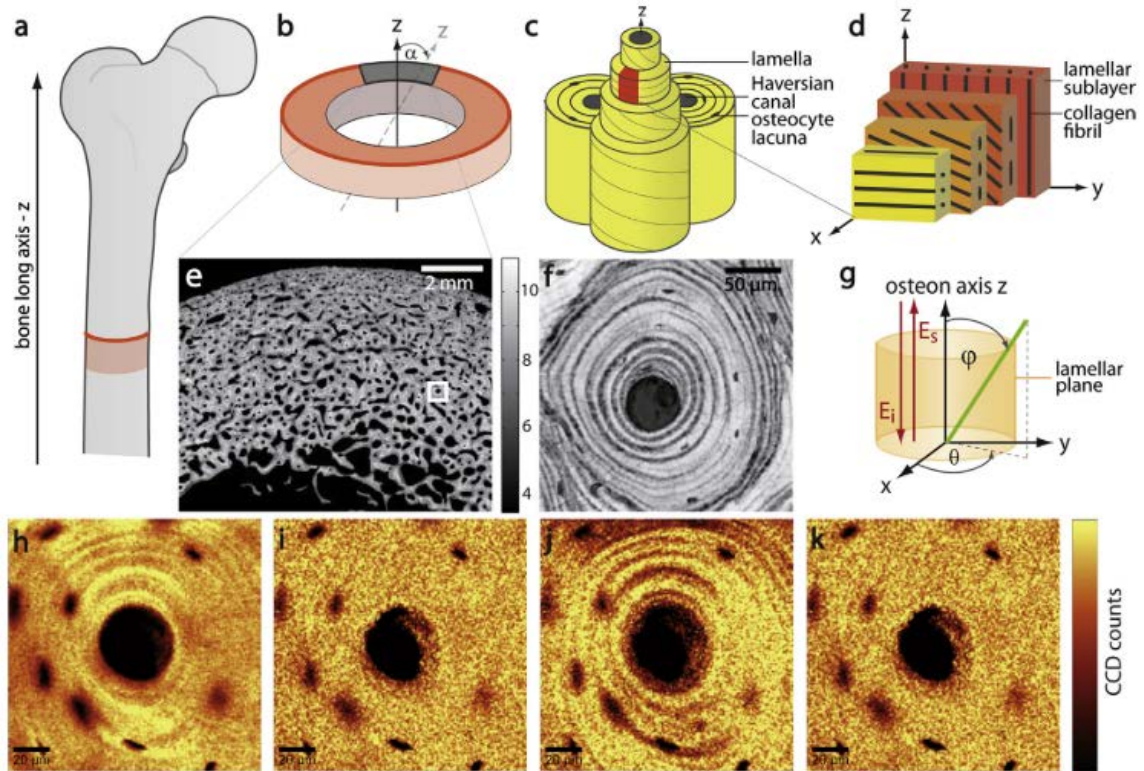
Figure 3.14: Sample preparation and application of Raman spectroscopy to cortical bone. (a,b) Schematic representation of a portion from the midshaft of a femur, isolated via transverse sectioning. (c) Lamellar structure of an osteon and (d) conceptual representation of collagen fibrils orientation within lamellae. (e,f) SEM images from a region of interest with a selected osteon for measurement. (h-k) Polarized Raman scans of the osteonal structure displaying: (h) vibrational mode ν_1 of PO_4, (i) vibrational mode ν_2 of PO_4, (j) vibrational mode amide I and (k) vibrational mode amide III. (h) and (j) display orientation contrast based on the polarization dependency of the corresponding vibrational modes, thus revealing the lamellar structure of the imaged osteon, whereas (j) and (k) do not display these characteristics of the corresponding modes. (adapted from [164]).

Chapter 4

Influence of experimental constraints on micromechanical assessment of micromachined hard-tissue samples

4.1 Related publication and declaration of contributions

Results of the presented chapter have been published in the "Journal of the Mechanical Behavior of Biomedical Materials" in 2020, entitled "Influence of experimental constraints on micromechanical assessment of micromachined hard-tissue samples" and co-authored by Rainer Hahn, Paul H. Mayrhofer, Andreas Steiger-Thirsfeld, Johannes Bernardi and Philipp J. Thurner.

Author contributions: The first author and author of the current thesis, Vedran Nedelkovski, wrote and edited the manuscript, performed the sample preparation via FIB milling, SEM imaging and FE simulations, data processing and data in-

terpretation. Rainer Hahn performed the mechanical tests with the picoindenter, SEM imaging and edited the manuscript. Paul H. Mayrhofer provided resources, supervision and edited the manuscript. Andreas Steiger-Thirsfeld provided training and supervision of FIB milling. Johannes Bernardi provided resources and edited the manuscript. Philipp J. Thurner provided resources, supervision of the work of Vedran Nedelkovski, suported data analysis and data interpretation, reviewed and edited the manuscript.

4.2 Introduction

Continuing technological advancement has enabled researchers to push the boundaries of manufacturing isolated samples for experimental mechanics down to the micro- and nanoscale. Focused ion beam (FIB) milling has emerged as an attractive and versatile technique for sample preparation at the micrometer length-scale, whereas mechanical testing instrumentation like nanoindentation, MEMS devices and atomic force microscopy (AFM), both stand-alone and in-situ during scanning electron microscopy (SEM) can be used for mechanical testing of FIB-made samples. A comprehensive review by Jiang et al. summarizes the application of such techniques, and, in particular the development of in-situ tensile testing of nanostructures, compression of micro-/nanopillars and AFM-based nanoindentation and micro-/nanoscale bending testing at these length scales [80]. The potential of these techniques, initially developed for the mechanical characterization of nanomaterials widely used in applications of nanotechnology, has inspired experimental investigation in fields dealing with biological nano- and microstructured materials, such as biomechanics.

In this context, bone can be considered as a nanocomposite biological material exhibiting interesting mechanical properties, i.e. optimizing contrasting qualities like stiffness and toughness, owing to a complex hierarchical structure, ranging from the nano- to the macroscale. In order to understand and predict bone's anisotropic me-

chanical behavior, testing of all structures at all length scales and understanding the way how these interact with each other is of vital importance.

Although many studies have been conducted at the macroscopic level of bone [26, 34, 170, 203], there are comparatively few experiments at the microscale on isolated samples enclosing individual microstructural elements [24, 37, 82–84, 109, 168, 169], except for nanoindentation experiments performed on bulk material [102, 181]. Partly this is because the preparation and mechanical testing of microscale bone samples still remains a challenge.

As mentioned, nanoindentation has extensively been used for mechanical characterization of bone at the microscale due to its straightforward application [102, 155, 181, 216]. With penetration depths of hundreds of nanometers to micrometers, this technique probes the bone tissue at the level of its microstructure – i.e. the bone lamella or respectively several lamellae. Bone lamellae are packed layers of mineralized collagen fibrils with thicknesses of 2 – 10 µm. In human cortical bone they are often concentrically arranged around a central Haversian canal and thereby constitute cylindrical structures that make up the next larger hierarchical level: osteons [154, 200]. The mechanical properties of individual bone lamellae are still poorly understood due to lack of experimental data. While there are standard techniques to extract mechanical properties from nanoindentation [137], there are also limitations, as high stress and strain gradients are imposed on the material and as the investigated volume cannot be assessed for flaws, leading to several issues in interpretation of data [3, 109, 161]. Thus, research in this area has in part focused on approaches for a more direct mechanical characterization, inducing (more) homogeneous stress state and localizing measurements to isolated micrometer-sized specimens.

Mechanical quantities such as elastic modulus and strength are material properties experimentally easily derived from a uniform stress state, usually realized through a uniaxial compression or tension test. Such tests can be done using FIB-machined micropillars, loaded with a conventional nanoindenter, equipped with a flat punch as a tip. Bending, in contrast, is a gradient dominated deformation inducing a non-

uniform stress (and strain) state in a structural element, i.e. a beam, which is dependent on both beam geometry in a nonlinear fashion, as well as material properties. In order to extract material properties, such as an "elastic" modulus, from a bending experiment, beam theories such as Euler-Bernoulli or Timoshenko have to be used, which have inherent assumptions regarding geometry (length to width to thickness ratios, cross-sectional second moment of area), constraints and material anisotropy (linear, elastic and isotropic material) of the sample [12, 68]. Nevertheless, the bending approach is also of interest as it can be done using an atomic force microscope, i.e. testing in fully hydrated conditions, which is often challenging to do with conventional nanoindentation devices, mainly due to inability of optical inspection and limiting positioning accuracy after submerging in liquid, as well as sample damaging risk during scanning probe imaging.

In the last decade, a number of biomechanics studies have been published that have used FIB milling for preparing specimens for mechanical testing at the microscale. One of the first such studies employed FIB milling on sections of human primary molars to produce microscopic cantilevered beams with triangular cross-section, which were subsequently bent with a conventional nanoindenter and Berkovich tip [24]. Further studies were conducted on microbeams of rectangular cross-section produced by FIB milling at the length scale of a single cortical bone lamella. Jimenez-Palomar et al. used in situ AFM bending of microbeams (10 μm x 2 μm x 2 μm in dimension) within the chamber of a scanning electron microscope (SEM) to investigate the effect of dehydration of bone tissue under high vacuum conditions [82] and the dependence of mechanical properties on collagen fibril orientation within the lamellae [84]. The microbeams were produced at the edge of a macroscopic sample and bent using a FIB-flattened AFM tip to minimize indentation of the tip into the microbeam during bending. From these studies values for elastic moduli in the range 1.2 – 3.7 GPa, flexural strength 632 – 1083 MPa and work-to-fracture 24.8 – 40.6 Jm^{-2} were reported for cortical bone from rat femora. In a further study, a different positioning of the microbeams relative to the AFM tip was used, so as to load the microbeams

in compression, by acting of the flattened AFM tip parallel to the microbeams' long axes [83]. Here, microbeams from femurs of ovariectomized rats, an animal model for osteoporosis, were reported to have lower elastic modulus (1.6 ± 1.3) GPa but higher strain at failure (10 ± 4) % compared to samples from control mice (2.9 ± 1.5) GPa and (6.3 ± 1.9) %. No difference in strength was reported between the two groups.

Schwiedrzik et al. used micropillar compression of FIB-milled samples from ovine osteonal lamellae in axial and transverse directions in both dry [168] and rehydrated [169] conditions. The micropillars were compressed both monotonically and cyclically beyond the elastic limit. Apparent moduli from cyclic micropillar compression in dry conditions were reported to be (31.16 ± 6.46) GPa in the axial direction and (16.5 ± 1.5) GPa in the transverse direction. Additionally, values for yield stress and ultimate stress both under vacuum and rehydrated conditions were obtained and the anisotropy ratio of the axial to the transverse yield stress was reported to reduce from 1.6 under vacuum conditions to 1.3 under rehydrated conditions. High-resolution SEM imaging was performed on the micropillars after testing and revealed that shear via a single slip plane was the most predominant mode of failure, with a minority of the axial micropillars exhibiting a brittle failure mode.

All of the microstructures produced by FIB milling in the above-mentioned studies remained attached to, i.e. were constrained by the bulk material they were produced from. The bulk material itself acts as an elastic half-space and thus contributing to the overall mechanical response of the structures. In the case of the micropillars, the obtained geometry exhibited also a tapering effect, stemming from the circular FIB milling procedure, which deviates from an assumed cylindrical shape, resulting in an inhomogeneous stress distribution over the pillar height. To overcome this issue, Luczynski et al. developed a protocol to mill out, extract and transfer untapered micropillars with square cross sections from the lamellae of bovine tibia onto a silicon wafer, which acts as a much more rigid substrate [109]. The microscopically welded micropillars were tested under compression within a single loading and unloading

cycle with a flat punch nanoindenter tip. Elastic moduli were derived from the unloading portion of the stress-strain curve and were in the range of 24.1 – 32.2 GPa.

Overall, experimental bone micromechanics is a pioneering field with a still limited number of publications thus far. This may be due to lack of availability of equipment and time-extensive sample preparation procedures. Nevertheless, bone micromechanics offers a promise: The complex hierarchical structure of bone represents a challenge for mechanical characterization; each hierarchical level (structural element and the interaction between two or more elements) influences the overall mechanical properties. On the macroscale, this may also include significantly large pores meaning the question of the bone material properties, and, if they are influenced with age and disease, becomes difficult to answer. This is much less the case at the microscale. Principally, FIB allows to extract and test samples on the level or containing a single bone lamella. While such samples leave out larger hierarchical levels they are in fact suited to answer the questions whether there are fundamental changes of bone micromechanics and material properties with age and disease. However, when doing micromechanics experiments it is important to assess the limitations of the different testing approaches to make sure data is correctly interpreted or at least the limitations for the performed measurements are known.

Therefore, the aim of this study is to assess the currently used methods for micromechanical testing of a complex material like bone by comparison to the mechanical response of a well-known homogeneous and ideally elastic-brittle material, in this case silicon. Additionally, finite element (FE) models were created for the most commonly used structures in micromechanical testing, to address effects arising purely from geometry and constraining by bulk material, as stresses subside in the bulk, when structures are not rigidly fixed, but constrained by the bulk [69]. Furthermore, the precision of the FIB-milling and SEM techniques become comparable to the sample dimensions at the microscale. The resolution limit of SEM and FIB is material and vacuum dependent, which in our case for silicon the production and imaging precision is $\pm$ 100 nm, thus significantly comparable to the smallest dimension in

our sample, i.e. the height (thickness) of the beam of 1 µm. Therefore, we estimate the uncertainties and calculate the error propagation of obtained results arising from precision of achievable sample dimensions and moreover, possible deviations in the second moment of area (where, apart from deviations in width and height also deviations in the cross-sectional shape from rectangular to arbitrary quadrangle also play a role) in bending experiments [196]. Here, we attempt to address uncertainty effects arising from geometrical errors during sample preparation and boundary conditions during testing to quantify error boundaries when analytical models comprising theoretical assumptions are used to evaluate experiments in currently used methods for direct mechanical characterization of bone at the microscale.

4.3 Materials and methods

4.3.1 FIB sample preparation

Microbeams were machined from a mm-sized piece of a commercially available (100) silicon wafer. The orientation of the top surface (normal vector) of a (100) wafer is the [100] crystal axis of silicon and the primary flat of the wafer is oriented along the [110] crystal direction [72]. The wafer piece used was mounted, such that the long axis of the machined microbeams is oriented parallel to the primary flat, i.e. the [110] direction.

The wafer piece was fixed onto a scanning electron microscopy (SEM) stub with silver paint (Plano GmbH, Wetzlar, Germany) and mounted on a custom-made holder with mounting pins oriented in an orthogonal fashion, allowing for micromilling in two perpendicular directions. Focused ion beam (FIB) milling was performed using a dual beam FIB system (Quanta 200 3D DualBeam, FEI, Hillsboro, Oregon, USA), incorporating both SEM and FIB within the same vacuum chamber and using ion beam currents ranging from 20 nA (coarse) to 0.5 nA (fine). Milling was performed near the wafer edge (parallel to the [110] direction), first, from the top to isolate a single

trench of defined length and width, and second, at an angle of 90° (from the side), as shown in figure 4.1. This determined the thickness of the double-clamped microbeam structure, i.e. attached on both ends to the bulk material, with a rectangular cross-section (see figures 4.1 and 4.1a). The production of single-clamped microbeams followed the same procedure with an additional final milling step in the middle of the structure, thus producing two single-clamped microbeams, i.e. attached only on one end to the bulk material (see figure 4.2b). The nominal dimensions (length x width x height) were (43 x 5 x 1) μm and (20 x 5 x 1.5) μm for the double-clamped and two single-clamped microbeams, respectively. During FIB milling effects like FIB damage, gallium ion implantation and redeposition of target ions occur due to the ion-solid interactions and are specific for every target material [52, 197]. Although such artifacts cannot be completely eliminated, sveral "good practice" steps can be applied to minimize their influence, like milling of trenches of small aspect ratios (i.e. primarily small depths, [52]), milling of structures with sufficient distance from other edges [95, 190] and removing small thicknesses per scan to avoid redeposition [193]. Additionally, the tapering angle of the FIB can be corrected by over-tilting the sample by ± 2° for silicon [52]. Galium ion implantation can be minimized by milling at large grazing angles (i.e. only side edges) and was calculated from Monte Carlo simulations to be confined within 30 nm from the surface [52]. All of these FIB milling artifacts were found to be negligible for the mechanical response of cantilevered structured from crystalline silicon [76].

4.3.2 Mechanical characterization

In situ bending during SEM

Mechanical testing was performed in situ during SEM using a Picoindenter (PI-85 SEM, Hysitron, Bruker, MA USA) mounted within the vacuum chamber of a field emission gun-SEM (Quanta 250 FEG, FEI, Hillsboro, Oregon, USA). A conical diamond tip of 60° opening angle and a tip radius of 1 μm was used for applying a
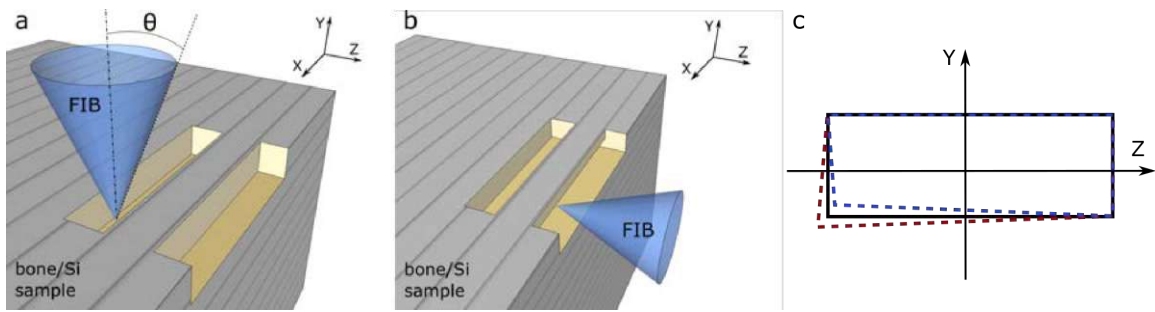
Figure 4.1: Schematic representation of FIB sample preparation. The beam structure is milled perpendicularly to the sample surface (a) first from the top and (b) second at 90° to the top surface, i.e. from the side. The angle Θ represents the tapering angle of approx. 2° of the FIB. (c) Potential deviation from a rectangular beam cross-section due to the tapering geometry of the FIB (tapering angle and deviation not to scale).
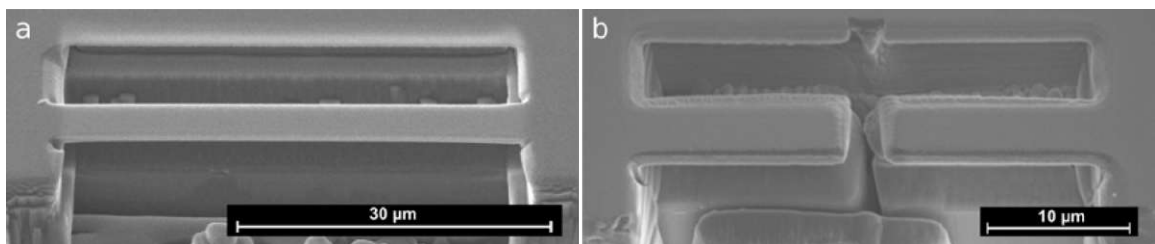
Figure 4.2: FIB-machined microstructures on a Si (100) wafer in a (a) double-clamped and (b) two single-clamped beam geometries.

bending force to the microbeam structures while minimizing indentation. To estimate the effect of indenter sink-in, bulk indentations were performed in the vicinity of the microbeams supports to obtain the apparent indent stiffness, which was found to be 2 orders of magnitude higher than the microbeams' structural stiffness. Displacement data of the bending measurements was corrected according to an analytical model of two springs in series, representing the stiffness of the indent and microbeam, respectively [98]. Differences of the corrected data was on the order of 1 % or less and combined with a visual inspection of the microbeam surface post-bending revealing no visible indent imprint, it was found that this effect is negligible and measured displacements were mainly due to the microbeams deflection. Positioning was monitored via SEM imaging and performed at a tilt angle of 10° of the SEM stage. Bending

measurements were performed in load control up to a maximum force of 100 μN. An example data set is shown in figure 4.3a. From the obtained force vs. displacement curves, a straight line was fitted to the top 25 % of the unloading portion of the curve to directly access the elasticity of the material and obtain the apparent stiffness S of the tested structure, as also indicated in 4.3a (red line) [109]. Bending experiments were performed at multiple positions along the beam's long axis in steps of approx. 1 μm to obtain multiple stiffness values vs. beam position [171]. Lateral positioning across the microbeam's width was monitored by normal distance measurements from both free edges (under consideration of the stage tilt angle of 10°) of the microbeam. Additionally, lateral, off-axis bending tests were performed at $\pm$ 1 μm from the longitudinal symmetry axis in the region $L/h > 10$. The lateral off-axis bending showed a lower apparent stiffness by 2.6 % due to an additional torsional deformation of the structure, which further supported the precision of the on-axis positioning. To remain within the scope of linear elastic bending of a slender beam, measurements were performed at positions $L/h > 10$ from the clamped ends of the microbeam structures, where L is the beam length and h is the height of the beam, as schematically depicted in 4.3b [72]. The obtained stiffness vs. beam position data, were fitted with equations (4.3) and (4.4) for the double-clamped and single-clamped beams, respectively, to determine a value for the effective elastic modulus of the structures (see section 4.3.2).

Determination of mechanical parameters

For the determination of the axial elastic modulus of Si in the [110] direction from the microbeam bending experiments, the analytical solutions for force and deflection of a double- and a single-clamped beam, according to the Euler-Bernoulli theory were used [12, 68]:

$$E_{dc} = \frac{1}{192} \frac{PL^3}{\nu I} \tag{4.1}$$
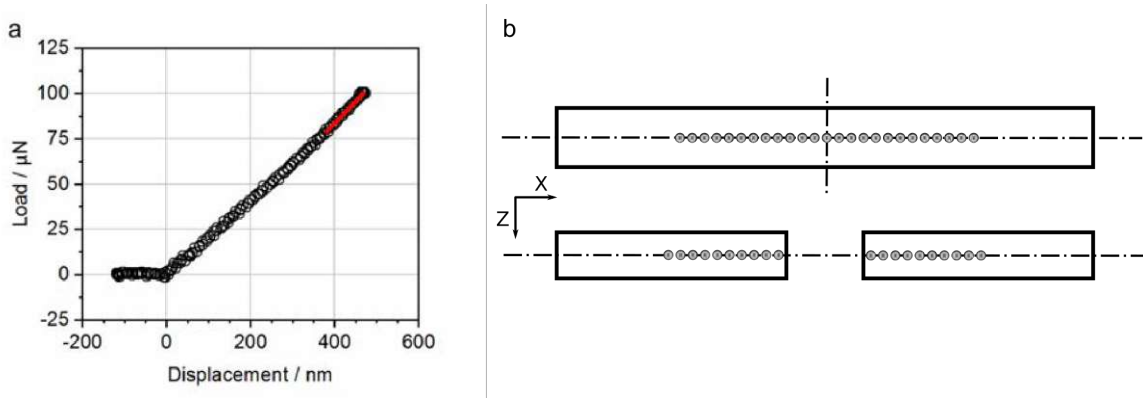
Figure 4.3: (a) Loading/unloading force vs. displacement curve obtained from a single bending experiment at a single beam position (e.g. middle of the double-clamped beam). A straight line (red) was fitted to the top 25 % of the unloading portion of the curve to obtain a stiffness value. (b) Schematic representation of the beam positions at which bending experiments were performed. Top view of the double-clamped microbeam (top) and the single-clamped microbeams (bottom). The coordinate origin was placed, such that $x = 0$ was located at the base (i.e. at the left support for the double-clamped and left single-clamped beam and at the right support for the right single-clamped microbeam and with the x-axis pointing to the free end of the single-clamped microbeam), as well as $z(0) = b/2$, i.e. the width center and $y(0) = h/2$, i.e. the height center of the microbeams.

and

$$E_{sc} = \frac{1}{3} \frac{PL^3}{\nu I} \tag{4.2}$$

, where E_{dc} and E_{sc} represent the elastic moduli calculated from a double- and single-clamped beam structure, respectively, P is the applied load, ν the deflection, L the beam length and I the second moment of area of the beam, given by $I = bh^3/12$ for a beam of rectangular cross-section, where b is the width and h is the height of the beam. In both equations, $S = P/\nu$ represents the stiffness and L the total length of the beam. During a bending experiment a load vs. displacement curve is obtained, fig. 4.3a. For small deflections ($\nu << L, b, h$ and slender beam geometries ($L/h > 10$ and $b/h < 5$ [72]) the bending remains in the linear elastic regime and a straight line

can be fitted to the bending curve to obtain a value for the stiffness of the structure.
Thus, from a single bending experiment at the middle of the double-clamped beam
(see figure 4.3a) and at the free end of a single-clamped beam (see figures 4.3b and
c), equations (4.1) and (4.2) were used to calculate the axial elastic modulus of the
beams.

To obtain more data for the determination of the elastic properties, multiple bending
measurements along the beam length can be used [68, 171], instead of a single bending
measurement. The dependence of the stiffness of the beam structure on the relative
beam position of the applied force, $S(x)$ is then given by:

$$S_{dc}(x) = 3E_{dc}I \frac{L^3}{x^3(L-x)^3} \tag{4.3}$$

and

$$S_{sc}(x) = \frac{3E_{sc}I}{x^3} \tag{4.4}$$

for the double-clamped (dc) and single-clamped (sc) beam, respectively. In these
equations the stiffness scales with the 3rd power of the relative beam position, thus
by fitting equations (4.3) and (4.4) to the multiple data points of the stiffness mea-
sured along the beam length, the elastic moduli E_{dc} and E_{sc} can be obtained as
fit parameters. In this study, Origin (Version 2017; OriginLab, Northampton, MA,
USA) was used for fitting and plotting of data. The non-linear fits were performed
using the Levenberg-Marquardt algorithm.

4.3.3   Effect of geometry

FE modeling

Linear elastic and static analysis of 3D finite element method (FE) models was per-
formed for simulation of both micropillar compression and microbeam bending. Pre-

and post-processing was done in HyperMesh and HyperView, respectively and the built-in solver Optistruct was used for calculation (HyperWorks Version 2019; Altair Engineering, Troy, MI, USA). For a systematic comparison, the structures were modelled both with (w/) and without (w/o) bulk material to investigate the effects of geometry and bulk material. Furthermore, two types of geometries of the micropillars, as found in the literature [109, 168] conical, tapered as well as prismatic, untapered were modelled. The dimensions of the models are summarized in Tables 4.2 and 4.4. The structures were meshed with continuum, hexagonal elements of 2nd order. For the micropillar models, the two axes symmetry was used and only a quarter of the geometry was modelled with application of the according symmetry constraints along the symmetry planes. Additionally, the microbeams were also modelled with 1D structural bar elements and 2D structural shell elements to compare the FE models with the analytical solution using a beam modulus ($E_x = 169$ GPa) as well as "plate modulus" ($E_x' = \frac{E_x}{(1-\nu_{xy}^2)} = 169.7$ GPa), respectively, since the beams length to width ratio $L/w < 5$ [72].

For the microbeam models, the silicon material was modelled as orthotropic material with the elastic constants chosen for the typical directions of a (100) Si wafer [72]: $E_x = E_z = 169$ GPa, $E_y = 130$ GPa, $\nu_{xz} = 0.064$, $\nu_{yz} = 0.36$, $\nu_{xy} = 0.28$, $G_{xz} = 50.9$ GPa and $G_{yz} = G_{xy} = 79.6$ GPa, where the x, y and z directions correspond to the directions of the beam's long axis, height and width, respectively. For the microbeam bone models and micropillars, the material was modelled as homogeneous and isotropic having an elastic modulus $E = 30$ GPa and Poisson's ratio $\nu = 0.3$, similar to cortical bone tested in longitudinal direction [109].

Loading of the microbeam structures was imposed by displacement of 0.5 μm in y direction of the top 8 nodes of the most central element (i.e. $x = L/2$, $z = w/2$ for the dc beam and $x = L$, $z = w/2$ for the sc beam, with element of size 1 μm), with DOFs 1, 2, 4, 5 and 6 left unconstrained to avoid unwanted stress concentrations. Stiffness and the different stress components node values were obtained from the FE calculation and used for comparison. Additionally, the symmetry of the clamping of

Table 4.1: FE results of simulated microbeam structures.

Model	DCB w/ bulk	DCB w/o bulk	SCB w/ bulk	SCB w/o bulk
Silicon				
Deflection [μm]	0.5	0.5	0.5	0.5
R. force [μN]	78.7	85.1	42.4	47.9
Stiffness [N/m]	157.5	170.3	84.8	95.9
Stiffness FE 1D [N/m]		170.0		89.1
Stiffness$_{analytical}$ [N/m]		170.0		89.1
Stiffness$_{analytical,\ platestiffness}$ [N/m]		170.8		89.5
$\sigma_{xx,max}$ [MPa]	499.4	587	437	528
Bone				
R. force [μN]	14.4	15.9	7.7	8.7
Stiffness [N/m]	28.8	31.7	15.5	17.3
$\sigma_{xx,max}$ [MPa]	91.5	120.2	79.6	105.4

Table 4.2: Dimensions of microbeam FE models.

Dimension	Length [μm]	Width [μm]	Height [μm]
DCB	43	5	1
SCB	20	5	1.5
Bulk	15	15	20

the beams bases was considered both during sample preparation within the FIB and numerically utilizing the FE models. During sample preparation, the microbeams were milled, such that 3 μm of bulk material was present on both sides from the beam's width edges, at the clamped base of the beam. The bulk asymmetry was further verified with the FE models both for the double-clamped and single-clamped beams, for two cases. In the first case one side of the bulk was removed up to 3 μm from the beam's width-edge and the model recalculated. This modification led to no changes in stiffness and stress values. In the second, extreme case, the bulk on one side of the beam was removed all the way up to the beam's edge, thus simulating a microbeam produced at the very edge of the macroscopic sample. For this case, a

Table 4.3: FE modeling results of simulated micropillar structures.

Model	Tapered w/ bulk	Tapered w/o bulk	Untapered w/ bulk	Untapered w/o bulk
Displacement [μm]	0.5	0.5	0.5	0.5
Stiffness [mN/μm]	12.7	17.2	12.7	17.4
Stiffness$_\text{Sneddon corr.}$ [mN/μm]	17.4	-	17.4	-
Stiffness$_\text{analytical}$ [mN/μm]	-	16.8	-	14.7[a] 16.9
$\sigma_{yy,max}$ [MPa]	-2811	-3807	-2496	-3445
$\sigma_{xx,max}$ [MPa]	-1201	-1407	-1217	-1323
$\sigma_{zz,max}$ [MPa]	-1201	-1407	-1217	-1323
$\sigma_{xy,max}$ [MPa]	796	790	773	826
$\sigma_{yz,max}$ [MPa]	798	-964	773	826
$\sigma_{zx,max}$ [MPa]	224	210	66	19

[a] for a cylindrical micropillar.

Table 4.4: Dimensions of micropillar FE models.

Dimension	Length [μm]	Width [μm]	Height [μm]	Upper diam. [μm]	Lower diam. [μm]	C.s. area [μm²]
Tapered	-	-	10	5	5.7	22.5[a]
Untapered	4.75	4.75	10	-	-	22.5
Bulk	50	50	50	-	-	-

[a] averaged cross sectional area.

decrease in stiffness and max. stress of 0.5 % for the double-clamped beam and 1.2 % in stiffness and 0.2 % in max. stress for the single-clamped beam was obtained. It was concluded that asymmetrical boundary conditions have a small and negligible effect on stiffness and stress distribution in the case of Si material. Nevertheless, as a good practice, we recommend considering symmetrical bulk milling of min. 3 μm from the beam's edges to minimize or completely eliminate such effects.

Loading of the micropillar structures was imposed by displacement of all nodes at the top of the micropillars by 0.5 μm in y direction and calculation of the reaction force. In the respective models, either the nodes of the bulk or the structure base were rigidly constrained by setting all DOFs to zero. Sliding of the top nodes of the micropillars was also constrained, thus simulating the experimental scenario of friction contact between the micropillar and the flat punch indenter tip commonly used in such experiments. For comparison, the micropillar FE models were also calculated with unconstrained lateral DOFs, simulating the opposite extreme case of frictionless contact between indenter tip and micropillar top.

Mesh convergence was performed with models of same geometry and half the number of elements within the specimen of interest, i.e. microbeams and micropillars. Stress values differed by less than 2 %, implying that the FE solution was in the convergent region and the mesh refinement of the models was sufficient.

Precision of dimensions

Equations (4.1) and (4.2) show the dependency of the resulting E value on several parameters. In addition to the measured load P and deflection ν from the microbeam bending experiment, also the geometrical parameters L and $I(= bh^3/12)$ appear. These length measurements are obtained from SEM images, the accuracy of which is determined by the resolution of the equipment used, as well as obstruction of visibility of the dimensions in question and the user's judgment. As L and particularly h scale with the 3rd power in the equations, the calculated uncertainty was estimated in terms of the Gaussian linear propagation of uncertainty, where the absolute value of the partial derivatives $|\partial E/\partial x_i|$ is summed for the calculation of the tolerance of the dependent variable. For a fit error value for $\Delta S = 0.25$ % and estimated read out errors of $\Delta L = 2.3$ %, $\Delta b = 2.3$ % and $\Delta h = 10$ % a $\Delta E = 30.9$ % as error boundary was obtained. Furthermore, the error boundary was assumed to represent the full width, 6σ, of a gaussian distribution around the true value of the measured parameters and also derived an overall uncertainty, i.e. standard deviation. This was

done by calculation of the square root of the sum of the squares of the respective errors and was found to be, in our case, 10 %.

Second moment of area deviation

Another effect arising from the FIB preparation is the deviation of the cross-sectional area of the beam from an ideal rectangular shape, due to the tapered shape of the FIB, fig. 4.1a and b. It is a common practice during FIB micromilling to compensate for this artifact, by tilting the sample by $\pm$ 2°, i.e. the FIB tapering angle as determined within the used instrument. In the milling procedure proposed here, three of the length edges of the microbeam structure are visible and can be inspected during preparation. However, the edge oriented towards the bulk cannot be imaged directly and so, while a rectangular shape of the beam cross-section is aimed for during milling, this cannot be experimentally fully verified. Assuming the maximum deviation of the edge to be produced by the tapering angle of the FIB to be $\pm$ 2°, the second moment of area was calculated of the quadrangle areas thus obtained, fig. 4.1c, yielding additional maximal uncertainty for the second moment of area of about $\Delta I = 22$ % leading to a similar uncertainty $\Delta E = 23$ %.

Sneddon correction

During micropillar compression tests, the micropillar base often is left attached to the bulk material it is milled out of, which acts as an elastic half-space and may also deform and contribute to the overall mechanical response of the system, an effect known as micropillar sink in. The indenter used generally measures the displacement between nanoindenter tip, i.e. contact point between nanoindenter tip and top of the micropillar, and the rigid base of the set up underneath the substrate. At the microscale, direct measurement of micropillar deformation is generally not available in conventional nanoindenter machines, so the deformation of the bulk material should ideally also be considered in the calculation of the micropillar strain. An analytical

solution was provided by Sneddon, calculating the depth of penetration D of an elastic half-space by a flat-ended rigid cylinder of radius a under applied load P as [174]:

$$D = \frac{P(1 - \nu)}{4Ga} \tag{4.5}$$

, where G and ν are the shear modulus and Poisson's ratio of the elastic half-space, respectively. By accounting for the displacement of the bulk material in the models with bulk and subtracting it from the total displacement, a corrected stiffness of the micropillar is obtained, as employed by Zhang et al. [210]. Fei et al. used the Sneddon correction on micropillar FE models to calculate the strain errors and the relative strain errors of the micropillars [42]. They found the strain errors to be on the order of 10^{-5} and the relative strain errors to be in the order of 1 %, thus providing a very accurate estimation of the micropillar strain for elastic materials. Here we used the Sneddon correction (4.5) on the micropillar models with bulk to subtract the displacement of the bulk from the total displacement to obtain corrected stiffness values, given in Table 4.3.

4.4 Results

4.4.1 In situ microbeam bending

One double-clamped microbeam of dimensions (43.07 x 4.4 x 1.08) µm, fig. 4.4a, and two single-clamped microbeams (20 x 5.5 x 1.5) µm, fig. 4.4b, and (20 x 5 x 1.5) µm, fig. 4.4c, were FIB-machined on a Si wafer, with the long axis of the beams oriented parallel to the [110] crystal direction of Si. The microbeams were bent with the in situ picoindenter within the chamber of a SEM in load control up to 100 µN. The obtained stiffness vs. beam position data are plotted in fig. 4.4 for the double- clamped (d) and two single-clamped microbeams (e,f), respectively. The data was analyzed by
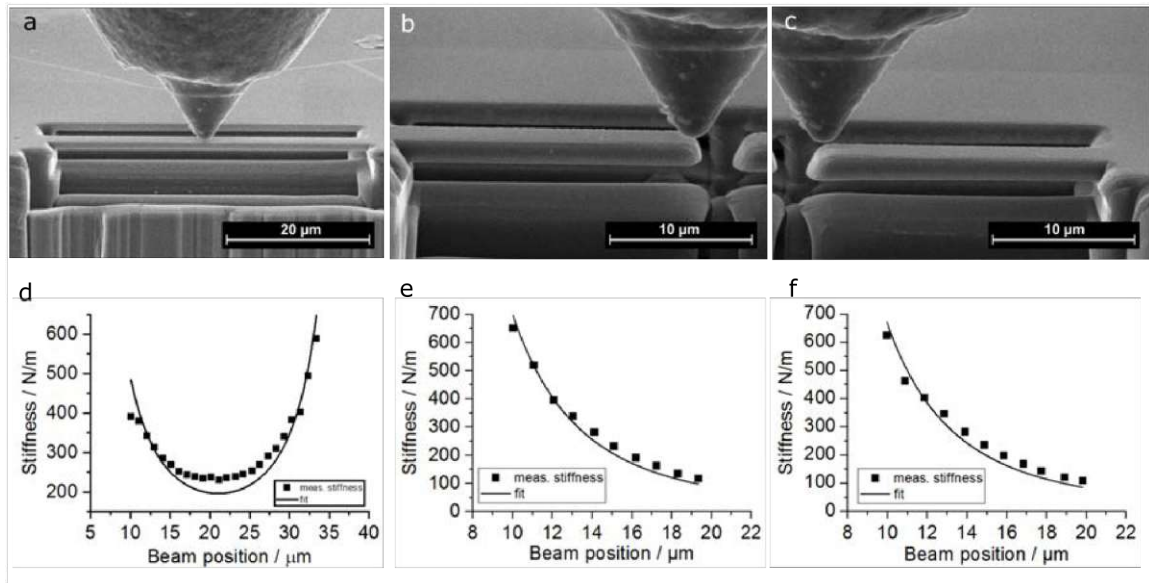
Figure 4.4: In situ bending of Si microbeams with long axis parallel to the [110] direction and with the tip of a SEM picoindenter in the (a) double-clamped and (b) and (c) single-clamped configuration. (d–f) Corresponding microbeam stiffness values measured along the microbeams' long axes, fitted with the corresponding deflection equation for the (d) double-clamped and (e) and (f) single-clamped geometry, respectively, to obtain a value for the elastic modulus E, (198 ± 5) GPa, (152.1 ± 3.8) GPa and (129 ± 31) GPa, respectively. (see text for more details).

fitting equations (4.3) and (4.4) for the double-clamped and single-clamped beams, respectively, to obtain the elastic modulus as a fit parameter. As can be seen the fits are in reasonable agreement with the measured data (R^2 values of 0.9 for the double-clamped, 0.98 for the left and 0.96 for the right single-clamped microbeams, respectively). The obtained values for the elastic modulus E were (198 ± 5) GPa, (152.1 ± 3.8) GPa and (129 ± 31) GPa, where the errors are standard errors of the fit, for the double-clamped and two single-clamped microbeams, respectively, and the theoretical value for Si in the [110] direction is 169 GPa [72].

4.4.2 FE modeling of microbeams

The microbeams structures were modelled as continuum 3D FE model to simulate the apparent bending behavior and the influence of the deformation of the bulk material by which the structures are con- strained. The dimensions of the microbeam models corresponded with the Si microbeams and are summarized in table 4.2. For a systematic comparison, the double- and single-clamped microbeams structures were simulated both constrained by the bulk material and rigidly constrained by setting all the DOFs of the end nodes to 0, fig. 4.5. Bending deformation of the microbeams was imposed by displacement of 0.5 μm of the top nodes of the central and end element for the double- and single-clamped beam, respectively, and calculation of the reaction force. The undeformed and deformed shape of the models is depicted scaled by a factor of 5 in fig. 4.5a-d. The apparent stiffness values were calculated as reaction force/displacement. Stiffness values from the 1D FE models and the analytical solutions, equations (4.3) and (4.4) are also given in table 4.1. The 1D FE structural elements are able to reproduce the analytical solution accurately. The respective 3D FE continuum models rigidly clamped (w/o bulk) show higher apparent stiffness by 1.1 %. The microbeam models clamped by the bulk material show lower apparent stiffness by 7 % and 11 % for the double-clamped and single-clamped beams, respectively, in comparison to the analytical solution.

Contour plots of the longitudinal stress component σ_{xx} of the four models are presented in fig. 4.5(e–h) and the values of the maximal σ_{xx} are summarized in table 4.1. The stresses show the expected distribution along the long axis and the cross section of the microbeams and the highest values of σ_{xx} are encountered at the constrained beam ends. Maximal σ_{xx} values were lower by 32.3 % and 24.5 % in the models constrained by the bulk, compared to rigidly constrained ones, for the double- and single-clamped microbeams, respectively. Furthermore, in the models constrained by the bulk, the stress is observed to decay over a length of about 3 μm into the bulk from the peak stress at the attachment edge.
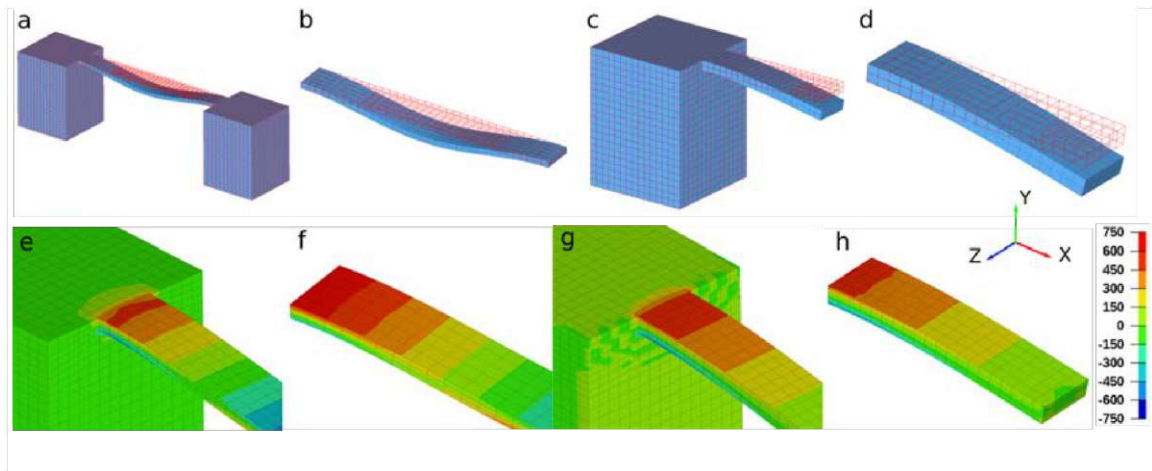
Figure 4.5: FE models of microbeam structures in the double- and single-clamped configurations. (a–d) Undeformed shape represented by red lines and deformed shape (scaled by a factor of 5). (e–f) Contour plots of σ_{xx} stresses of the respective models. In (a), (c), (e) and (g) the microbeam base is constrained by the bulk material. In (b), (d), (f) and (h) the microbeam base is rigidly constrained by all DOFs set to 0.

4.4.3   FE modeling of micropillars

The micropillars structures were modelled as continuum 3D FE models to simulate the apparent compression behavior and the influence of the deformation of the underlying bulk material by which the structures are constrained. The dimensions of the micropillars models were chosen on the same order of magnitude as found in the literature [109, 168] and are summarized in table 4.4. For a systematic comparison the tapered and untapered micropillars were simulated both either constrained by the bulk material or rigidly constrained (i.e. situated on a relatively much stiffer substrate) by setting all the DOFs of the bottom nodes of the micropillars to 0, fig. 4.6. Deformation of the micropillars was imposed by displacing all top nodes of the micropillars by 0.5 μm, and calculation of the reaction force. The undeformed and deformed shape of the models is depicted scaled by a factor of 5 in fig. 4.6a-d. The apparent stiffness values were calculated as reaction force/displacement. Theoretical stiffness values (Stiffness$_{\text{analytical}}$) were calculated as a system of springs in series with changing and constant circular cross sections for the tapered and untapered conical

micropillars, respectively, as well as a cuboid of same dimensions as the untapered micropillar and an elastic modulus of 30 GPa (see table 4.3), to compare with the stiffness values obtained from the FE models. The theoretical and FE-derived stiffness values were found to be on the same order of magnitude. The micropillar models with bulk showed a lower apparent stiffness by about 25 % compared to the models without bulk (on a stiff substrate). The tapered micropillar without bulk showed a lower stiffness by 1.2 % compared to the untapered one. Further, the Sneddon correction was applied to the models attached to the bulk, to correct for the effect of the bulk deformation and was found to reproduce the stiffness values of the respective models without bulk accurately (see table 4.3).

Additionally, the distribution of the σ_{yy} normal stresses (fig. 4.6(e–h))and σ_{xy} shear stresses (fig. 4.6(i–l)) of the models were plotted as contour plots and the maximum values of all stress components were summarized in table 4.3. From the σ_{yy} contour plots (Fig. 4.6(e–h)) it is evident that the stresses experienced due to compression are not confined to the micropillar but extend considerably also into the bulk below the micropillar. In addition, the models including bulk material also show locally positive, i.e. tensile stresses within the surrounding bulk material. Overall, the stress distributions appear more homogeneous in the untapered models compared to the tapered ones. Stress concentrations occur in the models at the tops and bases of the micropillars due to the idealized constraints. In additional models with unconstrained lateral DOFs at the top of the micropillars, simulating a frictionless contact the stress propagation arising from top edges of the micropillar were eliminated (data not shown). In these models differences in the distributions are observed for the σ_{xy} contour plots similar to the ones shown in (Fig. 4.6(i–l)).

4.5   Discussion

Experimental mechanical characterization of materials at the microscale has been used for inorganic materials and is being extended towards biological materials, which
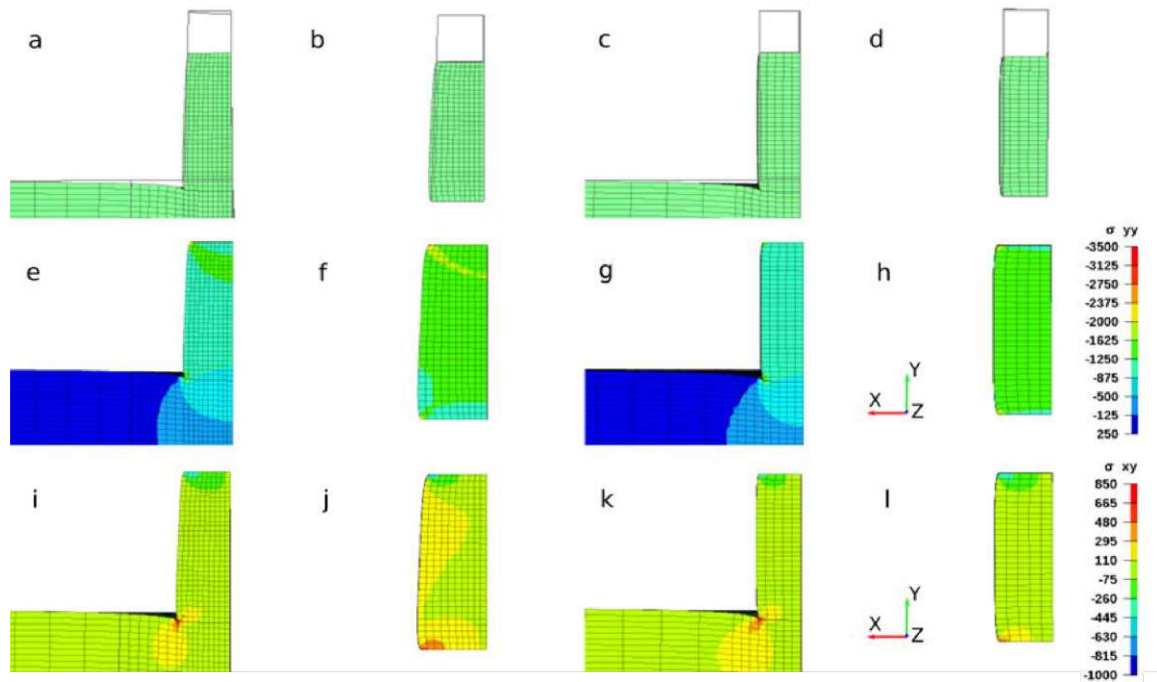
Figure 4.6: FE models of tapered (columns headed by a and b) and untapered (columns headed by c and d) micropillar structures. (a–d) Undeformed shape represented by grey profile lines and deformed (compressed) shape (scaled by a factor of 5). (e–h) Contour plots of normal axial (σ_{yy}) stress, (i–l) contour plots of shear (σ_{xy}) stress of the respective models. (a), (c), (e), (g), (i) and (k) The micropillar base is constrained by the bulk material, which results in local positive/tensile normal stresses in the bulk below the micropillar. (b), (d), (f), (h), (j) and (l) The micropillar base is rigidly constrained by all DOFs set to 0 at the very bottom.

poses additional challenges in both sample preparation and mechanical testing. As such, there are essentially no testing standards or few best practice guidelines to date. Instead, often standards for macroscopic mechanical testing are consulted and adapted to fit within the constraints and boundaries of feasibility of the used equipment. Moreover, the variation (heterogeneity and anisotropy) and complex hierarchical structure of biological tissues present additional challenges for precise evaluation and interpretation of mechanical data.

4.5.1   Microbeam bending

The published work on experimental bone micromechanics of isolated microstructures to date comprises of mechanical testing in bending [24, 82, 84] and compression [83, 109, 168, 169]. One possibility of validation of a mechanical setup is the use of a material with well-known mechanical properties at the microscale and/or independent of size, such as the crystalline structure of silicon. In this study silicon microbeams were milled out on a commercially available silicon wafer with well-known orientation of the crystal lattice and the microbeams were produced, such that the beams' long axis is parallel to the [110] crystal direction of silicon, with elastic constants $E = 169$ GPa and $\nu = 0.36$, in which the loading during bending predominantly takes place. Evaluation of bending experiments requires the use of beam theories, e.g. Euler-Bernoulli or Timoshenko, where the elastic modulus derivation from measurements is non-linearly dependent on the beam dimensions. The precision limit of the FIB equipment on the one hand and the user dependent read out errors of dimensions obtained by SEM (~ 100 nm) on the other hand, are an order of magnitude below the size of the microbeams and can substantially influence the derivation of E via experimental errors with up to 30 % uncertainty. Another characteristic of the milling procedure is limited accessibility of all four long edges of the microbeam by SEM. Since the microbeam remains attached to the bulk material, the visual evidence and precise measurement of the cross-sectional shape is impossible (fig. 4.1c), as one long edge cannot be visualized via SEM. An estimated uncertainty arising from the deviation of the second moment of area of the microbeam's cross-section was estimated to influence E up to 23 %. This large uncertainty due to deviation of the beam cross-section is in agreement with the estimation of the influence of the deviation of the pentagonal cross-sectional shape and thus second moment of area of Ag nanowires loaded in bending, which ranged 9.6 % – 38.5 % [196]. These major sources of uncertainties regarding the obtainable microbeam geometry can add up to a total of 53 % uncertainty in the calculation of E from such experiments. The obtained values from the silicon microbeams of (198 ± 5) GPa, (152.1 ± 3.8) GPa

and (129 ± 31) GPa, for the double-clamped and two single-clamped microbeams, respectively, lie within these boundaries. It seems that with careful milling and geometrical measurement the errors obtained are significantly lower compared to the estimate, in fact, the standard deviation of the estimated upper error boundaries was calculated to be 10 %. In our case, the elastic constant had errors of 17 % for the double-clamped beam and 10 % and 24 % for the single clamped beams, respectively. An additional effect that leads to modified apparent mechanical behavior arises because the microbeams remain attached and thus, mechanically constrained by the same bulk material they are milled out of. This means microbeams are effectively attached to an elastic quarter-space, which also deforms resulting in a systematic error [69]. To investigate this bulk effect, linear static 3D FE models were created of an idealized geometry resembling the silicon microbeam dimensions (table 4.2) and the apparent stiffness values were obtained. The models with bulk underestimated the stiffness values by 7 % and 11 % for the double-clamped and single-clamped beam, respectively. This effect is not as prominent as the geometrical uncertainties and can be easily accounted for. As the microbeams remain attached to the bulk, the induced flow stress at the microbeams' supports subsides into the bulk during bending, within ≈ 3 μm range from the beam base and thus reduction in the maximal experienced longitudinal stress σ_{xx} (table 4.1), which can lead to an underestimation of yield and strength properties. Interestingly, the single-clamped beams investigated experimentally were close to this prediction being 10 % and 24 % below the theoretically expected value, however, interpretations of results need to take the above discussed aspects into account, as potentially large geometrical uncertainties and bulk deformation can be superposed and mutually compensate.

We conclude that for current micro-bending experimental designs the uncertainties and thus the scatter of obtained mechanical results can be high and well over 10 % (up to 24 % in our case). Additional effects of the interaction of the spherical indenter tip with the microbeam, such as elastic or plastic indentation of the tip into the microbeam and precision of the positioning of the tip on the microbeam, which can

lead to additional twisting and torsion of the microbeam, still remain unaccounted for. Eliminating and correcting for all of these effects might lead to a more accurate evaluation of micro-bending experiments. Importantly, our experiments on Si microbeams did yield results close to the modeling prediction, especially in the case of single-clamped beams. We do not know why this has been the case, but we speculate that with only one attachment point the uncertainty of the attachment geometry, which limits e.g. the effective beam length is lower. For future improvement, it would certainly be of interest to investigate the reproducibility of this effect.

4.5.2   Micropillar compression

Mechanical testing under uniaxial compression induces a more homogeneous stress state within a tested specimen compared to bending. This allows for a straightforward calculation and interpretation of mechanical parameters. Whereas, macroscopically, samples can be isolated, geometrically dimensioned up to a relatively high precision and constraints can be controlled and applied according to a specific design and standard for testing, this is not directly transferable to the microscale. For microscale mechanical testing, samples are prepared and manipulated within a high vacuum chamber of an SEM using the FIB technique. The micron-sized samples produced cannot easily be manipulated or transferred, and, usually remain attached to the bulk material they are made from. In micro-compression tests, the bottom of the sample remains attached to the bulk material. That means it mechanically acts as an elastic half-space underneath the sample and deforms during testing, contributing to the overall mechanical response, which is recorded from the testing setup. This clearly needs to be taken into account, for an accurate calculation of mechanical parameters.

Here we employed linear, static FE models to compare apparent mechanical behavior of the most commonly found geometries used for micropillar compression applied to bone. Our models comprised the circularly FIB milled, tapered and the rectangularly FIB milled, untapered micropillars, both either attached to the bulk or rigidly con-

strained at the base, i.e. without bulk. The rigidly constrained case at the base has recently been experimentally achieved by detaching the micropillars from the bulk and transferring them to a Si substrate using a micromanipulator [109]. From the FE models, the reaction force was calculated upon a prescribed displacement and an apparent stiffness value was obtained (table 4.3) from this. To validate these results a theoretical value was also calculated for a cuboid of the same dimensions (table 4.4) and material constants ($E = 30$ GPa and $\nu = 0.3$ for bone). The modelled micropillars and the obtained values by FE calculations were found to be in good agreement with the theoretical value. The models with bulk showed an approx. 26 % lower apparent stiffness compared to the models without bulk, predominantly due to the deformation of the underlying half-space, an effect known as the micropillar sink-in. To account for this effect, the Sneddon correction [174] for a flat ended cylinder indenting into an elastic half-space, can be applied [42, 47, 210]. Fei et al. investigated in detail the accuracy of the Sneddon correction applied to FE models and found the corrected strain errors to lie in the order of 10^{-4}, thus providing a sufficient correction, which is also observed in the results presented in table 4.3. One of the aims of this study was to provide a systematic comparison of untapered and tapered micropillar geometries and quantify the influence on measured apparent stiffness. The differences between the apparent stiffness values of the tapered and untapered models presented here was calculated to be in the order of 1 % and 0.1 % for the models without bulk and the models with bulk, respectively, which lies within the range of numerical accuracy of FE models and was thus found to be negligible and can be well corrected by application of the above mentioned Sneddon correction [42].

Considering the apparent mechanical behavior, the main concerns about determination of the micropillar strains arising from the tapered geometry and the underlying bulk can be well accounted for and eliminated by the Sneddon correction. However, looking further at the distribution of the stresses and eventual deformation mechanisms beyond the elastic limit, caution needs to be taken considering several effects for interpretation of experimental results of such microscale experiments. Contour

plots of the normal axial compressive stresses σ_{yy} and the σ_{xy} shear stresses of the modelled micropillars are plotted in fig. 4.6(e–h) and fig. 4.6(i–l), respectively. In the models with bulk, substantial stresses within the bulk are apparent within a distance of approx. 2/3 of the micropillar's height (not entirely shown). This needs to be taken into consideration for the relative dimensions of the bulk compared to the micropillar, as non-elastic deformation can also occur within the underlying volume especially if defects such as pores are present. In such cases, the application of the Sneddon correction [47] would not be sufficient.

The homogeneous distribution of the normal stresses in the tapered micropillars compared to the untapered ones is confined within the cross section, an effect which is reported in other FE micropillar studies [42] and is also reproduced in the FE models in this study. Regarding the magnitude of the induced stresses, it was shown that the choice of the reference diameter for calculation of the normal stress in micropillar compression experiments on copper significantly influences the obtained stress magnitudes, especially in the post-yield regime [94]. For best comparability, the dimensions of the untapered micropillars in this study were chosen, such that the cross-sectional area is the same as the averaged cross-sectional area of the tapered micropillars. The accuracy of further options for calculation of the stresses within a tapered micropillar were investigated by Fei et al., who found that the calculation of the average stresses at the top and the bottom surface of the micropillar gives the most accurate result for strains up to 0.4 %, as opposed to calculation of the stresses by using the average diameter or average radius of the micropillar [42]. Despite some improvement with an alternative choice of calculation of stresses, they concluded that a micro-compression test cannot be accurately applied for measurement of the Young's modulus. However, compared to micro- and nanoindentation tests, which induce a multiaxial stress state with high stress gradients in a bulk material underneath a sharp indentation tip, from which mechanical parameters can only be indirectly inferred, a micropillar compression test induces a, not completely, but much more, uniform stress state within an

isolated microscopically sized volume, the assumption of uniaxial stress can still be considered appropriate to within 10 % of the value [110].

Another issue regarding the induced stresses during a micropillar compression test is their distribution within the micropillar and how this might contribute to observed deformation mechanisms. The highest obtained stresses in the micropillar models in this study occur as stress concentrations at the edges at the top and bottom of the micropillars. This is in agreement with micropillar FE models found in literature and arises from the lateral movement constraint of the top and bottom surfaces simulating the friction between the flat indenter tip and the top of the micropillar and the constraint of the micropillar base by the bulk, respectively, as well as the idealized 90° angle at the edge in the FE models, effects elaborately studied by [210], [94]. For materials exhibiting strain hardening behavior the highest probability for damage initiation is at the top edges of the micropillar. The propagation of the post-yield strain hardening of the material then continues diagonally towards the center of the micropillar, either resulting in a slip plane, or meeting a crack from the opposite direction, thus creating a hardened wedge at the top of the micropillar, which then splits the micropillar apart [47, 99]. The latter effect has been reported in micropillar compression studies conducted on bone [168, 169]. Additional deformational effects arising from the restricted lateral movement and misalignment of the equipment relative to the micropillar long axis can lead to bending and rotation of the structure, which were both discussed in FE models [94] and reported experimentally [47, 110]. Thus, interpretation of deformation mechanisms from micropillar compression experiments need to be done with great care and consideration of structural effects, which can potentially obscure "true" material properties and deformation mechanisms of the tested material. In this context, the choice of geometry, i.e. tapered vs. untapered, might clearly be the untapered micropillars. However, this comes at the cost of sample numbers. Untapered micropillars require a more elaborate protocol with fewer automation possibilities.

4.6 Conclusion

The influence of geometrical deviations and experimental constraints was investigated for micrometer-sized microbeams and micropillars used for micromechanical characterization of materials in micro- bending and micro-compression experiments. For validation of microbending, double- and single-clamped Si microbeams were FIB-milled. Additionally, the effect of the bulk was studied employing FE models of microbeams and micropillars.

Si microbeams were bent on multiple positions along their length resulting in effective elastic moduli E within 24 % deviation. The main sources of uncertainties arise from limited precision of microscale sample preparation and non-linear dependence microbeam geometry with a theoretically estimated worst-case of 53 % relative error. The deformation of constraining bulk was studied via FE modeling and found to introduce additional uncertainty up to 11 %. Thus, we conclude that the accuracy of determination of elastic moduli from microbeam bending experiments is strongly dependent on geometrical deviations and needs to be done with great care.

For micropillar compression, FE modeling predicted the effect of tapering of the micropillars to be negligible (1 % error). While the deformation of underlying bulk, accounted for 25 % error, this can be sufficiently eliminated using the Sneddon correction. However, inhomogeneous distribution of the normal and shear stresses due to testing geometry for both tapered and untapered micropillars may lead to structural deformation mechanisms masking "true" material deformation and damage behavior. To further understand and decouple such effect non-linear FE models incorporating damage behavior should be studied.

In summary, micromechanics experiments can yield important insights but experiments, data analysis and interpretation need to be done with great care to avoid the interpretation of artifacts. Further research is required to elucidate the influence of used sample geometries and load cases on failure behavior observed in micromechanical tests.

Chapter 5

Microbeam bending of hydrated human cortical bone lamellae from the central region of the body of femur shows viscoelastic behavior

5.1 Related publication and declaration of contributions

Results of the presented chapter have been published in the "Journal of the Mechanical Behavior of Biomedical Materials" in 2022, entitled "Microbeam bending of hydrated human cortical bone lamellae from the central region of the body of femur shows viscoelastic behavior" and co-authored by Orestis G. Andriotis, Karin Wieland, Christoph Gasser, Andreas Steiger-Thirsfeld, Johannes Bernardi, Bernhard Lendl, Michael L. Pretterklieber and Philipp J. Thurner.

Author contributions: The first author and author of the current thesis, Vedran Nedelkovski, wrote and edited the manuscript, performed study design, sample prepa-

ration via FIB milling, SEM imaging, AFM setup design and AFM-based mechanical testing, data processing and data interpretation. Orestis G. Andriotis provided resources, training, support and supervision of the AFM-based mechanical testing and data processing, reviewed and edited the manuscript. Karin Wieland and Christoph Gasser supported the study design, performed Raman spectroscopy measurements on the bone microbeam samples, Raman spectroscopy data processing and data interpretation, reviewed and edited the manuscript. Andreas Steiger-Thirsfeld provided training and supervision of FIB milling. Johannes Bernardi provided resources and edited the manuscript. Bernhard Lendl provided resources and supervision for Raman spectroscopy. Michael L. Pretterklieber provided bone material for sample preparation and edited the manuscript. Philipp J. Thurner provided resources, supervision of the work of Vedran Nedelkovski, suported the study design, data analysis and data interpretation, reviewed and edited the manuscript.

5.2   Introduction

Bone tissue is a nanocomposite biological material of both organic and inorganic phases, with a hierarchical structure ranging from the nano- to the macroscale [154, 200]. The mechanical response of whole bones, therefore, represents a complex interplay of the mechanical properties of structures, their interfaces and the way they interact at every length scale, as well as the influence of the variably sized porosities present in the tissue [20, 26, 50, 135, 170]. To understand whole bone mechanics and the affecting factors leading to its alterations, experimental data and understanding of the mechanical behavior at every length scale is necessary. In this context, mechanical properties of bone structures at lower length scales, e.g. single lamellae, remain largely unknown, mainly due to size- and hydration-related experimental challenges. At the micrometer length-scale, the relevant structural elements in cortical bone are bone lamellae. These represent packed layers (2 – 10 µm in thickness) of mineralized collagen fibrils and are often formed as concentric layers with alternating orientation

around a central (Haversian) canal in the process of bone remodeling, to ultimately form the structure of the next hierarchical level, the osteon [154, 200].

Mechanical testing of bone material at the microscale has, to date, been largely conducted by micro/nanoindentation experiments [102, 181]. This is an attractive technique, due to its relatively straightforward sample preparation and application as well as a high measurement throughput. However, during nanoindentation, high stress and strain gradients are imposed onto the material and calculation of mechanical parameters requires several theoretical assumptions for analysis of the obtained data, sometimes leading to ambiguous measurement curves for a material with dissipative mechanisms [25, 181]. Moreover, performing nanoindentation requires extensive preparation of a flat sample surface and dehydration as measurements are usually conducted in dry conditions. Nanoindentation measurements in wet conditions, though feasible, offer limited positioning options and information of the tested volume and underlying structures or porosities at the microscale and also might lead to damage of the sample during scanning-probe-based imaging [215].

To access material properties, defined via a homogeneous stress state, experimental efforts have been made in the last decade towards mechanical testing of isolated, micron-sized bone specimens of defined geometry, e.g. by Luczynski et al. [109]. Nevertheless, despite these efforts, the actual number of studies and samples investigated still remains small (seven publications since 2009), with a significant number of experiments conducted in dry, ambient conditions due to small sample size and experimental challenges. A common feature of all the studies mentioned below is the use of focused ion beam (FIB) based milling. This technique has proven to be important for machining of variously shaped microscopic specimens, also from biological materials like bone. For example, Chan et al. used FIB milling to isolate individual cantilever microbeams of triangular cross section and tested them in bending using a conventional nanoindenter [24]. The samples investigated were enamel prisms from human primary molars, which is mineralized tissue, somewhat similar to bone. Further studies exist investigating rat bone material, where cantilever bone microbeams

of rectangular cross section were machined and subsequently tested with an in situ flattened atomic force microscopy (AFM) cantilever tip in bending and compression. These studies assessed the influence of dehydration by vacuum exposure time [82], fibril orientation within the microbeam [84] and bone pathology [83] on bone mechanical properties at the microscale. To test the anisotropic post-yield properties and damage mechanisms of bone material, Schwiedrzik et al. employed a protocol of micropillar compression on ovine osteonal bone in both axial and transverse direction, initially in dehydrated state [168] and later also under hydrated conditions [169]. The protocol of bone micropillar compression was further developed by Luczynski et al. to extract "true" elastic properties of the bone material [109]. For a more homogeneously induced stress state within the test specimens, they prepared micropillars from bovine cortical bone with rectangular and uniform cross section by FIB milling and subsequently transferred the micropillars onto a much more rigid substrate, to eliminate the deformation of the underlying bulk material. By analyzing the unloading portion of the force vs. displacement curve they were able to obtain values for the elastic modulus in the range of 30 GPa. In addition to experimental work, also numerical simulation studies have been performed in attempt to unravel mechanical mechanisms of bone lamellae and their constituents. Numerical studies range from molecular modeling [117], finite element (FE) modeling of several mineralized collagen fibrils [75] and different lamellar arrangements [107, 195], to multiscale simulations via neural networks [186], where values of up to 40 GPa for the average Young's modulus of mineralized collagen fibrils have been reported.

Investigation of mechanical properties at lower length scales aims at the determination of mechanical properties at the length scale of individual lamellae of bone tissue, ideally on samples with homogeneous extra-cellular matrix (ECM), such as mineralized collagen fibrils. These fibrils are ideally predominantly oriented in a (known) parallel fashion, which would minimize variability and allow to decouple the influence of material anisotropy and higher hierarchical structural effects. At the microscale, porosities and defects such as lacunae and microcracks should be avoided, such that

suitable regions of interest (ROI) in the tissue can be identified and chosen for testing. Additionally, the number of interfaces should be significantly reduced to probe isolated structural elements at the given length scale, e.g., single bone lamellae. Such experiments open possibilities for a systematic study of diverse effects that may influence tissue mechanics due to age or disease, provided that such effects manifest themselves at this level.

Given the fact that most micromechanical experiments in bone are still conducted in dry conditions, we aimed, in this study, to examine the effect of hydration, which we hypothesize to significantly influence the results, and, to a limited extent, donor age on the mechanics of human cortical bone tissue at the microscale. For this purpose, we realized an atomic force microscopy (AFM)-based microbeam bending setup and protocol to test small microbeams both in dehydrated and rehydrated state.

5.3 Materials and methods

5.3.1 Sample preparation

Four right femurs from four male human body donors aged 65, 78, 85 and 94 years were obtained from the Division of Anatomy at the Medical University in Vienna. The use of body donor material was approved by the Ethics Committee of the Medical University of Vienna (EK Nr: 1744/ 2016). Larger cortical bone pieces (approx. 10 cm in length) were cut from the central region of the shaft of femur (fig. 5.1a), with a hand saw and then into smaller parallel pieces (approx. 2 cm in length) with a diamond band saw (Exakt 300 CP, Norderstedt, Germany), (fig. 5.1b). Subsequent parallel longitudinal and transverse cuts were performed with a low speed saw (Isomet LS, Buehler, Lake Bluff, Illinois, USA) to obtain a small bone cube of (2 x 2 x 2) mm^3 size (Fig. 5.1c and d). The cube was then glued (5 min two component epoxy glue, UHU, Baden, Ger- many) onto a custom-made tripod holder to expose three orthogonal surfaces of the sample with the longitudinal surface oriented upwards
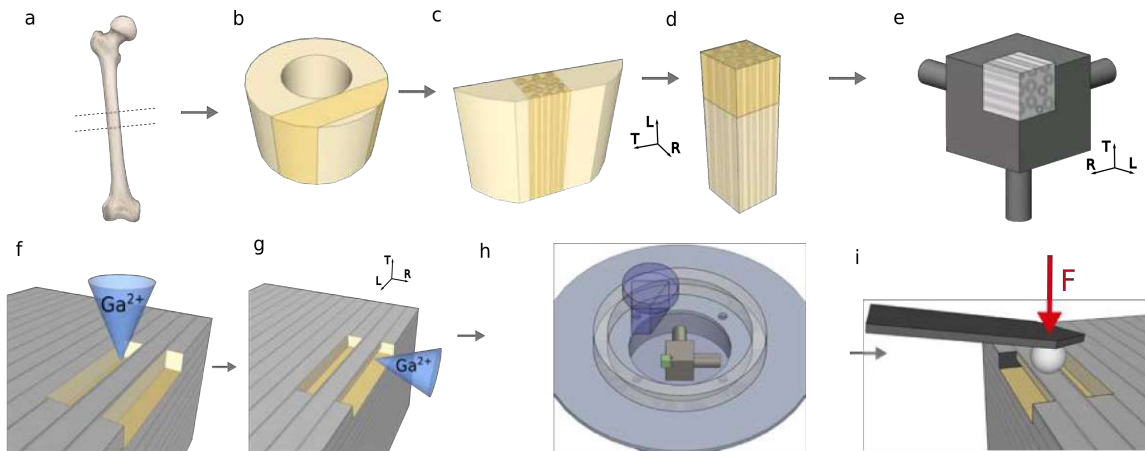
Figure 5.1: Schematic overview of the entire testing workflow. (a) Bone samples were extracted from the middle portion of the body of human femora. (b–d) Low-speed saw parallel cuts to obtain a small bone cube of dimensions (2 x 2 x 2) mm³. Bone sample orientation is indicated via reference system: L - longitudinal, T - transverse, R - radial. (e) The bone cube is mounted on a tripod holder, such that the longitudinal cut is oriented upwards. The three exposed bone sample surfaces are subsequently ultramilled and sputter-coated with 4 nm AuPd. (f, g) FIB milling steps for fabrication of the microbeam structures. (f) FIB milling of a micron-sized trench from the top, consisting of a single bone lamella and (g) from the side underneath the trench to produce a double-clamped microbeam structure. (h) The tripod with the bone sample (green) is mounted into an open water bath allowing access of the AFM-cantilever holder (blue) to the sample from the top. (i) Bending of microbeam structure in air and HBSS using an AFM cantilever, furnished with a glass microsphere. (Subfigures (b-g, i) not to scale, see text for more information).

(fig. 5.1.e). The bone sample surfaces were then ultramilled using a diamond blade ultramiller (Leica SP2600, Leica, Nussloch, Germany) to obtain flat surfaces, after which the bone sample was stored in air at room temperature for a minimum of 24 h so that free unbound water is slowly removed and possible damage from quick drying due to high vacuum exposure is reduced. Lastly, the air-dried sample was sputter-coated with a 10 nm layer of AuPd (60:40) to enable electron and ion microscopy.

The tripod holder was subsequently mounted on the stage of a dual beam focused ion beam (FIB) system (Quanta 200 3D DualBeam, FEI, Hillsboro, Oregon, USA)

incorporating both scanning electron microscopy (SEM) and FIB within the same vacuum chamber. The goal of the FIB preparation steps was to obtain a microbeam structure, double-clamped at both supports by the bulk, which was to be bent along the microbeam length, according to a protocol applied to nanocrystalline diamond microbeams [171]. This geometry was preferred over single-clamped microbeam structures machined from bone [24, 82], due to higher better structural integrity during extensive FIB milling steps, transfer between the SEM/FIB and AFM systems and during rehydration.

FIB milling was performed at 30 keV, which provided an optimal setting of sputter yield versus damage of bone material [24, 82, 168], using Ga^+ ion currents ranging from 20 nA (coarse) to 0.5 nA (fine). The latter provided sufficient finish of the 25 μm long side surfaces of the microbeams and minimized ion exposure time, as well as sample drift. Bone microbeams structures were FIB milled near the bone sample edge, first, from the top to isolate a single trench of defined length and width (fig. 5.1f) and second, at an angle of 90∘ (from the side), to obtain a microbeam structure, double-clamped by the surrounding bone material (fig. 5.1g).

Bone microbeams were machined in a lamellar region of the bone sample and the coated, top surface of the microbeams and their surrounding (approx. 50 μm × 50 μm) was polished with low ion currents of 1 nA to remove the metal coating to eliminate possible effects on the mechanics and to facilitate Raman spectroscopy (fig. 5.2b). Extensive FIB treatment can lead to damage and Galium ion implantation in the material [197]. However, based on Monte Carlo simulations ([168] and references therein), it was found that damage was confined within 25 nm and ion implantation within a 15 nm region beneath the surface and was thus concluded to be negligible compared to geometrical deviation that might occur during the FIB milling process [127]. The microbeams were produced such, that they consisted of a single bone lamella, where the long axis of the beam is oriented parallel to the longitudinal direction of the bone sample (fig. 5.1e, f, g), with a nominal geometry of L x b x $h = (25$ x 4 x $1)$ μm^3, where L is the length, b the width and h the height of the

microbeam. The actual obtained dimensions were taken from the SEM images, from the top for the width b (fig. 5.2c) and from the side for the length L and height h (fig. 5.2d). The tapered angle of the FIB was corrected for by milling at angles of $\pm$ 2°. The dimensions of microbeams were chosen such, that the whole beam would fit into the AFM scanning piezo range (30 µm $\times$ 30 µm), a single microbeam would be comprised out of a single bone lamella (2 µm – 5 µm in width) and the estimated desired stiffness (in the range of 200 N/m, same as the nominal spring constant of the AFM cantilevers used) was tuned by a corresponding beam thickness (approx. 1 µm for a linear, elastic beam of $E = 30$ GPa). A total of 4 microbeams per donor (i.e. N = 16) were machined for this study, with dimensions as measured by SEM of L x b x h = (25.1 $\pm$ 0.1) x (3.3 $\pm$ 0.5) x (1.1 $\pm$ 0.1) µm³ (see also table B.1 in appendix B for individual dimensions of all microbeams).

5.3.2   AFM mechanical characterization

After FIB milling the tripod sample holder was transferred and mechanically fixed into a custom-made water bath (fig. 5.1h) enabling measurements in both air and aqueous environment. The water bath was placed on the motorized stage of the atomic force microscope (AFM) equipped with a top-view video microscope with 12x magnification (NanoWizard 3 ULTRA SpeedA, JPK Instruments AG, Berlin, Germany). AFM-imaging and mechanical testing was performed in force-mapping mode, during which every pixel is represented by a force vs. displacement curve (i.e. force curve), using a high stiffness AFM cantilever (RTESP-525, k_{nom} = 200 N/m, Bruker, Billerica, Massachusetts, USA) to match the stiffness range of the bone microbeams for optimum measurement sensitivity, i.e. to achieve a cantilever deflection (D in nm) to z-piezo movement (z in nm) ratio of about 0.5 [89]. The AFM cantilever was furnished with a borosilicate glass microsphere of 5 µm diameter (fig. 5.1i) according to a protocol previously published [89]. The choice of the glass microsphere size was based on estimation for achieving sufficient imaging resolution for identifying the produced cantilevers while minimizing indentation effects during
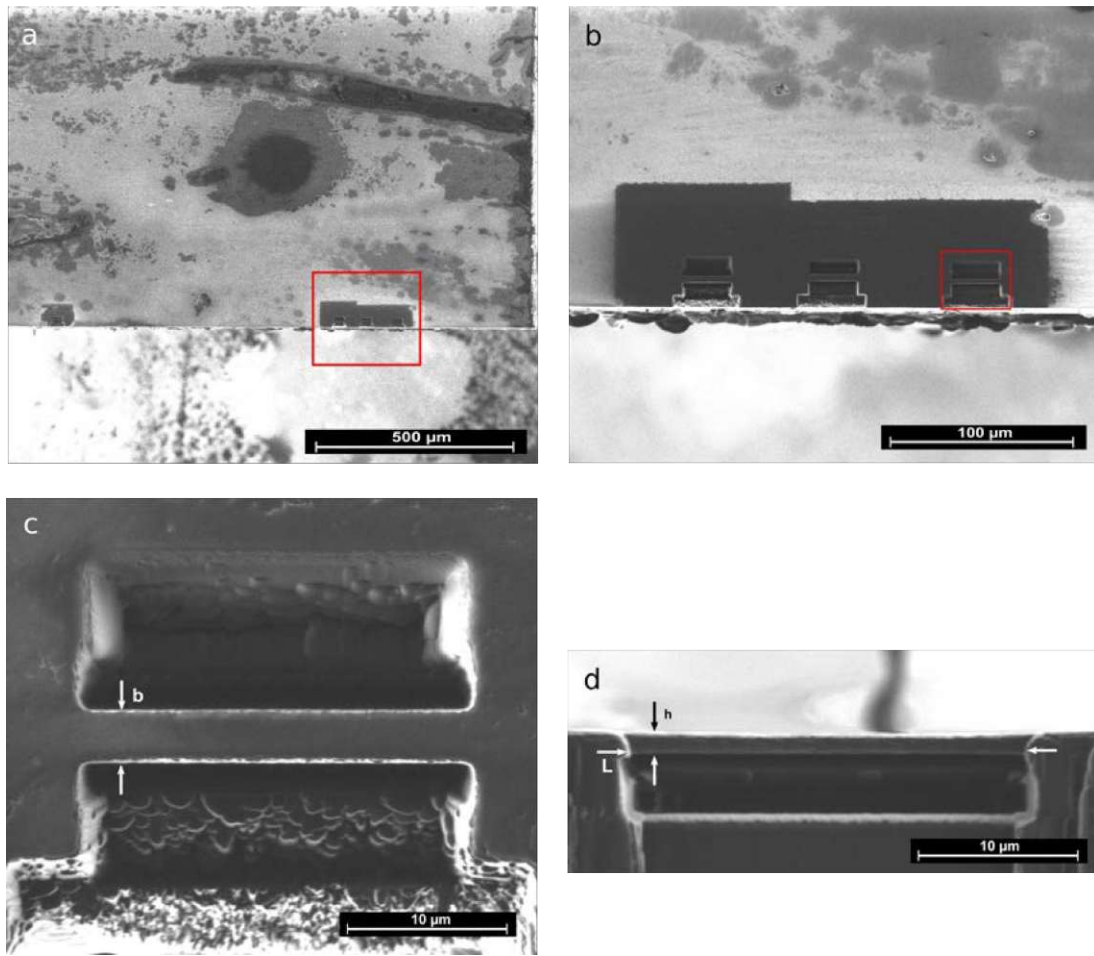
Figure 5.2: (a–c) Top view and (d) side view SEM images of the bone sample. (a) Overview of the bone sample top surface and ROI, where microbeams are FIB-milled at the edge. (b) Lamellar ROI where 3 microbeams were produced. The light area remains sputter-coated, whereas the dark area indicates the local region where the AuPd coating was removed by FIB-polishing to expose the bone material. (c) Top view image of a single microbeam, from which the width b of the microbeam is measured. (d) Side view image of a single microbeam, from which the height h and length L of the microbeam are measured.

bending. Prior to preparation of the colloidal AFM probe, the sharp tip of the AFM probe was removed via FIB milling and the probe was initially calibrated by two methods, a) according to the Sader method [159] in the tipless configuration in air and b) by bending of Si microbeams of known stiffness in the mounted microsphere configuration [127]. The inverse optical lever sensitivity of the AFM cantilever was

determined by averaging 16 force curves performed on a freshly cleaved mica surface prior to each experiment run, either in air or in Hank's Balanced Salt Solution (HBSS) at room temperature. The raw data is displayed as the AFM cantilever deflection in Volts vs. z-displacement of the piezo in nm. The upper part of the unloading curves were linearly fitted, and the inverse of the slope (nm/Volts) was used as optical lever sensitivity of the cantilever.

Imaging in both air and HBSS was performed in force mapping mode with force maps of rectangular shapes and a pixel size of approx. 0.5 μm. Maximum force of $F_{max} = 2$ μN and loading/unloading rate of 1 μm/s were used. Imaging was started in the vicinity of the microbeam structure, which was then approached step-wise until the microbeam base could be distinguished in the image to avoid damage of the structure or the cantilever (fig. 5.3a). After the microbeam base was identified, the motorized stage of the AFM was used to re-position the sample such that the whole beam could be imaged, i.e. was accessible to the AFM probe, for precise positioning during the bending measurements (fig. 5.3b). For microbeam bending measurements a force map over the microbeam top surface with 25 pixels over the beam length and 3 pixels over the beam width was recorded, resulting in a pixel size of approx. 1 μm (fig. 5.4a). Force curves were measured with a loading/unloading rate of 0.5 μm/s, first up to $F_{max} = 16$ μN (resulting in max. beam deflection of < 100 nm) in air and, second up to $F_{max} = 12$ μN (resulting in max. beam deflection of <300 nm) in HBSS after 2 h of rehydration time. The fact that the loading/unloading bending curves could be measured reproducibly without decrease in loading/unloading stiffnesses, both in air and in HBSS, was an indicator that the double-clamped microbeam structure remained stable, without permanent deformation. Any plastic deformation would be detectable as decreased load bearing capacity of the structure and a decreased stiffness in the load vs. deflection curve (see also section 5.4.1 and fig. 5.4).

Multiple force curves along the long axis of the microbeam were evaluated to obtain the bending modulus [171]. For this, only the force curves from the central pixel row of the force map were used (fig. 5.4a). Furthermore, to remain within the
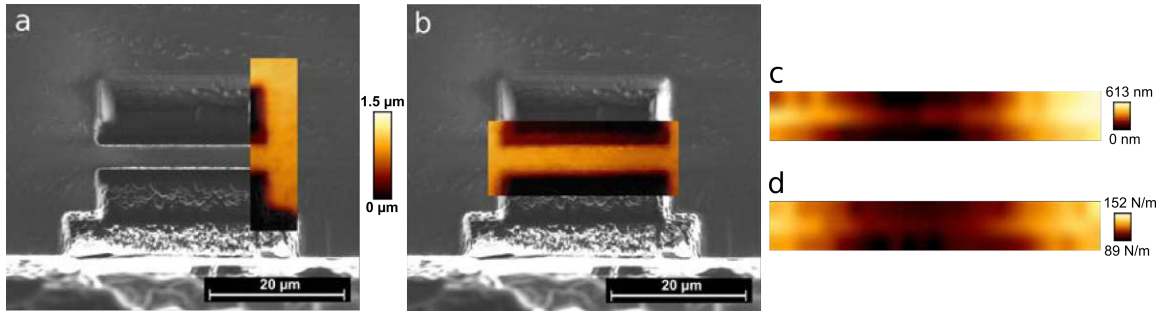
Figure 5.3: (a, b) Overlayed AFM force-map images over a SEM image of a single microbeam, (c, d) AFM force-map images of a microbeam bending measurement. (a) The microbeam is first located by AFM imaging searching for the microbeam's base in force-mapping mode. (b) Subsequently, the whole beam is imaged for a precise positioning of the bending measurement force-map. Imaging force-maps display the setpoint height (for a contact force of 2 μN) of the AFM cantilever. (c) Setpoint height representative force-map image used for a microbeam bending measurement with a resolution of 25 x 3 pixels. (d) Measured slope image obtained during a microbeam bending measurement exhibiting the expected color gradient. (See text for more information).

scope of linear elastic bending of a slender beam (i.e. small deflections $\nu << L, b, h$, ratios $L/h > 10$ and $b/h < 5$) only force curves at positions $L/h > 10$ from the clamped ends of the microbeam structures were used for analysis. Postprocessing of measured curves was performed with the JPK SPM Data Processing software (JPK Instruments AG, Berlin, Germany). First, the displacement data of the force curves was corrected by subtracting the AFM cantilever deflection to obtain force vs. beam deflection curves (fig. 5.4b). Then, the upper 5 % of the unloading portion of the curves was fitted with a line to obtain a value for the apparent elastic stiffness of the structure, at a particular beam position similar to the protocol for micropillar compression developed by Luczynski et al. [109]. By plotting the obtained bending stiffness vs. beam position values and fitting the data with the equation for a double clamped (dc) beam [68, 171]:

$$S_{dc} = 3E_{dc}I\frac{L^3}{x^3(L-x)^3} \tag{5.1}$$
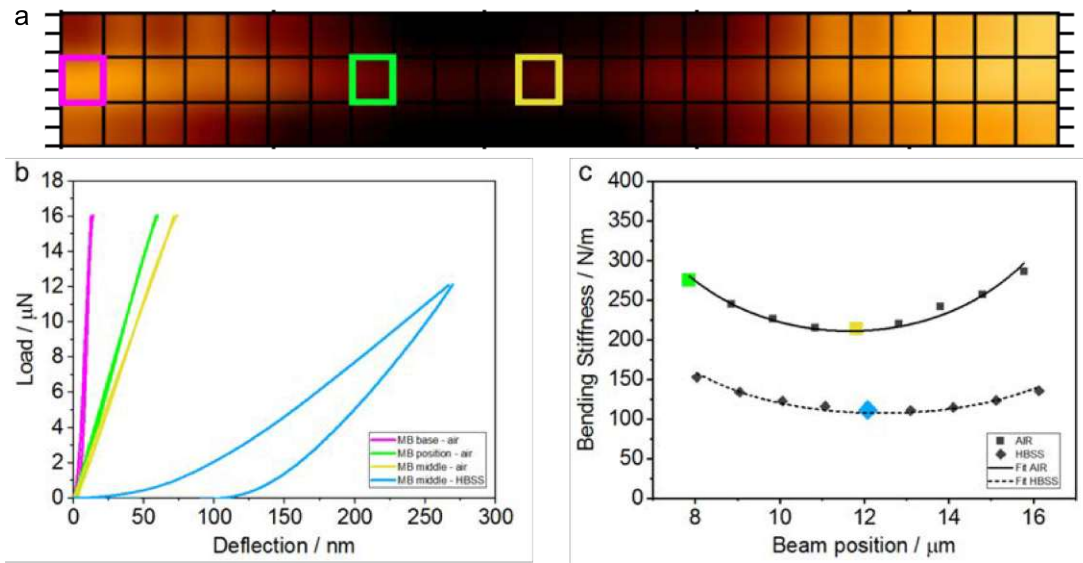
Figure 5.4: (a) Force-map with 25 x 3 pixels used for bending of microbeams with three marked pixels corresponding to bending curves in (b). (b) Representative force vs. deflection curves obtained from a single microbeam at different beam positions measured in air (magenta, green and yellow) and measured in HBSS (blue curve), corresponding to the colored pixels in the force-map from (a). (c) Bending stiffness vs. beam position data as obtained from the respective force vs. deflection curves from (b), measured both in air (upper data) and in HBSS (lower data) with the respective fitted lines used for calculation of the bending moduli. The slight offset in the position coordinates in (c) stems from the manual positioning of the pixel map in the AFM control software and lies well within the position resolution of ± 1 μm. (See text for more information).

representing the dependency of the beam stiffness on the bending position x, second moment of area $I = bh^3/12$ and beam length L, a value for the bending modulus E_{dc} of the beam structure was derived as a fit parameter (fig. 5.4c). Fitting of data was performed in Origin (Version 2017, OriginLab, Northampton, MA, USA) using the Levenberg-Marquardt algorithm.

5.3.3 Raman spectroscopy

To obtain information on fibril orientation within the microbeams, Raman spectroscopy on the samples was performed after mechanical testing, to exclude possible alteration of the mechanical properties due to laser radiation, utilizing an adapted version of a published protocol for Raman mapping of collagen fibril orientation within osteonal lamellae [164]. Raman measurements were performed using the WITec alpha 300RSA+ confocal Raman microscope (WITec GmbH, Ulm, Germany). A 633 nm HeNe laser (35 mW, laser class 3 B) with the laser power set to 20 mW was employed in combination with a 100x water immersion objective (Olympus, N.A. 1.0) resulting in a theoretical lateral resolution of approx. 260 nm. The backscattered Raman photons were collected in reflection mode. After passing an edge filter, the red shifted Stokes light is detected in the according, fiber-coupled (50 μm fiber diameter = confocal pinhole) spectrometer (UHTS 300 spectrometer optimized for excitation wavelengths in the visible, f/4, 300 mm focal length) equipped with a 300 grooves/mm blazed grating (BLZ = 500 nm) and a highly sensitive, thermoelectrically-cooled Charged-Coupled Device (CCD; Andor Newton DU970-BV, Andor Technology Ltd., Belfast, UK) detector achieving a spectral resolution of approximately 6 cm^{-1}. The linearly polarized Raman laser is fiber-coupled (single mode fiber/polarization maintaining) to the microscope with a polarization unit for manual adjustment of the polarization angle in steps of 30° or a multiple thereof.

Raman maps of human bone beams were performed in aqueous environment with the sample placed in a custom-made water bath that was fixed on a motorized piezo stage (< 2 nm positioning accuracy) mounted on top of a $x - y$ stage (< 1 μm reproducibility). For each polarization angle (-90°, -60°, -30°, 0°, 30°, 60°, 90°) a Raman map at the same measurement position was recorded resulting in 7 image scans for a single beam. Balancing overall measurement time and signal to noise ratio (SNR), an integration time of 1 s per pixel was used covering an area of (50 x 8) μm^2 with a step size of 1 μm. ControlFIVE software (WITec GmbH, Ulm, Germany) was used for spectrum acquisition and instrument control.

To focus on the spectral range of interest and reduce the number of data points, the spectra were cut selecting the spectral range from 360 cm^{-1} to 4100 cm^{-1} using ProjectFIVE software (WITec GmbH, Ulm, Germany). Further data processing was performed in Python 3.6. First, Savitzky-Golay smoothing (window size: 13; 0th order polynomial) was applied to improve the SNR of single spectra before baseline correction using Eilers's and Boehlens's asymmetric least squares smoothing algorithm ($\lambda=$ 104, p = 0.001, 10 iterations) mainly to remove fluorescence that negatively impacts the spectrum's baseline. The focus of the Raman laser was optimized before each experiment consisting of 7 image scans (one for each polarization angle). Hence, variations in Raman intensity might be encountered from scan 1 to 7. Normalization to the symmetric stretch vibration of PO_4^{3-} at 960 cm^{-1} [164] was performed for better visualization and comparison of all single spectra recorded at the same measurement spot/pixel but at different laser polarization angles. The intensity of the Amide I band around 1660 cm^{-1} changes significantly depending on the polarization angle of the Raman laser and the orientation of collagen fibrils. The area of the Amide I band was determined based on integration of the baseline-corrected spectrum between 1534 cm^{-1} and 1750 cm^{-1}. The Amide I band area normalized to 1 as a function of the polarization angle was fitted using equation (5.2) to determine the parameters a, b and c for the Raman polarization image [164]:

$$I = a(1 + b(\cos(2(\beta - c)))) \tag{5.2}$$

with a being the average Amide I band area normalized to 1 (= color-coding in the Raman polarization map), b representing the amplitude of the modulation of the Amide I band as a function of the laser polarization angle β (= arrow length in Raman polarization map), and c being the phase shift of the same fit (= arrow orientation in the Raman polarization map). Spectra below a SNR threshold of 200 were excluded from data evaluation.

5.4 Results

5.4.1 Microbeam bending

Single bone lamella microbeam structures of dimensions $L = (25.1 \pm 0.1)$ μm, $b = (3.3 \pm 0.5)$ μm and $h = (1.1 \pm 0.1)$ μm were micromachined via FIB and imaged via SEM (fig. 5.3a and b). After transfer onto the AFM, the microbeams were located by imaging in force-mapping mode. Figure 5.3 shows overlayed force-map images over an SEM image, of the microbeam base (fig. 5.3a) and of the whole microbeam (fig. 5.3b). Despite the edge-blurring due to imaging with a rounded, spherical tip, sufficient height contrast was achieved to identify the microbeam structures in AFM images.

AFM-based microbeam bending was performed via a 25 x 3 pixel force-map as shown in figure 5.4a. Bending was monitored and verified by acquiring setpoint height, i.e. beam deflection (fig. 5.3c), and measured slope (fig. 5.3d) images of the used force-map. In a setpoint height image, the achieved total deflection of the system (AFM cantilever + microbeam) at the pre-set maximum force (F_{max}) is displayed. The largest displacement is displayed as the lowest achieved position and set to 0 (black pixels in the force-map) and the smallest displacement is displayed as the highest achieved position in the force-map relative to the lowest point (613 nm in fig. 5.3c) and assigned with the brightest color. In the measured slope image (fig. 5.3d), the apparent stiffness of the AFM cantilever + microbeam system, calculated from the slope of the force curve (force vs. displacement of the AFM z-piezo), is displayed, where the lowest (89 N/m) and highest (152 N/m in fig. 5.3d) measured apparent stiffness values are represented by the false colors black and bright yellow, respectively. Both the bending setpoint height and measured slope images show the expected gradient of the color plot; considering the longitudinal direction of the microbeam, the smallest deflection and highest apparent stiffness, occurs at both the supports of the beam. Apparent stiffness then decreases with the 3rd power (see eq.

(5.1)) along the length of the beam towards the middle ($= L/2$). With regard to the transverse direction of the microbeam, a higher apparent stiffness is measured at the symmetry axis, i.e. middle of the width of the beam ($= b/2$) position, where the beam experiences pure bending, compared to an off-axis bending, where torsional effects increase the deflection in addition to deflection caused by bending, leading to lower measured apparent stiffnesses on each side of the middle of the beam.

Bone microbeams were generally bent in a deflection regime that largely avoids damage (see also discussion), first in air, and, subsequently, submerged in HBSS after 2 h of rehydration time. The displacement data of the force curves were corrected for the AFM cantilever deflection to obtain force vs. microbeam deflection curves. Four microbeam bending curves are shown in figure 5.4b. Three curves (magenta, green and yellow) represent bending curves in air at three different positions along the length of the microbeam, corresponding to the three marked pixels of respective color in the force-map in fig. 5.4a. The blue curve represents a bending curve in HBSS at the middle position of the same microbeam after 2 h rehydration time. Bending in HBSS was performed with a lower $F_{max} = 12$ µN (compared to bending in air, $F_{max} = 16$ µN), since larger deflections were experienced in the rehydrated state, to avoid failure of the microbeam. Both loading and unloading curves were recorded during bending measurements. The upper 5 % of the unloading portion of the bending curves was fitted with a straight line to obtain a value for bending stiffness. Only curves on the longitudinal centerline of the microbeams were used for analysis (see section 5.3.2). The bending stiffness values were plotted against beam position (fig. 5.4c) and data was fitted with equation (5.1) to obtain a value for the apparent bending modulus (fit parameter). The green, yellow and blue data points correspond to the respective bending curves in fig. 5.4b. The bending modulus of microbeams was found to decrease significantly upon rehydration. Moreover, the mechanical response also changed qualitatively in the rehydrated state. The bending curves in air display an almost perfect linear, elastic behavior, characterized by linear loading and unloading curves with same apparent stiffnesses, whereas the bending curves in HBSS display

a higher unloading stiffness compared to the loading curve, which is suggestive of dissipative mechanisms during loading of the structure.

Microbeam bending in air and HBSS was performed on all bone microbeams from all donors and the corresponding obtained bending moduli were plotted as mean $\pm$ std. dev. of $3-5$ bending measurements (see figure B.1 in appendix B) against donor age in fig. 5.5. For all microbeams there is a substantial reduction of bending modulus upon rehydration of up to 5 times for a single microbeam (sample 7). Samples without a corresponding value in HBSS (blue data) failed either during bending in air or upon rehydration. Microbeams, e.g. sample 3, where both bending modulus values in air and HBSS were higher than the plotted scale (> 55 GPa), were regarded as outliers and excluded from further analysis. In a previous study it was found that errors arising from uncertainties in sample geometry and dimensions from the preparation process can be large and as high as 53 %, as an upper boundary [127]. Three out of four longitudinal edges of the microbeam can be inspected and measured during the FIB milling and SEM imaging process, respectively. The fourth edge, that is oriented towards the bulk material cannot be directly imaged, so errors in the length measurements of the beam, as well as deviations in the cross-sectional geometry (shape) and thus the calculated second moment of area could occur. Such sample preparation artifacts can however be minimized by slow and precise milling with low ion currents. Furthermore, despite careful milling, remnants of bone material could be present under the microbeam rendering it more stiff. For the chosen donor number and age group, no trend or correlation of bending modulus with respect to age was observed.

However, differences in the mechanical response were observed compared to bending in air after rehydration (figs. 5.4 and 5.6). Whereas bending in air shows almost linear elastic apparent behavior, cortical bone microbeams exhibit viscoelastic behavior in rehydrated state. The energy dissipated by the system, W_{dis}, is represented by the area enclosed between the loading and unloading curves ($W_{dis} = W_{loading} - W_{unloading}$, light and dark blue areas in fig. 5.6). Viscoelastic behavior is further evident from
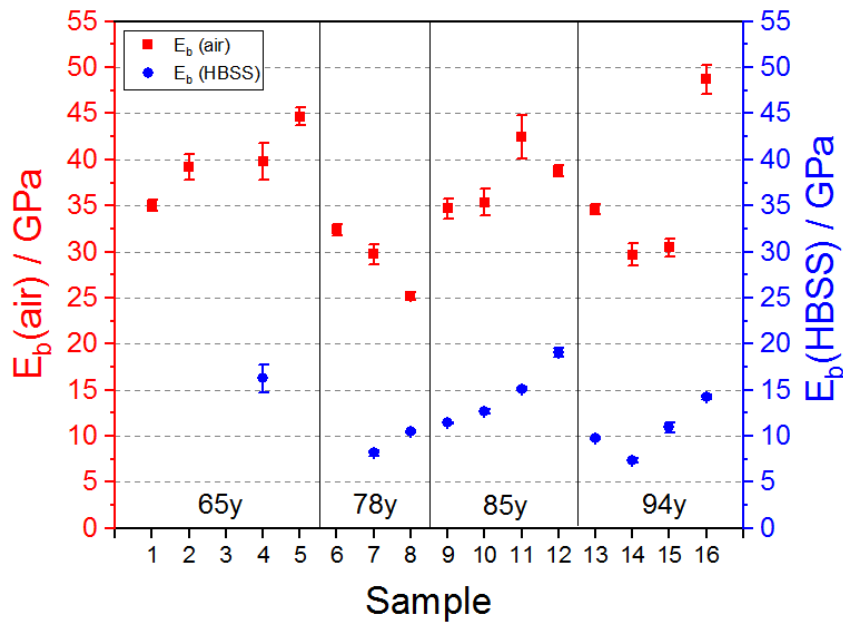
Figure 5.5: Bending modulus values of all microbeams and donors as obtained from the microbeam bending measurements conducted in air (red data) and in HBSS (blue data) against donor age (numerical values can be found in table B.2 in appendix B). Missing data indicate outliers (sample 3) and microbeams that failed during bending measurements in air or upon rehydration (samples 1, 2, 5 and 6).

displacement rate dependency of the bending behavior with higher rates resulting in an increase in bending stiffness.

The relative dissipated energy, calculated as the area between the loading and unloading curves divided by the total work done (W_{dis}/W_{tot}, where $W_{tot} = W_{loading}$) during microbeam bending measurements in HBSS for all microbeams and donors is plotted in figure 5.7a. From these data, an average for each donor in HBBS and air is derived and plotted against donor age, fig. 5.7b. As can be seen from figure 5.7b energy dissipation is highest in the youngest donor, whereas samples from other donors of higher age only reach about half the value.
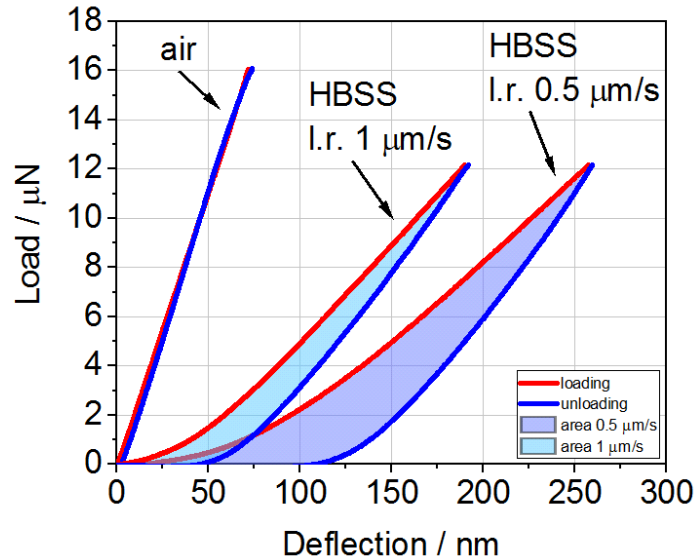
Figure 5.6: Force vs. deflection curves at the middle of a microbeam measured in air and in HBSS with two different loading rates (l.r.) of 1 μm/s and with 0.5 μm/s. The shaded blue areas represent the dissipated energy during loading of the structure and indicate a viscoelastic behavior.
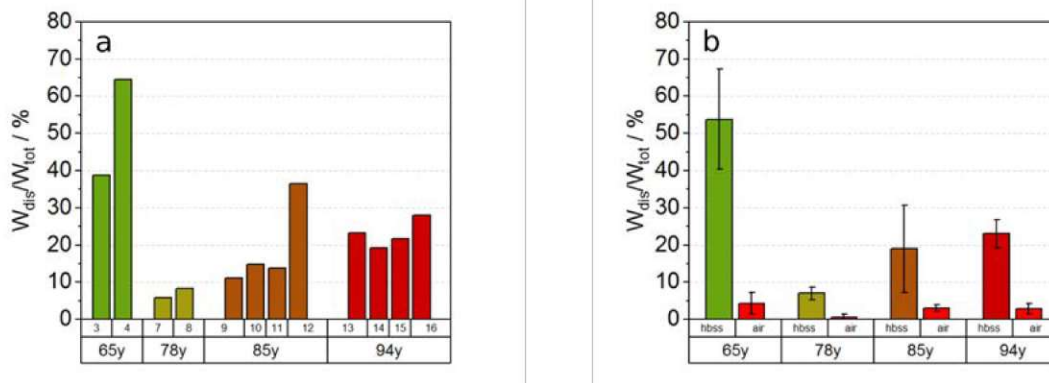
Figure 5.7: (a, b) Relative dissipated energy, calculated as the area under the loading curve minus the area under the unloading curve, i.e. $W_{dis} = W_{loading} - W_{unloading}$ over total work, W_{dis}/W_{tot}, plotted for all samples of all donors. (b) Averaged donor W_{dis}/W_{tot} in air and HBSS for all donors. Numerical values can be found in table B.3 in appendix B.

5.4.2 Raman spectroscopy

After mechanical testing with AFM, the macroscopic bone samples containing the microbeams were transferred onto a Raman microspectroscopy setup, where Raman spectra were collected from the mi- crobeams in an aqueous environment to minimize damage. Linearly polarized incident light in seven different polarization directions was used to obtain Raman spectra on the bone microbeams in a spatially resolved fashion. Raw spectra smoothing, baseline correction and normalization, as well as fit of the Amide I band area vs. polarization angle of a representative pixel, i.e. microbeam position are shown in figure 5.8.

Sufficient Raman scattering signal intensities could be collected from the available micron-sized interaction volume across the microbeams and the bulk material at their supports. From the Raman spectra at multiple polarization angles and multiple microbeam positions, the polarization-dependent Amide I band (fig. 5.9a) and its scaled band area plotted against polarization angle (fig. 5.9b) could be fitted with the model (eq. (5.2)) to ultimately reconstruct collagen fibril orientation maps for a single microbeam, fig. 5.9c, overlayed with a light microscopy image. Such pixel maps could provide overviews of the orientation of the collagen molecules, which were largely oriented along the microbeams long axis, albeit not perfectly and with some variation. The success rate of Raman measurements was low. Out of the 16 mechanically tested microbeams, only four could be successfully measured via Raman spectroscopy. This was due to experimental limitations in precision of repositioning, i.e. obtaining Raman spectra from the same individual interaction volumes (represented by pixels in the Raman map, fig. 5.9c) of the microbeams after repositioning for every polarization setting. The Raman maps display inhomogeneity of fibril orientation, even at the length scale of single lamellae, which we illustrate here in figure 5.9c, obtained from one of the measurements. The surrounding bulk at the supports of the microbeam (right side of microbeam in fig. 5.9c) suggests an overall orientation of fibrils, which extends into the microbeam to some extent. Furthermore, variations in homogeneity at this length scale can occur as much as total transitions from an anisotropic to
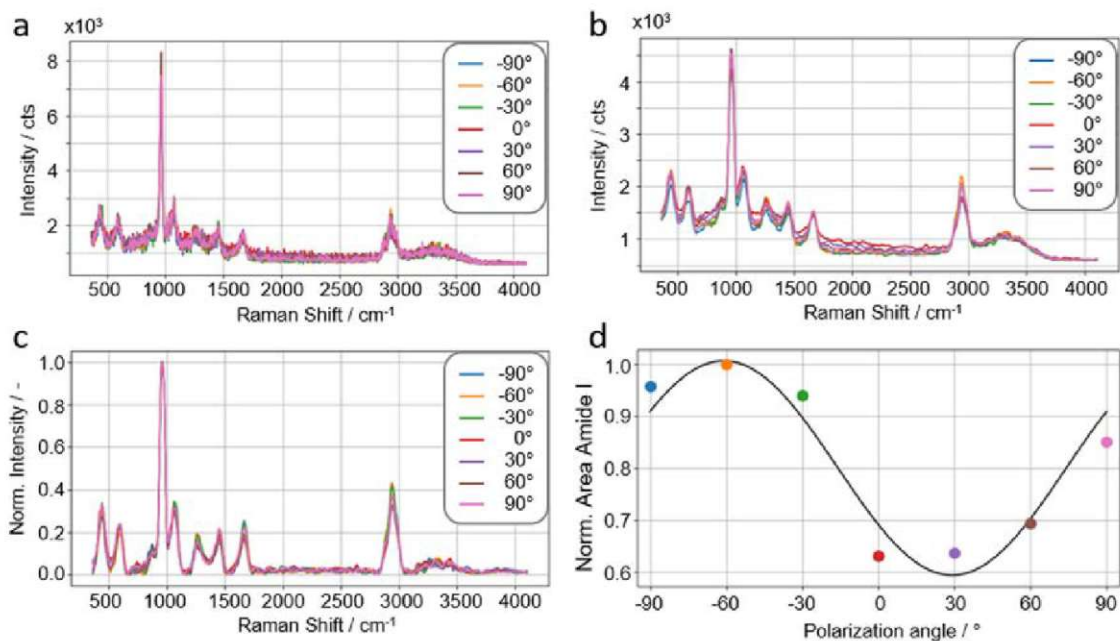
Figure 5.8: (a) Unprocessed Raman spectra representing one pixel recorded at different polarization angles prior to (b) Savitzky-Golay smoothing (0th order polynomial, window size: 13) and (c) baseline correction (Eilers's and Boelens's asymmetric least squares smoothing algorithm [39] with $\lambda = 104$, p = 0.001, 10 iterations). Normalization to the symmetric stretch vibration of PO_4^{3-} at 960 cm^{-1} was performed for better comparison. (d) The Amide I band area, i.e. integration of the baseline corrected spectrum between 1534 cm^{-1} and 1750 cm^{-1}, was scaled between 0 and 1 and plotted as a function of the polarization angle indicating a modulation of the Amide I band intensity based on the collagen fibril orientation.

isotropic Raman response (left side of microbeam in fig. 5.9c), i.e. in-plane to out-of-plane fibrils, respectively.
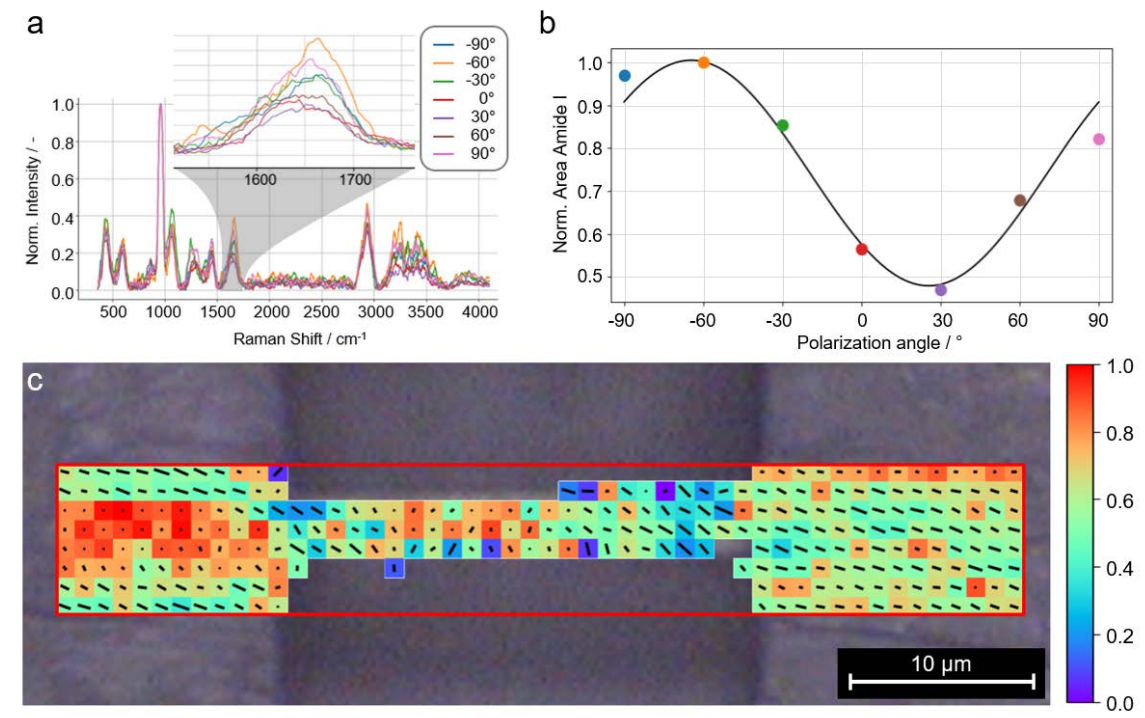
Figure 5.9: (a) Processed Raman spectra corresponding to one pixel of the pixel map in panel c with an enlargement of the Amide I band area (inset in panel a). (b) Modulation of the integrated Amide I band as a function of the laser polarization angle. (c) Raman polarization map representing the scaled mean of the Amide I band area for each pixel by color-coding. The orientation of collagen fibrils is indicated by the angle of the black line in each pixel. A point indicates isotropic Raman response, whereas the presence of a black line shows (arrow) distinct fibril orientation in a specific direction (i.e. anisotropic Raman response).

5.5 Discussion

5.5.1 Micro-mechanical testing

Direct mechanical testing of bone tissue at the microscale is an emerging field, with only few studies that performed bending on isolated cortical bone microbeams [82, 84]. In these studies, bending was performed in situ within the vacuum chamber of a FIB device in a dehydrated state, with a flattened AFM tip. Moreover, bone samples in these studies were treated with ethanol, which was shown to irreversibly alter

the organic matrix and the mechanical properties of bone [61]. To prevent possible alterations of bone material properties due to chemical treatment, such steps were excluded during our sample preparation, nevertheless we cannot completely exclude alteration of bone material properties due to the sample preparation protocol used. In this study, we employed AFM with a high stiffness AFM probe (200 N/m nom.) furnished with a glass microsphere ($\varnothing$ = 5 μm) both in air and fully submerged in buffer solution to test chemically untreated bone microbeams in dehydrated and rehydrated state to investigate the role of hydration on bone tissue micromechanics. For such experiments, an AFM setup is well suited. It offers a tunable system stiffness (k = 0.01 N/m – 200 N/m) and sensitivity based on AFM probe selection, to first image the sample with negligible force prior to conducting actual mechanical tests, ease of operation both in dry and fluid environment and changeover without the need for sample removal. Using our AFM setup we imaged and mechanically characterized human cortical bone samples essentially consisting of individual cortical bone lamella, both in dehydrated and rehydrated state. The microbeams were generally tested in a way to avoid damage and failure, such that measurements could be performed on the very same specimens in both conditions in a reproducible manner (figs. 5.2 and 5.3). Avoiding damage and providing reproducibility of bending measurements on 75 positions on a microbeam without per- manent damage is a requirement for obtaining a single pixel map. This was achieved by bending with small deflections, remaining in a non-damaging, and in the case of our microbeams, linear region (dried state) only, which was determined in preliminary experiments (data not shown). Elastic deformation is defined as fully reversible, without residual permanent deformation upon unloading, which in our measurements was verified by recording both loading and unloading force vs. deflection curves (fig. 5.6) in dry state. Deviation from elastic behaviour and loss of load bearing capacitiy would be revealed in measured curves. Moreover, bending force-maps were repeated up to 5 times and summarized as a standard deviation of data (fig. 5.5 and fig. B.1). Nevertheless, few of the microbeams failed after measurement in air or during rehydration. These microbeams

(3 out of 16), were likely already damaged or contained a defect. Measured data was validated and calibrated by bending of silicon microbeams (see Appendix B). Values of bending moduli in the range of 25 GPa – 50 GPa in dehydrated condition were obtained, comparable to nanoindentation studies on cortical bone [102, 181], and were found to substantially reduce after rehydration. Furthermore, the mechanical behavior of microbeams changed from almost perfectly linear elastic to viscoelastic upon rehydration.

The bending modulus E_b obtained from bending at multiple positions along the length of microbeams reduced up to 5 times after rehydration of 2 h (cf. sample 7 in fig. 5.4). The elastic (Young's) modulus is defined as the ratio of induced stress within a body to its relative deformation, i.e. strain when acted upon with a mechanical force and represents a constant mechanical parameter for a given material when loaded in a reversible, elastic manner. Since this property changes after rehydration, as observed in our experiments, it appears that there is a transition between intrinsic material deformation mechanisms dependent on hydration state of the bone material and mechanically speaking, a transformation into a different material. Water is the third largest component, comprising approx. 20 % of bone's volume and plays a significant role in bone mechanics, as discussed in a comprehensive and detailed review by [56]. Furthermore, water is also present at every hierarchical structural level of bone tissue from the free unbound water in pores, bound water between and within lamellar fiber arrays, mineralized collagen fibrils and fibril-mineral interface down to the structural water incorporated within the structure of the collagen protein back bone as well as within the mineral crystal lattice ([56] and references therein). In our study, samples were kept hydrated in HBSS between sample preparation steps and no chemical or thermal dehydration steps were applied. The dehydration of the samples was imposed solely by high vacuum exposure during FIB milling (approx. 8 h) and storage in air ($<$ 48 h) prior to testing. Jimenez-Palomar et al. reported from weight measurements, that only free water was removed from the bone material when vacuum exposure time was no longer than 2 h [82]. At a length scale of several micrometers, where

a small microscopic volume is isolated and comprised of a single bone lamella, a prolonged high vacuum exposure may lead to further removal of the more loosely bound water of the underlying structures at this length scale i.e. the bundles of mineralized collagen fibrils [136]. In contrast, the structural water more tightly bound to the collagen protein back bone and within the mineral crystal lattice requires a much higher energy to be removed, which is only achieved at higher temperatures > 120 °C [136]. Since no heating steps were applied in our protocol, we assume that water at the nanometer length scale was not removed from the samples. At the level of mineralized collagen fibrils, however, as the material dehydrates, the water between the collagen proteins and mineral crystals/molecules is removed leading to a decrease in distance between them [146]. Consequently, this tighter packing upon dehydration leads to an increase in stiffness [101, 201], which can be supported by the load transfer mechanism from the organic collagen phase to the mineral phase resulting in an overall stiffer composite material [60]. Such mechanisms might in turn lead to an increased apparent modulus measured in the dehydrated state as observed in our experiments.

Furthermore, dehydration beyond removal of the loose pore water also affects the viscoelastic behavior of bone tissue at the lamellar level. In our experiments the same bone microbeams were bent in a regime of small deflections to avoid damage at multiple positions both dehydrated in air and rehydrated in HBSS (fig. B.1). The complete bending cycles consisting of loading and unloading force vs. deflection curves were recorded during measurements (fig. 5.6). For linear elastic deformation both loading and unloading curves exhibit linear and reversible behavior, i.e. the slopes representing the stiffness of the structure of both curves are essentially identical and the curves overlap, as observed in our experiments conducted in air. Should there be additional, inelastic deformation superimposed to a purely elastic deformation, this would be revealed by different load bearing capability reflected in different slopes of the loading and unloading curves, as observed in our measurements conducted in HBSS. Since elastic energy is defined as the fully retrievable energy upon

unloading, the true elastic stiffness should be extracted from the unloading portion of the curve [109]. Supporting of the transition from elastic to viscoelastic behavior upon rehydration is also the rate dependency of the bending curves measured in HBSS (figs. 5.5 and 5.6). This is in good agreement with findings from creep measurements ([136] and refs. therein) and dynamic indentation [141]. We conclude that hydration state plays a significant role even at the hierarchical level of single lamella in bone tissue. At this level, and certainly within the samples tested in this study, the only true porosities containing loosely or unbound water are the canaliculi. Therefore, we argue that the inelastic behavior observed when bending samples in rehydrated state stems from draining of fluid from canaliculi and from deformation mechanisms in the mineral-mineral interface between crystals on neighboring collagen fibrils or neighboring crystals on the same collagen fibril. Proposed models of bone ultrastructure as well as immunohistochemical studies postulate that this interface is densely populated with non-collagenous proteins (NCPs) such as ostepontin, bone sialoprotein and osteocalcin amongst others [60, 121, 181, 185]. Many NCPs are highly negatively charged, i.e. attract water upon bone hydration and have been postulated to enable sliding between hydroxyapatite mineral crystals and mineralized collagen fibrils. Therefore, our findings demonstrate that (micro-)mechanical experiments on bone need to be performed in fully (re)hydrated state to obtain physiologically relevant data, as the material properties of bone are clearly affected by hydration state and only in a fully hydrated state the viscoelastic properties of the material are present in their full form.

No correlation of bending modulus with respect to age was observed for the donor group both in dehydrated or rehydrated condition. However, increased apparent stiffnesses during unloading were observed in all rehydrated measurements. The mechanical work imposed on and released by the system can be calculated as the area under the force vs. displacement curve during loading and unloading, respectively. In the dehydrated elastic case, almost all of the work done, i.e. 90 % – 100 %, is recovered upon unloading. In contrast, significant energy dissipation on the order

of 10 % – 70 % of the work is present in rehydrated state within the same samples (fig. 5.7). Here, the data further suggest a potential trend of lower dissipated energy with higher donor age, but only for the rehydrated case. This is in agreement with lower amount of bound water found in aged bone as measured by nuclear magnetic resonance (NMR) in correlation with three point bending testing [134]. Furthermore, viscoelastic properties were related to water content versus changes of the collagen protein [207]. Additionally, the bound water in the tissue, measured by magnetic resonance techniques, was found to significantly decrease with donor age > 70 y [56], which is the age region covered in our experiments. This decreased ability of the tissue to store water with increasing age may lead to a progressive change from viscoelastic to more elastic and stiffer behavior as well as a decrease in the ability to dissipate energy during loading at the material level of bone tissue.

5.5.2 Fibril orientation

An important parameter related to the anisotropy of bone and in our case to the actual stiffness of the microbeams machined from cortical bone lamellae is fibril orientation within the lamella. The microbeams in our study were produced on the longitudinal cut plane of the small bone piece, and a ROI of parallel ordered lamellae was chosen for the production of the microbeam structures. With this procedure, the long axis of the microbeams was aimed to be oriented parallel to the longitudinal direction of the femur, with the assumption of main fibril orientation to be predominantly parallel to the long axes of microbeams. To verify fibril orientation several methods have been proposed in literature, which are of destructive type, such as FIB sectioning along a symmetry axis [168, 169], transmission electron microscopy [153, 169], AFM imaging after EDTA treatment [92], and of non-destructive type, like backscattered electron microscopy performed under high vacuum within the chamber of an SEM [84], and Raman microspectroscopy imaging [164]. In order not to affect the tissue and its mechanical properties as well as performing measurements in hydrated state, investigations of the fibril orientation in this study were attempted

after mechanical testing within the AFM via Raman microspectroscopy imaging. For this purpose, a Raman setup was used allowing for collection of spectra in aqueous environment, which provides both hydration and cooling of the sample and minimizes thermal damage to the microbeams. The method of reconstruction of fibril orientation maps from Raman spectra [164] was then used to obtain orientation pixel maps of the isolated micron-sized volume of the microbeams (fig. 5.9). Sufficient Raman signal could be obtained from the microbeam volume to observe that heterogeneities are still present within the tissue, even at this small length-scale. Imaging of the surrounding bulk material at the microbeams supports, where the chosen lamella extends from, did support the assumption of the predominant fibril orientation being parallel to the microbeam's long axis. Whereas, Schrof et al. developed the 3D Raman mapping protocol on an osteon, which is a larger hierarchical structure of cortical bone, we here show that this technique may be extended down to measure even samples at the single micrometer length-scale for information of collagen fibril orientation within individual bone lamellae in an aqueous environment, albeit with experimental limitations. Determination of fibril orientation at the lower microscale in a more physiological, (re)hydrated state is a challenging task. Extending the capability of the technique towards the spatial resolution limit of an optical Raman setup of < 1 μm, both in lateral and depth directions, and the precision of targeting the same individual interaction volumes of the microbeam after repositioning of polarization directions proved to be an experimental impediment for extracting fibril orientation of all microbeams. Still, the obtained Raman maps suggest substantial inhomogeneities in fibril orientation, even at the length scale of single lamellae, which in turn is expected to have direct implications on their mechanical response. For these reasons of limited availability of information on fibril orientation within, and limited number of microbeams, a quantitative correlation of microbeam mechanics and their fibrillar layout could not be performed. Fibril orientation remains an under-investigated property of bone mechanics and our data indicate a larger inhomogeneity in bone tissue at the lamellar length scale than assumed so far. Further

development and improvement of Raman microspectroscopy is a promising approach for determination of fibril orientation at the sub-micron level, which in turn might explain the variability in measured mechanical parameters of small structures of bone tissue.

5.5.3 Limitations

Performing mechanical testing of mineralized biological tissue at the microscale is an experimentally challenging task with corresponding limitations that need to be acknowledged. Bone tissue in organisms is in a physiological, hydrated state. The samples in our study undergo extensive treatment prior to mechanical testing: coating with a conductive metal layer, dehydration by prolonged exposure to high vacuum, SEM, FIB-milling and rehydration. Although a limited exposure time of 2 h to high vacuum during FIB milling was shown to have a negligible effect on the mechanics of chemically treated bone material [82], a prolonged exposure time to high vacuum might have a more substantial effect on water extraction from chemically untreated tissue beyond free pore water and, in turn, alter tissue mechanics. Moreover, whether a rehydrated state fully reflects the original hydrated state and whether a repeated process of dehydration and rehydration is reversible regarding tissue mechanics, remains to be investigated.

Precision of dimensions, positioning and sample geometry, as well as attachment to the bulk material have a substantial effect on determination of mechanical parameters from bending experiments at the microscale. In our study, the positioning of the AFM cantilever on the beam could not be visually verified like in situ, within SEM, picoindeters or in situ AFM and had to indirectly be verified from force-map imaging and gradients in bending force-maps (fig. 5.3).

Furthermore, orientation of fibrils within microbeams may play a significant role on their mechanics [84]. While we attempted to determine fibril orientation via Raman microspectroscopy [164], only 4 microbeams could be measured in our experiments

due to experimental difficulties. The missing information on 12 further samples remains a limitation. We cannot asses how much of the variation in sample properties is due to variation in fbril orientation. In this context a full correlation of mechanics with fibril orientation of single bone lamellae is also not feasible. Additionally, although large porosities in the tissue i.e. lacunae and Haversian canals can be avoided at the microscale, the role of remaining canalicular porosity on lamellar mechanics still needs to be investigated.

Finally, a more representative micromechanical characterization would be given by testing of larger number of samples, from different microregions as bone is a highly inhomogeneous material. However, preparation of samples via FIB-milling is a time intense and expensive technique with approx. 4 h of preparation time per beam, which limits the throughput and number of samples that can be prepared and tested.

As our results suggest a trend of change in viscoelastic properties related to age, bone material from more donors spanning a larger age group should be used in future studies to further elucidate age effects on micromechanical properties of cortical bone.

5.6 Conclusion

The influence of hydration state and age on the mechanics of single cortical bone lamella from four human femurs was investigated by bending of FIB-milled microbeams via modified stiff AFM probe. Bending modulus values reduced up to 5 times for individual microbeams when going from dehydrated to rehydrated state. Additionally, mechanical behavior transitioned from almost linear elastic to viscoelastic between dry and rehydrated state. No trend of change in the unloading stiffness with respect to age was observed but a possible trend of lower dissipated energy in rehydrated state. We conclude that also without any significant porosities water plays an important role in bone mechanics enabling sliding at interfaces at the length scale of individual mineralized collagen fibrils.

Chapter 6

Micropillar compression of healthy and osteoporotic human cortical bone from the femoral neck

6.1 Related publication and declaration of contributions

Results of the presented chapter have been prepared into a manuscript, entitled "Micropillar compression of healthy and osteoporotic human cortical bone from the femoral neck", co-authored by Olaf Lahayne, Martin Frank, Krzysztof W. Luczynski, Andreas Steiger-Thirsfeld, Johannes Bernardi, Christian Hellmich, Philipp J. Thurner, which is intended to be submitted for publication in a relevant biomechanics journal.

Author contributions: The first author and author of the current thesis, Vedran Nedelkovski, wrote and edited the manuscript, performed study design, sample preparation via FIB milling, SEM imaging and mechanical testing of the bone micropillars, data processing and data interpretation. Olaf Lahayne provided resources,

training and support with mechanical testing with the nanoindenter and edited the manuscript. Martin Frank assisted with data processing and data interpretation and edited the manuscript. Krzysztof W. Luczynski provided training and protocol regarding sample preparation via FIB milling and mechanical testing of the bone micropillars. Andreas Steiger-Thirsfeld provided training and supervision of FIB milling. Johannes Bernardi provided resources and edited the manuscript. Christian Hellmich provided resources, support with data interpretation and edited the manuscript. Philipp J. Thurner provided resources, supervision of the work of Vedran Nedelkovski, suported the study design, data analysis and data interpretation, reviewed and edited the manuscript.

6.2   Introduction

The effects of osteoporosis on the mechanics of cortical bone tissue are a matter of ongoing debate. While it is accepted that cortical bone deteriorates with age in terms of fracture toughness, the underlying mechanisms are not completely clear. It is thought that such processes may be amplified in osteoporosis, which mainly manifests in a decrease in bone mass and bone mineral density (BMD). However, BMD alone is often insufficient for a complete characterization of the onset and development of the pathology and, clinically more relevant, for estimation of fracture risk factors and decision on treatment. This has motivated research going beyond macroscopic structural changes i.e. investigating compositional and mechanical properties of the extracellular matrix (ECM), i.e. the material that makes up bone tissue, at the microscopic level. In particular, the question arises, whether there are detectable changes in the mechanical material properties of bone material (alongside substantial loss of bone mass)? Unraveling the mechanical behavior of bone tissue is challenging due to its complex hierarchical structure from the nano- to the macroscale. At a given length-scale, e.g. single bone lamella at the microscale, the apparent mechanical response of the structure (the bone lamella) is a result of the mechanical properties

of its constituents. Here the mineralized collagen fibrils, their chemical and physical state (crosslinks, hydration, composition), the way they interact with each other through crosslinks, electrostatic interactions, Ca-bridges, water molecules and non-collagenous proteins (NCPs) [66]. All of the above may principally undergo alteration in the course of a pathology potentially leading to changed mechanical properties at microscopic as well as higher organizational levels. The appeal of the lamella, is that it is devoid of all pores, except canaliculi and efficiently captures the smallest building block of bone, i.e. the mineralized collagen fibril.

Recent advancements in experimental mechanical characterization at the single to several micrometer length-scale using focused ion beam milling (FIB) for isolation of micron-sized volumes of (bone) material have created the possibility to conduct mechanical tests at the level of single bone lamellae [24, 82–84, 109, 168, 169]. These techniques are advantageous over conventional nanoindentation, as a more homogeneous mechanical stress state is induced within a specimen (compared to a complex multiaxial stress state beneath an indent) [109]. Hence, they give direct access to stress and strain states, as well as to corresponding mechanical properties, such as elasticity and strength [109]. In the framework of conventional biomechanics textbooks [34], the term elasticity is used for the slope of a linear portion of the stress-strain curve in the loading regime of a mechanical test. This is consistent with the traditional mechanics of metals. However, the term "elasticity" has undergone significant changes over time [147]. A particularly comprehensive and fundamental notion of the term "elasticity" has been established in the framework of rational mechanics and thermodynamics [27, 31], where it relates to the internal energy, which can be back-transformed into efficient mechanical work (and is not dissipated into heat). Such an elastic back-transformation occurs during unloading, and a difference between loading and unloading trajectories clearly indicates the occurrence of dissipative processes. To acknowledge the presence of dissipative effects, we here resort to the terms "loading modulus" and "unloading modulus", in order to avoid terminological ambiguity. With the unloading modulus exceeding the loading modulus, the

linear portion in the loading portion of the stress-strain curve refers to elasto-plastic or elasto-visco-plastic deformations, and not to elasticity in the rigorous thermodynamics sense [108, 109]. Moreover, and along a similar reasoning, any offset from this linear portion does not indicate the onset of yielding (the material may be yielding already), but merely a change or transition in the elastoplastic hardening behavior. To avoid corresponding sources of confusion as well, we will refer to transition strain and transition stress throughout the remainder of this study. Sample availability and preparation at smaller length-scales also become a challenge. However, testing of bone as a hierarchically structured, porous material at the level of single lamella enables mechanical characterization and investigation at the material level of bone tissue by targeted, specific choice of a microscopic region of interest. At the same time large porosities like Haversian canals and lacunae can be avoided, which can substantially influence mechanical response in nanoindentation, if located below an indent, and of larger, macroscopic samples. Thus, "true" material properties can be decoupled from structural effects such as porosity by testing at lower length-scales.

Measuring mechanical parameters requires samples with a defined shape and geometry, which in the case of bone material, unlike usual engineering materials, are not readily available or can be specifically designed and produced. Moreover, bone is a heterogeneous biological material with a large intra-organ and intra-donor variability, so, e.g. measurements performed at the tibia cannot be directly transferred to the proximal femur [208] and ideally, regions of interest for testing and discovering local pathology related changes of the tissue are the sites where fracture occurs. The most common fractures suffered due to osteoporosis are the vertebral bodies, forearm, humerus and the femoral neck. Whereas extracting bone tissue samples from patients suffering fractures in the spine and arm is not directly feasible, many of the patients suffering from a femoral neck fracture need to undergo a hip replacement surgery, where the femur is dissected along the intertrochanteric line and the proximal femur including the femoral neck discarded. Collecting this tissue from osteoporotic patients during surgery provides invaluable material for research from a relevant fracture site.

Available literature on the subject of changes of mechanical properties of bone due to osteoporosis at the microscale is unclear and offers contradictory results and interpretations [83]. Moreover, different techniques (mechanical, imaging, spectroscopic), tissue type and organ (trabecular/cortical, tibial/femoral/vertebral), donor type (animal, human) as well as age make systematic comparison difficult. Mechanical properties like elastic modulus (loading modulus according to the terminology adopted in the present paper) have been shown to: (i) not change in bone from ovariectomized rats (OVH), an animal model for osteoporosis [59], and osteoporotic female human femurs [46], (ii) to reduce in OVH rats [113] and (iii) to increase in senescence accelerated mice (SAMP6), an animal model for senile osteoporosis [172], but decrease in strength due to decreasing mineral content. Such interpretations are directly related to the details regarding the mechanical testing technique, sample size and geometry and definition and analysis of mechanical parameters including underlying assumptions.

The aim of this study was to perform micromechanical characterization of human osteoporotic bone tissue and compare it to tissue from age-matched donors (control). We hypothesized measurable and significant changes of some or all of the extracted mechanical parameters (namely, loading modulus, unloading modulus, transition strain, transition stress, strength etc.) between the two groups. We employed micropillar compression of micron-sized bone micropillars comprised of a single cortical bone lamella which offers a direct analysis and a straight-forward interpretation of mechanical data compared to nanoindentation [109, 168]. For our experiments we used bone tissue from the cortical shell of the femoral neck of both female and male human donors, to probe differences at a relevant fracture site, which, to the best of our knowledge, has not been carried out yet.

6.3 Materials and Methods

6.3.1 FIB sample preparation

Human femoral neck samples (fig. 6.1a, b) were collected from osteoporotic and cadaveric donors [78]. The osteoporotic samples were obtained from resected proximal femora from patients undergoing hip arthroplasty due to low-trauma fractures at University Hospital Southampton NHS Foundation Trust (UHS). The cadaveric samples were provided by Innoved Institute LLC (Besenville, IL, USA) and IIAM (International Institute for the Advancement of Medicine, Edison, NJ, USA) from frozen unembalmed proximal femora removed from cadaveric donors with no known history of fracture or bone disease. Bone samples from 9 female and 6 male donors were used in this study. The female group consisted of 5 osteoporotic and 4 cadaveric donors with an age rage (57 - 86) years and the male group consisted of 3 osteoporotic and 3 cadaveric donors with age rage (54 - 80) years. 4 micropillars per donor, i.e. 60 micropillars in total were prepared out of which 43 were used for analysis.

Macroscopic cortical bone sections were cut longitudinally from the infero-medial (IM) quadrant of the cortical shell of the femoral neck with approximate dimensions of (10.5 x 10 x 0.5) mm^3, (length x height x thickness), using a low speed saw (Isomet LS, Buehler, Lake Bluff, Illinois, USA), fig. 6.1b. Each bone section was mounted onto a scanning electron microscopy (SEM) stub with silver adhesive (Plano GmbH, Wetzlar, Germany) and subsequently coated by a 10 nm layer of AuPd (60 : 40) to enable electron- and ion microscopy. A mm-sized piece of a commercially available (100) silicon wafer was glued next to the bone sample on the SEM stub providing a stiffer substrate for immobilization and compression of the micropillars [109].

Focused ion beam (FIB) milling of micropillar structures was performed in a dual beam system (Quanta 200 3D DualBeam, FEI, Hillsboro, Oregon, USA), incorporating both SEM and FIB within the same vacuum chamber, according to a protocol by [123] for production of prismatic, non-tapered micropillars of rectangular cross
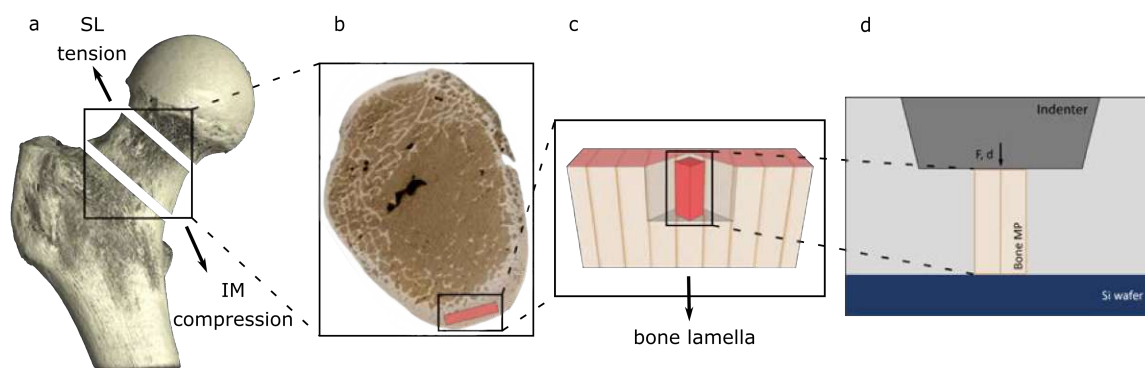
Figure 6.1: Schematic representation of sample preparation and testing. (a) Femoral neck samples are collected from resected proximal femora, where the infero-medial (IM) and supero-lateral (SL) portions are predominantly loaded in compression and tension, respectively. (b) Macroscopic cortical bone sections, represented as a red top area, are obtained from the IM portion of the femoral neck sections. (c) A prismatic, non-tapered, micron-sized beam of rectangular cross-section and comprised of a single bone lamella is prepared by FIB milling. (d) Two micropillars (MP) are sequentially cut from the microbeam and transferred onto a Si wafer and compressed with a flat punch tip in a nanoindenter. (Figures not to scale. For more information refer to the text)

section. FIB milling was performed at 30 keV using Ga^+ ion currents ranging from 20 nA (coarse) to 0.5 nA (fine) at incident angles 0° and $\pm$ 45° in a lamellar region to initially isolate a beam structure (approx. 20 µm in length) with a rectangular cross section, comprising of a single bone lamella, still attached to the bone bulk material, fig. 6.1c. Subsequently, an in-built nano-manipulator needle (Kleindiek Nanotechnik GmbH, Reutingen, Germany) and ion-beam-induced tungsten (W) deposition (IBID) was used to cut and transfer one half of the beam onto the Si wafer substrate next to the bone piece [109]. The transfer process was repeated for the second half of the beam, thus obtaining two micropillar structures of nominal dimensions (10 x 3.5 x 3.5) µm³, (height x width x width), from one pre-milled rectangular beam structure. Finally, a circle marking of 0.5 µm depth and 20 µm diameter was milled on the Si substrate around the micropillars from the top for better visual identification in the nanoindenter setup, fig. 6.2a, c.
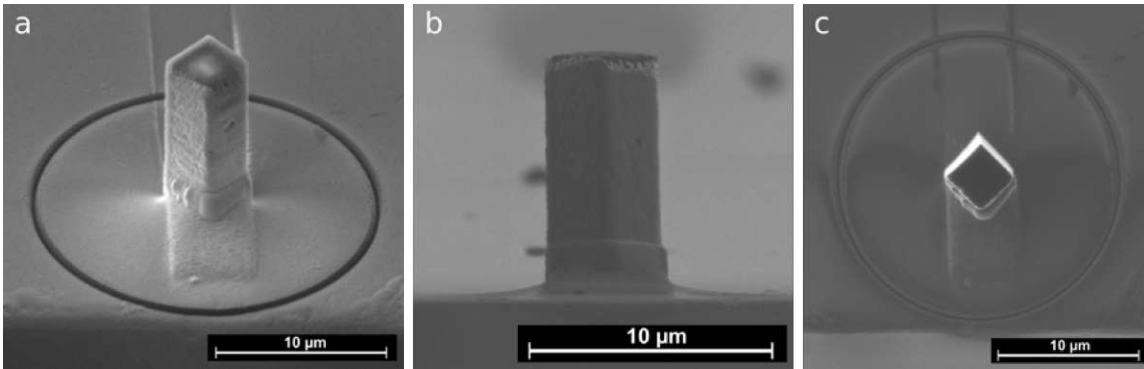
Figure 6.2: SEM images of a representative micropillar, (a) view from an oblique angle with the ring marking of 20 μm diameter around the micropillar, (b) from the side and (c) from the top.

During FIB milling gallium ion implantation occurs due to the ion-solid interactions and is specific for every target material [52, 197]. Gallium ion implantation can be minimized by milling with small currents and at large grazing angles (i.e. only side edges) and was calculated from Monte Carlo simulations to be confined within 15 nm from the surface and found to be negligible for the mechanical response of bone micropillars [52, 168]. Additionally, the tapering angle of the FIB, which is specific for every instrument and sample material was corrected by over tilting the sample by ± 2°, as determined for bone within the used setup.

6.3.2   Micropillar compression

Compression tests on micropillars were performed in air with a flat-punch tip (flat-ended cone with 10 μm flat-end-radius and 90° cone angle, HYS-TI-0227, Hysitron, Minnesota, USA) within a conventional nanoindenter (Hysitron TriboIndenter TI900, Hysitron/ Bruker, Minnesota, USA). Loading of the micropillars was performed in displacement control in a cyclic, loading/partial unloading manner, with a loading and unloading displacement of 50 nm and 25 nm, respectively and loading/unloading rate of 5 nm/s, for total of 12 intermittent cycles with an amplitude up to a maximum of 600 nm or until failure, similar to a loading protocol from [168]. The choice for such

a load function was made with the intent to obtain unloading (here as a measure of a "truer" elastic) moduli, both in the pre- and post-transitional (yield) region, since inelastic deformation may occur and be overlayed during loading, which would not be revealed in a e.g. monotonic loading/unloading case. Moreover, for such delicate and valuable samples that can only be tested once, more information about the mechanical response per strain measure could be collected.

Recorded force and machine compliance corrected displacement data obtained from the nanoindenter software was converted to Cauchy stress and logarithmic strain $\ln U$ (where U is the stretch in the longitudinal sample axis) using the height and cross sectional area for each micropillar as measured from SEM images [168]. The unloading portions of the curve were divided in three time-equidistant parts and linearly fitted, out of which the second, middle portion always exhibited highest R^2 value, i.e. was most linear and was chosen to represent the apparent unloading modulus of the sample for a certain deformation. Unloading moduli were plotted against $\ln U$ and were tested for significant differences within the sex subgroups. For this, the data within a sex subgroup were subdivided in five strain $\ln U$ subclasses (0.00 - 0.001, 0.001 - 0.002, 0.002 - 0.003, 0.003 - 0.004 and 0.004 - 0.005), in which the two subgroups osteoporotic and the cadaveric were tested for significant differences.

Additionally, the envelope curve was also analyzed by removing the unloading/reloading portions of the measured curve and fitting of the linear portion, the slope of which represents the apparent loading modulus. Most of the curves exhibited a toe region (fig. 6.3a), due to initial alignment of the indenter tip and the micropillar sample upon initiation of compression. For the purpose of determination of the transition point and related parameters (see section 6.2), the linear fit of the most linear portion of the loading curve (past the toe region) was extended to the intercept with the x-axis and the obtained strain offset was subtracted from the strain data [183]. From the envelope curve the mechanical parameters: loading modulus, transition stress and transition strain (as determined by the 0.2 % offset rule), strength represented by the max. stress measured and strain at max. stress were obtained for all analyzed
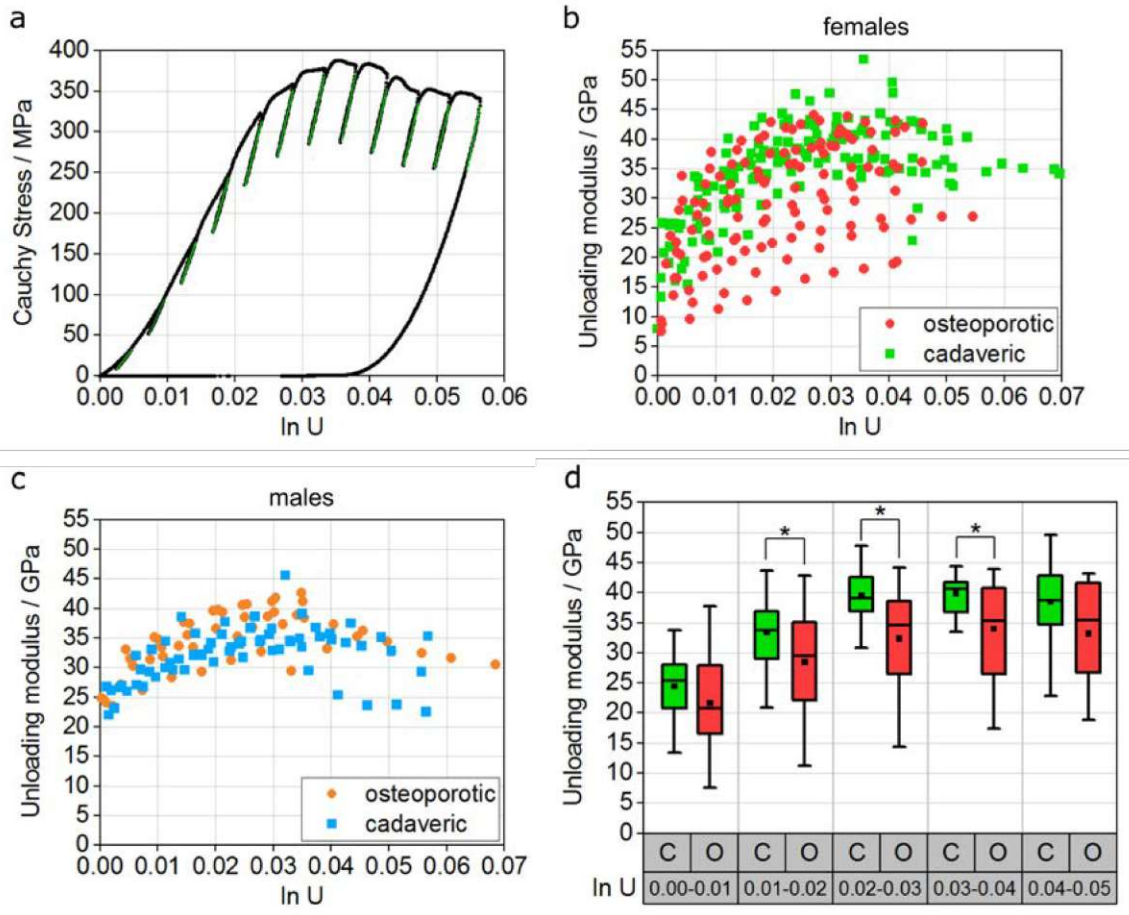
Figure 6.3: Unloading moduli vs. logarithmic stretch ($\ln U$) obtained from micropillar compression. (a) A representative Cauchy stress vs. $\ln U$ measurement of a single micropillar, where the unloading portions are linearly fitted, represented by green lines (see section 6.3.2). (b) Evolution of unloading moduli with increasing strain for all micropillars of the female subgroup and (c) of the male subgroup. (d) Boxplots of strain classes subdivided data, obtained from (a), tested for significant differences in unloading moduli for the female subgroup in different strain ranges (C: control, O: osteoporotic). There were no significant differences within strain classes subdivided data, obtained from (c), in the males subgroup (fig. C.1).

samples and plotted as boxplots for the osteoporotic (O) and cadaveric control (C) groups of both female and male samples.

Plotting and statistical analysis of data was performed in Origin (Version 2019, OriginLab, Northampton, MA, USA). Normality of data distribution was checked

both with the Shapiro-Wilk and Kolmogorov-Smirnov test. Differences of distributions was calculated with the t-test and additionally with the Mann-Whitney U-test, where distributions did not pass the Shapiro-Wilk test of normality. Significance level was chosen at 0.05.

6.4 Results

Cortical bone micropillars of dimensions (9.98 ± 0.81) μm x (3.60 ± 0.63) μm x (3.43 ± 0.38) μm were milled out from a single lamella of the femoral neck samples and transferred onto a Si wafer substrate, fig. 6.2a. The dimensions of the micropillars were taken from the side and the top for the height and edge lengths, respectively, fig. 6.2b, c.

From the compression test of micropillars within the nanoindenter, the raw obtained force vs. displacement data were converted to Cauchy stress vs. logarithmic strain curves, using the true dimensions of every micropillar, a representative measurement of which is shown in figure 6.3a. The unloading portions of the curves were fitted with a straight line (green lines in fig. 6.3a) to obtain values for an apparent unloading modulus. These values were found to increase with increasing deformation up to approx. 0.02 strain and plateau in the post-transition regime (see section 6.2), as observed in a previous study of bone micropillar compression [168]. The evolution of the unloading moduli with increasing strain for all micropillars was plotted for the female and male subgroups in figures 6.3b and c, respectively. In both groups unloading moduli with values higher than 30 GPa, as measured for bovine cortical bone micropillars [109], are observed and can reach up to approx. 50 GPa for some samples. Individual micropillars stemming from the same donor, but from adjacent or different microscopic ROIs displayed notable different mechanical behavior as well as unloading modulus values. In a previous study it was shown that variability of composition of cortical bone tissue at the microscale can be large, which in turn impacts the mechanical response of microscopically prepared samples [126]. For this

reason individual micropillars were treated as individual samples for further mechanical analysis. In the female subgroup, from which more micropillar samples were prepared and tested, a larger scatter across the unloading modulus range is observed (fig. 6.3b) for the osteoporotic samples (red circles) compared to the cadaveric ones (green squares), which is not observed in the male subgroup (of smaller sample size). The unloading modulus data was subdivided in strain subclasses. Here, significant differences between the samples of the female osteoporotic and cadaveric subgroups were detected for the subclasses at 0.01 - 0.04 strain, fig. 6.3d. Such differences were not detected for the male subgroup (fig. C.1).

The envelope curve (excluding the unloading portions) was analyzed by fitting of the linear appearing region to obtain an apparent loading modulus. Values of apparent loading moduli were overall lower compared to unloading moduli indicating superimposed non-elastic deformation during compression. The apparent loading modulus data was summarized as box plots, where the female subgroup showed larger bandwidth of loading modulus compared to the male group, fig. 6.4. No significant difference in loading modulus was observed between osteoporotic and cadaveric samples in either female or male subgroup.

A similar observation was made for stress parameters, obtained from the envelope curve of the compression experiment. Compared to literature, the magnitude of transition stress and strength values obtained from micropillar compression is up to 5 times larger compared to macroscopic mm-sized samples, e.g. transition stress in tension (107.7 ± 12.3) MPa [10], and compression strength (135.73 ± 3.65) MPa, for the age group $(51 - 70)$ years [65]. However, these values were obtained from testing hydrated specimens. Both transition stresses and ultimate stresses, i.e. strength values are summarized in boxplots in figure 6.5. Similar as for the loading modulus, no significant difference was observed between measured osteoporotic and cadaveric distributions, within sex subgroups.

Mean values of transition strains were comparable for all subgroups and lie at approx. 0.02 strain (fig. 6.6a and b), as reported for cortical bone at the microscale [168]. No
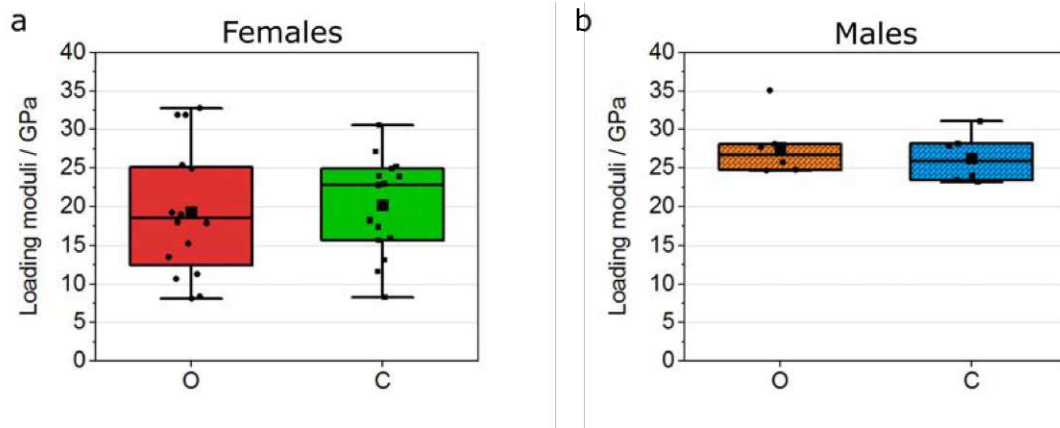
Figure 6.4: Boxplots representation of loading modulus of all samples as obtained from the envelope curve during micropillar compression for (a) female and (b) male subgroups. (a) Red and green boxplots represent the osteoporotic and cadaveric subgroups of the female samples, respectively. (b) Orange and blue boxplots represent the osteoporotic and cadaveric subgroups of the male samples, respectively.

significant difference was obtained between osteoporotic and cadaveric distributions, within the sex subgroups. Strain at max. stress within the female subgroup was the only mechanical parameter with significant difference between osteoporotic (0.042 ± 0.007) and cadaveric (0.034 ± 0.006) distributions (fig. 6.6c), as determined from the envelope curve. Values of all plotted box plots (mean, standard deviation and median) in this subsection are summarized in the comprehensive table C.2 in appendix C.

6.5 Discussion

Determination of the material properties of biological tissues poses many challenges compared to engineering materials, ranging from sample availability and preparation methods over suitable instrumentation and measurement techniques to implied theoretical assumptions and data analysis. The mechanical characterization of bone tissue brings on the additional challenge of its complex hierarchical structure with different structural elements and interfaces at every length scale. Recent developments of experimental techniques for mechanical characterization at the microscale have made
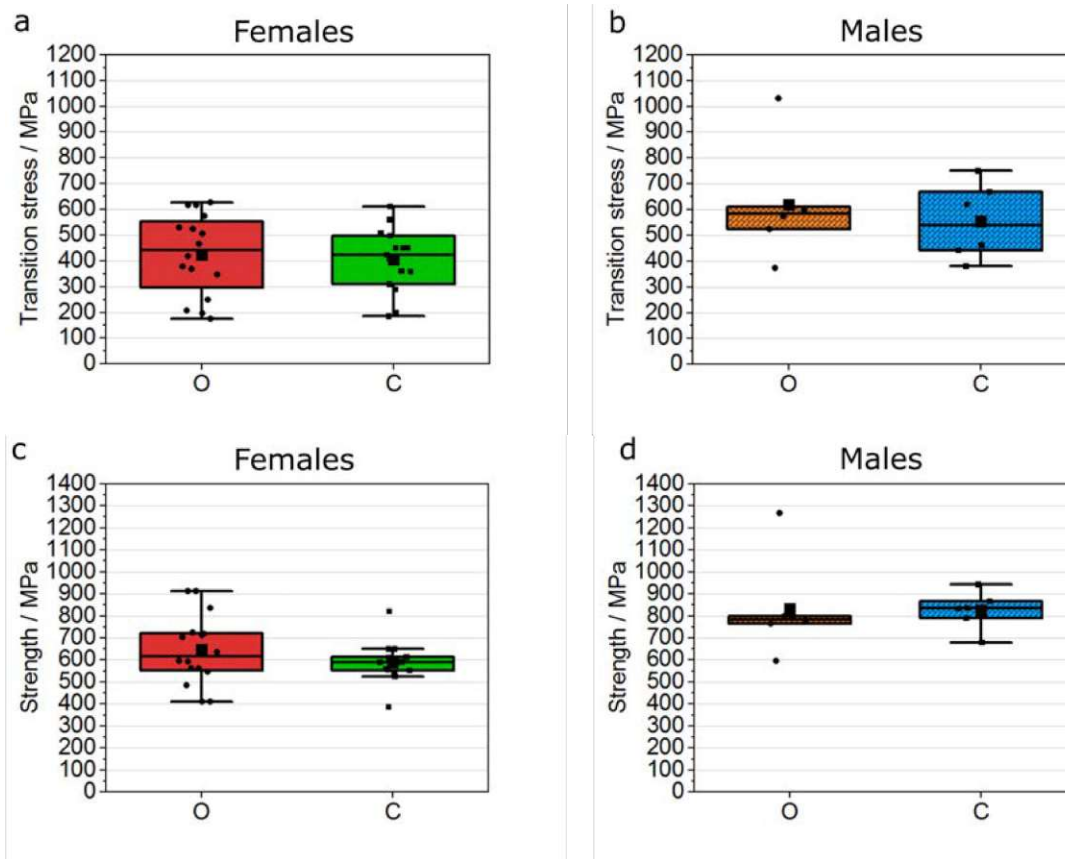
Figure 6.5: Boxplots representation of stress values of all samples as obtained from
the envelope curve during micropillar compression. (a) and (b) Transition stress values of the female and male subgroup, respectively. (c) and
(d) Strength values of the female and male subgroup, respectively. Red
and green boxplots represent the osteoporotic and cadaveric subgroups
of the female samples, respectively, and orange and blue boxplots represent the osteoporotic and cadaveric subgroups of the male samples,
respectively. All subgroup populations were normally distributed according to both the Shapiro-Wilk and Kolmogorov-Smirnow tests of
normality, except for strength values of the osteoporotic subgroup of
the females (c, red box plot) and the osteoporotic subgroup of the males
(d, orange box plot), that only passed the Kolmogorow-Smirnow test
of normality.
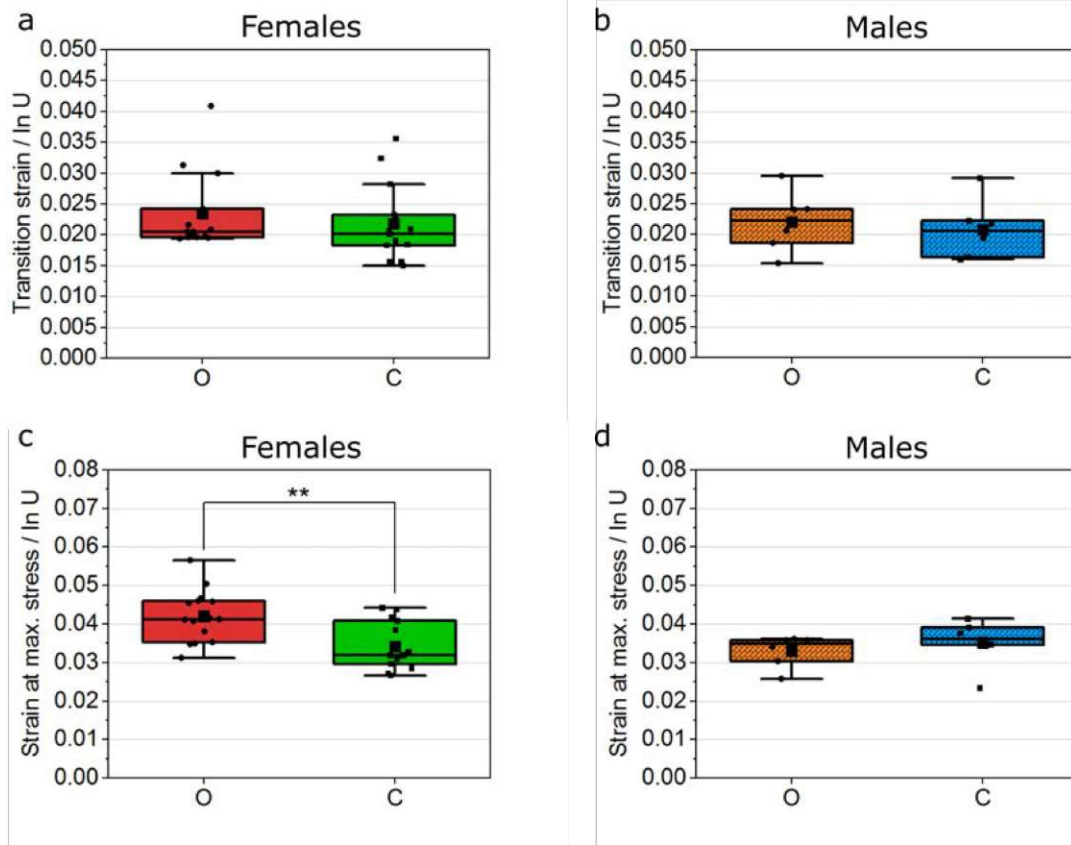
Figure 6.6: Boxplots representation of strain (logarithmic stretch $\ln U$) values of all samples as obtained from the envelope curve during micropillar compression. (a) and (b) Transition stains of the female and male subgroups, respectively. (c) and (d) Strain at max. stress values of the female and male subgroups, respectively. Red and green boxplots represent the osteoporotic (O) and cadaveric (C) subgroups of the female samples, respectively, and orange and blue boxplots represent the osteoporotic and cadaveric subgroups of the male samples, respectively. Transition strain values of the female subgroup, plot (a), as well as the strain at max. stress values of the female control subgroup (c, green box plot) did not pass the Shapiro-Wilk test of normality. However, all box plots passed the Kolmogorow-Smirnow test of normality. Only the strain at max. stress values of the female osteoporotic and control subgroups, plot (c), were significantly different according to both the t-test and Mann-Whitney U test, at p < 0.01.

it feasible to test bone at the lamellar level [24, 82–84, 109, 168, 169]. Particularly in the context of osteoporosis, where increasing porosity of the tissue is thought to be largely affecting mechanical performance, such techniques offer a possibility of probing the truer mechanical and material properties by avoiding large porosities at the microscale, such as enlarged lacunae, Haversian and Volkmann canals as well as trabecularized portions of cortical bone [138].

The measured mechanical parameters in our study correspond well with previous studies of micropillar compression of cortical bone and confirm a considerable size effect, i.e. higher measured values at the microscale, where large porosities and geometrical effects are excluded [168, 169]. Indeed, at larger length scales, porosity plays a significant role in mechanical behavior of macroscopic bone samples, where elastic modulus, transition stress and strength were significantly correlated to porosity on the one hand [118] and changes in geometry of the cortical neck, where thinning of the neck during osteoporosis was found to be the strongest predictor of sustaining a hip fracture, on the other hand [138].

To obtain relevant data for femoral neck fracture, which are frequent in the elderly, we investigated whether the bone material is different between osteoporotic fracture patients and healthy age-matched controls. For this we employed uniaxial compression of micron-sized pillars from the cortical shell of the infero-medial portion of the femoral neck, which is predominantly loaded in compression. Preparing micropillars of rectangular cross section leads to a homogeneous stress state within the sample when loaded in compression, necessary for obtaining a "true" measure of elasticity of the material. Moreover, the transfer of the micropillars onto a much stiffer substrate (here Si wafer) eliminates the influence of a superimposed deformation of the underlying bone material. Elastic energy is defined as the reversible work that can be retrieved from the deformed system when loading is removed, thus a modulus of elasticity should be extracted from the unloading portion of the curve, as non-elastic deformation, especially damage/plasticity can be overlaid during loading [109]. For an ideal linear elastic material, loaded and (partially) unloaded (in the elastic range)

160

curves are linear and on top of each other. The slope of the curves then represents the elastic modulus. All tested micropillars in this study exhibited larger unloading compared to loading moduli and slight hysteresis pointing to dissipative deformation mechanisms. Furthermore, strain hardening behavior (instead of a purely elastic response) was observed by increase of the unloading modulus with strain, reaching a plateau in the post-transition regime, as observed by a previous study of bone micropillars [168]. The order of magnitude (20 GPa - 30 GPa) of measured unloading moduli corresponds to values previously obtained from cortical bone micropillars [109, 168], however, also substantially surpass and reach up to 50 GPa. This might be due to higher mineralization of the bone tissue obtained from (older) human donors. Previous studies [109, 168] have used bone samples from animals (ovine and bovine) harvested at a much younger organism age, whereas reports of data from human are scarce.

The bone samples from both male and female subgroups used in this study were collected from donors in the age range (54 – 86) years. All parameters, that did not exhibit significant differences between the osteoporotic and cadaveric subgroups (i.e. apparent loading modulus, transition stress, strength, transition strain and additionally strain at max. stress) were pooled and tested for correlation with respect to donor age but no significant correlations were found within the used cohorts in this study, see table C.1. This is in line with the reported age independence of microindentation data performed on femoral cortical bone with donors age > 40 years [118] and references therein.

Due to the comparative small number of male samples we did not evaluate statistical differences between sex subgroups. So apparent differences between sex groups, e.g. apparent loading moduli and stress values (transition stress and strength) suggesting larger mean values for the male subgroup should be taken with a grain of salt. This does not exclude that male samples are indeed stiffer and stronger, which could be due to higher mineralization levels of bone tissue in males [163]. Sex-dependent differences of bone are more prominent on larger, i.e. tissue and whole bone length

scales, where cortical area and bone size, strength and robustness (transverse cross-sectional width relative to bone length), respectively, where found to be larger in men [163]. Osteoporosis is considered a disease mostly relevant for post-menopausal women as a result of estrogen deficiency. While the pathology is also present in men, it comes with a delayed onset of risk of fracture incidence of approx. 10 years, particularly after a previous fragility fracture, treatments with oral glucocorticoids or androgen deprivation therapy [1]. These findings are suggestive of different molecular mechanisms and effects on bone material quality, as well as progression of the disease compared to females. Also for this reason, sex subgroups were plotted and analyzed separately in our study and no statistical evaluation was performed between them.

No significant changes were determined between the osteoporotic and cadaveric subgroups for all obtained mechanical parameters in this study, except for unloading moduli (fig. 6.3) and strain at max. stress (fig. 6.6) in the female subgroup.

The mechanical behavior of bone tissue, also at the microscale, is a result of the properties and the interplay of its structural elements and constituents. At this length scale, changes in the mineral and organic phases due to pathology are manifold and interrelated. In turn, their effects on the measured mechanical response are equally complex and intertwined, as discussed in the following.

Mineral content is considered to provide stiffness and strength to bone tissue [138]. Also, mineralization of bone tissue was found to be independent of age and sex [118], the effect of the former being in line with our observations of absence of correlations of mechanical parameters related to mineralization (transition stress and strength) with respect to age (table C.1). Further supportive of these results are also findings of minor impact of mineralization on microindentation data, performed on human cortical bone from the femur [118] as well as cortical and trabecular bone of ovariectomized rats [59, 113]. On the other hand, during osteoporosis, prolonged estrogen deficiency was found to significantly reduce mean mineralization in bone tissue [138], although the reduction was found to be very non-uniform across microscopic regions of the tissue, e.g. trabeculae of the proximal femur, with some regions exhibiting even

increased mineralization. This might explain the small differences in mechanical parameters between osteoporotic and cadaveric subgroups observed in our experiments. However these simplified considerations alone do not take into account the organic phase of bone.

With less mineralization of the tissue in osteoporosis, mechanical loading might be transferred more onto the organic phase, which is comprised of collagen and non-collagenous proteins (NCPs). The protein structure of type I collagen fulfills several functions: providing a template for mineralization, absorbing energy during fracture, providing viscoelasticity of the material when in a hydrated state [121] and is further stabilized by enzymatic crosslinks and advanced glycation end products (AGEs) [104]. The enzymatic crosslinks are considered to have a positive effect by providing structural stability of the fibrils, but on the other hand, accumulation of increased number of AGEs are considered to restrict intermolecular movement between the collagen molecules rendering the fibrils more brittle. Both types of crosslinks were found to be altered in the non-favorable direction during osteoporosis, i.e. the number of mature, stabilizing enzymatic crosslinks was reduced and the number of AGEs were increased [138]. Such changes lead to reduced amount of fibril deformation and result in osteoporotic tissue that is restricting deformation [213]. Moreover, such a mechanism could be supported by molecular modeling, where crosslinking density regimes considerably changes mechanical behavior reflected in significant changes of tensile modulus but provide minimal changes in strength [21].

The regulation of the quality of the collagen protein structure during post-translational modifications, the process of mineralization as well as the interfibrillar connectedness is provided by the different NCPs [104, 181]. In osteoporotic patients, increased levels of two such NCPs, osteocalcin (OCN) and osteopontin (OP) were found [138], both of which play a role in the mineralization and bone remodelling process [104].

Another, often less considered part of the organic phase, the NCPs, apart from influencing the regulatory mechanisms of the major constituents, collagen and mineral, can also play a direct role in mechanics of bone, with their current understanding of

acting as a glue at the organic-inorganic interface between constituents and structures in bone's material [41, 121, 138, 144, 182, 184, 185]. In particular, the sliding between fibrils has been associated with NCPs, which were found to affect time-dependent deformation of osteoporotic tissue [213].

In this context, altered interaction of the mineral and collagen phase mediated by NCPs may have implications on the load transfer mechanisms between these phases and ultimately on the mechanical properties of the tissue. In our study, the only significant difference between the osteoporotic and cadaveric tissue in the female subgroup in the post-transition regime was determined for the strains at max. stress (fig. 6.6c), but there was no significant difference in the corresponding strength values of the same samples (fig. 6.5c). This implies a larger deformation of the osteoporotic samples under the same magnitude of stress, i.e. unaltered apparent load bearing capacity (of the mineral and collagen), and at the same time altered deformation capability, i.e. inter-fibrillar movement, which could be due to changes in the deformation mechanisms of osteoporotic bone tissue.

The above discussed macroscopic effects of changes in porosity as well as geometry during osteoporosis are the result of a shifted balance of osteoblastic and osteoclastic activity leading to an increased bone material resorption, processes where NCPs play a crucial regulatory role in bone metabolism and establishing of the extra-cellular matrix [104]. It appears that, apart from the "hard" inorganic mineral phase of bone material, changes in the "soft" organic phase can have a substantial impact on bone's mechanics across all length scales. Further investigations of combining micro- and macromechanical testing with correlation to presence and structure of proteins could help to elucidate mechanisms of bone pathologies. Such understanding could ultimately lead to early identification of biomarkers for a pathology, before bone fracture risk factors are increased due to an advanced stage of a disease. Regardless of the mechanisms and limitations of number of donors and samples (see below), our results provide information on variability of cortical bone material properties at the microscale.

The experimental characterization of bone tissue at the lamellar length-scale is a challenging task and limitations need to be addressed. The fabricated micropillars in our study underwent a prolonged high vacuum exposure during preparation and were subsequently tested in air in a dehydrated state. The present difference between loading and unloading moduli is suggestive of a plastic or damaging behavior and the slight hysteresis in unloading-reloading events is suggestive of viscoelastic behavior. The latter, however, was observed to be substantially reduced upon sample dehydration in a previous study on bone mirobeam bending [126]. Therefore, in hydrated conditions it is to be expected that micropillars will be less stiff and show also greater viscous character. Furthermore, since the inelastic portion of the deformation is reduced, dehydration might obscure differences in mechanical behavior between osteoporotic and control bone tissue as observed in our results. Due to experimental limitations, we could not perform compression measurements in fully hydrated conditions in this study.

The number of micropillars and donors from all subgroups is limited due to an extensive sample preparation protocol, limiting the statistical insights gained in our study. Overall, no significant differences between the osteoporotic and cadaveric subgroups were observed for most of the mechanical parameters obtained from experiments. On the one hand, differences in mechanical parameters at the lamellar length-scale might remain undetected within the donor cohort used in this study or might occur predominantly on larger tissue length-scales affecting mainly tissue porosity on the other hand, thus confirming the general understanding of osteoporosis. Moreover, due to substantial alteration of mineralization, NCPs and crosslinks amount and manifold mechanisms present in the tissue in the course of osteoporosis discussed above, additional compositional information would be necessary in further studies to ultimately link compositional to mechanical changes due to bone tissue pathologies, such as osteoporosis.

6.6   Conclusion

Micropillar compression of human cortical bone lamella from the infero-medial portion of the femoral neck was achieved to investigate into differences of apparent mechanical behavior of bone tissue due to osteoporosis. Values of unloading moduli, as a measure of elasticity, were in the range of order (20 - 30) GPa of previously published studies on micropillar compression of bone, but also surpassed and reached up to 50 GPa in the post-transition regime. Higher mean values were observed in the male subgroup compared to the female subgroup, which might be indicative of different sex-based underlying mechanisms of the pathology and warrants further research. In all of the mechanical parameters no significant differences were obtained between the osteoporotic and control subgroups, except for unloading modulus and strain at max. stress in the female subgroup. Hydration state and compositional information might have a substantial contribution for uncovering influences of osteoporosis on mechanical performance of bone tissue at lower length scales and should be addressed in further studies.

Chapter 7

Summary

The main goal of this thesis was to perform mechanical testing of cortical bone at the lower microscale, at the level of single bone lamellae. In particular, bone of human origin was used, since previous studies of this type were only conducted on bone samples of animal origin. From all structures found on the hierarchical levels of cortical bone material, single lamellae are the least mechanically characterized structures in isolated form so far. Moreover, this length scale might be considered as the "truer" material level of cortical bone tissue, since contributions of larger porosities, e.g. Haversian canals or bone cells lacunae can be avoided. Performing micromechanical experiments on isolated bone structures is an emerging field, with only several published studies in the last decade. Thus, the first study of this thesis was dedicated to investigation of the reliability and validity of mechanical parameters obtained from such micromechanical tests, which have not been discussed in literature yet. Next, since bone is a biological material embedded in a physiological hydrated environment, the role of water, i.e. hydration state and to a certain degree the effect of donor age on microbeams machined from a single lamellae were investigated in both dehydrated and fully submerged, rehydrated state. In the final study, potential changes in mechanical properties of cortical bone material due to the pathology of osteoporosis were investigated on micropillars machined from a relevant fracture site

167

– the femoral neck. The main findings of the studies presented in this thesis were the following:

- In microbeam bending experiments, elastic moduli are obtained with potential error of around 24 %, however, a theoretical worst-case estimation leads to uncertainties as high as 53 %. This is mainly due to the strong dependency of equations on geometrical properties of the samples and deviations from these due to limited precision of sample preparation at the microscale. Additionally, the deformation of the constraining bulk material can add up to 11 % uncertainty to obtained values.

- In micropillar compression, the deformation of the underlying bulk can lead to uncertainties up to 25 %, but can be sufficiently eliminated by application of the Sneddon correction. Tapering of micropillars does not result in large uncertainties (1 %), however, leads to an inhomogeneous stress distribution within micropillars, which can lead to superposed structural deformation mechanisms.

- The mechanical behavior of single lamella microbeams transitions from almost purely linear elastic when dehydrated to viscoelastic with reduction of bending moduli up to 5 times upon rehydration.

- A trend of reduced dissipated energy of bone microbeams, subjected to bending, with increasing donor age was observed, only for the rehydrated microbeams. This is further indicative of the importance of water and hydration state on the mechanical properties of bone tissue.

- In micropillar compression tests of mature human samples, single lamella micropillars exhibit a strain hardening viscoelastic behavior with unloading moduli reaching up to 50 GPa, when tested in air.

- In micropillar compression, higher mean values of mechanical parameters were observed in the male compared to the female subgroup. This could be indicative of sex based differences of underlying mechanisms in the context of osteoporosis and should be further investigated.

- No changes in mechanical parameters of osteoporotic vs. healthy control micropillars were observed, except for lower unloading moduli and higher strain at max. stress in the female osteoporotic subgroup. The study was limited by a low donor number so results should not be extended to whole populations. Moreover, hydration state and compositional information might have a substantial influence on the mechanical behavior and should be further researched.

In summary, performing mechanical testing at the microscale on isolated micronsized specimens should be carefully planned and well designed, since the accuracy and precision of obtained mechanical parameters depend strongly on geometrical dimensions and sample preparation techniques via FIB milling reach precision limits. This further applies to transferring mechanical concepts from engineering materials to hard biological tissue. Bone material has mainly been considered as a linear elastic solid, whereas it displays viscoelastic behavior. Moreover, the effect of hydration state on the mechanical behavior of bone material could be clearly demonstrated with bone samples transitioning to a mechanically different material of lower modulus and energy dissipation mechanisms upon rehydration. Lastly, being a living tissue, bone is subject to physiological and pathophysiological changes, which may lead to complex alterations in the mechanics of the material. In addition to hydration state, composition may also contribute to the mechanical behavior of bone material. Thus, physiological and pathophysiological changes should be assessed in the full context of composition as well as fiber orientation at the microscale. Then, with the insights gained and further testing of larger number of donors, statements on larger populations would be possible.

Outlook

The feasibility of mechanical assessment at the microscale of isolated microscopically-sized specimens is an exciting and emerging field, offering measuring possibilities at length scales previously unreachable. Mechanical parameters of materials are best obtained from well-defined, homogeneous stress states induced within a sample. These are best achieved in compression and tensile tests, so application of microtensile

testing in addition to the presented microcompression and microbending would be necessary for a comprehensive mechanical investigation of bone material properties at the microscale. However, ideally, for physiologically relevant data such tests should be performed under fully submerged and rehydrated conditions, since hydration plays a dominant role in bone mechanics. Next, rather than conventional mechanical testing as conducted on linear elastic engineering materials, testing protocols developed for assessment of viscoelastic properties should be applied for characterization of bone material, such as cyclic partial unloading, relaxation tests, dynamic mechanical testing as well as loading at different strain rates.

The manifold of bone composition and the complexity of bone tissue metabolism and biological factors present additional aspects that influence mechanical response of the material, particularly in the context of bone pathologies and should be included and correlated to mechanical data in future mechanical analyses of bone. Such insights would contribute towards a better in depth understanding of the complex and fascinating material properties of bone and furthermore contribute to the development of better diagnostic and treatment tools for bone pathologies.

Appendix A

AFM-based microbeam bending at two beam positions

When performing bending of a microbeam with an AFM probe, which itself is a cantilevered beam, the elastic, i.e. bending modulus E can be also calculated from bending at two arbitrary microbeam positions (provided that the bending is performed at sufficient distance from the supports, resulting in sufficient deflection of the tested microbeam). During bending, the two structures of the tested microbeam and the AFM probe cantilever can be considered as a spring system of two springs in series, where the springs represent the bending stiffness of both structures.

When the AFM cantilever bends the microbeam, in the deformed state the force f acting on both structures is the same, thus it can be written

$$f = k_c d_c = k_B d_B = k_{eff}(d_c + d_B) = k_{eff} z \qquad (A.1)$$

, where k_c represents the stiffness of the AFM cantilever, k_B represents the stiffness of the microbeam, d_c and d_B are the displacements of the AFM cantilever and microbeam, respectively, k_{eff} is the total effective stiffness of the system (AFM cantilever and microbeam) and z is the total z-displacement of the cantilever piezo reg-

istered by the instrument. As presented in section 3.3.2, the deflection of the AFM cantilever can also be obtained using the optical lever sensitivity S multiplied by the measured voltage U on the photo diode,

$$k_c US = k_B(z - US) \tag{A.2}$$

, where $(z - US)$ is then the displacement of the microbeam. Rearranging (A.2) gives

$$US(k_c + k_B) = zk_B \tag{A.3}$$

, which can be further rearranged in the form

$$U = \frac{k_B}{k_c + k_B} \frac{1}{S} z \tag{A.4}$$

Regarding the two signals that are measured by the AFM system during such a bending experiment, the voltage on the photo diode U and the (total) displacement of the cantilever piezo z, equation (A.4) represents a voltage vs. z-displacement curve, where

$$Q = \frac{k_B}{k_c + k_B} \frac{1}{S} \tag{A.5}$$

is the slope of this curve and is denoted as Q.

Considering the microbeam, the deflection of a double-clamped (dc) beam can be calculated as:

$$\nu_{dc} = \frac{Px^3(L-x)^3}{3EIL^3} \tag{A.6}$$

, where P is the load, x a position on the beam where the load is applied, L the span length of the microbeam, E the bending modulus and I the second moment of

area of the beam. The stiffness of the microbeam is then the slope of the load vs. displacement curve:

$$k_B = \frac{P}{\nu_{dc}} = \frac{3EIL^3}{x^3(L-x)^3} \tag{A.7}$$

and the microbeam constants in the numerator can be expressed as a single constant to give

$$K_B = 3EIL^3 => k_B = \frac{K_B}{x^3(L-x)^3} \tag{A.8}$$

Substituting equation (A.8) into equation (A.5) gives Q as a function of the bending position x:

$$Q(x) = \frac{K_B}{S(k_c x^3(L-x)^3 + K_B)} \tag{A.9}$$

with its inverse

$$\frac{1}{Q} = Q^{-1} = S(\frac{k_c}{K_B}x^3(L-x)^3 + 1) \tag{A.10}$$

Two spring system stiffnesses at two beam positions x_1 and x_2 can then be put into a ratio

$$\Theta = \frac{Q^{-1}(x_1)}{Q^{-1}(x_2)} = \frac{Q(x_2)}{Q(x_1)} = \frac{S(\frac{k_c}{K_B}x_1^3(L-x_1)^3 + 1)}{S(\frac{k_c}{K_B}x_2^3(L-x_2)^3 + 1)} \tag{A.11}$$

, where S is eliminated, leading to

$$\Theta(\frac{k_c}{K_B}x_2^3(L-x_2)^3 + 1) = \frac{k_c}{K_B}x_1^3(L-x_1)^3 + 1 \tag{A.12}$$

APPENDIX A. AFM-BASED MICROBEAM BENDING AT TWO BEAM POSITIONS

Multiplying the above equation by K_B and rearranging to bring all terms with K_B on the left side yields

$$\Theta K_B - K_B = k_c x_1^3 (L - x_1)^3 - \Theta k_c x_2^3 (L - x_2)^3 \tag{A.13}$$

from which an expression for K_B follows

$$K_B = \frac{k_c(x_1^3(L - x_1)^3 - \Theta x_2^3(L - x_2)^3)}{\Theta - 1} \tag{A.14}$$

Substituting back into equation (A.8) an expression for calculation of E for a double clamped beam, by using the known stiffness of an AFM cantilever k_c and measuring the system stiffnesses at two position $Q(x_1)$ and $Q(x_2)$ (to calculate Θ) is finally obtained as:

$$E_{dc} = \frac{1}{3IL^3} \frac{k_c(x_1^3(L - x_1)^3 - \Theta x_2^3(L - x_2)^3)}{\Theta - 1} \tag{A.15}$$

.

For the case of a single-clamped beam the procedure can be applied analogously, by using the stiffness equation for a single-clamped beam

$$k_B = \frac{3EI}{x^3} \tag{A.16}$$

summarizing the beam constants as

$$K_B = 3EI \tag{A.17}$$

using equation (A.10) as

$$\frac{1}{Q} = S(\frac{k_c}{K_B}x^3 + 1) \tag{A.18}$$

174

and building the ratio

$$\Theta = \frac{Q^{-1}(x_1)}{Q^{-1}(x_2)} = \frac{Q(x_2)}{Q(x_1)} = \frac{(\frac{k_c}{K_B} x_1^3 + 1)}{(\frac{k_c}{K_B} x_2^3 + 1)} \tag{A.19}$$

to finally obtain

$$E_{sc} = \frac{1}{3I} \frac{k_c x_1^3 - \Theta k_c x_2^3}{\Theta - 1} \tag{A.20}$$

.

Appendix B

Supplementary Information to Chapter 5

Reproducibility of MB bending measurements plots

Bone microbeams were bent in a deflection regime that largely avoids damage, i.e. in the linear or apparent linear region. Bending was done at multiple locations over a 25 x 3 pixel map as described in section 5.3.2. To verify the assumption of avoiding damage accumulation during bending, distributed bending tests over a 2D map (i.e. at multiple positions along the beam length and width) were repeated several times both in air and in HBSS after 2 h rehydration. All bending data obtained from one representative microbeam (sample 16) are plotted in figure B.1. For the shown beam three bending maps were recorded in air (red) and five bending maps were recorded in HBSS (blue). It is apparent that there is a good overlap of both measured and fitted data, from which the bending modulus E_b is calculated. The curves clearly show that the measures are repeatable pointing to no or very little damage.

Calibration of the AFM cantilever

The AFM cantilever was calibrated according to two methods as described in section 5.3.2, a) according to the Sader method [159] and b) by bending of Si microbeams of known stiffness [127]. One Si microbeam (of dimensions (L x b x w) = (43.07 x 4.4 x

Table B.1: Dimensions of all bone microbeams

Donor	Beam sample	Donor age [y]	L [µm]	b [µm]	h [µm]
1	1	65	24.86	2.97	0.9
1	2	65	24.94	2.37	0.94
1	3	65	25.12	3.4	1
1	4	65	25.03	3.04	1
1	5	65	25.16	2.84	1
2	6	78	25.11	3.4	1.17
2	*	78	25.16	3.67	1.1
2	7	78	25.02	3.81	1.16
2	8	78	25.01	2.91	1.22
3	9	85	24.99	3.55	1.2
3	10	85	25.02	3.5	1.1
3	11	85	25.03	4.1	1.1
3	12	85	25	3.65	1.16
4	13	94	25.07	2.58	1.23
4	14	94	25	3.48	1.1
4	15	94	25.08	3.35	1.15
4	16	94	25.22	3.56	1.16
		Mean	25.05	3.30	1.11
		StdDev	0.09	0.45	0.10

* one microbeam from donor 2 broke off prior to testing, so no bending data could
be obtained.

1.08) µm³) in the double-clamped configuration (fig. B.2) and two Si microbeams (of
dimensions (L x b x w) = (20 x 5.5 x 1.5) µm³ and (20 x 5 x 1.5) µm³) in the single-
clamped configuration (fig. B.3) were bent at multiple positions along the length of
the microbeams, initially with an in situ picoindenter (PI-85 SEM, Hysitron, Bruker,
MA USA) mounted within the vacuum chamber of a field emission gun-scanning
electron microscope (SEM) (Quanta 250 FEG, FEI, Hillsboro, Oregon, USA) and
subsequently with the AFM cantilever. Stiffness values correspond well (within 11
% precision), especially in the middle range of the double-clamped beam (fig. B.2),
where, in the case of bending with an AFM cantilever, measured displacements suf-
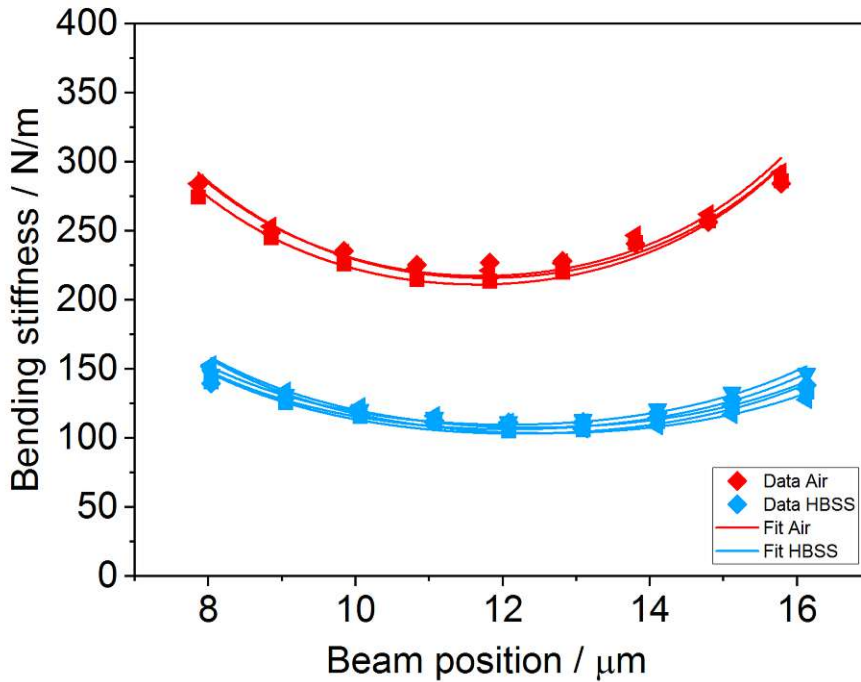
Figure B.1: Representative bending stiffness vs. beam position data of a single microbeam tested nondestructively and reproducibly. Red data is obtained from three consecutive bending measurements in air and blue data is obtained from five consecutive bending measurements in HBSS. The apparent offset in the position coordinates is due to the manual positioning of the pixel map within the AFM control software and lies well within the position resolution of the pixel map ($\pm$ 1 μm).

ficiently include deflections due to bending of the Si microbeam and differences and deviations due to machine compliance between the two testing setups are minimized (i.e. the picoindenter is a much stiffer setup than the flexible AFM cantilever of comparable stiffness as the tested microbeam). The offset in the position coordinates is due to the manual positioning of the bending pixel map within the AFM software and lies within the position resolution of the pixel map ($\pm$ 1 μm).

Microbeam bending results
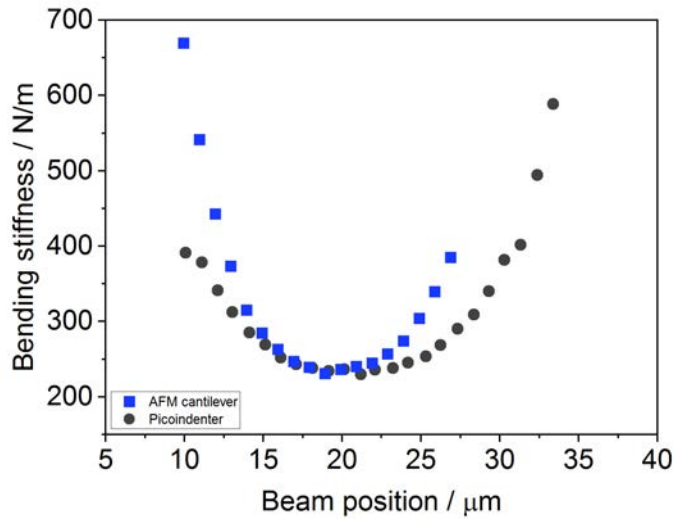
Figure B.2: Bending data along the length of a double-clamped Si microbeam obtained from an in situ picoindenter (dark grey) and AFM cantilever (blue).
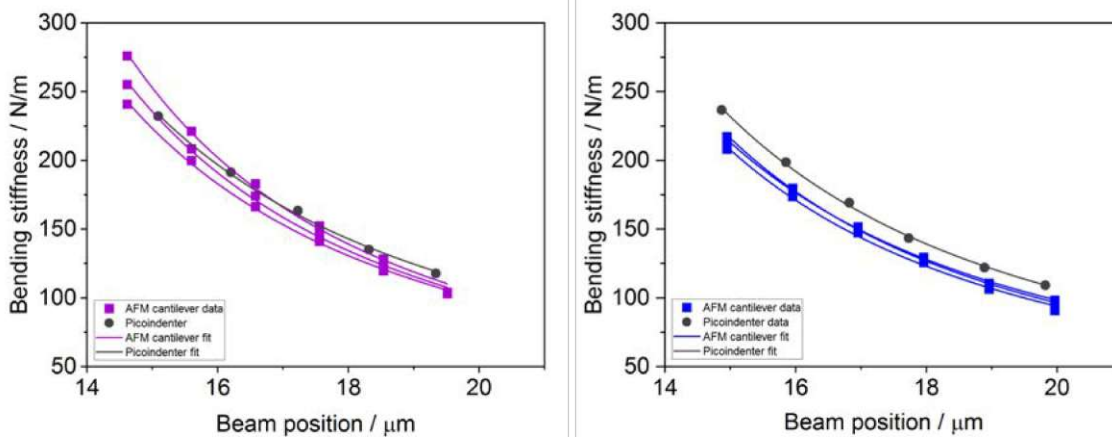
Figure B.3: Bending data along the length of two single-clamped Si microbeams obtained from an in situ picoindenter (dark grey) and three bending measurements by AFM cantilever (violet and blue for the two microbeams, respectively).

Table B.2: Values of bending moduli (E_b) of microbeams obtained in air and HBSS, corresponding to figure 5.5. Data are given as $E_b\pm$ Std.Dev as obtained from 3 - 5 consecutive bending measurements (see Chapter 5). Sample 3 was regarded as an outlier and missing data of samples 1, 2, 5 and 6 represent microbeams that failed during bending measurements in air or upon rehydration.

Sample	Donor age [y]	E_b(air) [GPa]	E_b(HBSS) [GPa]
1	65	35.0 ± 0.6	
2	65	39.2 ± 1.4	
3	65	89.3 ± 0.9	36.0 ± 4.1
4	65	39.8 ± 2.0	16.2 ± 1.5
5	65	44.7 ± 0.9	
6	78	32.4 ± 0.6	
7	78	29.7 ± 1.1	8.2 ± 0.3
8	78	25.1 ± 0.4	10.5 ± 0.1
9	85	34.7 ± 1.1	11.4 ± 0.1
10	85	35.4 ± 1.5	12.7 ± 0.2
11	85	42.5 ± 2.3	15.1 ± 0.2
12	85	38.7 ± 0.6	19.1 ± 0.5
13	94	34.6 ± 0.6	9.7 ± 0.1
14	94	29.7 ± 1.2	7.3 ± 0.2
15	94	30.4 ± 1.0	10.9 ± 0.5
16	94	48.7 ± 1.5	14.2 ± 0.2

Table B.3: Dissipated energy W_{dis}, total energy W_{tot} and relative dissipated energy W_{dis}/W_{tot} calculated form the areas under the loading and unloading curves, corresponding to figure 5.7.

Sample	Donor age [y]	W_{dis} HBSS [pJ]	W_{tot} HBSS [pJ]	W_{dis}/W_{tot} HBSS	W_{dis} air [pJ]	W_{tot} air [pJ]	W_{dis}/W_{tot} air
3	65	0.65	1.69	0.39	-0.02	0.20	-0.08
4	65	0.46	0.72	0.64	0.02	1.08	0.02
7	78	0.09	1.62	0.06	0.01	0.81	0.01
8	78	0.10	1.25	0.08	0.00	0.87	0.00
9	85	0.17	1.53	0.11	0.02	0.75	0.03
10	85	0.22	1.51	0.15	-0.02	0.72	-0.03
11	85	0.14	1.05	0.14	-0.01	0.55	-0.02
12	85	0.42	1.16	0.36	-0.02	0.56	-0.04
13	94	0.20	0.87	0.23	0.01	0.17	0.03
14	94	0.29	1.53	0.19	-0.01	0.21	-0.05
15	94	0.22	1.00	0.22	-0.01	0.67	-0.02
16	94	0.28	0.99	0.28	0.01	0.48	0.02

Appendix C

Supplementary Information to Chapter 6

Table C.1: Linear regression (R^2) and significance values of mechanical parameters obtained via micropillar compression vs. donor age

Parameter	Females		Males	
	R^2	p	R^2	p
Loading modulus	0.02	0.40	0.20	0.35
Transition stress	0.13	0.23	0.08	0.54
Strength	0.06	0.40	0.30	0.22
Transition strain	0.01	0.70	0.02	0.78
Strain at max. stress	0.10	0.30	0.01	0.86

Table C.2: Box plot values of obtained mechanical parameters in this study (figures 6.3d, 6.4, 6.5, 6.6, as well as figure C.1). Values in each table cell are given as mean ± std.dev. (top), median (middle) and number of micropillar samples from which these values are calculated (bottom).

	Females (O)	Females (C)	Males (O)	Males (C)
Unloading modulus [GPa]				
$\ln U$ 0.00 - 0.01	21.7 ± 8.3	24.4 ± 5.5	28.6 ± 4.0	27.5 ± 2.0
	20.8	25.4	28.7	26.9
	(n = 29)	(n = 29)	(n = 12)	(n = 14)
$\ln U$ 0.01 - 0.02	28.5 ± 8.7	33.4 ± 5.4	34.0 ± 3.3	32.5 ± 2.5
	29.5	33.8	33.6	32.1
	(n = 32)	(n = 29)	(n = 12)	(n = 14)
$\ln U$ 0.02 - 0.03	32.3 ± 8.4	39.5 ± 4.2	37.6 ± 3.2	35.0 ± 2.0
	34.6	39.1	38.6	34.6
	(n = 28)	(n = 29)	(n = 12)	(n = 14)
$\ln U$ 0.03 - 0.04	34.0 ± 8.0	39.9 ± 4.1	38.0 ± 4.3	35.7 ± 4.1
	35.3	40.6	38.8	35.0
	(n = 23)	(n = 28)	(n = 9)	(n = 11)
$\ln U$ 0.04 - 0.05	33.2 ± 8.7	38.5 ± 6.6	35.8 ± 1.3	32.1 ± 5.3
	35.5	38.7	35.8	34.2
	(n = 12)	(n = 18)	(n = 4)	(n = 7)
Loading modulus [GPa]	19.2 ± 8.2	20.1 ± 6.3	27.6 ± 3.9	26.2 ± 2.9
	18.5	22.8	26.6	25.9
	(n = 16)	(n = 15)	(n = 6)	(n = 7)
Transition stress [MPa]	424 ± 157	404 ± 123	617 ± 220	553 ± 146
	441	423	584	540
	(n = 16)	(n = 15)	(n = 6)	(n = 6)
Strength [MPa]	645 ± 156	589 ± 90	832 ± 226	824 ± 88
	616	591	785	834
	(n = 16)	(n = 15)	(n = 6)	(n = 6)
Transition strain [$\ln U$]	0.023 ± 0.006	0.022 ± 0.006	0.022 ± 0.005	0.021 ± 0.005
	0.021	0.020	0.022	0.021
	(n = 15)	(n = 15)	(n = 6)	(n = 6)
Strain at max. stress [$\ln U$]	0.042 ± 0.007	0.034 ± 0.006	0.033 ± 0.004	0.035 ± 0.006
	0.041	0.032	0.035	0.036
	(n = 15)	(n = 15)	(n = 6)	(n = 6)
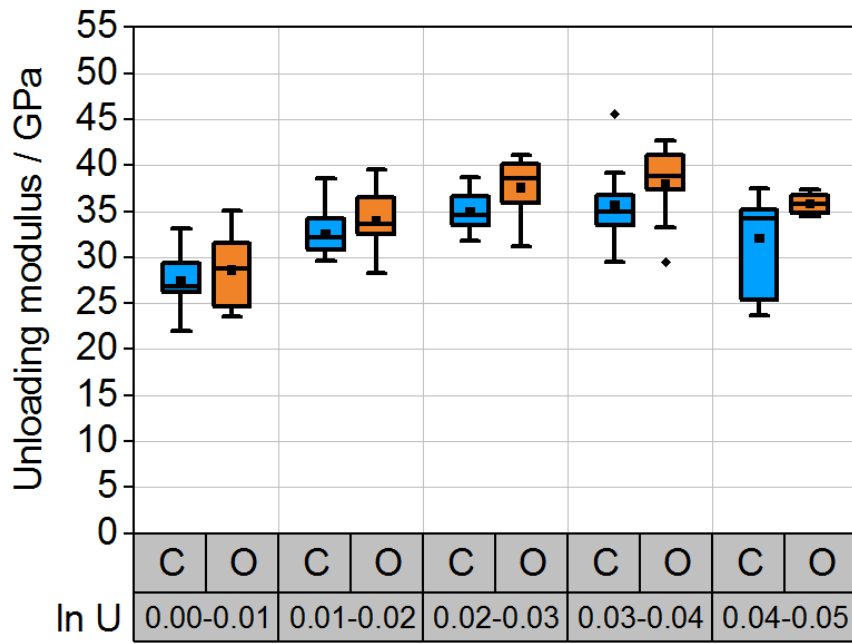
Figure C.1: Unloading moduli vs. logarithmic stretch $(\ln U)$ obtained from micropillar compression. Boxplots of strain classes subdivided data, obtained from fig. 6.3c, tested for significant differences in unloading moduli for the male subgroup in different strain ranges (C: control, O: osteoporotic). There were no significant differences between strain classes subdivided data in the males subgroup.

APPENDIX C. SUPPLEMENTARY INFORMATION TO CHAPTER 6

Bibliography

[1] R. A. Adler. Osteoporosis in men : a review. *Bone research*, 2(January):1–8, 2014.

[2] O. Akkus, A. Polyakova-Akkus, F. Adar, and M. B. Schaffler. Aging of Microstructural Compartments in Human Compact Bone. *Journal of Bone and Mineral Research*, 18(6):1012–1019, 2003.

[3] Z. André. Continuum Micromechanics: Survey. *Journal of Engineering Mechanics*, 128(8):808–816, aug 2002.

[4] O. G. Andriotis. *Nanostructure and mechanics of collagen fibrils from osteogenesis imperfecta mice and chronic asthma assessed with atomic force microscopy.* Thesis for the degree of doctor of philosophy, University of Southampton, 2013.

[5] O. G. Andriotis, W. Manuyakorn, J. Zekonyte, O. L. Katsamenis, S. Fabri, P. H. Howarth, D. E. Davies, and P. J. Thurner. Nanomechanical assessment of human and murine collagen fibrils via atomic force microscopy cantilever-based nanoindentation. *Journal of the Mechanical Behavior of Biomedical Materials*, 39:9–26, 2014.

[6] ASTM E9-09. ASTME9-09 Standard Test Methods of Compression Testing of Metallic Materials at Room Temperature. Standard, American Society for Testing and Materials (ASTM), Jan. 2018.

[7] A. J. Bailey and M. S. Shimokomaki. Age related changes in the reducible cross-links of collagen. *FEBS Letters*, 16(2):86–88, 1971.

BIBLIOGRAPHY

[8] S. Bailey, G. E. Sroga, B. Hoac, O. L. Katsamenis, Z. Wang, N. Bouropoulos, M. D. McKee, E. S. Sørensen, P. J. Thurner, and D. Vashishth. The role of extracellular matrix phosphorylation on energy dissipation in bone. *eLife*, 9:1–19, 2020.

[9] M. Balooch, S. Habelitz, J. H. Kinney, S. J. Marshall, and G. W. Marshall. Mechanical properties of mineralized collagen fibrils as influenced by demineralization. *Journal of structural biology*, 162(3):404–410, jun 2008.

[10] H. H. Bayraktar, E. F. Morgan, G. L. Niebur, G. E. Morris, E. K. Wong, and T. M. Keaveny. Comparison of the elastic and yield properties of human femoral trabecular and cortical bone tissue. *Journal of Biomechanics*, 37(1):27–35, 2004.

[11] E. Benca, A. Reisinger, J. M. Patsch, L. Hirtler, A. Synek, S. Stenicka, R. Windhager, W. Mayr, and D. H. Pahr. Effect of simulated metastatic lesions on the biomechanical behavior of the proximal femur. *Journal of Orthopaedic Research*, 35(11):2407–2414, nov 2017.

[12] P. Benham, R. Crawford, and C. Armstrong. Mechanics of engineering materials, 1990.

[13] J. G. Betts, K. A. Young, J. A. Wise, E. Johnson, B. Poe, D. H. Kruse, O. Korol, J. E. Johnson, M. Womble, and P. DeSaix. Exercise, Nutrition, Hormones, and Bone Tissue. In *Anatomy & Physiology*, chapter 6.6. Openstax CNX, Houston, Texas, 2013.

[14] X. Bi, G. Li, S. B. Doty, and N. P. Camacho. A novel method for determination of collagen orientation in cartilage by Fourier transform infrared imaging spectroscopy (FT-IRIS). *Osteoarthritis and Cartilage*, 13(12):1050–1058, 2005.

[15] X. Bi, C. A. Patil, C. C. Lynch, G. M. Pharr, A. Mahadevan-Jansen, and J. S. Nyman. Raman and Mechanical Properties Correlate At Whole Bone- and Tissue- Levels in a Genetic Mouse. *J. Biomech.*, 44(2):297–303, 2011.

[16] G. M. Blake and I. Fogelman. The role of DXA bone density scans in the diagnosis and treatment of osteoporosis. *Postgraduate Medical Journal*, 83:509–517, 2007.

[17] L. Bozec, G. van der Heijden, and M. Horton. Collagen Fibrils: Nanoscale Ropes. *Biophysical Journal*, 92(1):70–75, 2007.

[18] M. L. Brandi. Microarchitecture , the key to bone quality. *Rheumatology*, 48(suppl 4):iv3 – iv8, 2009.

[19] T. Buchwald, M. Kozielski, and M. Szybowicz. Determination of Collagen Fibers Arrangement in Bone Tissue by Using Transformations of Raman Spectra Maps. *Spectroscopy*, 27:107–117, jun 2012.

[20] J. A. Buckwalter, M. J. Glimcher, R. R. Cooper, and R. Recker. Bone Biology. *JBJS*, 77(8), 1995.

[21] M. J. Buehler. Nanomechanics of collagen fibrils under varying cross-link densities: Atomistic and continuum studies. *Journal of the Mechanical Behavior of Biomedical Materials*, 1(1):59–67, 2008.

[22] S. P. Canelón and J. M. Wallace. β-Aminopropionitrile-induced reduction in enzymatic crosslinking causes in vitro changes in collagen morphology and molecular composition. *PLoS ONE*, 11(11):1–13, 2016.

[23] R. Carretta, B. Luisier, D. Bernoulli, E. Stüssi, R. Müller, and S. Lorenzetti. Novel method to analyze post-yield mechanical properties at trabecular bone tissue level. *Journal of the Mechanical Behavior of Biomedical Materials*, 20:6–18, 2013.

[24] Y. L. Chan, A. H. W. Ngan, and N. M. King. Use of focused ion beam milling for investigating the mechanical properties of biological tissues: A study of human primary molars. *Journal of the Mechanical Behavior of Biomedical Materials*, 2(4):375–383, 2009.

[25] X. Chen, N. Ogasawara, M. Zhao, and N. Chiba. On the uniqueness of measuring elastoplastic properties from indentation: The indistinguishable mystical materials. *Journal of the Mechanics and Physics of Solids*, 55(8):1618–1660, 2007.

[26] J. H. Cole and M. C. Van Der Meulen. Whole bone mechanics and bone quality. *Clinical Orthopaedics and Related Research*, 469(8):2139–2149, 2011.

[27] B. D. Coleman and W. Noll. The thermodynamics of elastic materials with heat conduction and viscosity. *Archive for Rational Mechanics and Analysis*, 13(1):167–178, 1963.

[28] C. J. Collins, O. G. Andriotis, V. Nedelkovski, M. Frank, O. L. Katsamenis, and P. J. Thurner. Bone Micro- and Nanomechanics. In *Encyclopedia of Biomedical Engineering*, volume 2, pages 22–44. 2019.

[29] D. M. Cooper, C. E. Kawalilak, K. Harrison, B. D. Johnston, and J. D. Johnston. Cortical Bone Porosity: What Is It, Why Is It Important, and How Can We Detect It? *Current Osteoporosis Reports*, 14(5):187–198, 2016.

[30] A. L. Costa, D. J. Shuman, R. R. Machado, and M. S. Andrade. Determination of the compliance of an instrumented indentation testing machine. *IMEKO TC5 Conference on Hardness Measurements Theory and Application in Laboratories and Industries, HARDMEKO 2004*, (January):30–35, 2004.

[31] O. Coussy. *Poromechanics*. John Wiley & Sons, Ltd, 2004.

[32] S. Cowin and J. Telega. Bone Mechanics Handbook, 2nd Edition. -. *Applied Mechanics Reviews*, 56(4):B61–B63, jul 2003.

[33] E. Cowin SC, editor. *Bone Mechanics Handbook*. CRC Press, 2nd edition, 2001.

[34] J. D. Currey. *Bones: Structure and Mechanics*. Princeton University Press, 2002.

[35] P. Derkx, A. L. Nigg, F. T. Bosman, D. H. Birkenhäger-Frenkel, A. B. Houtsmuller, H. A. Pols, and J. P. Van Leeuwen. Immunolocalization and quantification of noncollagenous bone matrix proteins in methylmethacrylate-embedded adult human bone in combination with histomorphometry. *Bone*, 22(4):367–373, 1998.

[36] B. O. Donmez, S. Ozdemir, M. Sarikanat, N. Yaras, P. Koc, N. Demir, B. Karayalcin, and N. Oguz. Effect of angiotensin II type 1 receptor blocker on osteoporotic rat femurs. *Pharmacological Reports*, 64(4):878–888, 2012.

[37] E. Donnelly. Methods for assessing bone quality: A review. *Clinical Orthopaedics and Related Research*, 469(8):2128–2138, 2011.

[38] E. Donnelly, S. P. Baker, A. L. Boskey, and M. C. H. van der Meulen. Effects of surface roughness and maximum load on the mechanical properties of cancellous bone measured by nanoindentation. *Journal of biomedical materials research. Part A*, 77(2):426–435, may 2006.

[39] P. Eilers and H. Boelens. Baseline Correction with Asymmetric Least Squares Smoothing. *Unpubl. Manuscr*, nov 2005.

[40] G. E. Fantner, J. Adams, P. Turner, P. J. Thurner, L. W. Fisher, and P. K. Hansma. Nanoscale ion mediated networks in bone: Osteopontin can repeatedly dissipate large amounts of energy. *Nano Letters*, 7(8):2491–2498, 2007.

[41] G. E. Fantner, T. Hassenkam, J. H. Kindt, J. C. Weaver, H. Birkedal, L. Pechenik, J. A. Cutroni, G. A. G. Cidade, G. D. Stucky, D. E. Morse, and P. K. Hansma. Sacrificial bonds and hidden length dissipate energy as mineralized fibrils separate during bone fracture. *Nature Materials*, 4(8):612–616, 2005.

[42] H. Fei, A. Abraham, N. Chawla, and H. Jiang. Evaluation of Micro-Pillar Compression Tests for Accurate Determination of Elastic-Plastic Constitutive Relations. *Journal of Applied Mechanics*, 79(6):061011, 2012.

BIBLIOGRAPHY

[43] M. Frank, A. G. Reisinger, D. H. Pahr, and P. J. Thurner. Effects of Osteoporosis on Bone Morphometry and Material Properties of Individual Human Trabeculae in the Femoral Head. *JBMR Plus*, 00(00):1–14, 2021.

[44] P. Fratzl. *Collagen - Structure and Mechanics.* Springer US, 2008.

[45] P. Fratzl and R. Weinkamer. Nature's hierarchical materials. *Progress in Materials Science*, 52(8):1263–1334, 2007.

[46] N. Fratzl-Zelman, P. Roschger, A. Gourrier, M. Weber, B. M. Misof, N. Loveridge, J. Reeve, K. Klaushofer, and P. Fratzl. Combination of nanoindentation and quantitative backscattered electron imaging revealed altered bone material properties associated with femoral neck fragility. *Calcified Tissue International*, 85(4):335–343, 2009.

[47] C. P. Frick, B. G. Clark, S. Orso, A. S. Schneider, and E. Arzt. Size effect on strength and strain hardening of small-scale [1 1 1] nickel compression pillars. *Materials Science and Engineering A*, 489(1-2):319–329, 2008.

[48] H. M. Frost. Bone's Mechanostat: A 2003 Update. *Anatomical Record - Part A Discoveries in Molecular, Cellular, and Evolutionary Biology*, 275(2):1081–1101, 2003.

[49] L. Galvis, J. W. C. Dunlop, G. Duda, P. Fratzl, and A. Masic. Polarized Raman Anisotropic Response of Collagen in Tendon: Towards 3D Orientation Mapping of Collagen in Tissues. *PLoS ONE*, 8(5):1–9, 2013.

[50] J. D. Gardinier, C. W. Townend, K.-P. Jen, Q. Wu, R. L. Duncan, and L. Wang. In situ permeability measurement of the mammalian lacunar–canalicular system. *Bone*, 46(4):1075–1081, 2010.

[51] D. M. Geraldes and A. T. M. Phillips. A comparative study of orthotropic and isotropic bone adaptation in the femur. *International Journal for Numerical Methods in Biomedical Engineering*, 30(9):873–889, sep 2014.

[52] L. A. F. C. Giannuzzi and F. A. N. C. S. U. Stevie, editors. *Introduction to Focused Ion Beams - Instrumentation, Theory, Techniques and Practice.* Springer, 2005.

[53] F. J. Giessibl. Atomic resolution on Si(111)-(7×7) by noncontact atomic force microscopy with a force sensor based on a quartz tuning fork. *Applied Physics Letters*, 76(11):1470–1472, 2000.

[54] F. J. Giessibl, H. Bielefeldt, S. Hembacher, and J. Mannhart. Imaging of atomic orbitals with the atomic force microscope - experiments and simulations. *Annalen der Physik (Leipzig)*, 10(11-12):887–910, 2001.

[55] R. Gottardi, U. Hansen, R. Raiteri, M. Loparic, M. Düggelin, D. Mathys, N. F. Friederich, P. Bruckner, and M. Stolz. Supramolecular Organization of Collagen Fibrils in Healthy and Osteoarthritic Human Knee and Hip Joint Cartilage. *PLOS ONE*, 11(10):e0163552, oct 2016.

[56] M. Granke, M. D. Does, and J. S. Nyman. The Role of Water Compartments in the Material Properties of Cortical Bone. *Calcified Tissue International*, 97(3):292–307, 2015.

[57] H. Gray, S. Standring, H. Ellis, and B. K. B. Berkovitz. *Gray's Anatomy: The Anatomical Basis of Clinical Practice.* Elsevier Churchill Livingstone, Edinburgh; New York, 39 edition, 2005.

[58] M. D. Grynpas, J. H. Tupy, and J. Sodek. The distribution of soluble, mineral-bound, and matrix-bound proteins in osteoporotic and normal bones. *Bone*, 15(5):505–513, 1994.

[59] X. E. Guo and S. A. Goldstein. Vertebral trabecular bone microscopic tissue elastic modulus and hardness do not change in ovariectomized rats. *Journal of Orthopaedic Research*, 18(2):333–336, 2000.

[60] H. S. Gupta, J. Seto, W. Wagermaier, P. Zaslansky, P. Boesecke, and P. Fratzl. Cooperative deformation of mineral and collagen in bone at the nanoscale. *Proceedings of the National Academy of Sciences of the United States of America*, 103(47):17741–17746, 2006.

[61] N. Hammer, C. Voigt, M. Werner, F. Hoffmann, K. Bente, H. Kunze, R. Scholz, and H. Steinke. Ethanol and formaldehyde fixation irreversibly alter bones' organic matrix. *Journal of the Mechanical Behavior of Biomedical Materials*, 29:252–258, 2014.

[62] F. Hang and A. H. Barber. Nano-mechanical properties of individual mineralized collagen fibrils from bone tissue. *Journal of the Royal Society Interface*, 8(57):500–505, 2011.

[63] F. Hang, H. S. Gupta, and A. H. Barber. Nanointerfacial strength between non-collagenous protein and collagen fibrils in antler bone. *Journal of the Royal Society Interface*, 11(92):1–7, 2014.

[64] P. K. Hansma, G. E. Fantner, J. H. Kindt, P. J. Thurner, G. Schitter, P. J. Turner, S. F. Udwin, and M. M. Finch. Sacrificial bonds in the interfibrillar matrix of bone. *Journal of Musculoskeletal Neuronal Interactions*, 5(4):313–315, 2005.

[65] R. Havaldar, S. Pilli, and B. Putti. Insights into the effects of tensile and compressive loadings on human femur bone. *Advanced Biomedical Research*, 3(1):101, 2014.

[66] C. Hellmich and F. J. Ulm. Are mineralized tissues open crystal foams reinforced by crosslinked collagen? - Some energy arguments. *Journal of Biomechanics*, 35(9):1199–1212, 2002.

[67] C. Hellmich, F.-J. Ulm, and L. Dormieux. Can the diverse elastic properties of trabecular and cortical bone be attributed to only a few tissue-independent

phase properties and their interactions? *Biomechanics and Modeling in Mechanobiology*, 2(4):219–238, 2004.

[68] R. C. Hibbeler. *Mechanics of Materials MasteringEngineering Access Code: Includes Pearson EText.* Pearson College Division, 2013.

[69] E. Hintsala, D. Kiener, J. Jackson, and W. W. Gerberich. In-Situ Measurements of Free-Standing, Ultra-Thin Film Cracking in Bending. *Experimental Mechanics*, 55(9):1681–1690, 2015.

[70] S. K. Ho, S. J. Eun, H. Y. Myung, and Y. Seoung-Oh. Osteoporosis and Sarcopenia Bone mineral density assessment for research purpose using dual energy X-ray absorptiometry. *Osteoporosis and Sarcopenia*, 4(3):79–85, 2018.

[71] R. Hooke. *De Potentia Restitutiva, or of Spring. Explaining the Power of Springing Bodies.* Printed for John Martyn Printer to the Royal Society, London, London, 1678.

[72] M. A. Hopcroft, W. D. Nix, and T. W. Kenny. What is the Young's modulus of silicon? *Journal of Microelectromechanical Systems*, 19(2):229–238, apr 2010.

[73] G. K. Hunter and H. A. Goldberg. Nucleation of hydroxyapatite by bone sialoprotein. *Proceedings of the National Academy of Sciences*, 90(18):8562–8565, sep 1993.

[74] S. Jaramillo Isaza. *Characterization of the mechanical and morphological properties of cortical bones by Nanoindentation and Atomic Force Microscopy.* PhD thesis, Université de Technologie de Compiègne (UTC), 2014.

[75] I. Jasiuk and M. Ostoja-Starzewski. Modeling of bone at a single lamella level. *Biomechanics and Modeling in Mechanobiology*, 3:67–74, 2004.

[76] B. N. Jaya, C. Kirchlechner, and G. Dehm. Can microscale fracture tests provide reliable fracture toughness values? A case study in silicon. *Journal of Materials Research*, 30(5):686–698, 2015.

[77] W. Jee. The Skeletal Tissues. In L. Weiss, editor, *Cell and Tissue Biology: A Textbook of Histology*. Baltimore: Urban & Schwarzenberg Inc., sixth edit edition, 1988.

[78] T. Jenkins, L. V. Coutts, S. D'Angelo, D. G. Dunlop, R. O. Oreffo, C. Cooper, N. C. Harvey, and P. J. Thurner. Site-Dependent Reference Point Microindentation Complements Clinical Measures for Improved Fracture Risk Assessment at the Human Femoral Neck. *Journal of Bone and Mineral Research*, 31(1):196–203, 2016.

[79] K. J. Jepsen, M. J. Silva, D. Vashishth, X. E. Guo, and M. C. Van Der Meulen. Establishing biomechanical mechanisms in mouse models: Practical guidelines for systematically evaluating phenotypic changes in the diaphyses of long bones. *Journal of Bone and Mineral Research*, 30(6):951–966, 2015.

[80] C. Jiang, H. Lu, H. Zhang, Y. Shen, and Y. Lu. Recent Advances on In Situ SEM Mechanical and Electrical Characterization of Low-Dimensional Nanomaterials. *Scanning*, 2017, 2017.

[81] X. Jiang, M. Gruner, F. Trémollieres, W. Pluskiewicz, E. Sornay-Rendu, P. Adamczyk, and P. F. Schnatz. Diagnostic accuracy of FRAX in predicting the 10-year risk of osteoporotic fractures using the USA treatment thresholds: A systematic review and meta-analysis. *Bone*, 99:20–25, 2017.

[82] I. Jimenez-Palomar, A. Shipov, R. Shahar, and A. H. Barber. Influence of SEM vacuum on bone micromechanics using in situ AFM. *Journal of the Mechanical Behavior of Biomedical Materials*, 5(1):149–155, 2012.

[83] I. Jimenez-Palomar, A. Shipov, R. Shahar, and A. H. Barber. Mechanical behavior of osteoporotic bone at sub-lamellar length scales. *Frontiers in Materials*, 2(February):1–7, 2015.

[84] I. Jimenez-Palomar, A. Shipov, R. Shahar, and A. H. Barber. Structural orientation dependent sub-lamellar bone mechanics. *Journal of the Mechanical Behavior of Biomedical Materials*, 52:63–71, 2015.

[85] I. Jimenez-Palomar, A. Shipov, R. Shahar, and A. H. Barber. Structural orientation dependent sub-lamellar bone mechanics. *Journal of the Mechanical Behavior of Biomedical Materials*, 52:63–71, 2015.

[86] O. Johnell and J. A. Kanis. An estimate of the worldwide prevalence and disability associated with osteoporotic fractures. *Osteoporosis International*, 17(12):1726–1733, 2006.

[87] R. Jungmann, M. E. Szabo, G. Schitter, R. Yue-Sing Tang, D. Vashishth, P. K. Hansma, and P. J. Thurner. Local strain and damage mapping in single trabeculae during three-point bending tests. *Journal of the Mechanical Behavior of Biomedical Materials*, 4(4):523–534, 2011.

[88] J. Kabel, B. van Rietbergen, M. Dalstra, A. Odgaard, and R. Huiskes. The role of an effective isotropic tissue modulus in the elastic properties of cancellous bone. *Journal of Biomechanics*, 32(7):673–680, 1999.

[89] L. Kain, O. Andriotis, P. Gruber, M. Frank, M. Markovic, D. Grech, V. Nedelkovski, M. Stolz, A. Ovsianikov, and P. Thurner. Calibration of colloidal probes with atomic force microscopy for micromechanical assessment. *Journal of the Mechanical Behavior of Biomedical Materials*, 85:225–236, 2018.

[90] J. A. Kanis. Assessment of osteoporosis at the primary health care level. Technical report, University of Sheffield, UK, 2007.

[91] J. A. Kanis, O. Johnell, A. Oden, H. Johansson, and E. McCloskey. FRAX™ and the assessment of fracture probability in men and women from the UK. *Osteoporosis International*, 19(4):385–397, 2008.

[92] O. L. Katsamenis, H. M. H. Chong, O. G. Andriotis, and P. J. Thurner. Load-bearing in cortical bone microstructure: Selective stiffening and heterogeneous strain distribution at the lamellar level. *Journal of the Mechanical Behavior of Biomedical Materials*, 17:152–165, 2012.

[93] O. L. Katsamenis, T. Jenkins, and P. J. Thurner. Toughness and damage susceptibility in human cortical bone is proportional to mechanical inhomogeneity at the osteonal-level. *Bone*, 76:158–168, apr 2015.

[94] D. Kiener, C. Motz, and G. Dehm. Micro-compression testing: A critical discussion of experimental constraints. *Materials Science and Engineering A*, 505(1-2):79–87, 2009.

[95] D. Kiener, C. Motz, G. Dehm, and R. Pippan. Overview on established and novel FIB based miniaturized mechanical testing using in-situ SEM. *Zeitschrift fuer Metallkunde/Materials Research and Advanced Techniques*, 100(8):1074–1087, 2009.

[96] J. H. Kindt, P. J. Thurner, M. E. Lauer, B. L. Bosma, G. Schitter, G. E. Fantner, M. Izumi, J. C. Weaver, D. E. Morse, and P. K. Hansma. In situ observation of fluoride-ion-induced hydroxyapatite-collagen detachment on bone fracture surfaces by atomic force microscopy. *Nanotechnology*, 18(13):135102, 2007.

[97] H. F. Knapp, G. C. Reilly, A. Stemmer, P. Niederer, and M. L. Knothe Tate. Development of preparation methods for and insights obtained from atomic force microscopy of fluid spaces in cortical bone. *Scanning*, 24:25–33, 2002.

[98] D. Kupka and E. T. Lilleodden. Mechanical Testing of Solid-Solid Interfaces at the Microscale. *Experimental Mechanics*, 52(6):649–658, 2012.

[99] Y. H. Lai, C. J. Lee, Y. T. Cheng, H. S. Chou, H. M. Chen, X. H. Du, C. I. Chang, J. C. Huang, S. R. Jian, J. S. Jang, and T. G. Nieh. Bulk and mi-

croscale compressive behavior of a Zr-based metallic glass. *Scripta Materialia*, 58(10):890–893, 2008.

[100] D. Larsson, B. Luisier, M. E. Kersh, E. Dall'Ara, P. K. Zysset, M. G. Pandy, and D. H. Pahr. Assessment of Transverse Isotropy in Clinical-Level CT Images of Trabecular Bone Using the Gradient Structure Tensor. *Annals of Biomedical Engineering*, 42(5):950–959, 2014.

[101] S. Lees. A mixed packing model for bone collagen. *Calcified Tissue International*, 33(1):591–602, 1981.

[102] G. Lewis and J. S. Nyman. The use of nanoindentation for characterizing the properties of mineralized hard tissues: State-of-the art review. *Journal of Biomedical Materials Research - Part B Applied Biomaterials*, 87(1):286–301, 2008.

[103] Y. Li and C. Aparicio. Discerning the Subfibrillar Structure of Mineralized Collagen Fibrils: A Model for the Ultrastructure of Bone. *PLOS ONE*, 8(9):e76782, sep 2013.

[104] C. Licini, C. Vitale-Brovarone, and M. Mattioli-Belmonte. Collagen and non-collagenous proteins molecular crosstalk in the pathophysiology of osteoporosis. *Cytokine and Growth Factor Reviews*, 49(September):59–69, 2019.

[105] C. P. Lin, W. H. Douglas, and S. L. Erlandsen. Scanning electron microscopy of type I collagen at the dentin-enamel junction of human teeth. *Journal of Histochemistry and Cytochemistry*, 41(3):381–388, 1993.

[106] H.-C. Liu, G. A. Dahlen, and J. R. Osborne. Critical Dimension Atomic Force Microscopy for Sub-50-nm Microelectronics Technology Nodes BT - Applied Scanning Probe Methods VIII: Scanning Probe Microscopy Techniques. In B. Bhushan, H. Fuchs, and M. Tomitori, editors, *Applied Scanning Probe Methods VIII*, pages 31–75. Springer Berlin Heidelberg, Berlin, Heidelberg, 2008.

[107] R. Lucchini, D. Carnelli, M. Ponzoni, E. Bertarelli, D. Gastaldi, and P. Vena. Role of damage mechanics in nanoindentation of lamellar bone at multiple sizes : Experiments and numerical modeling. *Journal of the Mechanical Behavior of Biomedical Materials*, 4(8):1852–1863, 2011.

[108] K. W. Luczynski, T. Brynk, B. Ostrowska, W. Swieszkowski, R. Reihsner, and C. Hellmich. Consistent quasistatic and acoustic elasticity determination of poly-L-lactide-based rapid-prototyped tissue engineering scaffolds. *Journal of Biomedical Materials Research - Part A*, 101 A(1):138–144, 2013.

[109] K. W. Luczynski, A. Steiger-Thirsfeld, J. Bernardi, J. Eberhardsteiner, and C. Hellmich. Extracellular bone matrix exhibits hardening elastoplasticity and more than double cortical strength: Evidence from homogeneous compression of non-tapered single micron-sized pillars welded to a rigid substrate. *Journal of the Mechanical Behavior of Biomedical Materials*, 52:51–62, 2015.

[110] X. Maeder, W. M. Mook, C. Niederberger, and J. Michler. Quantitative stress/strain mapping during micropillar compression. *Philosophical Magazine*, 91(7-9):1097–1107, 2011.

[111] A. E. Maghraoui and C. Roux. Review DXA scanning in clinical practice. *Quarterly Journal of Medicine*, 101:605–617, 2008.

[112] R. Mahnken. *Lehrbuch der Technischen Mechanik - Elastostatik*. Springer Vieweg, 2015.

[113] L. Maïmoun, T. C. Brennan-Speranza, R. Rizzoli, and P. Ammann. Effects of ovariectomy on the changes in microarchitecture and material level properties in response to hind leg disuse in female rats. *Bone*, 51(3):586–591, 2012.

[114] T. Maurer, M. H. Stoffel, Y. Belyaev, N. G. Stiefel, B. Vidondo, S. Küker, H. Mogel, B. Schäfer, and J. Balmer. Structural characterization of four different naturally occurring porcine collagen membranes suitable for medical applications. *PLOS ONE*, 13(10):e0205027, oct 2018.

[115] M. D. McKee and A. Nanci. Osteopontin at mineralized tissue interfaces in bone, teeth, and osseointegrated implants: Ultrastructural distribution and implications for mineralized tissue formation, turnover, and repair. *Microscopy Research and Technique*, 33(2):141–164, feb 1996.

[116] S. J. Mellon and K. E. Tanner. Bone and its adaptation to mechanical loading: A review. *International Materials Reviews*, 57(5):235–255, 2012.

[117] M. Milazzo, G. S. Jung, S. Danti, and M. J. Buehler. Mechanics of Mineralized Collagen Fibrils upon Transient Loads. *ACS Nano*, 14:8307–8316, 2020.

[118] M. J. Mirzaali, J. J. Schwiedrzik, S. Thaiwichai, J. P. Best, J. Michler, P. K. Zysset, and U. Wolfram. Mechanical properties of cortical bone and their relationships with age, gender, composition and microindentation properties in the elderly. *Bone*, 93:196–211, dec 2016.

[119] E. F. Morgan, G. L. Barnes, and T. A. Einhorn. Chapter 1 - The Bone Organ System: Form and Function. pages 3–20. Academic Press, San Diego, 2013.

[120] E. F. Morgan, G. U. Unnikrisnan, and A. I. Hussein. Bone Mechanical Properties in Healthy and Diseased States. *Annual Review of Biomedical Engineering*, 20:119–143, 2018.

[121] S. Morgan, A. A. Poundarik, and D. Vashishth. Do Non-collagenous Proteins Affect Skeletal Mechanical Properties? *Calcified Tissue International*, 97(3):281–291, 2015.

[122] S. Mosca, C. Conti, N. Stone, and P. Matousek. Spatially offset Raman spectroscopy. *Nature Reviews Methods Primers*, 1(1):21, 2021.

[123] T. Nagoshi, A. Shibata, Y. Todaka, T. Sato, and M. Sone. Mechanical behavior of a microsized pillar fabricated from ultrafine-grained ferrite evaluated by a microcompression test. *Acta Materialia*, 73:12–18, 2014.

[124] R. K. Nalla, J. J. Kruzic, J. H. Kinney, M. Balooch, J. W. Ager, and R. O. Ritchie. Role of microstructure in the aging-related deterioration of the toughness of human cortical bone. *Materials Science and Engineering C*, 26(8):1251–1260, 2006.

[125] A. Nanci. Content and Distribution of Noncollagenous Matrix Proteins in Bone and Cementum: Relationship to Speed of Formation and Collagen Packing Density. *Journal of Structural Biology*, 126(3):256–269, 1999.

[126] V. Nedelkovski, O. G. Andriotis, K. Wieland, C. Gasser, A. Steiger-Thirsfeld, J. Bernardi, B. Lendl, M. L. Pretterklieber, and P. J. Thurner. Microbeam bending of hydrated human cortical bone lamellae from the central region of the body of femur shows viscoelastic behavior. *Journal of the Mechanical Behavior of Biomedical Materials*, conditiona, 2021.

[127] V. Nedelkovski, R. Hahn, P. H. Mayrhofer, A. Steiger-Thirsfeld, J. Bernardi, and P. J. Thurner. Influence of experimental constraints on micromechanical assessment of micromachined hard-tissue samples. *Journal of the Mechanical Behavior of Biomedical Materials*, 106(August 2019):103741, 2020.

[128] X. Neil Dong and X. Edward Guo. The dependence of transversely isotropic elasticity of human femoral cortical bone on porosity. *Journal of Biomechanics*, 37(8):1281–1287, 2004.

[129] S. Nobakhti, O. L. Katsamenis, N. Zaarour, G. Limbert, and P. J. Thurner. Elastic modulus varies along the bovine femur. *Journal of the Mechanical Behavior of Biomedical Materials*, 71(March):279–285, 2017.

[130] S. Nobakhti, G. Limbert, and P. J. Thurner. Cement lines and interlamellar areas in compact bone as strain amplifiers - Contributors to elasticity, fracture toughness and mechanotransduction. *Journal of the Mechanical Behavior of Biomedical Materials*, 29:235–251, 2014.

[131] M. Nordin and V. H. Frankel. *Basic Biomechanics of the Musculoskeletal System.* Lippincott Williams & Wilkins, 2012.

[132] F. Nudelman, K. Pieterse, A. George, P. H. Bomans, H. Friedrich, L. J. Brylka, P. A. Hilbers, G. De With, and N. A. Sommerdijk. The role of collagen in bone apatite formation in the presence of hydroxyapatite nucleation inhibitors. *Nature Materials*, 9(12):1004–1009, 2010.

[133] J. S. Nyman and A. J. Makowski. The Contribution of the Extracellular Matrix to the Fracture Resistance of Bone. *Current Osteoporosis Reports*, 10(2):169–177, 2012.

[134] J. S. Nyman, Q. Ni, D. P. Nicolella, and X. Wang. Measurements of mobile and bound water by nuclear magnetic resonance correlate with mechanical properties of bone. *Bone*, 42(1):193–199, 2008.

[135] J. S. Nyman, M. Reyes, and X. Wang. Effect of ultrastructural changes on the toughness of bone. *Micron*, 36(7-8):566–582, 2005.

[136] J. S. Nyman, A. Roy, X. Shen, R. L. Acuna, J. H. Tyler, and X. Wang. The influence of water removal on the strength and toughness of cortical bone. *Journal of Biomechanics*, 39(5):931–938, 2006.

[137] W. Oliver and G. Pharr. Measurement of hardness and elastic modulus by instrumented indentation: Advances in understanding and refinements to methodology. *Journal of Materials Research*, 19(01):3–20, 2004.

[138] G. Osterhoff, E. F. Morgan, S. J. Shefelbine, L. Karim, L. M. McNamara, and P. Augat. Bone mechanical properties and changes with osteoporosis. *Injury*, 47:S11–S20, 2016.

[139] OverlordQ. Atomic force microscope block diagram.svg. `https://commons.wikimedia.org/wiki/File:Atomic_force_microscope_block_diagram.svg`, 2020. last accessed: 16. February 2023.

BIBLIOGRAPHY

[140] E. P. Paschalis, E. DiCarlo, F. Betts, P. Sherman, R. Mendelsohn, and A. L. Boskey. FTIR microspectroscopic analysis of human osteonal bone. *Calcified Tissue International*, 59(6):480–487, 1996.

[141] S. Pathak, J. Gregory Swadener, S. R. Kalidindi, H.-W. Courtland, K. J. Jepsen, and H. M. Goldman. Measuring the dynamic mechanical response of hydrated mouse bone by nanoindentation. *Journal of the Mechanical Behavior of Biomedical Materials*, 4(1):34–43, 2011.

[142] J. A. Petruska and A. J. Hodge. A SUBUNIT MODEL FOR THE TROPOCOLLAGEN MACROMOLECULE. *Proceedings of the National Academy of Sciences*, 51(5):871 LP – 876, may 1964.

[143] Ponor. Electron-matter interaction volume and various types of signal generated - v2.svg. https://commons.wikimedia.org/wiki/File:Electron-matter_interaction_volume_and_various_types_of_signal_generated_-_v2.svg, 2020. last accessed: 16. February 2023.

[144] A. A. Poundarik, T. Diab, G. E. Sroga, A. Ural, A. L. Boskey, C. M. Gundberg, and D. Vashishth. Dilatational band formation in bone. *Proceedings of the National Academy of Sciences of the United States of America*, 109(47):19178–19183, 2012.

[145] P. M. Prodinger, P. Foehr, D. Bürklein, O. Bissinger, H. Pilge, K. Kreutzer, R. V. E. Rothe, and T. Tischer. Whole bone testing in small animals : systematic characterization of the mechanical properties of different rodent bones available for rat fracture models. *European Journal of Medical Research*, 23(8):1–11, 2018.

[146] R. K. Rai and N. Sinha. Dehydration-Induced Structural Changes in the Collagen–Hydroxyapatite Interface in Bone by High-Resolution Solid-State NMR Spectroscopy. *The Journal of Physical Chemistry C*, 115(29):14219–14227, jul 2011.

[147] K. R. Rajagopal. The elasticity of elasticity. *Zeitschrift fur Angewandte Mathematik und Physik*, 58(2):309–317, 2007.

[148] S. A. Reid. A study of lamellar organisation in juvenile and adult human bone. *Anatomy and Embryology*, 174(3):329–338, 1986.

[149] L. Reimer. *Scanning Electron Microscopy Physics of Image Formation and Microanalysis*. Springer-Verlag Berlin Heidelberg GmbH, second edi edition, 1998.

[150] A. G. Reisinger, M. Frank, P. J. Thurner, and D. H. Pahr. A two-layer elasto-visco-plastic rheological model for the material parameter identification of bone tissue. *Biomechanics and Modeling in Mechanobiology*, 19(6):2149–2162, 2020.

[151] A. G. Reisinger, D. H. Pahr, and P. K. Zysset. Principal stiffness orientation and degree of anisotropy of human osteons based on nanoindentation in three distinct planes. *Journal of the Mechanical Behavior of Biomedical Materials*, 4(8):2113–2127, 2011.

[152] I. Revenko, F. Sommer, D. T. Minh, R. Garrone, and J.-M. Franc. Atomic force microscopy study of the collagen fibre structure. *Biology of the Cell*, 80(1):67–69, jan 1994.

[153] N. Reznikov, R. Shahar, and S. Weiner. Acta Biomaterialia Bone hierarchical structure in three dimensions. *Acta Biomaterialia*, 10(9):3815–3826, 2014.

[154] J. Y. Rho, L. Kuhn-Spearing, and P. Zioupos. Mechanical properties and the hierarchical structure of bone. *Medical Engineering and Physics*, 20(2):92–102, 1998.

[155] J. Y. Rho, T. Y. Tsui, and G. M. Pharr. Elastic properties of human cortical and trabecular lamellar bone measured by nanoindentation. *Biomaterials*, 18(20):1325–1330, 1997.

[156] R. O. Ritchie, J. H. Kinney, J. J. Kruzic, and R. K. Nalla. A fracture mechanics and mechanistic approach to the failure of cortical bone. *Fatigue and Fracture of Engineering Materials and Structures*, 28(4):345–371, apr 2005.

[157] P. Roschger, P. Fratzl, J. Eschberger, and K. Klaushofer. Validation of quantitative backscattered electron imaging for the measurement of mineral density distribution in human bone biopsies. *Bone*, 23(4):319–326, oct 1998.

[158] P. Roschger, E. P. Paschalis, P. Fratzl, and K. Klaushofer. Bone mineralization density distribution in health and disease. *Bone*, 42(3):456–466, 2008.

[159] J. E. Sader, J. W. Chon, and P. Mulvaney. Calibration of rectangular atomic force microscope cantilevers. *Review of Scientific Instruments*, 70(10):3967–3969, 1999.

[160] M. Saito and K. Marumo. Collagen cross-links as a determinant of bone quality: A possible explanation for bone fragility in aging, osteoporosis, and diabetes mellitus. *Osteoporosis International*, 21(2):195–214, 2010.

[161] J. Salençon. *Handbook of Continuum Mechanics - General Concepts Thermoelasticity*. Springer-Verlag Berlin Heidelbeig, New York, 2001.

[162] N. Sasaki, A. Tagami, T. Goto, M. Taniguchi, M. Nakata, and K. Hikichi. Atomic force microscopic studies on the structure of bovine femoral cortical bone at the collagen fibril-mineral level. *Journal of Materials Science: Materials in Medicine*, 13(3):333–337, 2002.

[163] S. H. Schlecht, E. M. R. B. Ms, and K. J. Jepsen. How Does Bone Strength Compare Across Sex , Site , and Ethnicity ? *Clinical Orthopaedics and Related Research®*, pages 2540–2547, 2015.

[164] S. Schrof, P. Varga, L. Galvis, K. Raum, and A. Masic. 3D Raman mapping of the collagen fibril orientation in human osteonal lamellae. *Journal of Structural Biology*, 187(3):266–275, 2014.

[165] S. C. E. Schuit, M. van der Klift, A. Weel, C. de Laet, H. Burger, E. Seeman, A. Hofman, A. G. Uitterlinden, J. van Leeuwen, and H. A. P. Pols. Fracture incidence and association with bone mineral density in elderly men and women: the Rotterdam Study. *Bone*, 34(1):195–202, 2004.

[166] H. P. Schwarcz, D. Abueidda, and I. Jasiuk. The ultrastructure of bone and its relevance to mechanical properties. *Frontiers in Physics*, 5(SEP), 2017.

[167] J. Schwiedrzik, R. Raghavan, A. Bürki, V. LeNader, U. Wolfram, J. Michler, and P. Zysset. In situ micropillar compression reveals superior strength and ductility but an absence of damage in lamellar bone. *Nature materials*, 13(June):1–8, 2014.

[168] J. Schwiedrzik, R. Raghavan, A. Bürki, V. LeNader, U. Wolfram, J. Michler, and P. Zysset. In situ micropillar compression reveals superior strength and ductility but an absence of damage in lamellar bone. *Nature materials*, (June):1–8, 2014.

[169] J. Schwiedrzik, A. Taylor, D. Casari, U. Wolfram, P. Zysset, and J. Michler. Nanoscale deformation mechanisms and yield properties of hydrated bone extracellular matrix. *Acta Biomaterialia*, 60:302–314, 2017.

[170] A. Sharir, M. M. Barak, and R. Shahar. Whole bone mechanics and mechanical testing. *Veterinary Journal*, 177(1):8–17, 2008.

[171] E. Sillero, O. A. Williams, V. Lebedev, V. Cimalla, C.-C. Röhlig, C. E. Nebel, and F. Calle. Static and dynamic determination of the mechanical properties of nanocrystalline diamond micromachined structures. *Journal of Micromechanics and Microengineering*, 19(11):115016, nov 2009.

[172] M. J. Silva, M. D. Brodt, Z. Fan, and J. Y. Rho. Nanoindentation and whole-bone bending estimates of material properties in bones from the senescence accelerated mouse SAMP6. *Journal of Biomechanics*, 37(11):1639–1646, 2004.

BIBLIOGRAPHY

[173] J. G. Skedros, C. J. Kiser, K. E. Keenan, and S. C. Thomas. Analysis of osteon morphotype scoring schemes for interpreting load history: Evaluation in the chimpanzee femur. *Journal of Anatomy*, 218(5):480–499, 2011.

[174] I. N. Sneddon. The relation between load and penetration in the axisymmetric boussinesq problem for a punch of arbitrary profile. *International Journal of Engineering Science*, 3(1):47–57, may 1965.

[175] G. E. Sroga and D. Vashishth. Phosphorylation of Extracellular Bone Matrix Proteins and Its Contribution to Bone Fragility. *Journal of Bone and Mineral Research*, 33(12):2214–2229, 2018.

[176] D. J. Stokes. Investigating Biological Ultrastructure using Environmental Scanning Electron Microscopy (ESEM). 2004.

[177] Sundar, R. How to find yield strain corresponding to 0.2 % offset yield stress? `https://www.researchgate.net/post/How_to_find_Yield_strain_corresponding_to_02_offset_yield_stress`, 2018. last accessed: 16. February 2023.

[178] M. E. Szabó and P. J. Thurner. Anisotropy of bovine cortical bone tissue damage properties. *Journal of Biomechanics*, 46(1):2–6, 2013.

[179] N. Tarcea, T. Frosch, P. Rösch, M. Hilchenbach, T. Stuffler, S. Hofer, H. Thiele, R. Hochleitner, and J. Popp. Raman Spectroscopy—A Powerful Tool for in situ Planetary Science. *Space Science Reviews*, 135(1):281–292, 2008.

[180] J. B. Thompson, J. H. Kindt, B. Drake, H. G. Hansma, D. E. Morse, and P. K. Hansma. Bone indentation recovery time correlates with bond reforming time. *Nature*, 414(6865):773–776, 2001.

[181] P. J. Thurner. Atomic force microscopy and indentation force measurement of bone. *Wiley Interdisciplinary Reviews: Nanomedicine and Nanobiotechnology*, 1(6):624–649, nov 2009.

208

[182] P. J. Thurner, C. G. Chen, S. Ionova-Martin, L. Sun, A. Harman, A. Porter, J. W. Ager, R. O. Ritchie, and T. Alliston. Osteopontin deficiency increases bone fragility but preserves bone mass. *Bone*, 46(6):1564–1573, 2010.

[183] P. J. Thurner, B. Erickson, R. Jungmann, Z. Schriock, J. C. Weaver, G. E. Fantner, G. Schitter, D. E. Morse, and P. K. Hansma. High-speed photography of compressed human trabecular bone correlates whitening to microscopic damage. *Engineering Fracture Mechanics*, 74(12):1928–1941, 2007.

[184] P. J. Thurner and O. L. Katsamenis. The role of nanoscale toughening mechanisms in osteoporosis. *Current Osteoporosis Reports*, 12(3):351–356, 2014.

[185] P. J. Thurner, S. Lam, J. C. Weaver, D. E. Morse, and P. K. Hansma. Localization of phosphorylated serine, osteopontin, and bone sialoprotein on bone fracture surfaces. *Journal of Adhesion*, 85(8):526–545, 2009.

[186] B. Tlili, H. Guizani, K. Aouadi, and M. Nasser. Multi-Scale Modeling of Mechanobiological Behavior of Bone. In *BioMechanics and Functional Tissue Engineering*, pages 1–24. IntechOpen, 2021.

[187] K. Torkar, W. Riedler, C. P. Escoubet, M. Fehringer, R. Schmidt, R. J. Grard, H. Arends, F. Rüdenauer, W. Steiger, B. T. Narheim, K. Svenes, R. Torbert, M. André, A. Fazakerley, R. Goldstein, R. C. Olsen, A. Pedersen, E. Whipple, and H. Zhao. Active spacecraft potential control for Cluster - Implementation and first results. *Annales Geophysicae*, 19(12 PART I):1289–1302, 2001.

[188] F. A. Trémollieres, J.-M. Pouillès, N. Drewniak, J. Laparra, C. A. Ribot, and P. Dargent-Molina. Fracture risk prediction using bmd and clinical risk factors in early postmenopausal women: Sensitivity of the who frax tool. *Journal of Bone and Mineral Research*, 25(5):1002–1009, 2010.

[189] C. E. Tye, G. K. Hunter, and H. A. Goldberg. Identification of the Type I Collagen-binding Domain of Bone Sialoprotein and Characterization of the

BIBLIOGRAPHY

Mechanism of Interaction *. *Journal of Biological Chemistry*, 280(14):13487–13492, apr 2005.

[190] M. D. Uchic and D. M. Dimiduk. A methodology to investigate size scale effects in crystalline plasticity using uniaxial compression testing. *Materials Science and Engineering A*, 400-401(1-2 SUPPL.):268–278, 2005.

[191] A. C. Ugural and S. K. Fenster. *Advanced Strength and Applied Elasticity*. Pearson, 4th edition, 2003.

[192] M. Unal and O. Akkus. Raman spectral classification of mineral- and collagen-bound water's associations to elastic and post-yield mechanical properties of cortical bone. *Bone*, 81:315–326, 2015.

[193] I. Utke, P. Hoffmann, and J. Melngailis. Gas-assisted focused electron beam and ion beam processing and fabrication. *Journal of Vacuum Science & Technology B: Microelectronics and Nanometer Structures*, 26(4):1197, 2008.

[194] J. A. Van Der Rijt, K. O. Van Der Werf, M. L. Bennink, P. J. Dijkstra, and J. Feijen. Micromechanical testing of individual collagen fibrils. *Macromolecular Bioscience*, 6(9):697–702, 2006.

[195] A. Vercher, E. Giner, C. Arango, J. E. Tarancón, and F. J. Fuenmayor. Homogenized stiffness matrices for mineralized collagen fibrils and lamellar bone using unit cell finite element models. *Biomechanics and Modeling in Mechanobiology*, 13:437–449, 2014.

[196] S. Vlassov, B. Polyakov, L. M. Dorogin, M. Antsov, M. Mets, M. Umalas, R. Saar, R. Lõhmus, and I. Kink. Elasticity and yield strength of pentagonal silver nanowires: In situ bending tests. *Materials Chemistry and Physics*, 143(3):1026–1031, 2014.

[197] C. a. Volkert, a. M. Minor, G. Editors, and B. May. Focused Ion Beam Microscopy and Micromachining. *MRS Bulletin*, 32(May):389–399, 2007.

[198] W. Wagermaier, H. S. Gupta, A. Gourrier, M. Burghammer, P. Roschger, and P. Fratzl. Spiral twisting of fiber orientation inside bone lamellae. *Biointerphases*, 1(1):1–5, 2006.

[199] S. Weiner and W. Traub. Bone structure: from ångstroms to microns. *The FASEB Journal*, 6(3):879–885, 1992.

[200] S. Weiner and H. D. Wagner. The Material Bone: Structure-Mechanical Function Relations. *Annual Review of Materials Science*, 28(1):271–298, 1998.

[201] T. J. Wess and J. P. Orgel. Changes in collagen structure: drying, dehydrothermal treatment and relation to long term deterioration. *Thermochimica Acta*, 365(1):119–128, 2000.

[202] P. E. West. *Introduction to Atomic Force Microscopy: Theory, Practice, Applications.* P. West, 2006.

[203] U. Wolfram and J. Schwiedrzik. Post-yield and failure properties of cortical bone. *BoneKEy Reports*, 5(AUGUST):1–10, 2016.

[204] World Health Organization. WHO Scientific Group on the Assessment of Osteoporosis At Primary Health Care Level. Technical report, 2004.

[205] Z. Wu, T. C. Ovaert, and G. L. Niebur. Viscoelastic properties of human cortical bone tissue depend on gender and elastic modulus. *Journal of Orthopaedic Research*, 30(5):693–699, 2013.

[206] J. Xu, J. Y. Rho, S. R. Mishra, and Z. Fan. Atomic force microscopy and nanoindentation characterization of human lamellar bone prepared by microtome sectioning and mechanical polishing technique. *Journal of biomedical materials research. Part A*, 67(3):719–726, dec 2003.

[207] J. Yamashita, X. Li, B. R. Furman, H. R. Rawls, X. Wang, and C. M. Agrawal. Collagen and bone viscoelasticity: A dynamic mechanical analysis. *Journal of Biomedical Materials Research*, 63(1):31–36, jan 2002.

BIBLIOGRAPHY

[208] Y. N. Yeni and T. L. Norman. Fracture toughness of human femoral neck: Effect of microstructure, composition, and age. *Bone*, 26(5):499–504, 2000.

[209] R. M. D. Zebaze, A. Ghasem-Zadeh, A. Bohte, S. Iuliano-Burns, M. Mirams, R. I. Price, E. J. Mackie, and E. Seeman. Intracortical remodelling and porosity in the distal radius and post-mortem femurs of women: a cross-sectional study. *The Lancet*, 375(9727):1729–1736, may 2010.

[210] H. Zhang, B. E. Schuster, Q. Wei, and K. T. Ramesh. The design of accurate micro-compression experiments. *Scripta Materialia*, 54(2):181–186, 2006.

[211] S. Zhao, M. Arnold, R. L. Abel, J. P. Cobb, S. Ma, U. Hansen, and O. Boughton. Standardizing Compression Testing for Measuring the Stiffness of Human Bone. *Bone and Joint Research*, 7(8):524–538, 2018.

[212] J. F. Ziegler and J. P. Biersack. *The Stopping and Range of Ions in Matter*, pages 93–129. Springer US, Boston, MA, 1985.

[213] E. A. Zimmermann, E. Schaible, B. Gludovatz, F. N. Schmidt, C. Riedel, M. Krause, E. Vettorazzi, C. Acevedo, M. Hahn, K. Püschel, S. Tang, M. Amling, R. O. Ritchie, and B. Busse. Intrinsic mechanical behavior of femoral cortical bone in young , osteoporotic and bisphosphonate- treated individuals in low- and high energy fracture conditions. *Nature Publishing Group*, (October 2015):1–12, 2016.

[214] V. Ziv, I. Sabanay, T. Arad, W. Traub, and S. Weiner. Transitional structures in lamellar bone. *Microscopy Research and Technique*, 33(2):203–213, feb 1996.

[215] P. K. Zysset. Indentation of bone tissue: A short review. *Osteoporosis International*, 20(6):1049–1055, 2009.

[216] P. K. Zysset, X. Edward Guo, C. Edward Hoffler, K. E. Moore, and S. A. Goldstein. Elastic modulus and hardness of cortical and trabecular bone lamellae

measured by nanoindentation in the human femur. *Journal of Biomechanics*, 32(10):1005–1012, 1999.

Vedran Nedelkovski

Address	Leystraße 46/26, 1200 Vienna, Austria
Email	ved.ned@gmail.com
Mobile	+4369919463000
Date of birth	12. March 1987
Nationality	Croatian, Macedonian

Education

2013 - present   **TU Wien**, Vienna (Austria)
Doctoral Programme in Natural Sciences, Dissertation field: Biomechanics

06/2015   **International Centre for Mechanical Sciences (CISM)**, Udine (Italy)
Summer School "Bone Cell and Tissue Mechanics"

2005 – 2013   **University of Vienna**, Vienna (Austria)
Master of Science (Magister der Naturwissenschaften)
Physics

2010   Erasmus exchange programme
Katholieke Universiteit Leuven, Leuven (Belgium)
Molecular biophysics

Work experience

2019 – present   **Development engineer**
epitome GmbH, Vienna (Austria)
Technology Team

2013 – 2018   **University assistant**
TU Wien, Vienna (Austria)
Institute of Lightweight Design and Structural Biomechanics

2011 – 2012   **Diploma student**
AIT Austrian Institute of Technology GmbH, Vienna (Austria)
Biosensor Technologies

Teaching Experience

2013 – 2018   **University assistant**
TU Wien, Vienna (Austria)
Institute of Lightweight Design and Structural Biomechanics

Grants

2014   **Hochschuljubiläumsfonds of the City of Vienna**
Project H-287902/2014

Publications

<u>Nedelkovski V.</u>, Lahayne O., Frank M., Luczynski K. W., Steiger-Thirsfeld A., Bernardi J., Hellmich C., Thurner P. J. - *Micropillar compression of healthy and osteoporotic human cortical bone from the femoral neck*, 2023, *to be submitted*

<u>Nedelkovski V.</u>, Andriotis O. G., Wieland K., Gasser C., Steiger-Thirsfeld A., Bernardi J., Lendl B., Pretterklieber M. L., Thurner P. J. - *Microbeam bending of hydrated human cortical bone lamellae from the central region of the body of femur shows viscoelastic behaviour*, Journal of the mechanical behavior of biomedical materials, 2022, 125, 104815

<u>Nedelkovski V.</u>, Hahn R., Mayrhofer P. H., Steiger-Thirsfeld A., Bernardi J., Thurner P. J. – *Influence of experimental constraints on micromechanical assessment of micromachined hard-tissue samples*, Journal of the mechanical behavior of biomedical materials, 2020, 106, 103741

Collins C. J., Andriotis O. G., <u>Nedelkovski V.</u>, Frank M., Katsamenis O. L., Thurner P. J. – *Bone Micro- and Nanomechanics*, Encyclopedia of Biomedical Engineering, Elsevier, 2019, 22-44

Kain L., Andriotis O. G., Gruber P., Frank M., Markovic M., Grech D., <u>Nedelkovski V.</u>, Stolz M., Ovsianikov A., Thurner P. J. - *Calibration of colloidal probes with atomic force microscopy for micromechanical assessment, Journal of the mechanical behavior of biomedical materials*, 2018, 85, 225-236

Frank M., Marx D., <u>Nedelkovski V.</u>, Fischer J., Pahr D. H., Thurner P. J. - *Dehydration of individual bovine trabeculae causes transition from ductile to quasi-brittle failure mode*, Journal of the mechanical behavior of biomedical materials, 2018, 87, 296-305

<u>Nedelkovski V.</u>, Schwaighofer A., Geiss A. F., Bliem C., Naumann R. L. C. - *Interactions of Photosynthetic Reaction Centers with Bc1 Complexes from Rhodobacter Sphaeroides Studied Using SEIRAS on a Nano-Structured Gold Surface*, International Journal of Bioorganic Chemistry, 2017, 2(2), 61-69

<u>Nedelkovski V.</u>, Schwaighofer A., Wraight C., Naumann R. L. C., Nowak C. – *Surface-Enhanced Infrared Absorption Spectroscopy (SEIRAS) of Light-Activated Photosynthetic Reaction Centers from Rhodobacter sphaeroides Reconstituted in a Biomimetic Membrane System*, Journal of Physical Chemistry C, 2013, 117 (32), 16357-16363

Conference Presentations

Podium presentations

<u>Nedelkovski V.</u>, Andriotis O. G., Steiger-Thirsfeld A., Bernardi J., Thurner P. J., *AFM-based microbeam bending of human femoral cortical bone lamellae in physiological conditions*, Podium presentation at the 25th Congress of the European Society of Biomechanics ESB, 2019, Vienna, Austria

<u>Nedelkovski V.</u>, Andriotis O. G., Hahn R., Mayrhofer P. H., Steiger-Thirsfeld A., Bernardi J., Thurner P. J., *AFM-based microbeam bending of human cortical bone at the lamellar level*, Podium presentation at the Vienna Young Scientists Symposium VSS, 2019, Vienna Austria

<u>Nedelkovski V.</u>, Andriotis O. G., Hahn R., Mayrhofer P. H., Thurner P. J., *Experimental micromechanical assessment of human cortical bone at the lamellar level*, Podium presentation at the Annual Meeting of the Austrian Cluster for Tissue Regeneration ACTR, 2019, Vienna, Austria

<u>Nedelkovski V.</u>, Andriotis O. G., Hahn R., Mayrhofer P. H., Thurner P. J., *AFM-based microbeam bending of human cortical bone lamellae from the femur midshaft*, Podium presentation at the 90th Annual Meeting of the International Association of Applied Mathematics and Mechanics GAMM, 2019, Vienna, Austria

<u>Nedelkovski V.</u>, Andriotis O. G., Thurner P. J., *Orientation-dependent micromechanical three-point-bending test of cortical bone*, Podium presentation at the 22nd Congress of the European Society of Biomechanics ESB, 2016, Lyon, France

<u>Nedelkovski V.</u>, Andriotis O. G., Thurner P. J., *Micromechanical three-point-bending test of lamellae in cortical bone*, Podium Presentation at the 21st Congress of the European Society of Biomechanics ESB, 2015, Prague, Czech Republic

Poster presentations

<u>Nedelkovski V.</u>, Lahayne O., Frank M., Luczynski K. W., Binder E., Pichler B., Hellmich C., Thurner P. J., *Micropillar compression of healthy and osteoporotic human cortical bone from the femoral neck*, Poster presentation at the 8th World Congress of Biomechanics WCB, 2018, Dublin Ireland

Skills

Languages	German: C1/C2 (ÖSD Zertifikat C1) English: C1/C2 (Certificate of Advanced English (CAE), Cambridge Exams) Dutch: B1 (Nederlandistik, University of Vienna) Croatian: mother tongue Macedonian: mother tongue
Professional	Rotational rheology Electron/ion microscopy (SEM, FIB) Atomic force microscopy (AFM), Nanoindentation Infrared Spectroscopy MS office, Origin, Matlab, Hyperworks, SolidWorks

Vedran Nedelkovski